THE 1978 YELLOWSTONE SNAKE RIVER PLAIN SEISMIC PROFILING EXPERIMENT

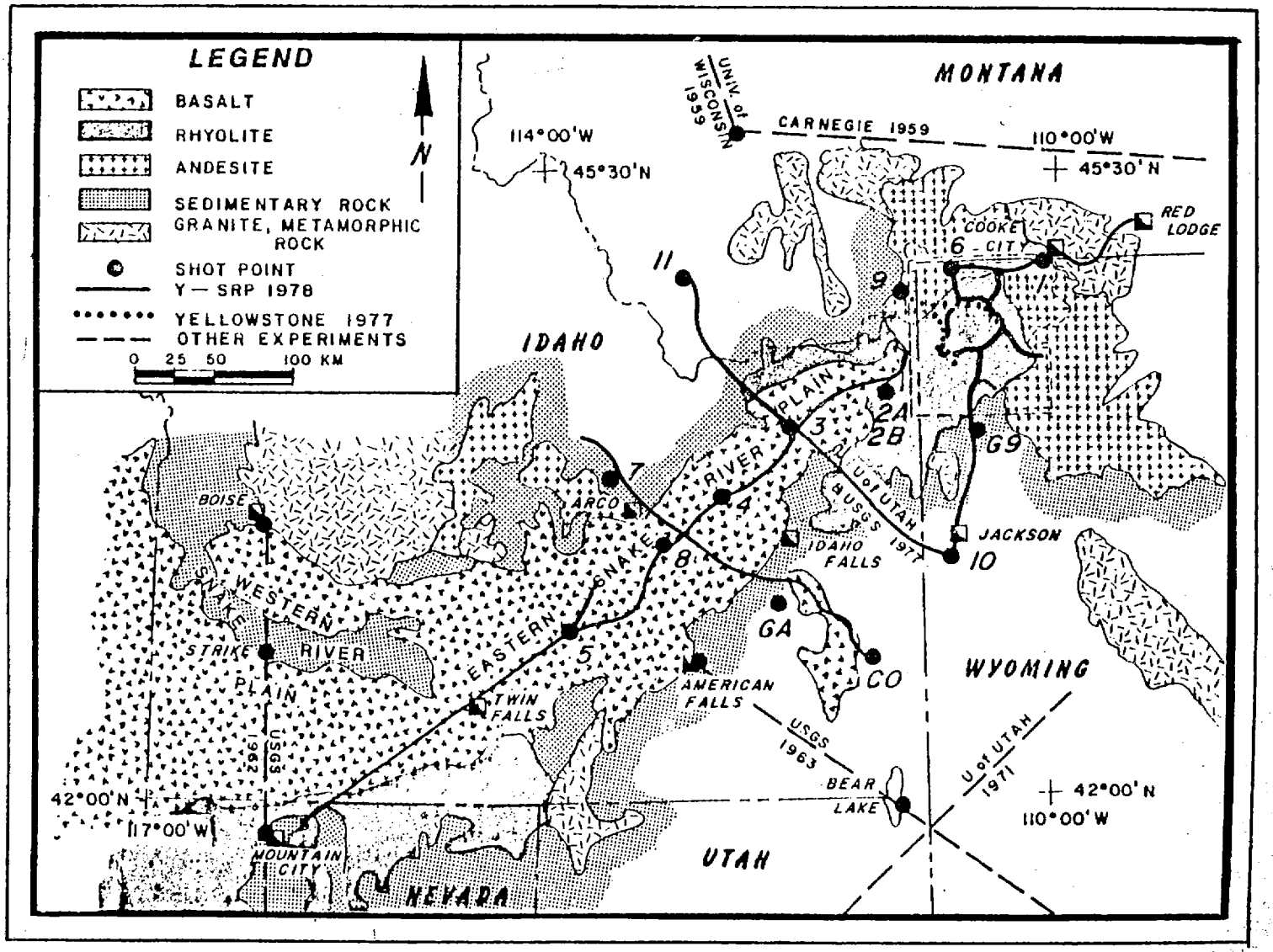

THE 1978 YELLOWSTONE-EASTERN SNAKE RIVER PLAIN SEISMIC PROFILING EXPERIMENT: CRUSTAL STRUCTURE OF THE YELLOWSTONE REGION AND EXPERIMENT DESIGN

R. B. Smith (Department of Geology and Geophysics, University of Utah, Salt Lake City, Utah 84112)

M. M. Schilly (Department of Geology and Geophysics, University of Utah, Salt Lake City, Utah 84112)[1]

L. W. Braile (Department of Geosciences, Purdue University, West Lafayette, Indiana 47907)

J. Ansorge (Geophysics Institute, Swiss Federal Institute of Technology, Zurich, Switzerland)

M. R. Baker (Department of Geosciences, Purdue University, West Lafayette, Indiana 47907)[2]

C. Prodehl (Geophysics Institute, University of Karlsruhe, Karlsruhe, West Germany)

J. H. Healy (U.S. Geological Survey, Menlo Park, California 94025)

St. Mueller (Geophysics Institute, Swiss Federal Institute of Technology, Zurich, Switzerland)

R. W. Greenfelder (Department of Geophysics, Stanford University, Stanford, California 94305)

[1]Now at the Amoco Prod. Co., Security Life Bldg., Denver, Colorado 80202
[2]Now at the Exxon Prod. Res. Co., Box 2189, Houston Texas 77001

ABSTRACT

In 1978 a long-line seismic profiling experiment was conducted in the Yellowstone-eastern Snake River Plain region of North America. This project was a cooperative U.S.-European scientific experiment that was aimed at deep seismic probing of the lithosphere in this major continental volcano-tectonic province using refraction and reflection methods. Fifteen shots were recorded that provided one- and two- dimensional coverage to distances of 300 km. From these data, travel time and synthetic seismogram modeling was used to evaluate an average crustal and upper-mantle, P-wave velocity and Q structure. Beneath the hydrothermally active and extensive Quaternary silicic volcanic rocks of the Yellowstone Plateau the crustal structure consists of a highly variable near-surface layer approximately 2 km thick, 3.0 km/s to 4.8 km/s, with a Q of 30. This layer corresponds to the weathered rhyolites and sedimentary caldera infill. Below the surface layer, a 3 km to 4 km thick unit of variable velocity, 4.9 km/s to 5.5 km/s with Q's of 50 to 200 is thought to represent the accumulation of the Yellowstone Pleistocene-Quaternary rhyolites, ash flow tuffs and possible Phanerozoic metamorphic equivalents. The crystalline upper-crust is characterized by a laterally inhomogeneous layer that varies in velocity from 4.0 km/s to 6.1 km/s with a Q of 300 and appears to be a cooling but still hot "granitic" body beneath the Yellowstone caldera. This unit is thought to be a remnant of the original magma chambers that produced the Quaternary silicic volcanic rocks of the Yellowstone Plateau and may still be a major contributor to the very high heat flow. A laterally homogeneous intermediate crustal layer 8 km to 10 km thick, has a velocity of 6.5 km/s with Q's of 100 to 300, and overlies a homogeneous 25 km thick

lower crust with a velocity of 6.7 km/s to 6.8 km/s and a Q of 300. The total crustal thickness is 43 km. The upper crustal layer, 4.0 km/s to 5.7 km/s, is thought to be the equivalent of the continental "granitic" layer that is normally 15 km to 20 km thick in the surrounding thermally undistrubed Archean crust. The thermally altered equivalent of this layer is 5 km thick beneath the Island Park region then increases in thickness to 8 km as a laterally variable, 4.0 km/s to 5.5 km/s, layer beneath the Yellowstone Plateau; but appears as a homogeneous layer, 6.1 km/s, beneath the Beartooth Mountains to the northeast. The high seismic attenuation and large lateral velocity variations in the upper-crust are consistent with a model in which Archean granitic gneiss is altered by partial fractionation, partial melting and metamorphism; processes that differentiate silicic melts and produce the rhyolites and ash flow tuffs that are now widely distributed across the Yellowstone Plateau. The primary source of heat for the Yellowstone hydrothermal system appears to be upper-mantle basalts that have penetrated the lower crust without significant variations in velocity structure, but have heated and thermally altered the upper crust and produced the silicic volcanism and high heat flow. This model is consistent with the petrologic evidence for a systematic propogation of silicic volcanic centers along the eastern Snake River Plain, at average velocities of 3.5 cm/yr, to their present location beneath Yellowstone. While these data do not bear directly on the origin and source of the heat i.e. mantle plumes, lithospheric features, mantle radiogenetic heat, basal lithospheric shearing, etc. they do provide a constraint on the configuration and lateral extent of crustal layers that reflect thermal and compositional boundaries.

INTRODUCTION

The 1978 Yellowstone-eastern Snake River Plain (Y-SRP) seismic experiment was conducted as the result of new interest in long-line seismic profiling for crust and mantle structure in the United States. In the early 1960's seismic refraction profiling by the U.S. Geological Survey and several U.S. universities was conducted for purposes of elucidating crustal structure with extensive work in the central Great Basin (Pakiser, 1963) and for investigations of regional variations in upper-mantle structure (Archambeau, Flynn, and Lambert, 1969). In the 1960's-1970's, European (Giese, Prodehl, and Stein, 1976) and Soviet seismologists (for example, Kosminskaya, 1971) further developed the deep-seismic sounding, DSS profiling, recording from land and sea sources.

In the mid- to late-1970's renewed interest in long-line seismic profiling was generated as the result of developments in synthetic seismogram theory, mathetmatical inversion, improved recording techniques, and the need to relate velocity structure to rock composition, temperature, and pressure. For example, detailed seismic profiles from large quarry blasts in the Great Basin and Rocky Mountains showed distinct lateral-velocity variations at scales comparable to surface tectonics (Braile et al., 1974) and evidence of an upper-crustal low-velocity layer coincident with a regional zone of high heat flow and active tectonism (Smith, Braile, and Keller, 1975). With the increased resolution from detailed profiles and the ability to model and resolve laterally-varying velocity structure, the seismic refraction-reflection method became an attractive technique for detailed evaluation of crustal structure.

In 1976-77 while one of us (R. B. Smith) was at the Swiss Federal Institute of Technology-Zurich the feasibility of a cooperative U.S.-European long-line seismic experiment for North America was discussed with St. Mueller and J. Ansorge of ETH-Zurich; and C. Prodehl and K. Fuchs of Karlsruhe University. This proposed project was planned as a cooperative scientific experiment as well as a demonstration of the cooperative use of equipment and personnel from several research groups. Because of the interest of the University of Utah and Purdue University in the development of detailed seismic refraction and reflection techniques, these U.S. universities agreed to organize and seek support for the experiment. In 1977, with principal funding from the National Science Foundation and the Geothermal Research Program of the U.S. Geological Survey, a major seismic experiment was planned for September 1978 that involved personnel and instrumentation from twelve U.S. and European organizations (Table 1). In addition two private companies recorded the explosions for research purposes. General information on the blasts (locations, origin times, blast sizes, etc.) were immediately made available to interested users and final seismic record sections were made available to the public via an announcement in EOS (November, 1979).

Selection of the Yellowstone-eastern Snake River Plain region for the seismic experiment was based upon the recognition that it represented a major continental, volcano-tectonic province (over 800 km long) and suggested a lithospheric source of heating that had thermally perturbed and altered an overlying Archean crystalline crust. The seismic parameters (velocity, layer thicknes, and Q) were expected to provide insight into the origin and evolution of the continental lithosphere. The role of

melting and its effect upon layer dimensions, velocity perturbations, and seismic attenuation were considered important features that related to the mechanisms of lithospheric-asthenosphere interaction as well as to the process of intraplate fragmentation and volcanism. Lateral-velocity variations across transition zones between the thermally perturbed and undistrubed crust as well as velocity variations within the now thermally active Yellowstone hydrothermal system were also considered important objectives.

Volcano-Tectonic Setting

A brief discussion of the tectonic setting of the Yellowstone region, presented here, also provides the background information for the accompanying papers of Lehman et al. (1981) and Schilly et al. (1981). Yellowstone National Park is located at the northeast end of the eastern Snake River Plain-Yellowstone volcano-tectonic system (Figure 1). At Yellowstone it's unusually high temperatures and contemporary deformation reflect dynamic processes in the crust and upper mantle (Smith and Christiansen, 1980). The combined effects of these features have been interpreted as the product of a lithospheric "hot spot"; quite unlike other volcanically active hot spots such as Hawaii and Iceland that are related to interplate deformation. Unlike the oceanic features, the Yellowstone-eastern Snake River Plain system is located more than 2,000 km from the western boundary of the north North American plate; hence this volcanic province is unusual in terms of continental volcanism.

Recognition of the Yellowstone area as an anomalous tectonic feature was first perceived in the role of plate tectonics by Morgan (1972) who suggested that the volcanism was a result of an upper-mantle plume. Later interpretations suggested that the bimodal rhyolite/basalt suite that characterizes the Yellowstone-Snake River Plain system originates from fundamental lithospheric processes (Smith and Christiansen, 1980); namely that the basaltic magma, chemically similar to that found in oceanic settings is formed in the upper mantle then rises through the silicic crust producing partial melting of the metamorphic components, generating a viscous, rhyolitic magma. The light silicic component then rises to the surface possibly facilitated by a lithospheric fracture system (Smith, 1978) and drives

the Yellowstone hydrothermal and magmatic systems. Heating and melting are thought to perturb the velocity layering of the crust and upper mantle by compositional and phase variations that are sufficiently large to be mapped by seismic techniques.

Topographically the eastern Snake River Plain, with elevations from 700 m to 1500 m, merges to a transition area at Island Park, then across the Yellowstone Plateau with an average elevation of 2200 m. Volcanism along the eastern Snake River Plain-Yellowstone system is primarily that of the bimodal rhyolite/basaltic suite. The silicic centers of volcanism have progressed systematically northeastward at 3.5 cm/yr (Armstrong, Leeman, and Malde, 1975) from southwestern Idaho beginning at 15 million years ago to the present site of activity at Yellowstone with its youngest volcanism of 50,000 to 70,000 years.

The Quaternary volcanic history of Yellowstone has been marked by continuous eruptions of rhyolites and ash flow tuffs beginning about 2.2 million years ago but interrupted by three climactic eruptions and caldera-forming collapses of the crust at 2.2 million years, 1.2 million years, and the most recent at 600,000 years that formed the Yellowstone caldera (R. L. Christiansen, 1978, personal communication; Christiansen and Black, 1972). Cummulatively 3,500 km^3 of silicic material was erupted in the Yellowstone region in Pleistocene-Quaternary time and the cumulative effects of the post-caldera collapse flows form the present topography. This large volume of silicic volcanics suggests the presence of magma chambers in the upper-crust and implies because of its youthfulness that residual magma or partial melts could still remain.

Further evidence of the unusual thermal processes in the earth's crust at Yellowstone are exhibited by the regional heat flow. The Yellowstone Plateau is surrounded by zones of low to average heat flow, ∿50 to 150 mWm^{-2}, however within the Yellowstone system the heat flow increases to over 1600 mWm^{-2} (Morgan et al., 1977; Smith and Christiansen, 1980)--more than 60 times the world average. The high heat flow is considered to be a combined effect of both conductive and convective heat transfer. The convective component associated with the hydrothermal systems is interpreted to have been active for at least the last 20,000 years and is thought to be the result of cooling magma beneath the plateau. The young volcanism and high heat flow suggest that magma and partial melt have existed quite recently beneath Yellowstone and the flow of heat through the caldera is thought to be due to cooling and crystallization of silicic magma bodies at depths of only a few kilometers.

Earthquake activity in the Yellowstone region is the highest of the Intermountain Seismic Belt and earthquakes as large as magnitude 7.1 have occurred in historic time. Earthquakes occur from the near-surface to depths of 20 km outside the Yellowstone caldera, but shallow markedly to maximum depths of about 5 km inside the caldera suggesting a thermal effect on brittle fracture. The pattern of epicenters and nodal planes from fault plane solutions in general follows the trends of Late Cenozoic fault zones; E-W on the west side of the Yellowstone caldera and N-S on the south side of the caldera but coalescing beneath the Yellowstone Plateau (Smith, 1978). This suggests widespread fracturing of the lithosphere and a large deviation in the stress field.

The contemporary crustal deformation of the Yellowstone Plateau has recently been demonstrated by geodetic releveling (Pelton and Smith,

1979; 1981, this volume) that showed in 53 years up to 723 mm of uplift in an area coincident with the caldera. The maximum uplift rate of 14 mm/yr is comparable to rates measured in other areas of active volcanism such as Hawaii and Iceland. Interpretations by Pelton and Smith (1979) suggest that the uplift may be the result of increased fluid pressure in a confined magma body.

Indirect evidence of an anomalous crust and upper-mantle at Yellowstone are evident by teleseismic P-wave delays larger than 1.5 sec (Iyer et al., 1981). The magnitude and distribution of the mapped P-wave delays have been interpreted to indicate a 15 percent velocity reduction within the crust and up to a 5 percent velocity reduction in the upper-mantle to depths of 250 km.

The area of large P-wave delays also coincides with a -60 mgal gravity anomaly. Modeling by Eaton et al. (1975) indicates that a mass deficiency for this regional gravity anomaly may not only be due to the low density sediments and caldera infill but also to low-density material in a sub-volcanic basement that may be magma or partial melt.

These geological and geophysical data point out anomalous crustal and upper mantle properties beneath Yellowstone. Low seismic velocities, low densities, high heat flow, and abrupt variations in the stress field in coincidence with the Quaternary volcanism favor crustal bodies as the sources of high heat and volcanic material.

Studies of these phenomena and evaluation of seismic techniques to outline the depth, extent and properties of the crustal structure at Yellowstone were considered important objectives. In particular we sought additional information on: (1) the delineation of the laterally-variable

P-wave velocity structure at scales comparable to that of surface geology; (2) an evaluation of velocity distributions and attenuation that may reflect differences in physical properties and pressure/temperature characteristics of a hydrothermal system; and (3) a detailed evaluation of the relationships between crustal structure, heat flow, crustal deformation, gravity anomalies, and earthquakes that may characterize young silicic volcanic systems.

SEISMIC EXPERIMENT DESIGN AND IMPLIMENTATION

Plans for the 1978 Yellowstone-Snake River Plain seismic experiment were initiated through discussions with colleagues from the Swiss Federal Institute of Technology and Karlsruhe University. Further ideas with seismologists from the U.S. Geological Survey and other U.S. universities were incorporated into the basic plans. The University of Utah and Purdue University were responsible for the general experiment design and organization that included the designation of station locations; shot-point sizes and locations; organization of field recording teams; production of seismic record sections; etc. Shot-point permiting, drilling, blasting, etc. was performed under a sub-contract to the Microgeophysics Corporation of Golden, Colorado.

The experiment conducted in September, 1978, (Figure 1) was divided into five phases: (1) test recording from the Bingham Canyon open-pit mine blasts in northern Utah; (2) the eastern Snake River Plain longitudinal profiles: 5NE, 4, 8, and 2SW (Braile et al., 1981, this volume; Sparlin, Braile, and Smith, 1981, this volume); (3) the two-dimensional Yellowstone National Park area profiles: 1SW, 2NE, 9, G9, and 6 (Schilly et al., 1981, this volume; and Lehman et al., 1981, this volume); (4) a northern cross-line profile from Jackson, Wyoming to southwestern Montana; profiles: 10, 3, and 11 (not yet interpreted); and (5) southern cross-line profiles from the Gay and Conda mines to Arco, Idaho; profiles: 7, Gay and Conda (Sparlin, Braile, and Smith, 1981, this volume).

Shotpoint Plans

Shot detonations were planned to occur at the beginning minute of time windows that were assigned from four to twelve minutes in duration. Shot times were selected in the early morning hours to provide the lowest ambient seismic noise.

For the Yellowstone portion of the experiment shot-points consisted of charge-filled (high pressure Tovex) drill holes with 1260 lbs to 7020 lbs of explosives per shot. Shots were fired at depths ranging from 60 feet to 105 feet, generally below water table, and with 75 feet to 100 feet of gravel tamping (Table 2).

Instrumentation

Several types of seismographs (Figure 2) were used in the experiment and varied from the smoked-paper and FM tape-recording portable earthquake seismographs with vertical-component seismomenters to the European three-component MARS, FM-recording systems (Berckhemer, 1976). The U.S. Geological Survey instruments consisted of FM-tape recording, vertical-component seismometers. Various other instruments were used providing up to 220 seismographs for the larger shots.

In general instruments were deployed in one or more profiles radiating from a shot-point, however in Yellowstone two-dimensional configurations were occupied along existing roads. Stations were spaced at 1 to 5 km and averaged 3 km.

Data Preparation

Upon completion of the experiment, data from the European MARS systems were digitized at the Geophysics Institute, Karlsruhe University. The smoked-paper records were digitized on an HP-9825 at the University of Utah. Digitized data, including that from the U.S. Geological Survey, was then merged and sorted to produce reduced travel-time seismic record sections that were corrected to an elevation of 2200 m, i.e. the average elevation of the Yellowstone Plateau.

Data were prepared in both unfiltered and filtered versions as a means of interpreting travel-times and amplitudes. First arrivals, because of their high frequency, were picked from the non-filtered raw data; whereas the general correlation of phases between records was sometimes better seen on filtered seismograms with a low frequency cut-off of 3.1 Hz and a high frequency cut-off of 10.9 Hz. To examine the variation of amplitude with distance the seismograms have also been plotted utilizing an amplitude normalizing filter that corrected various instrument frequency responses (Figure 2) to a standard curve (Baker, Braile, and Smith, 1981).

REGIONAL CRUSTAL STRUCTURE OF YELLOWSTONE

Travel-Time Phase Interpretations

Regional crustal velocity models of the Yellowstone region have been interpreted from profiles 2NE and 1SW. These profiles traverse the Island Park transition area, the general Yellowstone Plateau (including the Yellowstone caldera) and the Precambrian crystalline complex of the Beartooth Mountains. General phase notation follows that of Figure 3. These profiles provided reversed ray-path coverage that emphasize the intermediate- to deep-crustal structure. However because of large lateral velocity variations in the Island Park caldera complex only an averaged model for this area will be given here. Because of the extended lengths of the profiles additional coverage was provided, i.e. profile 2NE (Figure 4a) extends beyond shotpoint 1 and included unreversed coverage of the Beartooth Mountains and profile 1SW (Figure 5a) extends beyond shotpoint 2 and provided unreversed coverage across the northeast end of the eastern Snake River Plain.

At short distance ranges (up to 20 km), profiles 2NE and 1SW show several branches that correspond to lateral velocity variations in the upper-crust; branches P_0, P_1, and P_2 (not interpreted in detail here); and linear branches corresponding to intermediate and deep crustal refractors, P_I, P*, and P_n; and the associated wide-angle reflection P_mP.

On profile 2NE the P* branch begins at about 40 km, at the southern edge of the Yellowstone caldera, and extends to about 80 km at the northeast side of the caldera. From 80 km to 115 km no refracted or reflected arrivals were evident suggesting strong backscattering or large attenuation. Beginning at 115 km a branch of the P* branch is seen as a strong arrival

that has been delayed almost 1 sec across the Yellowstone caldera. This branch continues to about 140 km as a single arrival then develops a multiple-cycle character to a distance of 183 km. In this range the velocity of both P* branches is 6.80 km/s.

On profile 1SW the P* branch is not as clear and because of large recording gaps correlation of the phase is more difficult. From 110 km the P* branch appears as a moderately strong, multi-cycle arrival and continues to about 155 km as a correlatable phase. Beyond this distance a large record gap makes the phase uncorrelatable across distant stations on the eastern Snake River Plain. In expanded-scale seismograms of this section (not shown here), a small arrival, P_I, preceding P* has an apparent velocity of 6.50 km/s suggestive of an additional layer at the top of the lower-crust.

The upper-mantle headwave, P_n, with an apparent velocity of 7.9 km/s is recorded as a weak arrival beyond 230 km on profile 1SW where its identification is based on correlations of small amplitude phases and its relative position with respect to the wide-angle reflections, P_mP. P_n was not expected to be observed on profile 2NE because the profile did not extend beyond the estimated cross-over distance near 220 km.

Identification of the wide-angle reflection, P_mP on profiles 2NE and 1SW was made from trace-to-trace correlations and comparisons with stronger P_mP arrivals on profiles 2SW and 5 from Braile et al., (1981). On profile 2NE the P_mP branch appears near its critical point at about 120 km as a multi-cycle arrival and is seen to the end of that record section. On profile 1SW, P_mP extends from 125 km to about 155 km where it is interrupted by the large recording gap, but it then appears as a later arrival from 220 km to the end of the recording at 300 km.

Synthetic Seismograms and Amplitude Modeling

Complete analyses of the seismic waveforms required the use of normalized-amplitude record sections that were corrected for the systematic decay of amplitudes as a function of distance from the source. Profiles 2NE (Figure 4b) and profile 1SW (Figure 5b) are shown after amplitude normalization following the method described by Baker, Braile, and Smith (1981, this volume). Amplitudes on these seismograms have been scaled by a factor multiplying the distance in kms to the 1.9 power necessary to increase the amplitude levels for interpretation and correlation.

In addition, Figure 6 shows the relative amplitude (peak-to-peak) decay as a function of distance. Both the amplitude decay and the normalized-amplitude seismograms were then modeled using the modified reflectivity method (Kind, 1978) including the effect of analastic attenuation, Q^{-1}. Starting models were derived from the travel-time interpretations, however it became clear that the travel-time data by themselves could not entirely account for the variations in amplitudes with distance nor the finer details of the wavelet forms.

Synthetic seismograms showed that modeling was particularly sensitive; (1) to the rapid decay of the P_2 phases with distance particularly on line 2NE, (2) the evidence of small first arrivals, P_I, preceeding the strong P* phase and the variation of amplitude width distance of P* at distances of 110 km to 160 km on line 1SW, and (3) the amplitude decay in the wide-angle reflections P_mP. The final synthetic seismograms (Figure 7 and 8) show the relative amplitudes and corresponding P-velocity and

Q structure. Because the synthetic seismograms assumed a homogeneous, flat-layering configuration they provide only an "average velocity", flat-layer interpretation.

The upper-crustal structure of the Yellowstone system because of its strong lateral heterogenieties was averaged from the results of Schilly et al. (1981) and Lehman et al. (1981) but two important characteristics emerged. First, the upper 10 km to 13 km appeared to be areas of very low Q from 50 to 300. The low Q was required to model the rapid amplitude decay of the initial P and P_g (P_1 and P_2) branches as seen in Figure 6. Areas of high attenuation correspond to thick accumulations of ash flow tuffs and rhyolite flows of the Yellowstone Plateau and areas that may overlie upper-crustal heat sources (melts, partial melts, or hot solid material).

Secondly, amplitude variations of the intermediate-crustal P* arrival show variations in the distance ranges 100 km to 180 km that were not modeled in the simpler travel-time technique. The amplitude decay was attributed to a thin 6.5 km/s lid at the top of the intermediate layer, as noted in profile 1SW, to overlie a higher velocity 6.8 km/s lower crustal layer.

The relatively weak Moho-refractor, P_n, appeared as a first arrival at distances from about 230 km and beyond on profile 2NE. This phase has apparent velocity of 7.9 km/s and was modeled with a relatively high Q of 1000.

The strong, later-arrivals, beginning at 120 km correspond to the wide-angle reflection, P_mP. Modeling the reflections, requires a critical point near 120 km with rapid increases to peak amplitudes at about 160 km

on profile 1SW and near 220 km on profile 2NE. Modeling of P_mP reflections in the eastern Snake River Plain by Braile et al. (1981), shows a close correspondence, the P_mP reflections in the Yellowstone area are weaker but multi-cycled suggesting a more complicated Moho interface. These data require that the intermediate and lower crust have a relatively low Q of 300.

Synthetic seismogram modeling thus provided additional information on the general crustal structure of the Yellowstone region, namely that both the upper- and lower-crust is comprised of a low Q (30 to 300) material compared to normal continental models. Evidence for an intermediate lid of 6.5 km/s in the upper-part of the lower crust was required to match the relative amplitudes and suggests additional vertical differentiation not seen in the simple travel-time interpretations.

Crustal Model

The generalized P-wave crustal velocity model for the Yellowstone region (Figure 9) extends from the Beartooth Mountains southwest across the Yellowstone caldera, the Island Park transition, to the upper portion of the eastern Snake River Plain. Note, because of the assumptions required of flat lying layers in the use of the synthetic seismograms the velocity structure is considered as an averaged model. The generalized structure has the following characteristics: (1) an averaged near-surface layer, 3.0 km/s - 5.5 km/s, that is interpreted to represent the volcanic layering that, principally composed of the rhyolite/basalt suite in the eastern Snake River Plain but becomes a complete silicic rhyolite-ash flow accumulation in the Yellowstone Plateau. Within the crystalline Precambrian crust

of the Beartooth Mountains and areas outside the caldera the upper-crustal velocities are 6 km/s and are interpreted to represent the Archean undistrubed crystalline basement composed of granitic gneiss; (2) the intermediate crust exhibits a 10 km lid (6.5 km/s) at depths of 10 km to 20 km; (3) a homogeneous and thick (25 km) lower-crustal section (6.7 km/s to 6.8 km/s) that extends to depths of about 43 km; and (4) the upper-mantle of the Yellowstone Plateau has an apparent velocity of 7.8 km/s to 7.9 km/s.

REGIONAL COMPARISON OF YELLOWSTONE CRUSTAL STRUCTURE

A comparison of the crustal structure from Yellowstone with that of the surrounding Rocky Mountain shows some distinct differences (Table 3). For example, the upper 10 km of the crust in Yellowstone shows strong lateral inhomogenieties, relatively low P-wave velocities and low Q's; properties are attributed to thick accumulations of the rhyolite and ash flow layers of the Pleistocene-Quaternary volcanic system and possible subsurface melts or hot but solid bodies. A surface rhyolite/basalt layer beneath the eastern Snake River Plain, is about 5 km thick, and thins progressively, as a composite rhyolite-ash flow layer, to zero thickness at the Beartooth Mountains where crystalline granitic gneiss is exposed at the surface. Beneath the Yellowstone caldera strong lateral velocity variations from 6.05 km/s to 4.0 km/s (Lehman et al., 1981) are compared to homogeneous layers with velocities of 6.0 km/s to 6.1 km/s for the surrounding thermally undistrubed upper-crust. The upper-crustal "granitic" layer is relatively thin, about 5 km, southwest of Island Park (Braile et al., 1981) and an averaged "granitic" layer thickens beneath the Yellowstone Plateau to ∿9 km. Southern Montana (McCamy and Meyer, 1964) and western Wyoming (Braile et al., 1975; Prodehl, 1979) have normal continental "granitic" layers that attain thicknesses of 15 km to 20 km and are thought to represent the thermally undisturbed Archean crust.

The intermediate- and lower-crustal layers have a more homogeneous character with comparable thicknesses of 10 km for the 6.5 km/s layer (Table 3). The lower-crust is a homogeneous 23 km to 25 km thick layer with a velocity of 6.7 km/s to 6.8 km/s, comparable to the surrounding region. A total

crustal thickness for the Island Park-Yellowstone Plateau-Beartooth Mountains of 43 km compares well with 45 km to 50 km crustal thicknesses seen in the surrounding Rocky Mountains (McCamy and Meyer, 1964; Braile et al., 1975). Upper mantle velocities of 7.9 km/s for the Yellowstone Plateau also compare with the 8.0 km/s for southern Montana and western Wyoming. These comparisons show that the upper crust of the thermally disturbed Yellowstone region appears as a seismically, laterally inhomogeneous section compared to that of the surrounding thermally undisturbed region. Whereas the intermediate and lower crustal structure corresponds well in both velocity and thickness. This suggests that the thermal-tectonic event that shaped the Yellowstone landscape beginning at 2.2 million years ago is still operating and has produced perturbations in the velocity and layer configuration of the upper ∿10 km. These models place the active thermal mechanism at Yellowstone in the upper-crust, whereas the lower crust seems to be relatively homogeneous, apparently immune to the thermal event.

The systematic variations of upper-crustal velocities and layer thicknesses beneath the eastern Snake River Plain and Yellowstone no doubt reflect the effects of a major lithospheric thermal anomaly that is evidenced by the systematic progression of the silicic volcanism along the trend of the eastern Snake River Plain to its present position beneath Yellowstone. A nearby analogy of a thermally perturbed continental crust is that of the Great Basin of Utah and Nevada (Smith, 1978) that shows a much thicker "granitic" upper-crustal layer (6.0 km/s), 15 km to 20 km thick; but a total 25 km to 30 km crust that appears to have been thinned from the bottom by partial melting or by upper-mantle underplating.

The crustal structure of the Yellowstone region thus appears to be in the juvenile stages of the progressive thermal attenuation of layers with corresponding phase and chemical changes. These mechanisms have produced a marked thinning of the upper crustal "granitic" layer along the eastern Snake River Plain perhaps by melting and partial fractionization where the high heat has been produced by mass transport of upper-mantle basalts giving rise to melting and metamorphism of metamorphic rocks and the resultant generation of the rhyolite components. These are then followed by extrusion of the basaltic parental magmas. In Yellowstone, lateral inhomogenieties suggest that the processes have not yet come to equilibrium and various degrees of melting and chemical variation occur beneath the plateau. However a parental "granitic" layer (see Lehman et al., 1981) appears to exist in coincidence with the Yellowstone caldera at shallow crustal depths (2 km to 10 km) which have been in turn overlain by the Quaternary rhyolite and ash flow tuffs.

CONCLUSIONS

The 1978 Yellowstone-eastern Snake River Plain seismic experiment was considered a highly successful cooperative research project that was designed to obtain new data on the dynamics and thermal evolution of an evolving continental lithosphere. This paper has presented the experiment design and organization as well as a generalized interpretation of the crustal structure of the Yellowstone region. Later papers will evaluate the significance of the seismic data in term of petrologic and geologic models. Accompanying papers in this volume provide more detailed interpretation of the seismic characteristics of the eastern Snake River Plain-Yellowstone volcanic province.

Above all, not only was the experiment successful in obtaining new data, but more importantly it brought together scientists and students from various U.S. and European research groups to engage in a cooperative scientific experiment. The success of the project is a demonstration of the ability for professionals from various organizations to focus on a common goal and should provide encouragement for similar ventures in the future.

ACKNOWLEDGMENTS

The 1978 Yellowstone-Snake River Plain seismic experiment was a major cooperative effort made possible through the support and help of many people. In particular personnel and instruments were provided from our European colleagues at the Geophysics Institute, Swiss Federal Institute of Technology and the Geophysics Institute, Karlsruhe University. Also the U.S. Geological Survey kindly provided a large compliment of instruments and personnel.

In addition to the authors of this paper several persons were involved with the seismic experiment including planning, field recording, shooting and data preparation. We are grateful to those providing this help: J. M. Brune, Paul Daggett, Nicholas Deichmann, Deiter Emter, Roger Felch, Marcus Grieder, Ted Handle, Bronson Hawley, David P. Hill, Fred Homuth, Martin Jentsch, Tim and Rose Kehoe, Will Kohler, Rolph Kunzler, Ralph Lamson, Matt Mabey, John Michaels, Carl Newton, Tom Owens, J. R. Pelton, K. F. Priestly, Tony Qamar, M. A. Sparlin, John Stewart, Debbie Wechsler, Steve Wegener, and Jim York. The Microgeophysics Corporation of Golden, Colorado did an excellent job in shotpoint operations and explosive management and we thank Roger Bowman, David Butler, Roger Grette, and Andy Staatz for their services.

Cooperation of several other agencies and personnel included: the National Park Serivce--Yellowstone National Park, John Townsley-Superintendent, Jerry Phillips, Alan Mebane, Mary Meagher, and Rich Hutchinson; Grand Teton National Park, Chuck McCurdy; the Grand Targhee National Forest, Brent Mace; and the Bureau of Land Management, Idaho Falls District Office.

David Blackwell of Southern Methodist University loaned five seismographs and helped secure the shotpoint four drill hole and Randy Keller, University of Texas-El Paso, loaned three instruments. Mitch Pitt and Craig Weaver of the U.S. Geological Survey provided data from the Yellowstone seismograph network.

Nicholas Deichmann, Tom Owens, and Mickie Kaminski helped in the laborous and difficult task of data digitization, sorting, merging, and editing required for final seismograms. Dave Chapman, University of Utah, kindly provided an HP-9825 for digitizing the smoked-paper records. Ron Ward of the University of Texas-Dallas and John O'Brien and Gary U. Hoover of the Phillips Petroleum Company provided reflection data for help in our interpretations.

Principal funding for the experiment was from the National Science Foundation, grant no. EAR-77-23707 to the University of Utah and EAR-77-23357 to Purdue University. Additional support was provided from the Geothermal Research Program of the U.S. Geological Survey, grant no. 14-08-0001-G-532. Supplementary support for salaries and no-cost use of equipment was provided by the European institutes as well as the U.S. Geological Survey.

This seismic experiment demonstrated the true nature of the cooperative use of equipment and persons to work toward a common goal. All personnel gave countless hours of their time, day and night, and of their suggestions. We thank all who have participated in the experiment and we are grateful for their expertise and support.

TABLES

Table 1.

Organization	Number of Instruments	Number of Personnel	Source of Funding
University of Utah	8	8	NSF
Purdue University	4	3	NSF, USGS-Geothermal Res. Proj.
ETH-Zurich	13	5	NSF, Swiss Federal Funds
Karlsruhe University	14	4	NSF, German Federal Funds
U.S. Geological Survey	100	12	USGS
Los Alamos Scientific Laboratory	13	5	Department of Energy
Stanford University	5	1	USGS-Geothermal Res. Proj.
New Mexico State University	5	2	USGS-Geothermal Res. Proj.
University of Montana	5	2	USGS-Geothermal Res. Proj.
University of Texas-Dallas	Reflection Array	4	USGS-Geothermal Res. Proj.
University of Nevada	10	3	USGS-Geothermal Res. Proj.
University of California-San Diego	10	2	USGS-Geothermal Res. Proj.
Southern Methodist University	5	0	No cost
University of Texas-El Paso	3	0	No cost

Table 2.

Yellowstone Region

SHOTPOINT	DATE	TIME (UCT)	LATITUDE D M S	LONGITUDE D M S	ELEVATION (M)	ELEVATION (FT)	DEPTH (M)	DEPTH (FT)	SIZE (kg)	SIZE (LBS)	HOLES	CONDITION OF SHOTPOINT
2A	9/17/78	11: 0: 5.684	44 17 6.8N	111 20 12.0W	1889	6200	32	105	2620	7020	2	BOREHOLE WET
2B	9/21/78	11: 0: 5.411	44 17 6.8N	111 20 12.0W	1889	6200	32	105	1086	2910	1	BOREHOLE WET
G9	9/21/78	11:30: 0.008	44 5 22.0N	110 41 2.0W	2072	6800	0	0	746	2000	0	GRAVEL PIT, WET
1	9/22/78	10: 0: 5.039	45 0 14.4N	110 1 37.6W	2225	7300	18	60	470	1260	1	BOREHOLE WET
6	9/22/78	12:30: 5.403	44 56 26.0N	110 44 17.8W	2240	7350	21	70	750	2010	1	BOREHOLE WET
11	10/02/78	10: 0: 0.008	44 52 16.6N	112 58 55.8W	2133	7000	61	200	1493	4000	1	BOREHOLE WET
3	10/02/78	10:15: 0.010	44 4 34.2N	111 56 16.4W	1691	5550	0	shallow	373	1000	1	BOREHOLE DRY (DEEP)
10	10/02/78	10:30: 0.017	43 19 47.4N	110 48 40.0W	2057	6750	12	40	1493	4000	MANY	SHALLOW HOLES

Table 3

	Eastern Snake River Plain[1]	Yellowstone Region	Western Wyoming[2]	Southern Montana[3]	Western Montana[3]
Upper-crustal, "granitic" layer thickness	5 km	7 km	15 km	15-20 km	20 km
P_g-velocity-km/s	(6.1)	(5.7-6.05)	(6.0, 5.7)	(6.0)	(6.0)
Intermediate-lower crustal layer thickness	32 km	32 km	23 km	25 km	25 km
P_I, P*-velocity, km/s	(6.5, 6.8)	(6.5, 6.8)	(6.75)	(6.9)	(7.4)
Total Crustal thickness	42 km	42 km	40 km	45 km	50 km
P_n-velocity, km/s	(7.9)	(8.0)	(7.9)	(8.0-8.4)	(8.2)

[1]Braile et al., 1981
[2]Prodehl, 1979; Braile et al., 1974
[3]McCamy and Meyer, 1964

REFERENCES

Archambeau, C. B. E. A. Flinn, and D. G. Lambert, Fine structure of the upper mantle, J. Geophys. Res, 74, 5825-5865, 1969.

Armstrong, R. L. W. P. Leeman, and H. E. Malde, K-Ar dating, Quaternary and Neogene volcanic rocks of the Snake River Plain, Idaho, Amer. J. Sci., 275, 225-251, 1975.

Baker, M. R., L. R. Braile, and R. B. Smith, Amplitude normalization of seismograms from multiple seismograph recording systems for the Yellowstone-Snake River Plain seismic refraction experiment, J. Geophys. Res., (this vol.), 1981.

Berckhemer, H., Standard equipment for deep-seismic sounding, in Explosion Seismology In Central Europe, eds. P. Giese, C. Prodehl, and A. Stein, Springer-Verlag, 115-118, 1976.

Braile, L. W., R. B. Smith, J. Ansorge, M. R. Baker, M. A. Sparlin, C. Prodehl, M. M. Schilly, J. H. Healy, St. Mueller, and K. H. Olsen, The Yellowstone-Snake River Plain seismic profiling experiment: crustal structure of the eastern Snake River Plain, J. Geophys. Res. (this vol.), 1981.

Braile, L. W., R. B. Smith, G. R. Keller, and R. P. Meyer, Crustal structure across the Wasatch Front from detailed seismic refraction studies, J. Geophys. Res., 79, 2669-2677, 1974.

Christiansen, R. L. and H. R. Blank, Jr., Volcanic stratigraphy of the Quaternary rhyolitic plateau in Yellowstone National Park, U.S. Geol. Survey Prof. Paper, 729-B, 18 pp., 1972.

Eaton, G. P., R. L. Christiansen, H. M. Iyer, A. M. Pitt, D. R. Mabey, H. R. Blank, Jr., I. Zietz, and M. E. Gettings, Magma beneath Yellowstone National Park, Science, 188, 787-796, 1975.

Giese, P., C. Prodehl, and A. Stein, editors, Explosion Seismology in Central Europe, Springer-Verlag, 429 p, 1976.

Iyer, H. M., J. R. Evans, G. Zandt, R. M. Stewart, J. M. Cookley, and J. N. Rolof, A deep magma body under the Yellowstone caldera, Wyoming: Delineation using teleseismic P-wave residuals and tectonic interpretations: Summary, Bull. Geol. Soc. America, 1981 (in press).

Kind, R., The reflectivity method for a buried source, J. Geophys. Res. 44, 603-612, 1978.

Kosminskaya, I. P., Deep Seismic Sounding of the Earth's Crust and Upper Mantle, Consultants Bureau, New York, translated by G. V. Keller, 184 p., 1971.

Lehman, J. L., R. B. Smith, M. M. Schilly, and L. W. Braile, Upper-crustal structure of Yellowstone from seismic and gravity observations, J. Geophys. Res., 1981 (this volume).

McCamy, K., and R. P. Meyer, A correlation method of apparent velocity measurements, J. Geophys. Res., 69, 691-699, 1964.

Morgan, P., D. D. Blackwell, R. E. Spafford, and R. B. Smith, Heatflow measurements in Yellowstone Lake and the thermal structure of the Yellowstone calera, J. Geophys. Res., 82, 3719-3732, 1977.

Morgan, W. J., Plate motions and deep mantle convection, in Shagan, R., ed., Studies in Earth and Space Sciences, Geol. Soc. Am. Mem. 132, 7-27, 1972.

Pakiser, L. C., Structure of the crust and upper mantle in the western United States: J. Geophys. Res., 69, 5747-5756, 1963.

Pelton, J. R. and R. B. Smith, Recent crustal uplift in Yellowstone National Park, Science, 206, 1179-1182, 1979.

Pelton, J. R. and R. B. Smith, Contemporary vertical surface displacements in Yellowstone National Park, J. Geophys. Res., 1981 (this volume).

Prodehl, C., Crustal structure of the western United States, Geol. Survey Prof. Paper 1034, 1979.

Schilly, M. M., R. B. Smith, J. A. Lehman, L. W. Braile, and J. Ansorge, Crustal velocity structure of Yellowstone from seismic refraction and reflection profiles, J. Geophys. Res., 1981 (this volume).

Sparlin, M. A., L. W. Braile, and R. B. Smith, Crustal structure of the eastern Snake River Plain determined from ray-trace modeling of seismic refraction data, J. Geophys. Res., 1981, (this volume).

Smith, R. B., Seismicity, crustal structure, and intraplate tectonics of the interior of the western Cordillera, eds. R. B. Smith and G. P. Eaton, Geol. Soc. Am. Mem. 152, 111-144, 1978.

Smith, R. B., L. W. Braile, and G. R. Keller, Upper crustal low-velocity layers: possible effect of high temperatures over a mantle upwarp at the Basin Range-Colorado Plateau transition, Earth and Planetary Sci. Letters, 28, 197-204., 1975.

Smith, R. B., and R. L. Christiansen, Yellowstone Park as a window on the earth's interior, Sci. American, 242, 104-117, 1980.

ILLUSTRATION CAPTIONS

Figure 1 Index map for 1978 Yellowstone-eastern Snake River Plain seismic experiment. Shot-points are indicated by solid circles; station locations; solid triangles correspond to sites occupied for profiles 1SW and 2NE, open circles are sites occupied for other profiles.

Figure 2 Frequency-response curves for the various types of seismographs used in the 1978 Y-SRP experiment. Solid lines correspond to instruments from the various organizations including the effects of filters. The dashed line corresponds to the amplitude normalized response curve after Baker, Braile, and Smith (1981).

Figure 3 Generalized ray path diagram and notation for the Yellowstone portion of the 1978 Y-SRP experiment.

Figure 4a Profiles 2NE record section of filtered seismograms. Travel-times are reduced at a 6 km/s reduction velocity. Seismograms are all corrected to a 2200 m elevation datum with a variable surface-layer velocity model. A 3.1 hz to 10.9 hz band-pass filter was applied. Phase identification follows the notation of Figure 3 and correlatable branches are shown by solid and dashed lines that were used to interpret the velocity structure.

Figure 4b Profile 2NE normalized amplitude record section. Amplitudes are scaled to the distance of the 1.9 power for plotting purposes. Phase notation and other nomenclature correspond to that of Figure 4a.

Figure 5a Profile 1SW record section of filtered seismograms. Travel-times are reduced at a 6 km/s reduction velocity. Seismograms are all corrected to a 2200 m elevation datum with a variable surface-layer velocity model. A 3.1 hz to 10.9 hz band-pass filter was applied. Phase identification follows the notation of Figure 3 and correlatable branches are shown by solid and dashed lines that were used to interpret the velocity structure.

Figure 5b Profile 1SW normalized amplitude record section. Amplitudes are scaled to the distance of the 1.9 power for plotting purposes. Phase notation and other nomenclature correspond to that of Figure 5a.

Figure 6 Relative amplitude decay curves for profiles 2E and 1SW from peak-to-peak amplitudes of the initial arrivals corresponding to the designated branch.

Figure 7 Synthetic seismogram for profile 2NE. Seismograms were generated using the modified reflectivity method including the effects of attenuation (Q^{-1}). Amplitudes were scaled by multiplying the distance by 1.9 for plotting and correlation.

Figure 8 Synthetic seismogram for profile 1S. See explanation in Figure 7.

Figure 9 Generalized P-wave velocity model for the Yellowstone region. Profile extends from eastern Snake River Plain northeast across the Yellowstone Plateau to the Beartooth Mountains. Velocity structure to the southwest corresponds to the model of Braile et al. (1981). Detailed data in the vicinity of the Island Park region are not shown. Surface topography and surficial geology are plotted to provide information on near-surface effects.

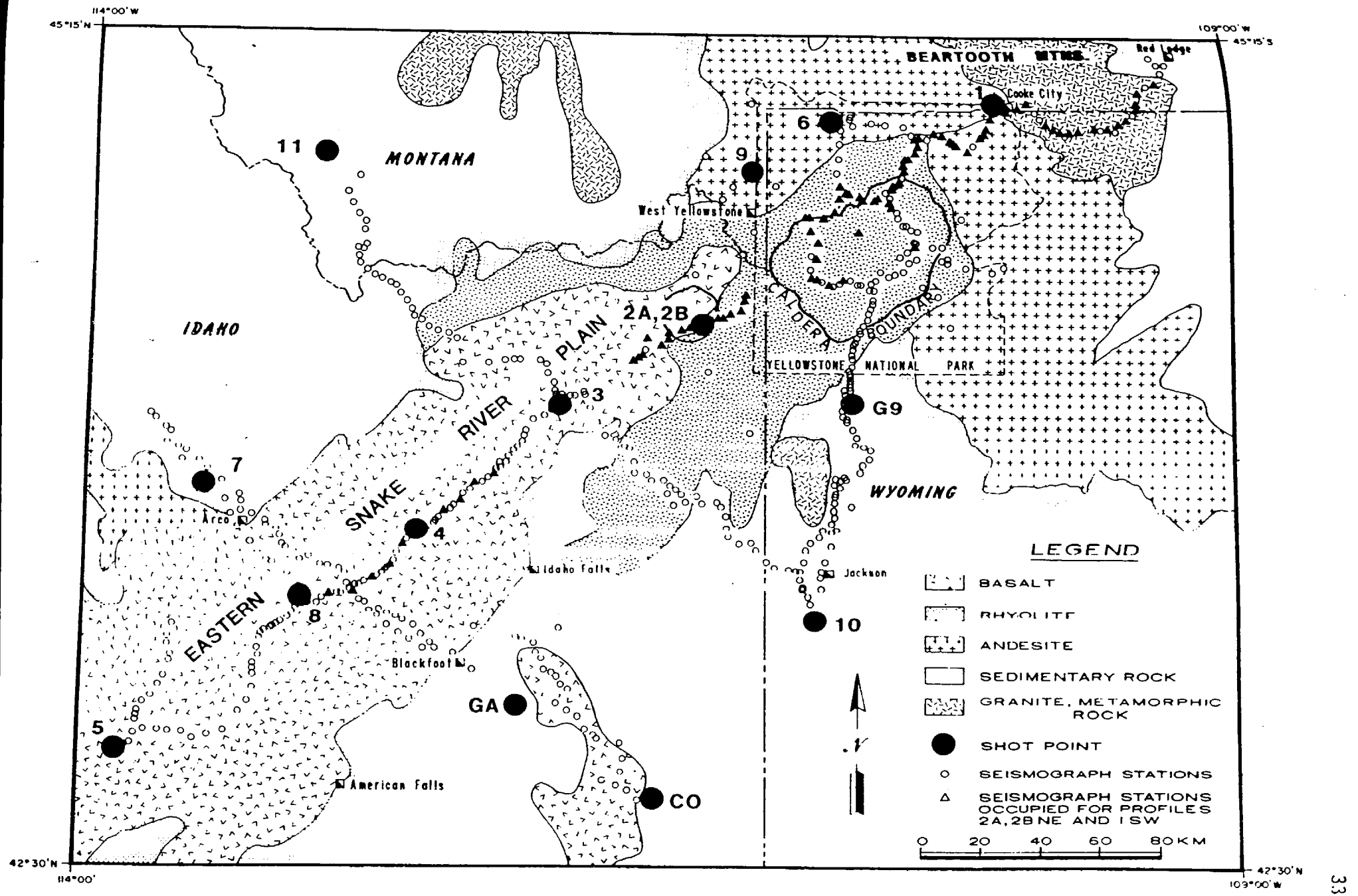
114°00' W
45°15' N
109°00' W
45°15' S
BEARTOOTH MTNS.
Red Lodge
Cooke City
1
6
11
MONTANA
9
West Yellowstone
IDAHO
2A, 2B
CALDERA BOUNDARY
YELLOWSTONE NATIONAL PARK
SNAKE RIVER PLAIN
3
G9
7
WYOMING
Arco
4
Idaho Falls
Jackson
10
EASTERN
8
Blackfoot
GA
5
American Falls
CO
LEGEND
BASALT
RHYOLITE
ANDESITE
SEDIMENTARY ROCK
GRANITE, METAMORPHIC ROCK
SHOT POINT
SEISMOGRAPH STATIONS
SEISMOGRAPH STATIONS OCCUPIED FOR PROFILES 2A, 2B NE AND I SW
0 20 40 60 80 KM
42°30' N
114°00'
109°00' W
42°30' N

Figure 1

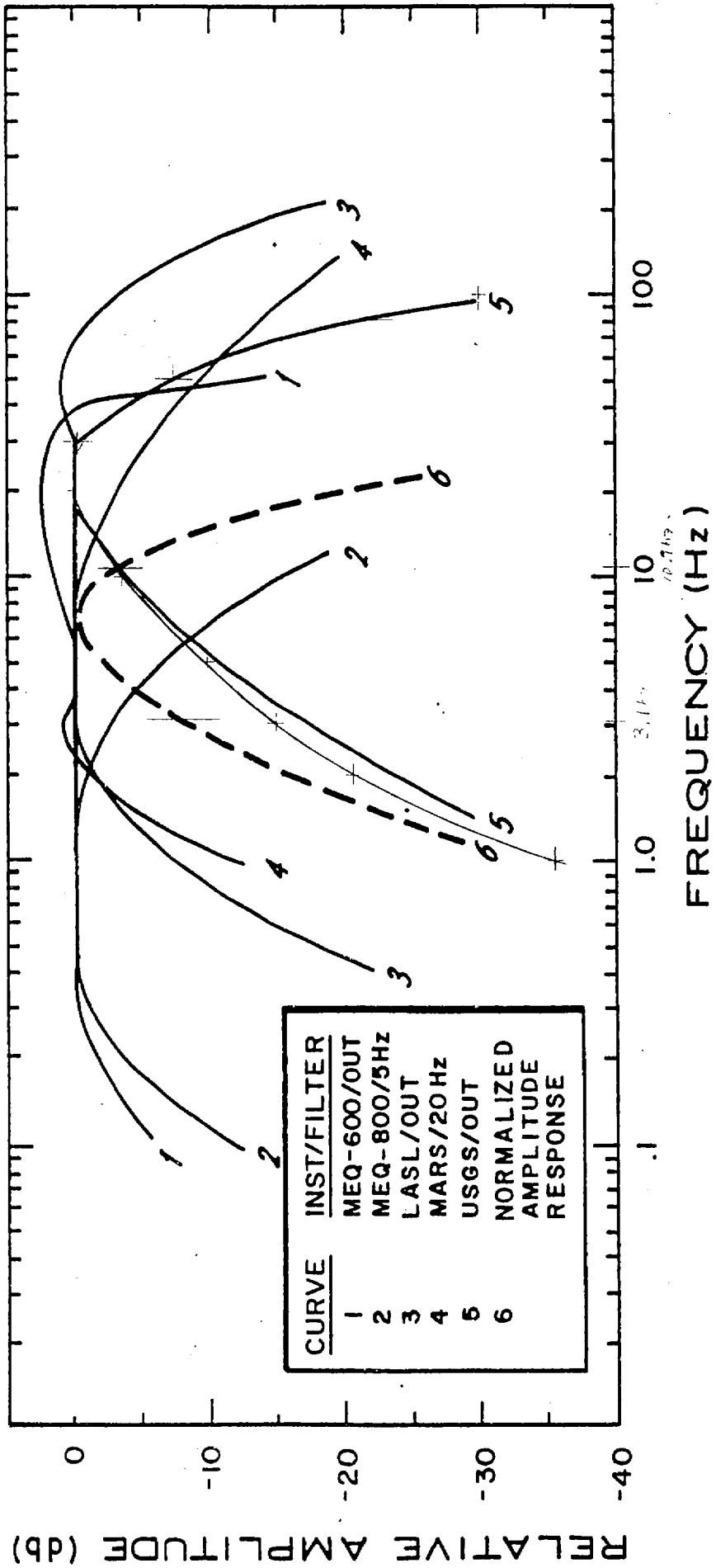
RELATIVE AMPLITUDE (db)
0
-10
-20
-30
-40
.1
1.0
10
100
FREQUENCY (Hz)
CURVE
INST/FILTER
1 MEQ-600/OUT
2 MEQ-800/3Hz
3 LASL/OUT
4 MARS/20 Hz
5 USGS/OUT
6 NORMALIZED AMPLITUDE RESPONSE

Figure 2

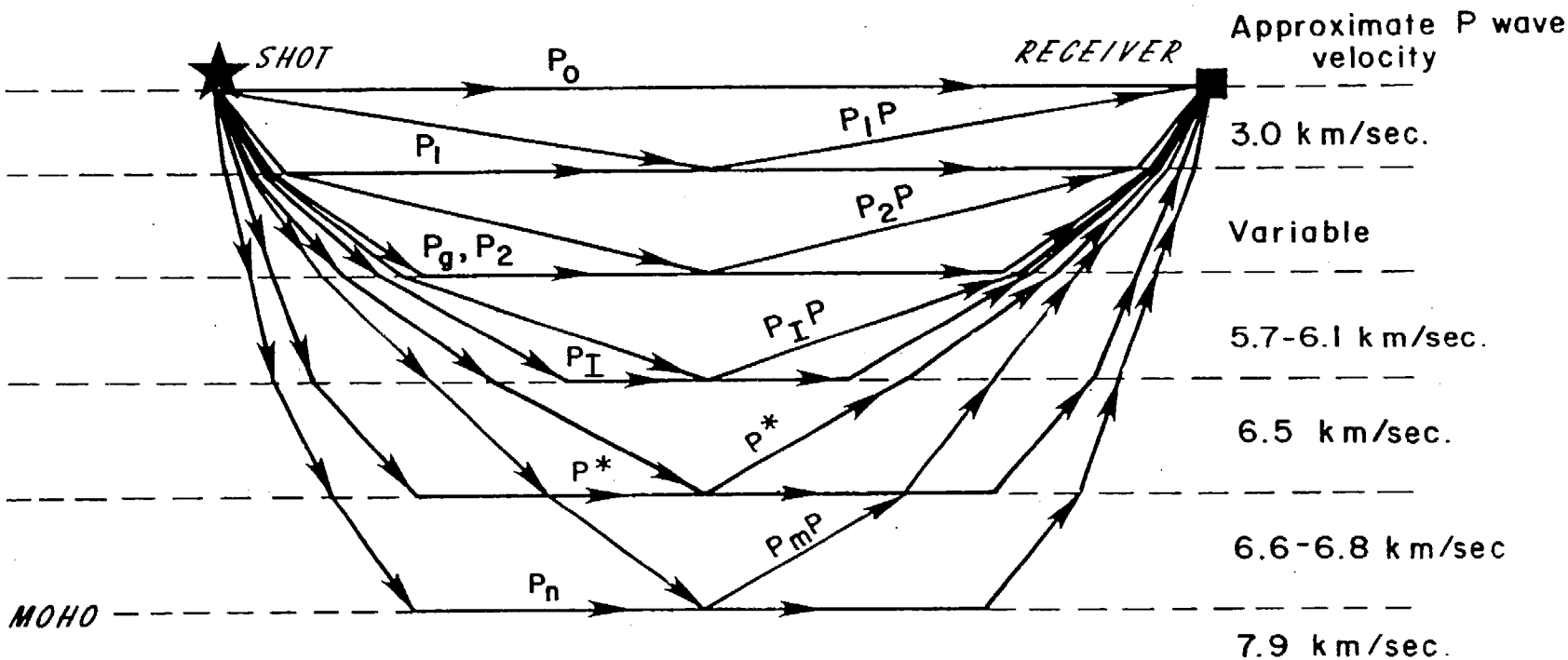
SHOT
RECEIVER
P_0
P_1P
P_1
P_2P
P_g, P_2
P_IP
P_I
P^*
P^*
P_mP
P_n
MOHO
Approximate P wave velocity
3.0 km/sec.
Variable
5.7-6.1 km/sec.
6.5 km/sec.
6.6-6.8 km/sec
7.9 km/sec.

Figure 3

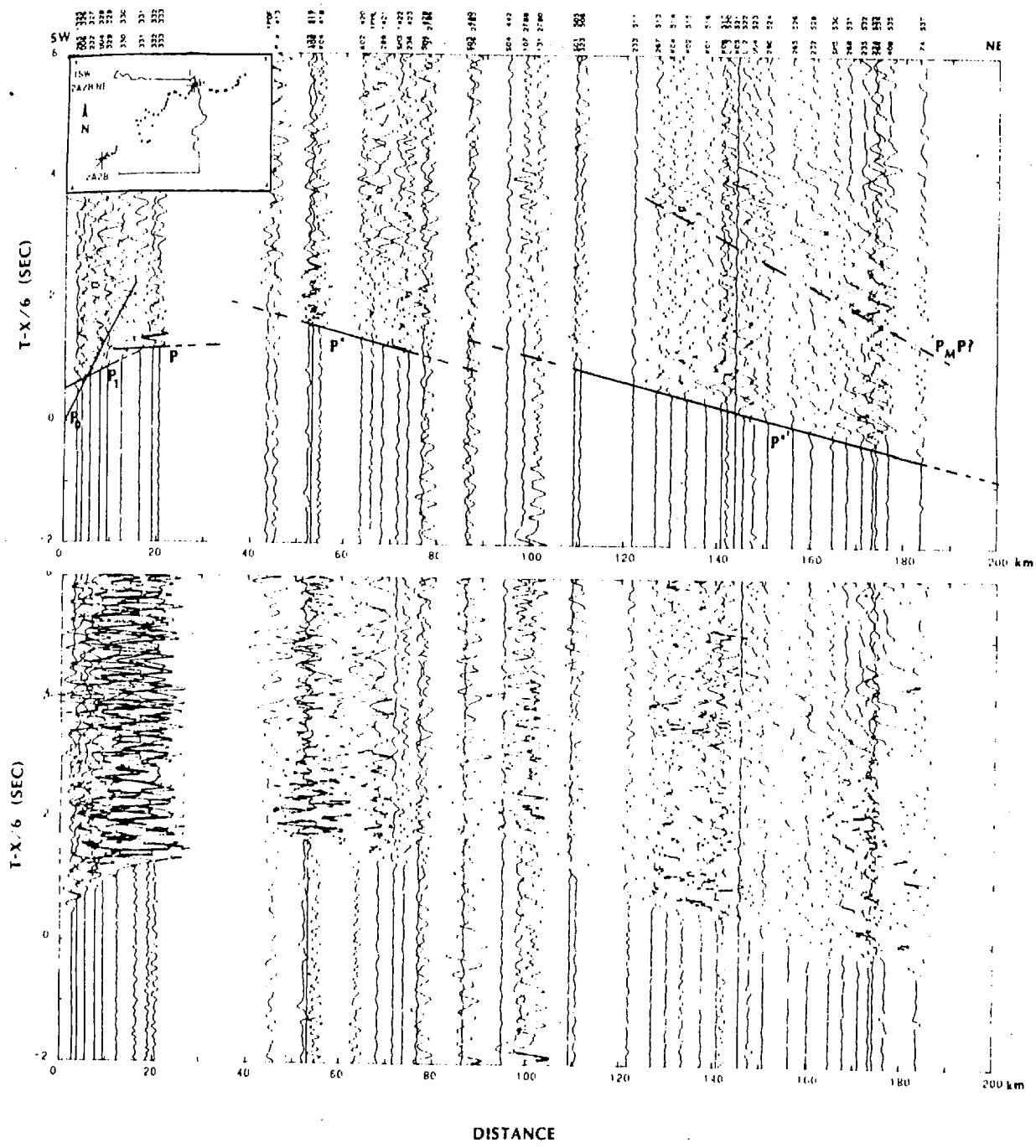
SW
NE
T-X/6 (SEC)
P
P*
P*'
PMP?
P1
P0
0
20
40
60
80
100
120
140
160
180
200 km
DISTANCE

Figure 4

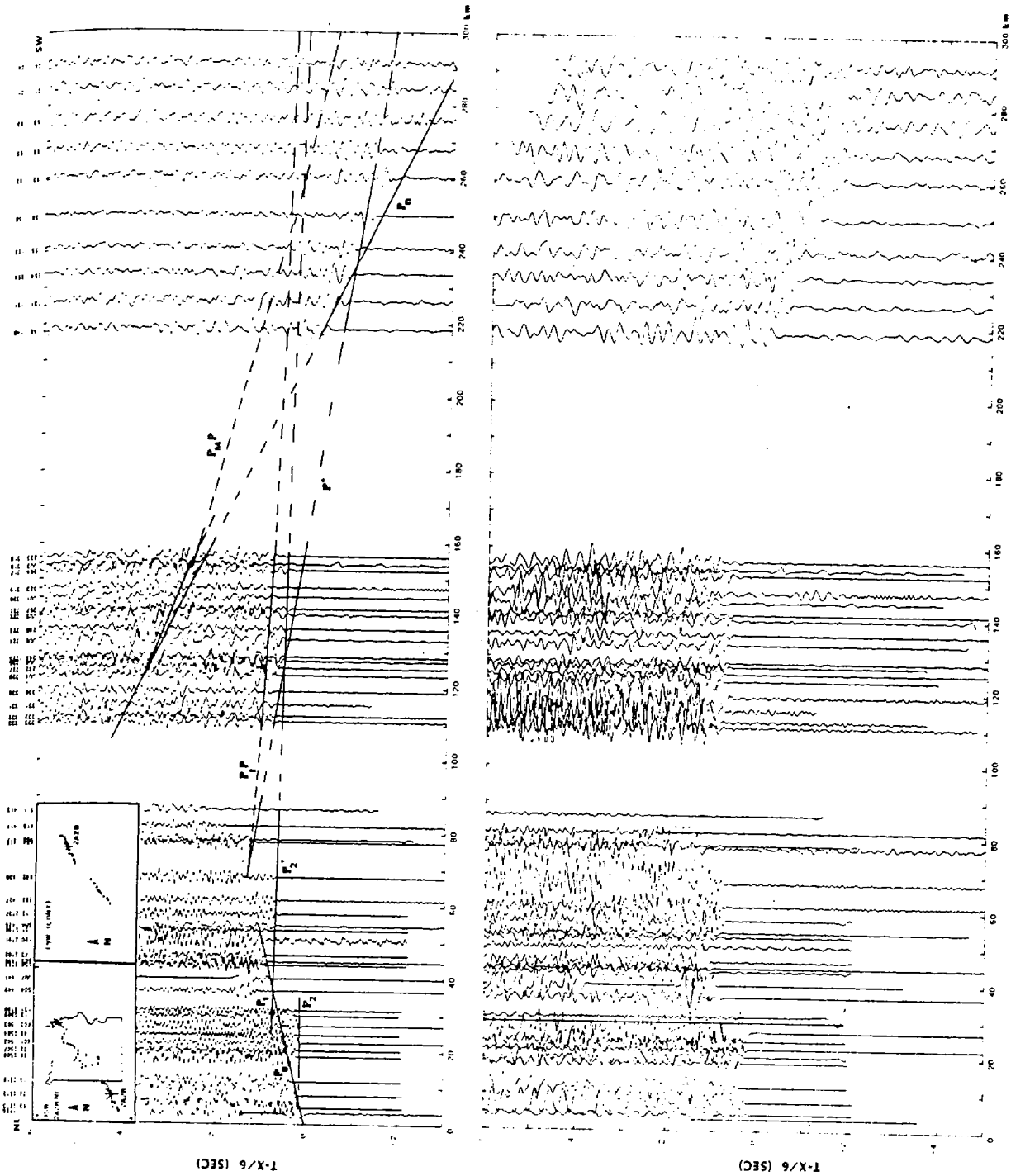

Figure 5

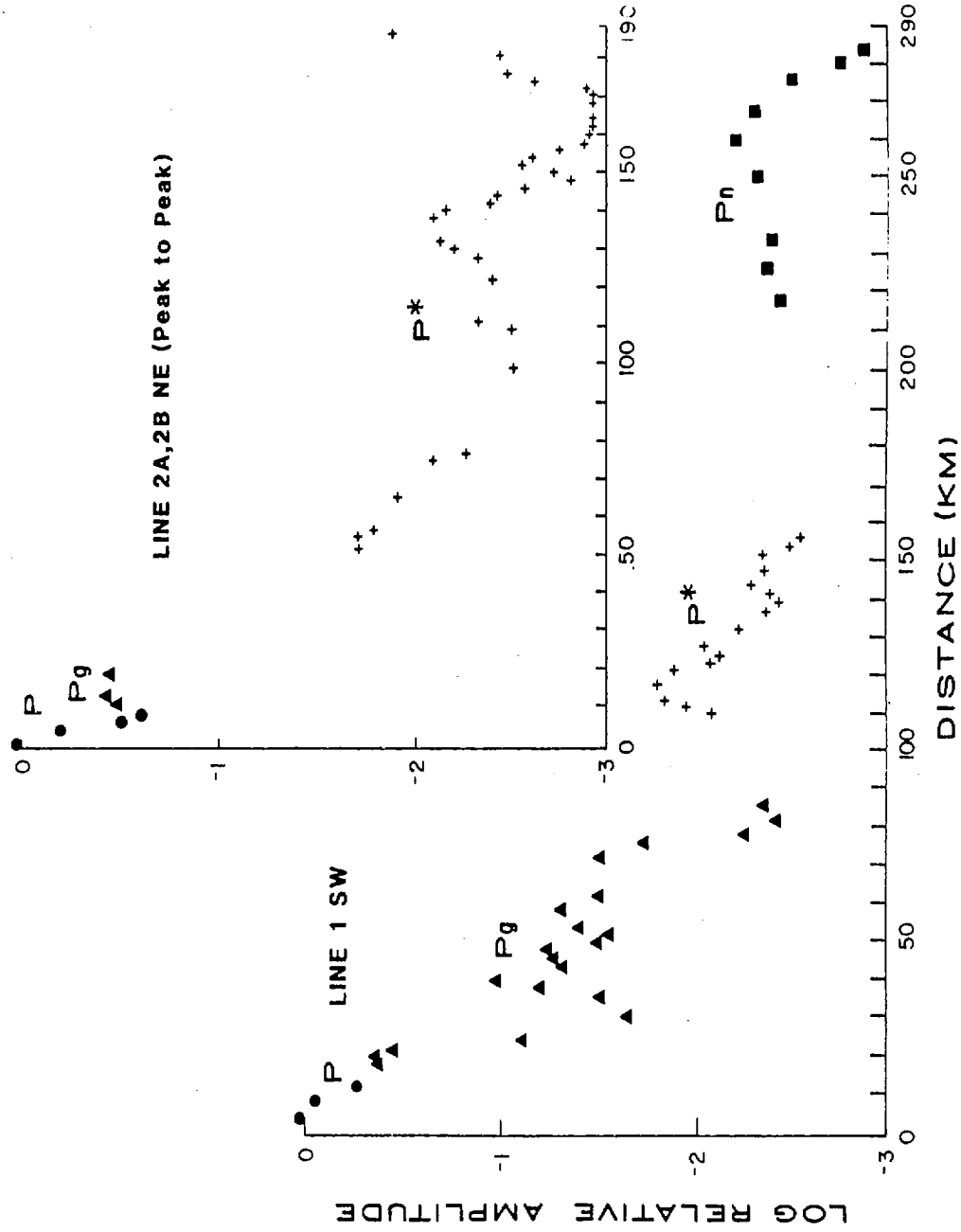
LINE 2A,2B NE (Peak to Peak)
P
Pg
P*
LINE 1 SW
P
Pg
P*
Pn
LOG RELATIVE AMPLITUDE
DISTANCE (KM)
0
-1
-2
-3
50
100
150
200
250
290

Figure 6

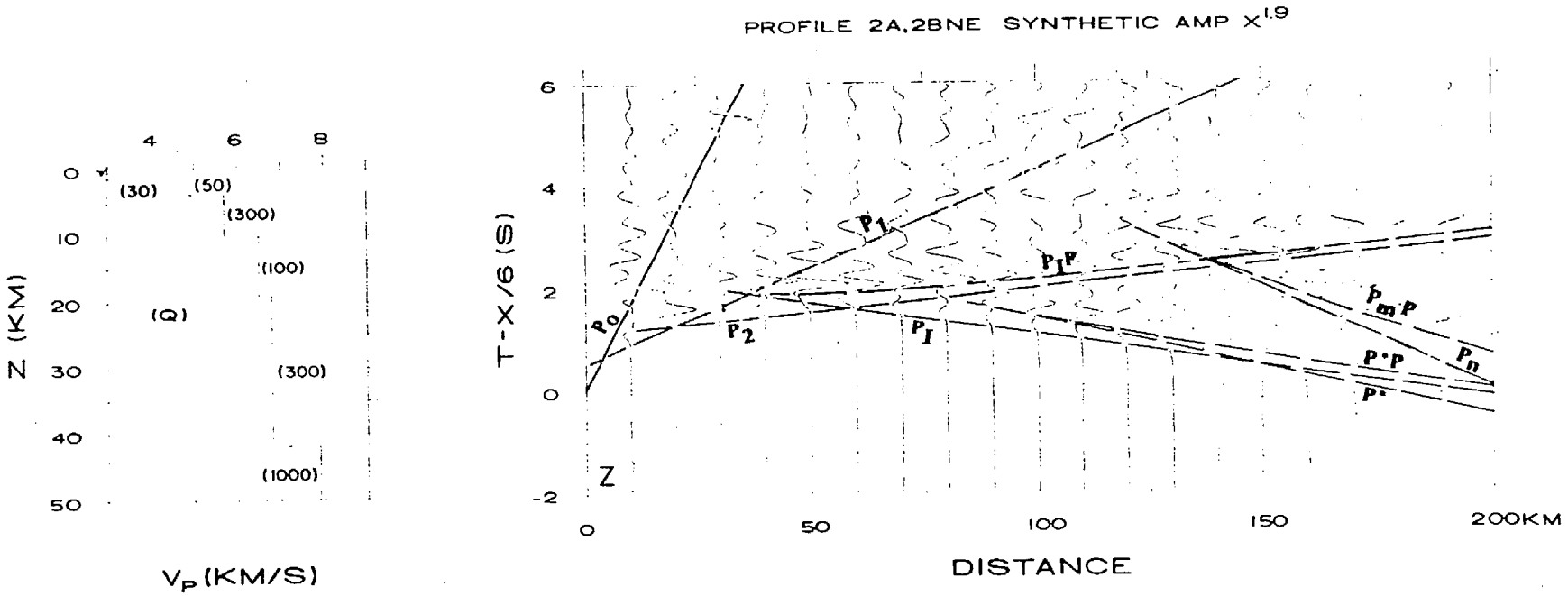
PROFILE 2A,2BNE SYNTHETIC AMP X^1.9
4
6
8
0
10
20
30
40
50
Z (KM)
(30)
(50)
(300)
(100)
(Q)
(300)
(1000)
V_P (KM/S)
6
4
2
0
-2
T-X/6 (S)
Z
P_1
P_1P
P_2
P_I
P_mP
P_n
P*P
P*
0
50
100
150
200KM
DISTANCE

Figure 7

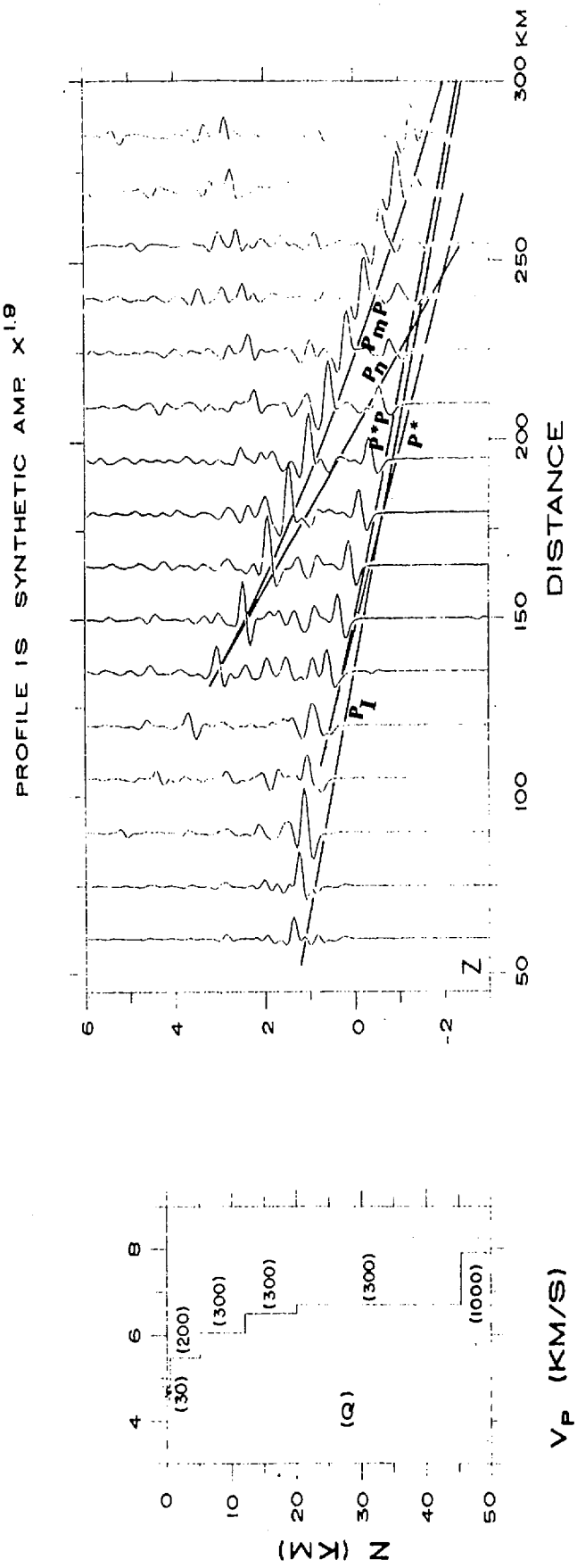
PROFILE IS SYNTHETIC AMP. X 1.9
300 KM
250
200
150
100
50
DISTANCE
Z
6
4
2
0
-2
P_I
P^*
P^*P
P_n
P_mP
Z (KM)
0
10
20
30
40
50
4
6
8
(30)
(200)
(300)
(300)
(300)
(1000)
(Q)
V_P (KM/S)

Figure 8

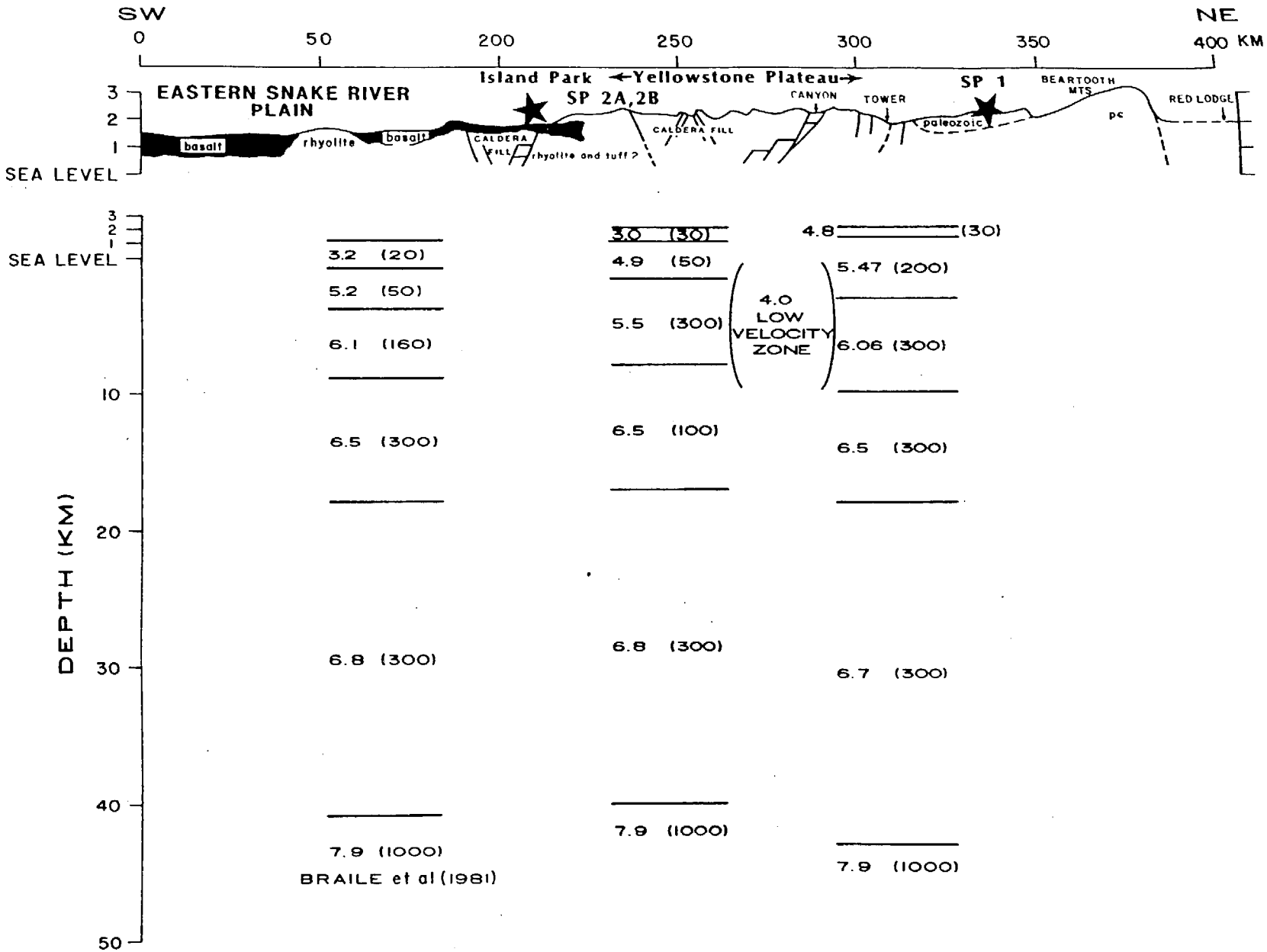
SW
NE
0
50
200
250
300
350
400 KM
Island Park
Yellowstone Plateau
SP 2A,2B
SP 1
EASTERN SNAKE RIVER PLAIN
basalt
rhyolite
basalt
CALDERA FILL
rhyolite and tuff?
CALDERA FILL
CANYON
TOWER
paleozoic
pc
BEARTOOTH MTS.
RED LODGE
SEA LEVEL
DEPTH (KM)
3.2 (20)
5.2 (50)
6.1 (160)
6.5 (300)
6.8 (300)
7.9 (1000)
BRAILE et al (1981)
3.0 (30)
4.9 (50)
5.5 (300)
6.5 (100)
6.8 (300)
7.9 (1000)
4.0 LOW VELOCITY ZONE
4.8 (30)
5.47 (200)
6.06 (300)
6.5 (300)
6.7 (300)
7.9 (1000)

Figure 9

THE YELLOWSTONE-SNAKE RIVER PLAIN SEISMIC PROFILING EXPERIMENT: CRUSTAL STRUCTURE OF THE EASTERN SNAKE RIVER PLAIN

L.W. Braile (Department of Geosciences, Purdue University, West Lafayette, Indiana 47907)

R.B. Smith (Department of Geology and Geophysics, University of Utah, Salt Lake City, Utah 84112)

J. Ansorge (Geophysics Institute, Swiss Federal Institute of Technology, Zurich, Switzerland)

M.R. Baker (Department of Geosciences, Purdue University, West Lafayette, Indiana 47907)[1]

M.A. Sparlin (Department of Geosciences, Purdue University, West Lafayette, Indiana 47907)[2]

C. Prodehl (Geophysics Institute, University of Karlsruhe, Karlsruhe, Germany)

M.M. Schilly (Department of Geology and Geophysics, University of Utah, Salt Lake City, Utah 84112)[3]

J.H. Healy (U.S. Geological Survey, Menlo Park, California 94025)

St. Mueller (Geophysics Institute, Swiss Federal Institute of Technology, Zurich, Switzerland)

K.H. Olsen (Los Alamos National Laboratory, Los Alamos, New Mexico 87545)

February 10, 1981

1) Now at: Exxon Production Research Company, Box 2189, Houston, TX 77001

2) Now at: Arco Oil & Gas Company, PO Box 2819, ARB 2615, Dallas, TX 75221

3) Now at: Amoco Production Company, Security Life Building, Denver, CO 80202

ABSTRACT

Seismic refraction profiles recorded along the eastern Snake River Plain (ESRP) in southeastern Idaho during the 1978 Yellowstone-Snake River Plain cooperative seismic profiling experiment are interpreted to infer the crustal velocity and attenuation (Q^{-1}) structure of the ESRP. Travel-time and synthetic seismogram modeling of a 250 km reversed refraction profile as well as a 100 km detailed profile indicate that the crust of the ESRP is highly anomalous. Approximately 3-6 km of volcanic rocks (with some interbedded sediments) overlie an upper-crustal layer (compressional velocity ~ 6.13 km/sec) which thins southwestward along the ESRP from a thickness of ≈ 10 km near Island Park Caldera to ~ 2 to 3 km beneath the central and southwestern portions of the ESRP. An intermediate-velocity (~ 6.5 km/sec) layer which is confined to the ESRP has replaced much of the upper-crustal layer. A thick (~ 22 km) lower crust of compressional velocity 6.8 km/sec, a total crustal thickness of ≈ 42 km and a P_n velocity of ~ 7.9 km/sec is observed in the ESRP similar to the western Snake River Plain and the Rocky Mountains Provinces. High attenuation is evident on the amplitude corrected seismic data due to low Q values in the volcanic rocks (Q = 20 to 200) and throughout the crust (Q = 160 to 300). Based on these characteristics of the crustal structure and the volcanic-age progression data reported by Armstrong et al. (1975), it is suggested that the ESRP has resulted from an intensive period of silicic volcanism associated with regional uplift and subsequent caldera collapse followed

2-5 million years later by a pervasive intrusion of high-density and velocity material into the upper crust, accompanying basaltic volcanism, and subsidence.

INTRODUCTION

During September and early October of 1978, a large-scale seismic refraction profiling experiment was carried out in the Yellowstone-Snake River Plain (Y-SRP) region of southern Idaho, northwestern Wyoming and southwestern Montana. The experiment was designed to investigate the crustal structure and tectonic evolution of the Yellowstone-Snake River Plain volcano-tectonic system and provide background geological and geophysical data on the geothermal potential of the area. The experiment was a cooperative seismic project involving investigators from several American universities, United States government agencies and two European geophysical institutes. In this paper and a companion paper (Smith et al., this volume), we present a description of the seismic experiment and an interpretation of the general crustal structure of the Yellowstone-Snake River Plain region. In this paper, the results of seismic refraction profiles recorded in the eastern Snake River Plain (ESRP) area will be emphasized.

During the Y-SRP seismic experiment, portable vertical-component or three-component seismographs were deployed at remote sites across the Yellowstone plateau, along the axis of the ESRP, and along a profile across the ESRP to record several blasts detonated for the purpose of investigating the crustal structure in this region. Station spacing was generally between 2 and 3 km. Charge sizes for the shotpoints were chosen and locations of the shotpoints selected in such a way as to obtain data on the deep crust and upper mantle of the region

in addition to the shallow volcanic and upper-crustal structure. However, the average station spacing of 2 to 3 km (including several gaps in coverage) preclude the possibility of detailed interpretation of the shallow structure except in isolated areas along the profiles. Shotpoint information for the ESRP phase of the experiment is shown in Table 1. Locations of the shotpoints and seismograph stations is illustrated on the index map in Figure 1. Five shotpoints and 2 quarry blasts were utilized to obtain seismic data pertaining to the crustal structure of the ESRP region. The combined ESRP data represent 2 principal profiles - one along the axis of the ESRP (herein called Profile SP2-SP5) and one profile approximately perpendicular to the axis of the ESRP (here called the Conda-SP7 profile) which has been described by Sparlin et al. (this volume). The SP2-SP5 profile consisted of 4 shotpoints with the two end shotpoints (SP2 and SP5) being the largest shots detonated during the seismic experiment. Interpretation of the SP2-SP5 profile will be the principal objective of this paper.

During the experiment, as many as 220 seismographs were deployed simultaneously for recording of the shotpoints detonated. These seismographs represent a wide variety of seismometer and recorder instrument types. After digitization, merging and editing of all of the seismograms recorded during the experiment, amplitude normalization of the data was performed utilizing an inverse filter technique described by Baker et al. (this volume). The final digital data have a sample interval of 0.02 seconds and are displayed as reduced-time record sections.

Previous geological and geophysical studies of the ESRP indicate that it is a volcanic filled depression which trends nearly perpendicular to the regional structures of the Basin and Range, Northern Rocky Mountains,

and Middle Rocky Mountains Provinces which bound the ESRP. To the northeast of the ESRP are the Island Park and Yellowstone Calderas which have displayed volcanic, seismic and hydrothermal activity within the last million years. Kirkham (1931) suggested that the ESRP is a simple downwarp and that faulting along the margins of the plain has been of minor importance. However, Sparlin et al., (this volume) have demonstrated the existence of major faulting along the northwestern boundary of the ESRP from seismic and gravity modeling. Gravity studies (Hill, 1963; Mabey, 1976, 1978; LaFehr and Pakiser, 1962) have identified a prominent positive gravity anomaly which approximately coincides with the axis of the ESRP, but is more localized toward the northern part of the downwarp in the western Snake River Plain. Deep crustal structure information from seismic data is absent in the ESRP, but a seismic refraction profile from Mountain City to Boise in the western Snake River Plain (Hill and Pakiser, 1966) has demonstrated that the western Snake River Plain consists of a thick, high-velocity crust with a surface layer of lower velocity volcanic materials. To the south of the ESRP, the northeastern Basin and Range Province is characterized by lower average crustal velocity and a crustal thickness of less than 30 km (Braile et al., 1973; Keller et al., 1975; Smith, 1977, 1978; Hill and Pakiser, 1966). Armstrong et al. (1975) utilized K-Ar dates of late Cenozoic silicic volcanic rocks of the ESRP to demonstrate a systematic age progression of volcanism along the ESRP. Their data indicate that silicic volcanic activity began about 15 million years ago in southwestern Idaho and progressed at an average rate of approximately 3.5 cm/yr northeastward toward its present site at the Yellowstone plateau. They also indicate that the initiation of basaltic volcanism has followed

this same time progression, however with a lag of approximately 2 to 5 million years after the silicic volcanism. In addition, the basaltic volcanism in the southwestern portion of the ESRP has remained active sporatically to the present. Today, the Yellowstone Caldera is representative of this silicic phase of volcanism which characterizes the volcanic progression and the Island Park region represents the leading edge of the basaltic volcanic activity. Brott et al. (1978) utilized heat flow data on the western Snake River Plain and an observed heat flow-elevation relationship for the western and eastern Snake River Plain to propose a tectonic model for the development of the Y-SRP volcanic province. According to their model, the time progression of volcanism along the eastern Snake River Plain is accompanied by intrusion into the crust and rapid transfer of heat to the surface by intrusion and eruptions. High heat flow adjacent to the margins of the ESRP is observed, but low values are observed in the ESRP itself due to groundwater circulation in the Snake River Plain acquifer (Brott et al., 1978). According to the model suggested by Brott et al., cooling of the crust after the intense silicic volcanic activity results in the subsidence which is presently observed as the eastern Snake River Plain downwarp. Alternate tectonic models have been proposed to describe the geologic evolution of the eastern Snake River Plain during the past 15 million years. Hamilton and Myer (1966) suggested that the ESRP consists of a tensional rift. Morgan (1972) and Smith and Sbar (1974) described the eastern Snake River Plain-Yellowstone system as the track of a mantle plume or hotspot. Finally, Taubeneck (1971) suggested that the ESRP was laterally faulted and the upper crust pervasively intruded by dikes.

SEISMIC REFRACTION DATA AND TRAVEL-TIME INTERPRETATION

A crustal velocity model has been developed by interpretation of the seismic refraction lines along the axis of the eastern Snake River Plain (SP2-SP5). The vertical component seismic refraction data for shotpoint 2 and shotpoint 5 are plotted in reduced-time record sections after amplitude normalization by the methods described by Baker et al. (this volume). The amplitudes of the seismograms shown on the record sections have been scaled by multiplying by distance to the 1.5 power for convenient plot scaling. Data from shotpoints 2 and 5 represent a reversed refraction profile emphasizing intermediate and deep crustal structure. Because of the distance between shotpoints 2 and 5, gaps in the observed seismic data coverage, and the 2 to 3 km average station spacing, the shallow velocity structure which is derived from these data represents an average over the entire profile length along the axis of the ESRP. More detailed interpretations of the shallow velocity structure of the ESRP are described later for shotpoint 8 (Figure 1) and by Sparlin et al. (this volume). The reduced-time record section for shotpoint 2 to the southwest is shown in Figure 2 and the reversed segment of this profile (shotpoint 5 recorded to the northeast) is shown in Figure 3. Both of these record sections are reduced with a reducing velocity of 6 km/sec. The data have been amplitude normalized and bandpass filtered with a 1 to 8 hz filter. In addition, the seismograms have been adjusted to a 1200 meter elevation datum assuming a near-surface velocity of

4.5 km/sec. The seismograms shown in the record sections for shotpoints 2 and 5 show generally good signal-to-noise ratio and the amplitude normalization procedure allows phase correlation as well as amplitude correlation along travel-time branches. Travel-time curves for a simple dipping, homogeneous layered model (Figure 8) are also shown on the seismic record sections for shotpoint 2 and 5. The phase nomenclature is described in Figure 2. Prominent arrivals on the shotpoint 2 and shotpoint 5 record sections include the phases P_2, P_5P and P_mP. The P_mP arrivals, which are reflections from the Mohorovicic discontinuity (Moho) are particularly evident as the large-amplitude, coherent-phase arrivals in the distance range of 120 to 250 km on the shotpoint 2 record section. While not as prominent, the P_mP arrivals on the shotpoint 5 section are also evident. These reflections are particularly important to interpretation of the crustal model for this reversed refraction profile. Due to the thickness of the crust and the high average velocity as shown by the model in Figure 8, the crossover distance for the P_n arrival is over 230 km. At this distance range on both the shotpoint 2 and shotpoint 5 profiles, the signal-to-noise ratio is generally low on the observed seismograms and consistent P_n arrivals are not observed. The choice of the travel-time curve for the P_n phase was based on the position of the near-critical reflections of the P_mP arrival and the optimum alignment of weak P_n arrivals in the distance range of 180 to 250 kilometers on the record sections. The resulting upper mantle velocity is 7.92 km/sec. However, due to the uncertainty of the arrival times of the P_n phase, as indicated on the record section, this velocity is uncertain. The thickness of the crust, however, is much more certain due to the presence of the strong P_mP arrivals which constrain the velocity of the lower crust and the crustal thickness. A

very weak refracted first arrival (P_4) is observed on both of the shotpoint 2 and shotpoint 5 record sections. However, its amplitude is so small relative to other phases that it is not evident on the record sections shown in Figure 2 and Figure 3. Enlarged-amplitude record sections showing the appropriate distance and time range for the P_4 arrival for shotpoints 2 and 5 are shown in Figures 4 and 5. Here it can be seen that while the P_4 arrival is weak and barely above the noise level on many of the seismograms, it is a coherent first arrival on the records between approximately 90 and 150 km. This phase has an apparent velocity of approximately 6.5 km/sec which is typically an intermediate velocity for crustal rocks. In addition, its crossover distance is small indicating that the top of this layer is shallow. An arrival with unusual character, but highly consistent phase correlation which follows P_4 by less than 1 second, is the P_5P arrival in the distance range of approximately 80 to 200 km. This phase was adequately modeled as a wide-angle reflection from the lower-crustal layer having a velocity of approximately 6.8 km/sec. The P_n and P_mP phases are best illustrated on 8 km/sec reducing velocity record sections for shotpoints 2 and 5 shown in Figures 5 and 6. In these sections, the large amplitude P_mP arrivals stand out as coherent phases and the weak correlation of P_n phases across the record is evident.

The primary differences between the shotpoint 2 and shotpoint 5 record sections are the presence of more coherent P_mP arrivals on the shotpoint 2 data and the absence of a thick $\approx$ 6 km/sec layer near shotpoint 5 which gives rise to a very short crossover distance for the P_4 phase. In contrast, the shotpoint 2 record section shows $\approx$ 6 km/sec arrivals to distances of approximately 70 km from the shotpoint.

The crustal model which has been used to calculate the travel-times which result in a good fit to the observed seismic data on the record sections shown in Figures 2 through 7 is illustrated in Figure 8. Modeling of the travel-times for the record sections was performed by inverse and trial and error calculations of travel-times for reflected and refracted phases for both record sections. The resulting velocity model consists of homogeneous dipping layers as shown in Figure 8. As noted earlier, the shallow structure of this velocity model must be considered as an average over the entire length of the shotpoint 2 to 5 reversed profile and is not meant to be representative of the detailed velocity structure in the entire distance range between the two shotpoints. In fact, shotpoint 8 and shotpoint 4 data as well as the Conda-SP7 profile discussed by Sparlin et al. (this volume) indicate somewhat greater detail in the shallow structure and some slight differences from the velocity model shown here. Although the layer boundaries on the ESRP average model (Figure 8) are shown to be continuous from shotpoint 5 to shotpoint 2, the deeper interfaces (Moho and top of lower crustal layer) are not constrained by the seismic data within a distance of ≈ 40 km of the shotpoints. The most prominent features of the ESRP average model (Figure 8) are the thick section of low-velocity volcanic and sedimentary materials in the near surface, the thinning of the 6.13 km/sec layer from the northeast to the southwest and the presence of an intermediate velocity (6.51 km/sec) layer at an extremely shallow depth beneath the eastern Snake River Plain. This anomalous layer was shown to have significant relief in a northwest-southeast direction by the ray-trace modeling presented by Sparlin et al. (this volume).

AMPLITUDES AND SYNTHETIC SEISMOGRAM MODELING

More detailed analysis of the seismic record sections recorded during the Y-SRP seismic experiment is illustrated by application of synthetic seismogram modeling to the record sections for shotpoint 8 recorded to the northeast and shotpoint 2 recorded to the southwest. The observed and synthetic seismic data for shotpoint 8 are shown in Figure 9. Data recovery in this area of the ESRP was particularly good and the relatively close station spacing and high signal-to-noise ratio in the first 100 km of this refraction line allows more detailed synthetic seismogram and amplitude modeling of the observed arrivals to infer the shallow crustal structure along the axis of the ESRP. Both the observed and the synthetic data shown in Figure 9 have been scaled by multiplying the amplitudes by distance to the 1.5 power. The general fall-off of amplitudes of various phases between the two record sections is comparable. The observed seismic data (Figure 9) for shotpoint 8 show several interesting features. First, amplitude maxima caused by near critical point reflection and constructive interference occur at distances of approximately 12 and 42 km. Rapid attenuation of all phases beyond approximately 50 km is evident on the observed record section when one considers that the amplitudes have been multiplied by distance to the 1.5 power. Modeling of the shotpoint 8 NE data was initially performed by calculation of travel-times for reflected and refracted phases. Subsequently, synthetic seismograms were calculated using the modified reflectivity method (Kind, 1978) for the anelastic

model which is shown in Figure 10. Many attempts were made to model the observed data with the synthetic seismograms and it was clear that the modeling procedure was very sensitive to the details of the velocity structure and the Q values used in the model. In particular, the abrupt attenuation of the P_2 phase in the distance range of 5 to 15 km required low Q values in the near-surface volcanic and sedimentary rocks. In addition, the position of high amplitude (near critical point) arrivals near 15 km and 40 km on the synthetic data was also very sensitive to velocity structure and Q values. Finally, attenuation of P_4 and P_5P arrivals in the distance range greater than 50 km was sensitive to the Q values of the intermediate layer and the lower crust. The synthetic data shown in Figure 9 show a remarkably good match to the general character, amplitude fall-off and phase relationships of many of the seismograms in the observed record sections. In fact, for several of the observed seismograms, a synthetic record can be overlain over the observed seismogram and near phase-to-phase correlation is observed. Of course, severe signal-to-noise ratio problems are evident on the observed data, particularly in the greater distance range, and several erratic-amplitude seismograms are also observed. However, the large number of stations allows a consistent trend in amplitude and phase character of the observed records to be evident on the record sections.

The derived model for the shotpoint 8 to the northeast record section (Figure 10) is a plane, homogeneous layered model representing an average velocity and Q structure for the shallow crust in the central portion of the ESRP just northeast of shotpoint 8. Although this modeling was restricted to laterally homogeneous structures, the derived velocity structure is consistent with the travel-time modeling using ray-tracing methods presented by Sparlin et al. (this volume). They

present evidence that lateral variation in velocity structure exists to the northeast of shotpoint 8. However, their laterally inhomogeneous velocity model indicates small dip on the interface at the top of the ≃ 5.2 km/sec layer beginning at about 25 km northeast of shotpoint 8. This slight lateral inhomogeneity would not be expected to appreciably alter the amplitude and general character of the observed seismic records and the synthetic seismogram modeling illustrated in Figure 9.

The velocity structure for the central area of the ESRP from the synthetic seismogram modeling of shotpoint 8 NE data (Figure 10) indicates that a thick section of volcanic and sedimentary rocks with velocities less than 5.2 km/sec overlie an extremely thin (≃ 2 km) upper-crustal layer of 6.13 km/sec velocity. Extremely low Q values are associated with the near-surface low-velocity rocks. The anomalous ≃ 6.5 km/sec velocity layer in the depth range of 9 to 16 km is also indicated to have a low Q value.

Synthetic seismogram modeling using the modified reflectivity method was also applied to the shotpoint 2 southwest record section in an attempt to model the deep crustal structure and particularly P_mP arrivals which are prominent on the observed record section. Calculated vertical component synthetic seismograms are shown in Figure 11 for the 80 to 250 km distance range appropriate to deep crustal arrivals from the derived model for shotpoint 2 SW data. The seismograms in this model have again been scaled by multiplying the amplitudes by distance to the 1.5 power, identical to the amplitude scaling which was performed on the observed data. Although the travel-time modeling of the shotpoint 2 to 5 record sections required a dipping layer model (Figure 8), we are restricted to plane homogeneous layered models for the

synthetic seismogram calculations and, therefore, the velocity structure derived by the synthetic seismogram modeling (Figure 12) must be considered to be an average over the length of the profile. The prominent arrivals P_5P and P_mP which were observed on the shotpoint 2 SW record section are evident on the synthetic seismograms calculated for the plane, homogeneous layered model. The weak first arrival (P_4) is also evident on the synthetic data although its amplitude is small and difficult to observe on the synthetic data plotted with the ampltiude scaling as shown in Figure 11. The travel-time curves drawn to match the arrivals in Figure 11 are calculated for the velocity structure shown in Figure 12. Comparison of the observed (Figure 2) and synthetic (Figure 11) seismic record sections indicate that the general amplitude and phase character of the arrivals compares favorably. For modeling the shotpoint 2 SW data, the two layers underlying the 3.3 km/sec surface layer on the shotpoint 8 NE model have been averaged and included in a single layer. In the course of the modeling, many attempts were made to vary the velocity and Q structure of the model in order to match the observed data as well as possible. Various Q values were tried, particularly for the lower crust, ranging from 150 to 2000. In addition, a velocity gradient transient zone for the Moho discontinuity at a depth of approximately 42 km was tested. Thicknesses of the transition zone from 1 to 10 km were attempted. However, the P_mP amplitudes show the best match for a simple first-order discontinutiy in velocity at the Moho. The shear-wave velocities corresponding to the compressional-wave velocities shown in the layered (Figure 12) model were selected corresponding to a Poisson's ratio of 0.25 (compressional velocity = $\sqrt{3}$ times shear velocity) with the exception of the lower crustal layer and upper mantle

for which the shear velocities are 3.6 and 4.2 km/sec respectively, consistent with the results of surface wave dispersion studies by Greensfelder and Kovach (this volume).

An additional approach to the comparison between the observed and synthetic data for shotpoint 2 SW is shown in Figure 13. Amplitudes of the arrivals for phases P_4, P_5P, and P_mP were read from the observed seismograms and plotted as a relative amplitude versus distance plot. The amplitude-distance curves defined by the synthetic data are also shown on the amplitude-distance diagram of Figure 13 for comparison. Several erratic-amplitude values are evident on the amplitude-distance plot and these are also evident on examination of the observed seismic record section (Figure 2). However, the general character of the amplitude-distance relations for the three phases is reasonably consistent, showing a consistent amplitude-distance trend. The P_mP phase shows a prominent peak in the amplitude-distance curve at approximately 130 to 140 km. The synthetic data show this peak at $\simeq$ 150 km which corresponds to the near-critical-point region of the reflected P_mP arrivals. Attempts to shift this amplitude peak to smaller distance ranges utilizing a low-velocity zone in the lower crust or transition zones to model the Moho discontinuity were unsuccussful in that although the amplitude peak was able to be shifted, the relative amplitudes between the three phases plotted and the amplitude fall-off rate of the P_mP arrival did not match the observed data. Observed amplitudes of the P_5P phase at distances greater than 190 km show an abrupt amplitude increase. However, this may be due to interference with other arrivals, particularly the P_n phase, in this distance range and thus these amplitudes were not modeled. The P_4 phase exhibits

a particularly complicated amplitude-distance trend with rapid attenuation of amplitudes with distance, two peaks in the amplitude-distance curve, and an abrupt localized area of low amplitudes at approximately 130 km. These effects are probably due, at least partially, to constructive and destructive interference. For example, the amplitude minimum at approximately 130 km corresponds to an area of the observed seismic data where P_4, a head wave refracted in the low Q, 6.5 km/sec layer, is a first arrival which would be expected to have very small amplitudes and attenuate rapidly with distance. Areas of larger amplitudes for the P_4 phase, approximately 90 km and approximately 160 km distance, correspond to regions of the travel-time curve (Figure 2) where other phases overlap with the P_4 arrivals. The amplitude-distance curve for the P_4 phase from the synthetic data illustrates this same character with a slight shift to shorter distance ranges. In general, a good match is seen between the observed and synthetic amplitude-distance data shown in Figure 13. Significant improvement in the fit would likely require consideration of two-dimensionality of the velocity structure which is not considered here due to the limitations of the reflectivity method synthetic seismogram calculations. However, such consideration would probably not be warranted due to the scatter of the amplitude-distance observations. The velocity and Q structure shown in the plane, homogeneous-layered model of Figure 12 was developed by consideration of many synthetic seismogram record section calculations. During this process, it was observed that properties of the amplitude-distance curves and character of the synthetic seismogram arrivals were sensitive to details of the velocity structure and the Q values of the layers. For example, an identical velocity structure as shown in Figure 12 was utilized to calculate

synthetic seismograms with a Q value of 1000 in the lower crust. However, the relative amplitudes between the P_4, P_5P and P_mP phases for the synthetic seismograms did not produce a satisfactory match to the observed data for this trial. A low-velocity zone introduced by a negative velocity gradient in the lower crust was also attempted. However, this modification resulted in a poor comparison to the relative amplitudes of the three phases and the amplitude-distance decay rate of the P_mP phase. Thus, although the synthetic seismogram modeling shown here does not correspond to an inverse method in which quantitative estimates of the uncertainty of model parameters can be given, the multiple attempts at modeling various features in the velocity and Q structure indicate that the model shown in Figure 12 is a reasonable structure for the crust of the ESRP and illustrate that the observed seismic data are fairly sensitive to small changes in velocity and Q structure.

CONCLUSIONS

Travel-time and synthetic seismogram modeling of seismic record sections for the eastern Snake River Plain of southeastern Idaho have indicated a highly anomalously crust. The crustal thickness is approximately 42 km and the average compressional velocity of the crystalline part of the crust (beneath the 5.2 km/sec volcanic layer) is 6.64 km/sec, an unusually high value. The high average velocity is primarily due to the presence of an extremely thin upper-crustal layer (velocity ≈ 6.13 km/sec) and presence of an intermediate layer (velocity ≈ 6.51 km/sec) which has apparently replaced much of the upper crust beneath the ESRP. The average crustal model of the ESRP indicates that the upper crustal layer thins progressively from the southwest to the northeast suggesting that the thinning is associated with the time-progressive volcanism and subsequent subsidence that has characterized the evolution of the crust in the eastern Snake River Plain area in the last 15 million years. The near-surface volcanic and sedimentary rocks are thickest in the southwest and thin toward Island Park Caldera to the northeast. They extend to a depth of at least 6 km beneath the central part of the ESRP. The proportion of silicic to basaltic volcanics also increases from southwest to northeast along the ESRP until the relative volume of basalt is insignificant near Island Park Caldera and the Yellowstone Plateau (Thompson, 1977). The crustal thickness of 42 km is approximately the same as that found under the Yellowstone plateau (Smith et al., this volume), that reported by Hill and Pakiser (1966) for the western Snake

River Plain in the vicinity of Boise, Idaho and the thickness inferred for the Middle Rocky Mountains (Willden, 1965; Braile et al., 1974). The velocity and depth to the top of the lower-crustal layer compares reasonably well with that found in the adjacent Basin and Range and Middle Rocky Mountains provinces (Hill and Pakiser, 1966; Willden, 1965; Braile et al, 1974).

Synthetic seismogram modeling of two of the record sections for the ESRP suggest that the crustal layers are highly attenuative. Low Q values are associated with the shallow volcanic rocks as well as deeper crustal layers. Although some lateral velocity structure variation along the axis of the ESRP (northeast-southwest) is indicated by the travel-time modeling presented here and by Sparlin et al. (this volume), the synthetic seismogram modeling for shotpoints 2 and 8 indicate that simple plane-layered models are adequate to explain the principal travel-time, amplitude and wave-form characteristics of observed seismic data along the axis of the ESRP. However, as clearly demonstrated by the ray-tracing modeling presented in Sparlin et al. (this volume) prominent lateral inhomogeneity across the ESRP (northwest-southeast direction) is required to match the observed data. The synthetic seismogram modeling, including the amplitude-distance measurements illustrated in Figure 13, was extremely useful in refining the details of the velocity structure of the ESRP model and in defining the Q values of the layered structure. Amplitude-distance curves are presented which provide a good match to the observed data. It is observed that these amplitude-distance relationships are highly sensitive to the velocity and Q structure of the derived model.

Although more detailed analysis will be required in the future, a few comments are appropriate here on the implications of the velocity structure which has been derived for the Yellowstone-Eastern Snake River Plain region to the tectonic models which have been proposed for the Y-SRP area. The pertinent observations of the crustal structure from Yellowstone proceeding southwest along the eastern Snake River Plain are that the crustal thickness and Moho velocity remain approximately constant at 42 km and 7.9 km/sec respectively and are continuous with the adjacent provinces except for the boundary with the Great Basin to the south. A lower-crustal layer with a depth to the top of approximately 15 km beneath the Yellowstone plateau and approximately 20 km beneath the ESRP with a velocity of 6.8 km/sec appears to be continuous along the entire Y-SRP system. A thick section of rhyolitic and basaltic volcanic rocks along with some sedimentary layers exists along the ESRP with the thickness increasing to over 6 km toward the southwest. Under the Yellowstone plateau, an upper crustal layer of 6 km/sec velocity, with low-velocity anomalies of 5.7 km/sec attributed to partial melting, attains a thickness of 12 to 15 km. However, beginning just southwest of the Island Park Caldera this upper-crustal layer thins significantly such that it is only about 2 to 3 km thick beneath the Conda-SP7 profile and shotpoint 5. Accompanying the thinning of the upper-crustal layer is an anomalous 6.5 km/sec layer which is present to shallow depths beneath the entire ESRP crust. These crustal velocity structure changes are approximately coincident with the position of the northeast trending leading edge of basaltic volcanism near the Island Park Caldera. When these observations are combined with the volcanic age progression relationships

described by Armstrong et al. (1975) and the thermal model proposed by Brott et al. (1978) for the evolution of the eastern Snake River plain, the following two-stage evolutionary model of the crust during the past 15 million years is suggested. Initially, a thermal perturbation of the crust results in 3 to 4 km of surface uplift, intense silicic volcanism and subsequent caldera collapse. During this stage, rising (basaltic?) magma, probably from the upper mantle, produces only minor velocity structure perturbations in the crust, but probably causes partial melting of a portion of the upper crustal layer (as evidenced by the low velocity upper crust beneath the Yellowstone area) during the process of rapid transfer of volcanic material and heat to the surface. Partial melting of upper or lower crustal rocks generates the silicic volcanism. This phase is presently represented by the Yellowstone plateau. Two to five million years later, the second phase of volcanic activity begins as represented by the inception of basaltic volcanism. During this phase, eruptions of basaltic magma are accompanied by significant subsidence and the upper crust is pervasively intruded by high-density, high-velocity material which is represented by the 6.51 km/sec layer in the ESRP. Continued cooling, subsidence due to thermal contraction, and minor periodic basaltic volcanic activity persists through the remainder of the at least 15 million year evolutionary sequence. This second phase is represented by the eastern Snake River Plain with the youngest portion of the phase representing the inception of basaltic volcanism corresponding to the Island Park Caldera to Rexburg, Idaho area and the remainder of the evolutionary sequence being represented by the southwestern part of the ESRP. Continued basaltic volcanism throughout the duration of the second phase

is of minor intensity and probably represents rapid ascent of magma through small dikes or pipes from the upper mantle. An example of these late-stage volcanics is found in the craters of the Moon, Idaho area. Considering the potential geothermal anomalies along the Y-SRP system, the recent basaltic volcanism would represent a minor thermal anomaly in the crust. However, partial melt zones in the upper crust associated with silicic volcanism could produce significant temperature anomalies but would be restricted to the Yellowstone Plateau and extreme northeastern part of the ESRP. Additional geothermal anomalies could be present near the axis of the ESRP due to shallow (7-10 km) intrusion of high density and velocity rocks or along the northwestern margin of the ESRP where a fault of at least 4 km offset could provide a route for upward migration of hot fluid.

ACKNOWLEDGEMENTS

It is difficult to give a complete list of all of the many people who have contributed to the 1978 Yellowstone-Snake River Plain seismic refraction profiling experiment. All of those who participated in some way to the planning, field work, data reduction, interpretation or report preparation are appreciated. Special thanks are due to those listed below for their cooperation and assistance in the project. The following institutions provided seismographs and personnel for the survey: U.S. Geological Survey; Geophysics Institute, ETH, Zurich, Switzerland; Geophysics Institute, University of Karlsruhe, Karlsruhe, Germany; University of Utah; Purdue University; University of Texas at El Paso; Los Alamos National Laboratory; University of Montana; Stanford University; University of Texas at Dallas; University of California at San Diego; New Mexico State University; University of Nevada, Reno; and Southern Methodist University. We are grateful to the following people who participated in the field work: Dave Hill, Jack Healy, Ralph Lamson, Steve Wegener, Will Koller, Stephan Mueller, Nicholas Deichmann, Marcus Grieder, Jorge Ansorge, Claus Prodehl, Manfred Rittershoffer, Martin Jentsch, Dieter Emter, Rolf Kunzler, John Michaels, Bronson Hawley, Debbie Wechsler, Tim Keho, Mike Schilly, Matt Mabey, Jack Pelton, Tom Owens, Mark Baker, Mark Sparlin, Tony Qamar, Ken Olsen, Fred Homuth, John Stewart, Jim York, Carl Newton, Roger Felch, Ted Handel, Paul Daggett, Roger Greensfelder, Jim Brune, Keith Priestly, Ron Ward, Bob Smith and Larry Braile. Dave Butler, Roger Bowman, Roger Grette and Andy Staatz of Microgeophysics Corporation

provided the drilling and blasting services. The assistance of several government agencies including the U.S. National Park Service (superintendent of Yellowstone Park, John Townsley), the Idaho National Engineering Laboratory (Paul Ruhter, John Green, R.J. Beers and Jack Barraclough), the U.S. National Forest Service (Teton and Targhee districts), and the Bureau of Land Management (Vic Bartkus and Mike Austin) in permitting and logistical help is appreciated. The cooperation of Gay Mine (Bob Hill and Jim Simmons) and Conda Mine (Bob Trushot and Bill Schmidt) personnel of the J.R. Simplot Co. in facilitating recording of the origin times of quarry blasts is appreciated. Dave Blackwell was instrumental in providing one of the shot holes. Nicholas Deichmann, Tom Owens, Mark Baker and Mike Schilly deserve special thanks for completing the difficult task of digitizing and editing the seismic data. Personnel from the University of Texas at Dallas and the Phillips Petroleum Company Research Lab cooperated in recording deep-reflection data from the shotpoints and provided their data and interpretation to us. Major support for this research was provided by the National Science Foundation Grant No. EAR77-23357 to Purdue University and Grant No. EAR77-23707 to the University of Utah and United States Geological Survey Geothermal Research Program Grant No. 14-08-0001-G-532 to Purdue University. Indirect support in the form of seismographs and personnel time was provided by the U.S. Geological Survey, Menlo Park; the Geophysics Institute of the Swiss Federal Institution of Technology, Zurich, Switzerland; the Geophysics Institute of the University of Karlsruhe, Karlsruhe, Germany; and the Department of Energy through Los Alamos National Laboratory.

REFERENCES

Armstrong, R.L., W.P. Leeman and H.E. Malde, K-Ar dating, Quaternary and Neogene volcanic rocks of the Snake River Plain, Idaho, Amer. J. Sci., 275, 225-251, 1975.

Baker, M.R., L.W. Braile and R.B. Smith, Amplitude normalization of seismograms from multiple seismograph recording systems for the Yellowstone-Snake River Plain seismic refraction experiment, Submitted to J. Geophys. Res., 1981.

Braile, L.W., R.B. Smith, G.R. Keller, R. Welch and R.P. Meyer, Crustal structure across the Wasatch Front from detailed seismic refraction studies, J. Geophys. Res., 79, 1295-1317, 1974.

Brott, C.A., D.D. Blackwell and J.C. Mitchell, Tectonic implications of the heat flow of the western Snake River Plain, Idaho, Bull. Geol. Soc. Amer., 89, 1697-1707, 1978.

Fenneman, N.M. and D.W. Johnson, Physical divisions of the United States: U.S. Geol. Surv. map, scale 1:7,000,000, 1946.

Greensfelder, R.W. and R.L. Kovach, Shear-wave velocities and crustal structure of the eastern Snake River Plain, Idaho, Submitted to J. Geophys. Res., 1981.

Hamilton, W. and W.B. Myer, Cenozoic tectonics of the western United States: Reviews of Geophysics, 4, 509-549, 1966.

Hill, D.P., Gravity and crustal structure in the western Snake River Plain, Idaho, J. Geophys. Res., 68, 5807-5818, 1963.

Hill, D.P. and L.C. Pakiser, Crustal structure between the Nevada Test Site and Boise, Idaho, from seismic-refraction measurements, in The Earth Beneath the Continents, Amer. Geophys. Union Mon. 10, 391-419, 1966.

Keller, G.R., R.B. Smith and L.W. Braile, Crustal structure along the eastern margin of the Great Basin from detailed refraction measurements, J. Geophys. Res., 80, 1093-1099, 1975.

Kind, R., The reflectivity method for a buried source, J. Geophysics, 44, 603-612, 1978.

Kirkham, V.R.D., Snake River downwarp, J. Geol., 39, 456-482, 1931.

LaFehr, T.R. and L.C. Pakiser, Gravity, volcanism and crustal deformation of the eastern Snake River Plain, U.S. Geol. Surv. Prof. Pap., 450-D, 76-78, 1962.

Mabey, D.R., Interpretation of a gravity profile across the western Snake River Plain, Geology, 4, 53-56, 1976.

Mabey, D.R., Regional gravity and magnetic anomalies in the eastern Snake River Plain, Idaho, J. Res. U.S. Geol. Surv., 6, 553-562, 1978.

Morgan, W.J., Plate motions and deep mantle convection, in Shagam, R., ed., Studies in Earth and Space Sciences: Geol. Soc. America Mem., 132, 7-22, 1972.

Smith, R.B. and M. Sbar, Contemporary tectonics and seismicity of the western United States with emphasis on the intermountain seismic belt, Geol. Soc. America Bull, 85, 1205-1218, 1974.

Smith, R.B., Intraplate tectonics of the western North American plate, Tectonophysics, 37, 323-336, 1977.

Smith, R.B., Seismicity, crustal structure and intraplate tectonics of the interior of the western Cordillera, Geol. Soc. Amer. Mem., 152, 111-144, 1978.

Smith, R.B., L.W. Braile, M.M. Schilly, J. Ansorge, C. Prodehl, J.H. Healy, J.R. Pelton, St. Mueller and M.R. Baker, The Yellowstone-Snake River Plain seismic profiling experiment: Yellowstone, Submitted to J. Geophys. Res., 1981.

Sparlin, M.A., L.W. Braile and R.B. Smith, Crustal structure of the eastern Snake River Plain determined from ray-trace modeling of seismic refraction data, Submitted to J. Geophys. Res., 1981.

Taubeneck, W.H., Idaho Batholith and its southern extension, Geol. Soc. Amer. Bull., 82, 1899-1928, 1971.

Thompson, R.N., Columbia/Snake River-Yellowstone magmatism in the context of western U.S.A. Cenozoic geodynamics, Tectonophysics, 39, 621-636, 1977.

Willden, R., Seismic-refraction measurements of crustal structure between American Falls Reservoir, Idaho and Flaming Gorge Reservoir, Utah, U.S. Geol. Surv. Prof. Pap., 525-C, 44-50, 1965.

TABLES

Table 1. Shotpoint information for the ESRP phase of the 1978 Y-SRP experiment.

FIGURE CAPTIONS

Figure 1. Index map of the eastern Snake River Plain of southeastern Idaho showing shotpoint locations (large solid circles) and seismograph station locations (small solid triangles). Province boundaries (dashed lines) are from Fenneman and Johnson (1946).

Figure 2. Reduced-time record section of vertical component seismograms for shotpoint 2 recorded to the southwest. Seismograms have been amplitude normalized and amplitudes were multiplied by distance to the 1.5 power for convenient plot scaling. The seismograms have been corrected to a 1200 m elevation datum assuming a surface-layer velocity of 4.5 km/s. A 1-8 hz bandpass filter has been applied. Theoretical travel-times for the dipping-layer velocity model of Figure 8 are also shown. The phase nomenclature is as follows. Layers are numbered 1 through 6 from the top down (Figure 8) and the refracted arrival (head wave) from the top of layer i is called P_i. The reflected wave from the interface at the top of layer i is called P_iP. P_1 is the direct wave; $P_6 = P_n$, the refraction from the Moho; and $P_6P = P_mP$, the reflection from the Moho.

Figure 3. Reduced-time record section of vertical component seismograms for shotpoint 5 recorded northeast. Seismograms are scaled in the same manner as described in Figure 2. Travel-times are shown for the model of Figure 8. The phase nomenclature is described in Figure 2.

Figure 4. Enhanced-amplitude plot of seismograms for shotpoint 2 southwest illustrating the emergent arrivals for phase P_4. Travel-time curves correspond to the model in Figure 8.

Figure 5. Enhanced-amplitude plot of seismograms for shotpoint 5 northeast illustrating the emergent arrivals for phase P_4. Travel-time curves correspond to the model in Figure 8.

Figure 6. Record section for shotpoint 2 southwest seismograms with a reducing velocity of 8 km/s chosen to emphasize the P_n and P_mP arrivals. Seismograms are scaled as described in Figure 2. Travel-time curves correspond to the model in Figure 8.

Figure 7. Record section for shotpoint 5 northeast seismograms with a reducing velocity of 8 km/s chosen to emphasize the P_n and P_mP arrivals. Seismograms are scaled as described in Figure 2. Travel-time curves correspond to the model in Figure 8.

Figure 8. Dipping-layer velocity model fit to the shotpoint 2 southwest (Figure 2) and shotpoint 5 northeast (Figure 3) record sections. Compressional wave velocities are given by the numbers within each layer. For comparison, the Conda-SP7 model (Sparlin et al., this volume) at the intersection with the SP2-SP5 profile is shown by the heavy bars (interface depths) and the velocities for this model are given by the numbers below the location of the intersection with the Conda-SP7 profile.

Figure 9. Observed (upper) and synthetic (lower) seismograms for shotpoint 8 northeast. The observed data were amplitude-normalized and scaled in the same manner as described in Figure 2. The synthetic data were calculated by the modified reflectivity method and the amplitudes have been scaled by multiplying by distance to the 1.5 power (identical to the observed data) for convenient plotting. Travel-time curves on both record sections correspond to the plane, homogeneous layered model shown in Figure 10. The phase nomenclature is described in Figure 2.

Figure 10. Plane, homogeneous layered velocity model for the travel-time curves and synthetic seismograms shown in Figure 9. Q-values are compressional wave quality factors for each layer utilized in the calculation of the synthetic seismograms.

Figure 11. Synthetic seismograms calculated by the modified reflectivity method for the plane, homogeneous layered model (Figure 12) corresponding to shotpoint 2 southwest. These seismograms should be compared with the observed data shown in Figure 2. The amplitudes have been scaled by multiplying by distance to the 1.5 power for convenient plotting. Travel-time curves for the model shown in Figure 12 are also shown. Notation is identical to that used in Figure 2. False arrivals (due to the limits in the integration over the phase velocity in the reflectivity method) are indicated by the pairs of arrows.

Figure 12. Plane, homogeneous layered velocity model for the travel-time curves and synthetic seismograms shown in Figure 11. Q-values are compressional wave quality factors for each layer utilized in the calculation of the synthetic seismograms.

Figure 13. Observed and calculated amplitude-distance curves for three arrivals on the shotpoint 2 southwest record sections. The amplitudes of observed arrivals for the P_4, P_5P and P_mP phases are shown by the solid symbols. The shaded regions represent the scatter of points corresponding to all but a small number of observations for each phase. The method of measurement of the amplitudes for both the observed (Figure 2) and synthetic (Figure 11) data is illustrated on the inset. The solid lines correspond to the amplitudes measured from the synthetic data. In measuring the amplitudes of the three arrivals on the observed and synthetic record sections, the convention used was to measure the amplitude of the first one to one and one half cycles of the waveform in the first approximately one-half second immediately following the arrival time given by the travel-time curve for the phase.

SHOTPOINT INFORMATION
EASTERN SNAKE RIVER PLAIN
1978 Y-SRP SEISMIC EXPERIMENT

SP	DATE	ORIGIN TIME	LATITUDE	LONGITUDE	ELEVATION (meters)	DEPTH (meters)	EXPLOSIVES (kilograms)	TYPE
8	12 Sept. 78	11 00 05.494	43 23.82N	113 03.76W	1591	21	1810	Borehole, dry
4	13 Sept. 78	11 00 05.709	43 37.53N	112 33.93W	1579	49	1825	Borehole, dry
5	14 Sept. 78	11 00 05.195	42 53.90N	113 48.57W	1286	40	3635	Borehole, wet
2A	17 Sept. 78	11 00 05.684	44 17.11N	111 20.20W	1890	32	3185	Borehole, wet
2B	21 Sept. 78	11 00 05.411	44 17.11N	111 20.20W	1890	32	1320	Borehole, wet
7	25 Sept. 78	11 00 05.340	43 45.16N	113 29.14W	1783	29	1020	Borehole, dry
CONDA	27 Sept. 78	01 12 52.811	42 45.24N	111 30.81W	2195	5	36300	Quarry Blast
GAY	03 Oct. 78	21 11 26.842	43 03.31N	112 06.22W	1796	5	22700	Quarry Blast

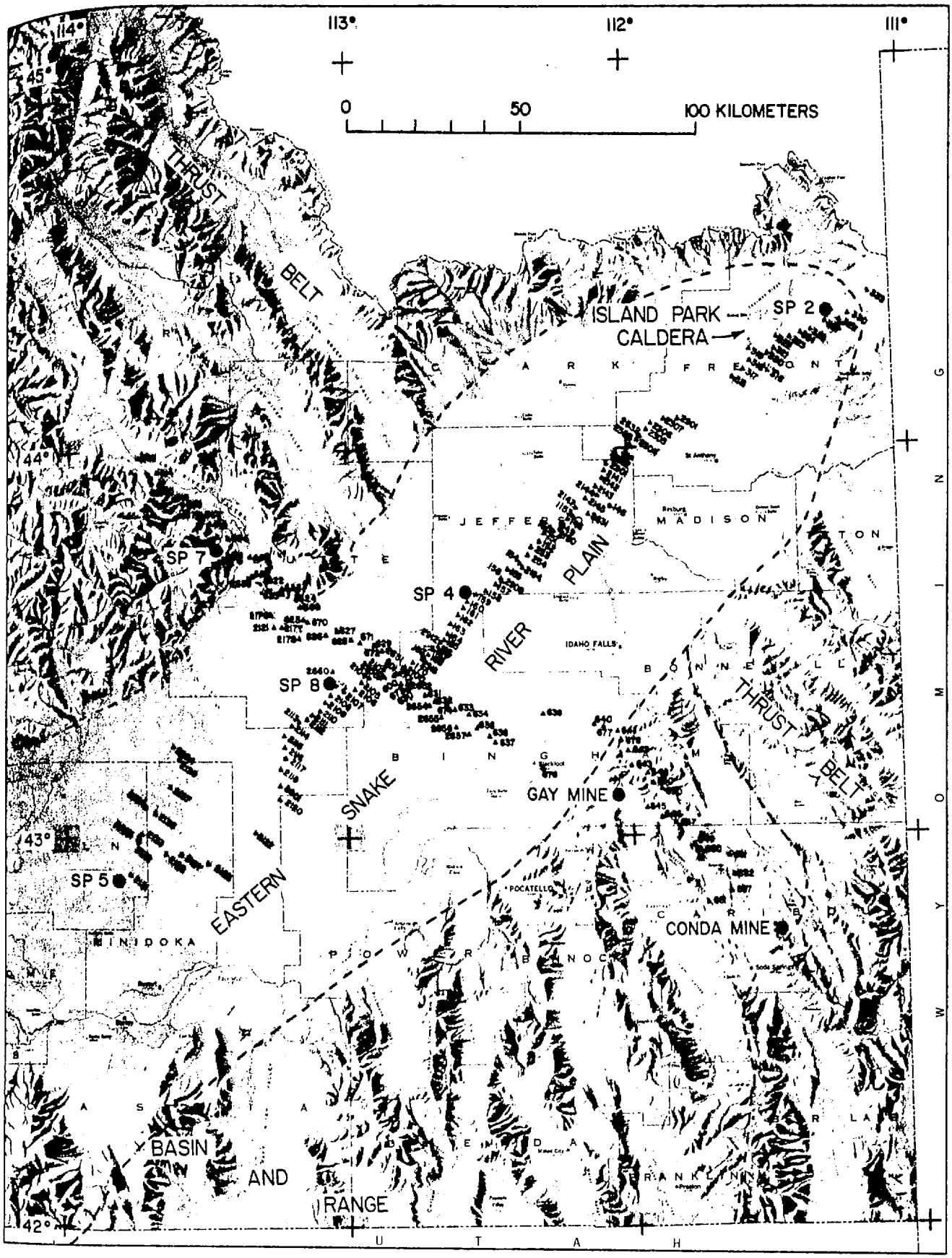
113°
112°
111°
114°
45°
44°
43°
42°
0
50
100 KILOMETERS
THRUST BELT
ISLAND PARK CALDERA
SP 2
SP 4
SP 5
SP 7
SP 8
SNAKE RIVER PLAIN
IDAHO FALLS
GAY MINE
CONDA MINE
POCATELLO
EASTERN
THRUST BELT
BASIN AND RANGE
JEFFERSON
MADISON
BINGHAM
BONNEVILLE
BINGHAM
POWER
CARIBOU
FREMONT
BANNOCK
ONEIDA
UTAH
WYOMING

Figure 1

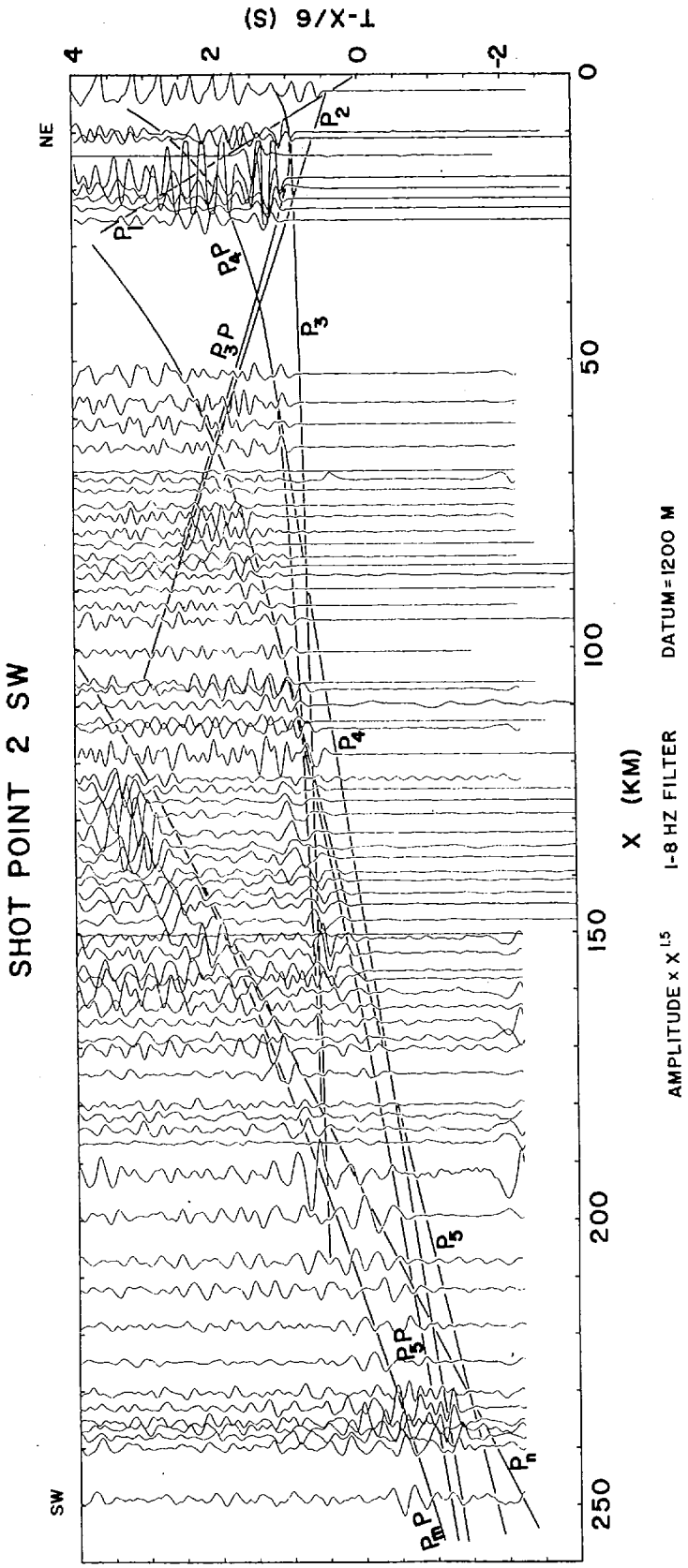
SHOT POINT 2 SW
T-X/6 (S)
4
2
0
-2
NE
SW
0
50
100
150
200
250
X (KM)
AMPLITUDE x X^1.5
1-8 HZ FILTER
DATUM=1200 M
P1
P2
P3
P4
P5
Pn
PmP
P3P
P4P
P5P

Figure 2

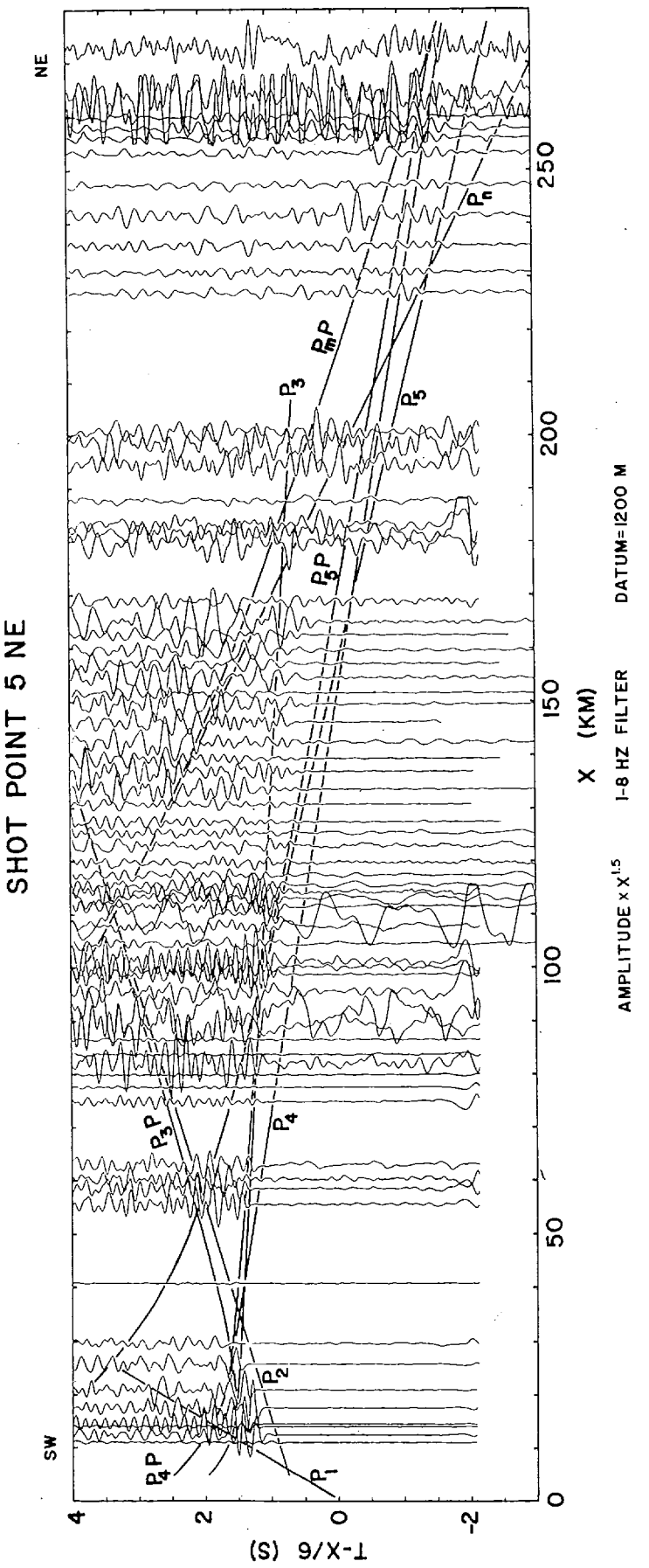
SHOT POINT 5 NE
NE
SW
P_1
P_2
P_3
P_4
P_5
P_m
P_4P
P_3P
P_5P
P_mP
T-X/6 (S)
4
2
0
-2
X (KM)
0
50
100
150
200
250
AMPLITUDE x X^1.5
1-8 HZ FILTER
DATUM=1200 M

Figure 3

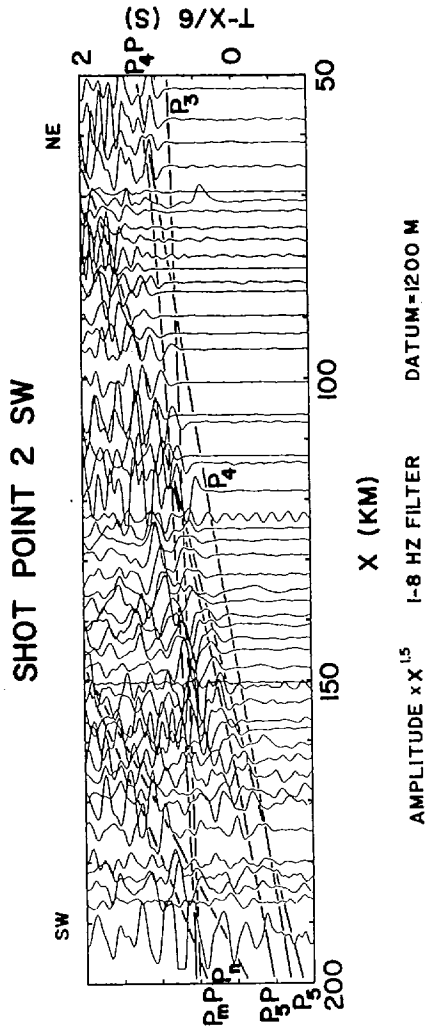
SHOT POINT 2 SW
NE
SW
T-X/6 (S)
2
0
50
100
150
200
X (KM)
AMPLITUDE x X^1.5
1-8 HZ FILTER
DATUM=1200 M
PP P4
P3
P4
Pm Pn
P3P P5

Figure 4

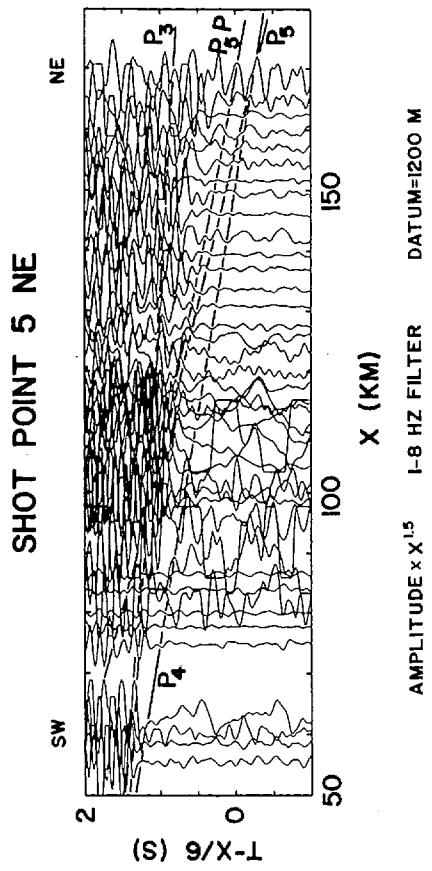
SHOT POINT 5 NE
NE
SW
P_3
P_4
P_5
P_6P
50
100
150
X (KM)
2
0
T-X/6 (S)
AMPLITUDE x $X^{1.5}$
1-8 HZ FILTER
DATUM=1200 M

Figure 5

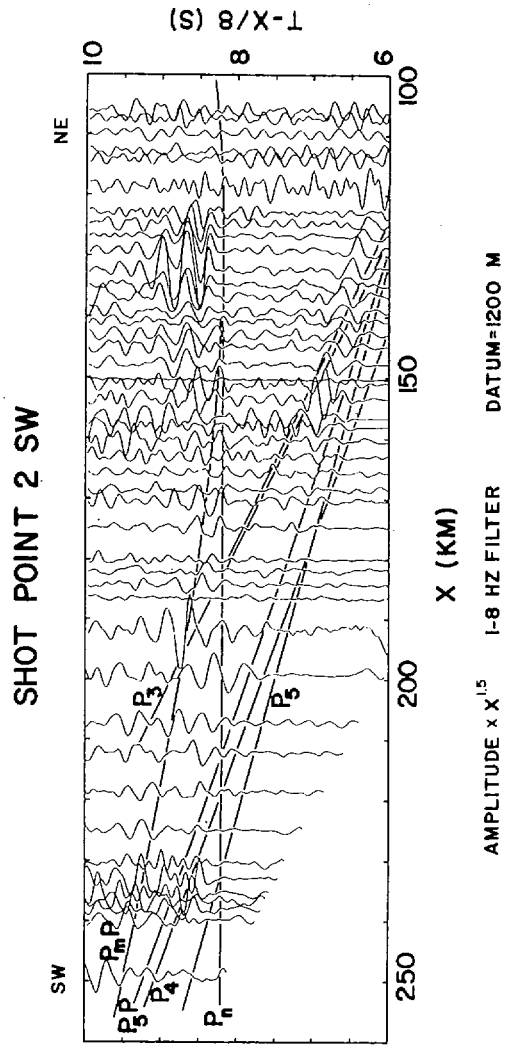
SHOT POINT 2 SW
NE
SW
T-X/8 (S)
10
8
6
100
150
200
250
X (KM)
AMPLITUDE x X^1.5
1-8 HZ FILTER
DATUM=1200 M
P3
P5
Pm
P2
P1
P4
Pn

Figure 6

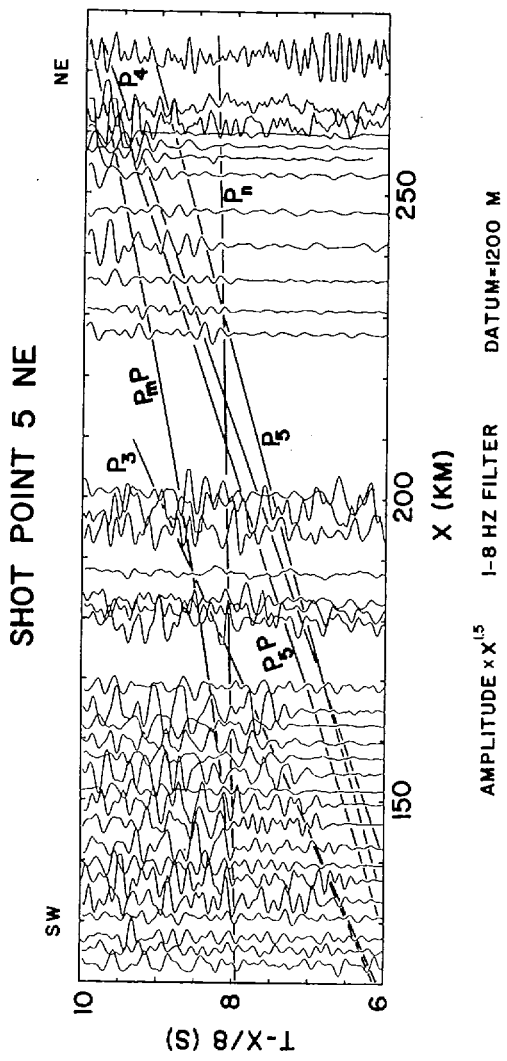
SHOT POINT 5 NE
NE
SW
P_4
P_n
P_mP
P_3
P_5
P_3P
250
200
150
X (KM)
AMPLITUDE x X^1.5
1-8 HZ FILTER
DATUM=1200 M
10
8
6
T-X/8 (S)

Figure 7

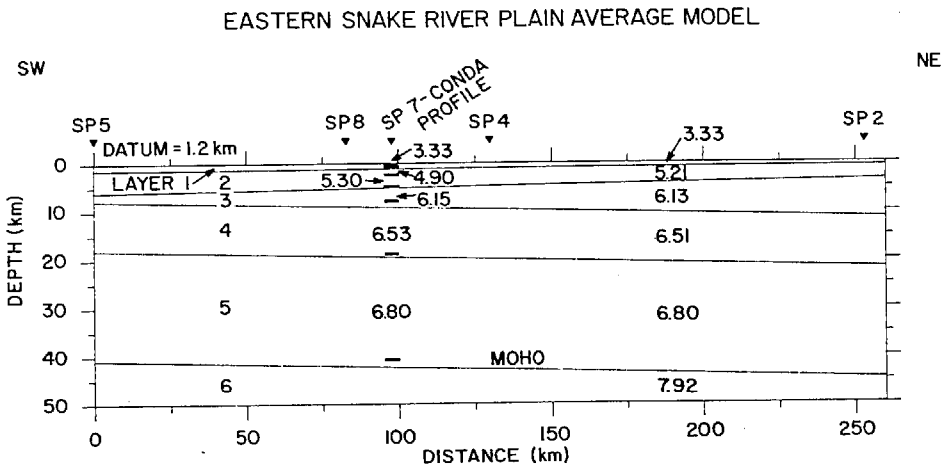
EASTERN SNAKE RIVER PLAIN AVERAGE MODEL
SW
NE
SP5
SP8
SP 7-CONDA PROFILE
SP4
SP2
DATUM = 1.2 km
3.33
3.33
LAYER 1
2
5.30
4.90
5.21
3
6.15
6.13
4
6.53
6.51
5
6.80
6.80
MOHO
6
7.92
DEPTH (km)
0
10
20
30
40
50
0
50
100
150
200
250
DISTANCE (km)

Figure 8

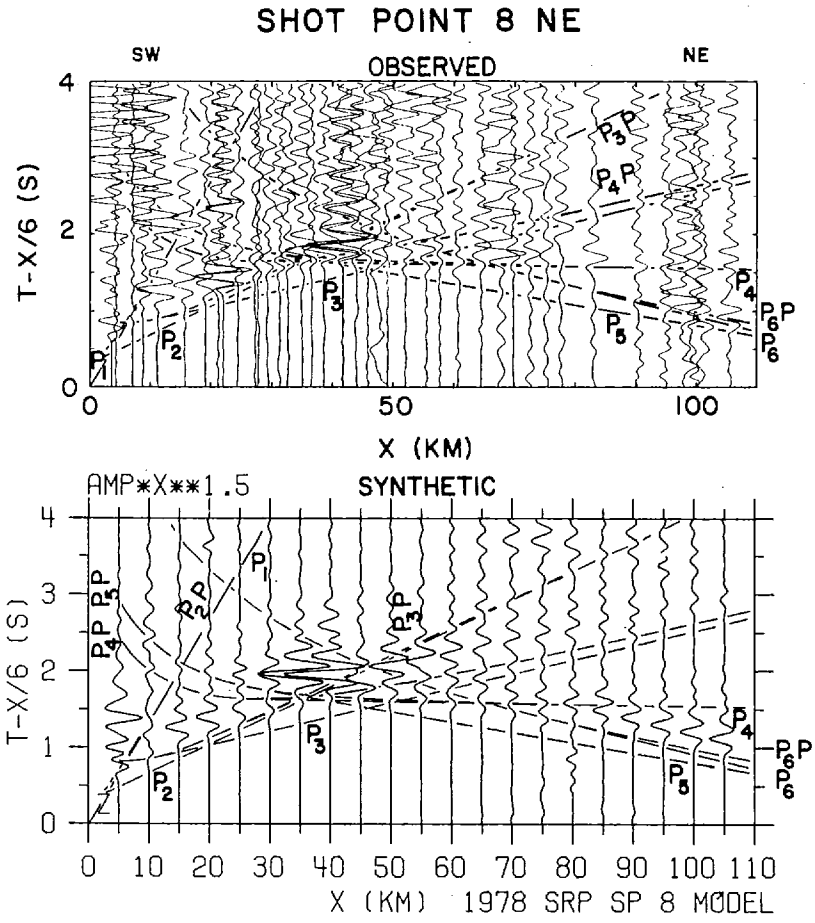
SHOT POINT 8 NE
SW
OBSERVED
NE
T-X/6 (S)
X (KM)
AMP*X**1.5
SYNTHETIC
X (KM) 1978 SRP SP 8 MODEL

Figure 9

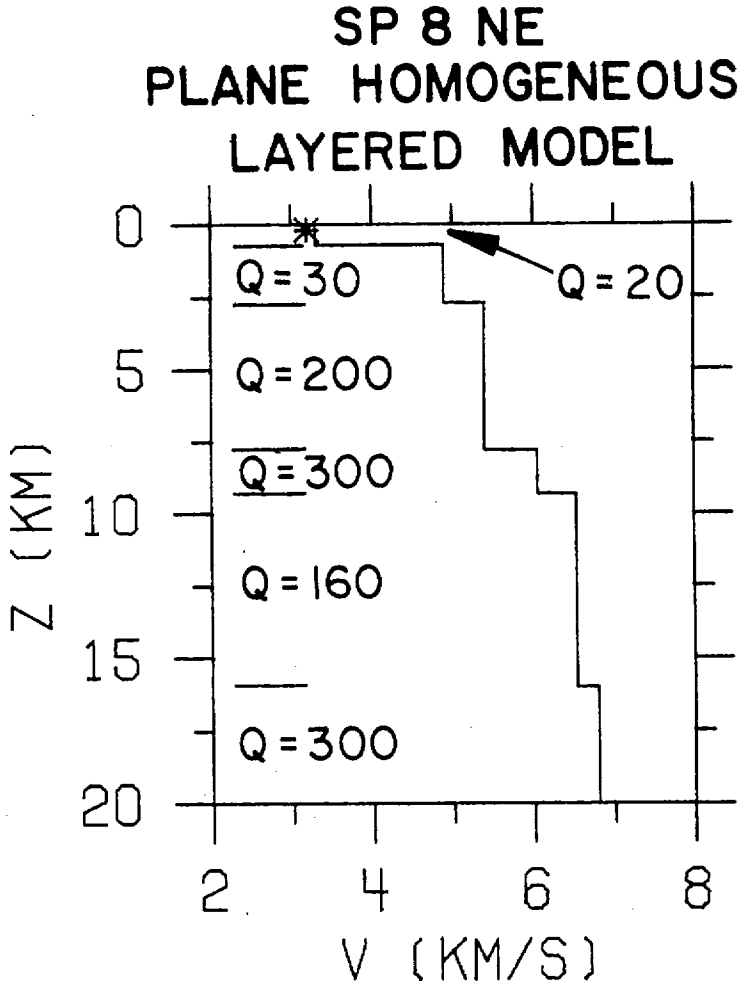
SP 8 NE
PLANE HOMOGENEOUS
LAYERED MODEL
Q=30
Q=20
Q=200
Q=300
Q=160
Q=300
0
5
10
15
20
Z (KM)
2
4
6
8
V (KM/S)

Figure 10

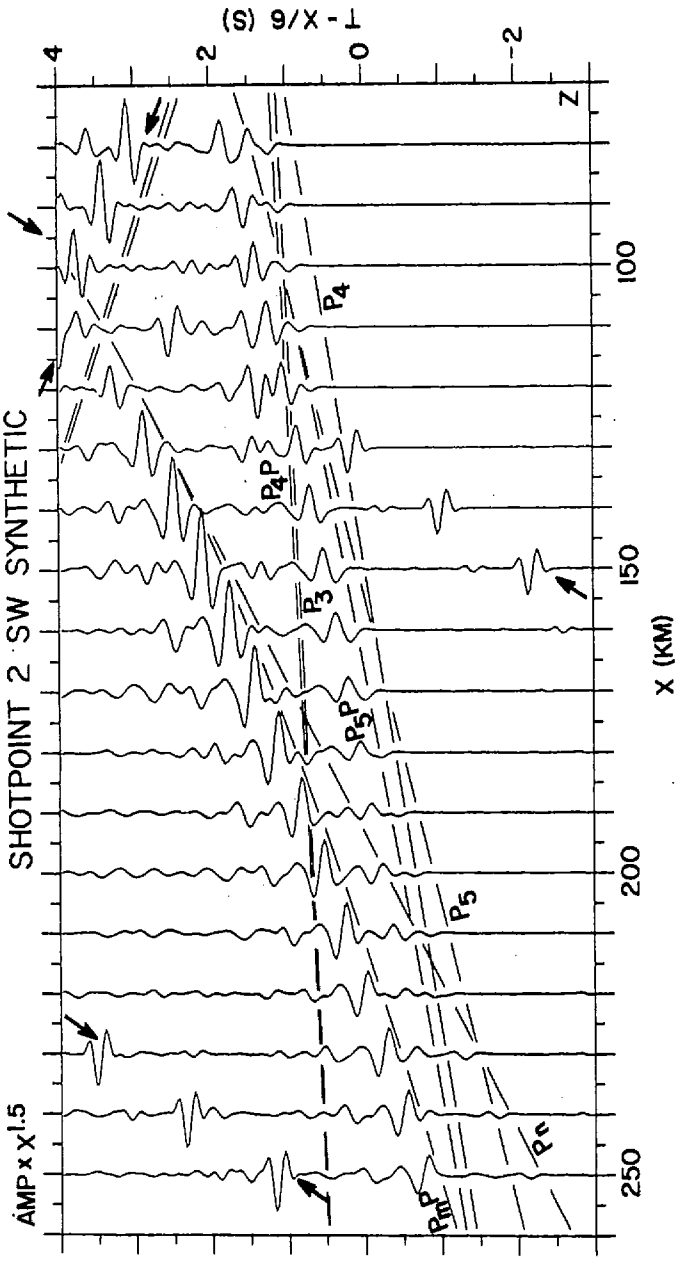
SHOTPOINT 2 SW SYNTHETIC
AMP x X1.5
T - X/6 (S)
4
2
0
-2
Z
100
150
200
250
X (KM)
P4
P4P
P3
P5P
P5
Pn
PmP

Figure 11

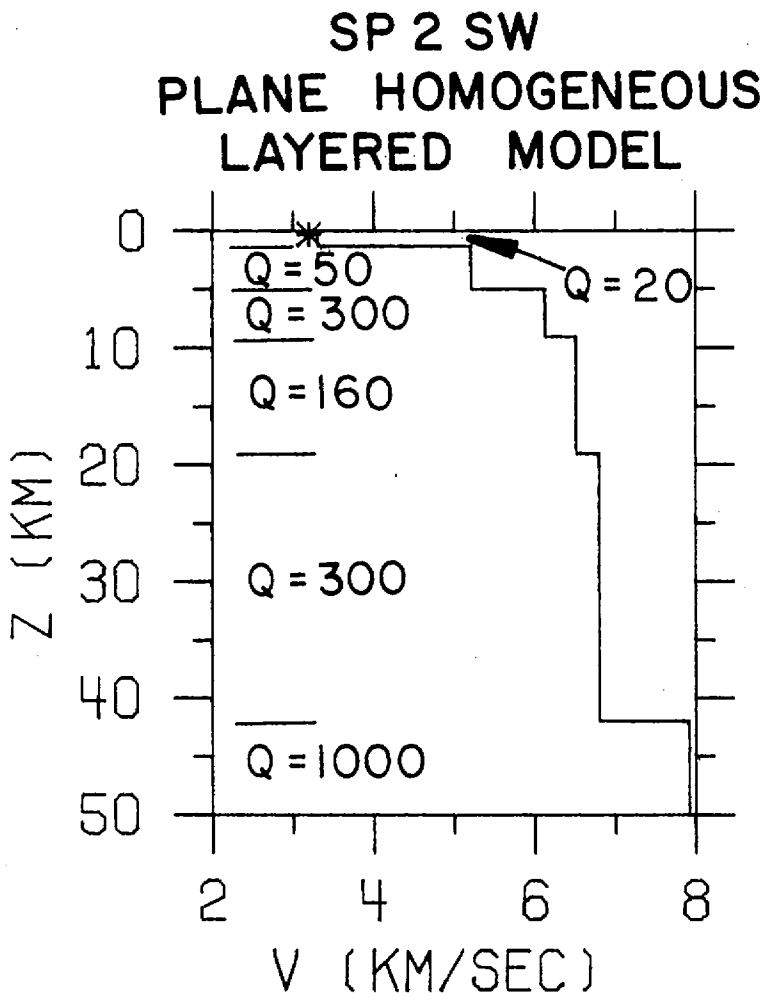
SP 2 SW
PLANE HOMOGENEOUS
LAYERED MODEL
Q = 50
Q = 300
Q = 160
Q = 300
Q = 1000
Q = 20
0
10
20
30
40
50
Z (KM)
2
4
6
8
V (KM/SEC)

Figure 12

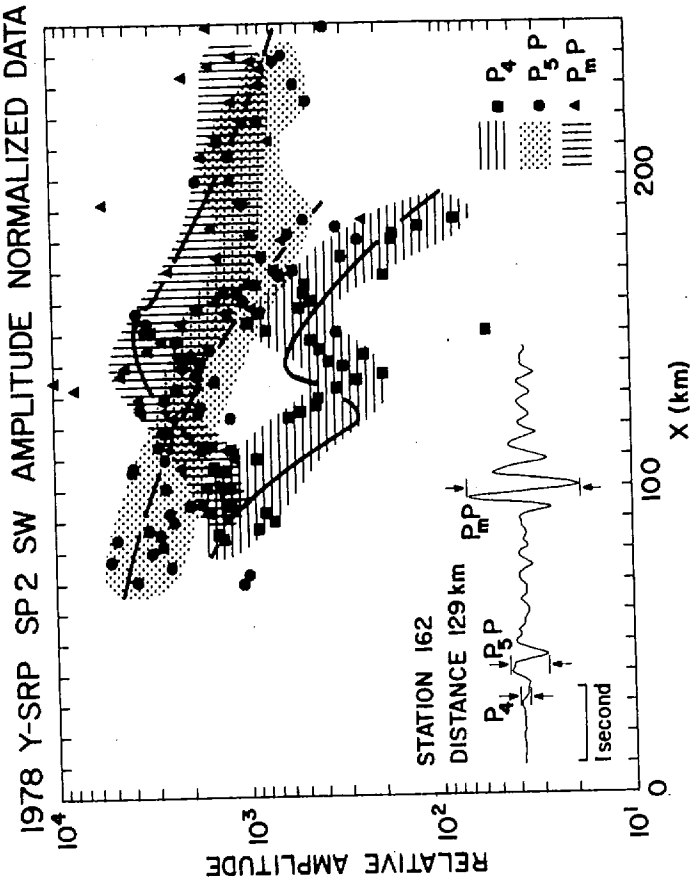
1978 Y-SRP SP 2 SW AMPLITUDE NORMALIZED DATA
RELATIVE AMPLITUDE
10^4
10^3
10^2
10^1
0
100
200
X (km)
P_4
P_5P
P_mP
STATION 162
DISTANCE 129 km
P_4
P_5P
P_mP
1 second

Figure 13

AMPLITUDE NORMALIZATION OF SEISMOGRAMS FROM MULTIPLE SEISMOGRAPH RECORDING SYSTEMS FOR THE YELLOWSTONE-SNAKE RIVER PLAIN SEISMIC REFRACTION EXPERIMENT

M.R. Baker (Department of Geosciences, Purdue University, West Lafayette, Indiana 47907)[1]

L.W. Braile (Department of Geosciences, Purdue University, West Lafayette, Indiana 47907)

R.B. Smith (Department of Geology and Geophysics, University of Utah, Salt Lake City, Utah 84112)

February 1, 1981

1) Now at: Exxon Production Research Company, Box 2189, Houston, TX 77001

ABSTRACT

A z-transform filter theory method for the normalization of the instrument responses of several seismographs is presented. In this method, an inverse filter is derived by consideration of the seismometer/recorder characteristics which may be applied to a given seismogram to convert the system frequency response to that of a reference system. Inverse filters are derived for the seismogaphs used on the 1978 Yellowstone-Snake River Plain seismic profiling experiment. It is shown by application to these data that the inverse filters are effective in amplitude normalization and that their use allows improvement in the amplitude and phase character of seismic record sections.

INTRODUCTION

In the design of a seismic refraction survey such as the 1978 Yellowstone-Snake River Plain experiment, it is desirable to have the largest number of recording instruments possible deployed for each shot. When the dominant objective is to maximize the number of seismographs, a vast assortment of instrument types results with differing resonant frequencies and damping constants for the seismometers and filter parameters for the signal conditioning portion of the seismograph. These variations in response between and within instrument types generally lead to a lack of amplitude control and a variation of arrival character which may make correlation of phases between seismograms difficult.

By numerically modeling the seismometer-seismograph systems, filters may be developed which, when applied to one instrument response, result in an approximation to the second instrument response. This normalization of amplitude versus frequency, and phase delay versus frequency responses, results in useable amplitude information and consistency of phase arrivals between records. Consistency of phase character leads to easier recognition of arrivals while the knowledge of amplitude information gives additional information and control in the geologic modeling and interpretation process.

The purpose of this paper is to present an application of a z-transform filter-theory approach to the amplitude

normalization of seismograph responses. The method is illustrated by application to amplitude normalization of the seismograms recorded in the 1978 Yellowstone-Snake River Plain (Y-SRP) seismic experiment (Braile et al., this volume; Smith et al., this volume). The importance of amplitude normalization to the data processing and interpretation of a large-scale seismic survey is emphasized by the variety of instrument response characteristics for the Y-SRP experiment. The instrument responses for the seismographs used in this experiment are shown in Figure 1 (from Schilly, 1979). The responses of the seismometers are not included in the curves shown. When the various resonant frequencies and damping factors of the seismometers are included, fourteen different instrument types were represented in the experiment. The wide variety of response curves shown in Figure 1 indicates the severity of the problem of amplitude normalization.

In this paper, amplitude normalization filters are illustrated by application to the Y-SRP seismic data. Amplitude normalization of the seismograms from the Y-SRP seismic profiling experiment yielded a uniform seismograph response with a peak frequency of about 6 hz. The normalized seismic record sections display lateral coherency of amplitude and phase character even between various instrument types.

DERIVATION OF FILTERS FOR SEISMOMETER/RECORDER RESPONSE NORMALIZATION

Several approaches have been examined in an attempt to find a workable solution to the problem of synthesis of an inverse filter to match instrument responses. The first attempt at synthesizing a filter used the Wiener minimum mean-square error criterion for arriving at the coefficients of the filter. Recordings of the same source at the same location for two seismographs were made and a least-squares inverse filter (Robinson, 1967) was derived which would convert one seismogram into the other by convolution with the filter. The method can be applied using recordings of the same source at the same site by multiple instrument types or by comparison of the calibration pulses for each individual seismograph. This procedure resulted in a reasonably good filter as long as the periods of the seismic signal were shorter than the filter length. Attempts at using long enough filters to accomodate the low frequency signals resulted in excessive edge-effect and eventual dominance of noise from roundoff error of the filter coefficients. A second approach was tried in which direct division of the z-transforms of the desired waveform by the input wavefrom was least-squares fit with a ratio of two polynomials to give a recursive form of the direct deconvolution filter. The instability of the division of mixed-phase waveforms, the numerical noise in the input

data, and the polynomial fitting process all combined to result in a total failure of this method. The final unsuccessful approach was to model individual calibration pulses with a ratio of sixth to tenth order polynomials with generation of the inverse filter by division of these polynomials. The polynomials modeling the calibration signal fit reasonably well but once again the numerical noise and the inability to factor and cancel common terms out of the ratio of polynomials led to unstable and otherwise useless filters. The successful approach used a theoretical modeling of the seismograph system by a ratio of z-polynomials. Once the z-polynomials are defined for each seismograph system, division of the polynomials for two of the instrument types yields an inverse filter which can be used to convert one instrument type to another.

The filters used to normalize one instrument response to a reference instrument type are generated by modeling the ideal frequency response of both the seismometers and seismographs separately with a ratio of z-polynomials, and then taking the ratio of these polynomials (equivalent to frequency domain division) to obtain the inverse filter. For instance, if there are two different seismometer types with the same recording instrument type with identical filter settings, it is only necessary to model the seismometer responses for the inverse filter.

As will be shown later, an arbitrary seismometer response can be modeled by the ratio of two second-order z-polynomials $A(z)/B(z)$, while the desired seismometer response is

given by C(z)/D(z), and the resultant impulse response of the inverse filter is given by the polynomial of equation (1).

$$F(z) = \frac{C(z)\ B(z)}{D(z)\ A(z)} \qquad (1)$$

This filter could be applied to the arbitrary input waveform using either the convolution method or the recursion method, but the convolution filters, even for simple second-order polynomials may have a prohibitive number of significant terms with its consequent edge-effect and roundoff errors: hence a recursive application is simpler, involves less error and computation time and is better able to handle the low-frequency phase corrections not possible with a truncated convolution operator. The inverse filter for the correction for the seismograph filter stages is handled in the same manner. The derivation of the filter coefficients for the seismometer, filter and total system response will be outlined in the following sections along with a brief description of the application of a recursive type of filter.

Seismometer Response Model

The model of a seismometer response may be achieved by considering to the differential equation describing the balance of forces in a damped resonant system. The standard electromagnetic seismometer can be modeled as a spring-mass system where both the voltage output, the damping and the mass factor are related by Faraday's Induction Law to the velocity of motion. With the arm at rest and a step function of current applied to a separate calibration coil corresponding

to a step function of acceleration on the seismometer arm, the differential equation of the system is of the form of equation (2) with its associated Laplace Transform, equation (3), where m is the mass, k the spring

$$\frac{d^2x}{dt^2} + 2\gamma\frac{dx}{dt} + \omega_o^2 x = u(t) \tag{2}$$

$$s^2L\{x\} + 2\gamma sL\{x\} + \omega_o^2 L\{x\} = \frac{1}{s} \tag{3}$$

constant, b the damping, γ the decay constant and ω_o^2 the square of the resonant frequency. Since we wish to find the seismometer output for an impulse, the solution for L{x} must be differentiated to obtain the system frequency response as illustrated in equations (4) and (5).

$$L\{x\} = \frac{1}{s(s^2 + 2\gamma s + \omega_o^2)} \tag{4}$$

$$L\{\frac{dx}{dt}\} = sL\{x\} = \frac{1}{s^2 + 2\gamma s + \omega_o^2} \tag{5}$$

The solution of equation (5) shown in equation (6) is of minor interest as the recursion filter will be generated from the frequency domain response: the only use of the time domain response is to estimate the parameters ω_o and γ which will be necessary for generating the inverse filter.

$$V_s(t) \propto \frac{dx}{dt} = \frac{\exp(-t)}{\sqrt{(\omega_o^2 - \gamma^2)}} \operatorname{Sin}\left(\sqrt{(\omega_o^2 - \gamma^2)}\, t\right) \tag{6}$$

Substitution of the equation for the bilinear z-transform into

equation (5) gives equation (7), where T is the sample interval. Collection of terms and simplification gives the polynomial approximation in equation (8),

$$V_s(z) = \frac{1}{n^2\left(\frac{1-z}{1+z}\right)^2 + 2\gamma n\left(\frac{1-z}{1+z}\right) + \omega_o^2} \qquad n = \frac{2}{T} \tag{7}$$

$$V_s(z) = \frac{1 + 2z + z^2}{1 - \left(\frac{2(n^2 - \omega_o^2)}{n^2 + 2\gamma n + \omega_o^2}\right)z + \left(\frac{n^2 - 2\gamma n + \omega_o^2}{n^2 + 2\gamma n + \omega_o^2}\right)z^2} \tag{8}$$

The first simplifying assumption which has been made in arriving at equation (8) is that a constant gain has been ignored; in order to know this gain, the mass, spring constant, calibration current, number of turns and geometry of both the calibration coil and the output voltage coil must be known. This overall gain occurs as a constant which may be factored from the numerator of equation (8) and will be determined later for the overall inverse filter by comparing recordings of blasts recorded at the same site with a collection of instruments. The second assumption which has been made is that the frequency warping characteristics (Claerbout, 1978) of the bilinear z-transform have been neglected since application to a solution of the form of equation (5) is difficult and the frequencies being considered are generally about one-tenth of the Nyquist frequency and thus are virtually unaffected by the warping.

The case of a single recording instrument type with two different seismometers is illustrated by an example from

the Y-SRP experiment. The standard seismograph (seismograms recorded on any other seismograph transformed by application of the inverse filter to the signal which 'would have been recorded' on the standard seismograph) is a Sprengnether MEQ 800 with 0-5 hz filter settings and an S-7000 seismometer set for one-hertz resonant frequency (Figure 1). The unnormalized seismograph consists of an MEQ 800 seismograph with a highly underdamped Geotech seismometer. The z-polynomials for the seismometers were obtained by modeling the calibration pulses (Figure 2a). Initial guesses for the parameters ω_o and γ for each of the seismometers were obtained by making measurements on these pulses and a number of test cases were run with trial and error alteration of the parameters until a reasonable fit of the SMU 5 curve to the T1 curve was obtained. The z-polynomial models for the Geotech and S-7000 seismometers are given in equations (9) and (10) respectively along with its controlling parameters.

$$\text{Geotech} \quad V_{sg}(z) = \frac{1 + 2z + z^2}{1. - 1.7821z + 0.8668z^2} \qquad \begin{matrix} \omega o = 15.2 \\ \gamma = 3.6 \end{matrix} \tag{9}$$

$$\text{S-7000} \quad V_{ss}(z) = \frac{1 + 2z + z^2}{1. - 1.7394z + 0.7488z^2} \qquad \begin{matrix} \omega_o = 5.2 \\ \gamma = 7.2 \end{matrix} \tag{10}$$

Thus the transfer function to convert from the Geotech to the S-7000 is given by equation (11), where the filter F(z) directly represents the recursion filter or may be used to generate the convolution filter impulse response by polynomial division.

$$F(z) = \frac{V_{ss}}{V_{sg}} = \frac{1. - 1.7821z + 0.8668z^2}{1. - 1.7394z + 0.7488z^2} \tag{11}$$

The procedure of applying the recursion filter follows quite easily when the properties of the z-transform corresponding to those of the Laplace and Fourier Transforms are applied: multiplication by z corresponds to the delay operator exp (-sT) and the multiplication of two z-transforms corresponds to time-domain convolution. For a given input time series X(z) and output time series Y(z), equation (12)

$$Y(z) = F(z)\ X(z) \tag{12}$$

describes the linear system operator F(z). Substitution of equation (11) into (12), and multiplying out the denominator gives equation (13), while collection of terms yields equation (14).

$$Y(z)\ (1. - 1.7391z + 0.7488z^2) = (1. - 1.7821z + 0.8668z^2)X(z) \tag{13}$$

$$Y = X - 1.7821zX + 0.8668z^2X + 1.7391zY - 0.7488z^2Y \tag{14}$$

This equation represents the application of recursion described by equation (11) where a value of output Y is determined from the input time series X and previously calculated output values zY and z^2Y.

The results of application of the filter of equation (11) to the calibration pulse from the Geotech seismometer is shown at the bottom of Figure 2a. It may be readily seen that some high frequency noise in the input pulse has become more apparent after inverse filtering. This arises from the nature of the

filter operation which utilizes an inherently unstable numerical differentiation and also results from the way in which the data set was obtained. The Geotech calibration pulse was digitized at maxima, minima and inflection points from a smoked-paper record, corrected for seismograph arm curvature and interpolated to a specified sample interval using a cubic polynomial fit to segments of the data. Correlation of the location of digitized points with the instabilities points to the problems arising from digitizer accuracy with smoked records and the fact that the polynomial used to fit the digitized points may not be of a form realizeable with a simple analog circuit. Despite these difficulties, the improvement of the response of the filtered calibration pulse is quite good.

Filter Response Model

The second step in normalizing instrument responses involves matching the filter characteristics of the various types of seismographs. As may be seen in Figure 1 (Schilly, 1979), a compilation of filter cutoffs of some of the instrument types used in the 1978 Yellowstone-Snake River Plain experiment indicates a wide variety of instrument types to be normalized to a common frequency and phase response. The MEQ 800 reference instrument has a two-stage Butterworth high-cut filter with a corner frequency at 5 Hz, falling off at 12 db/octave, and a single-stage low-cut filter with a corner frequency at 0.25 Hz. The frequency domain representations for n-stage high and low-cut Butterworth filter are given in equations (15) and (16) respectively,

$$F_h = \left(\frac{a}{s + a}\right)^n \tag{15}$$

$$F_l = \left(\frac{s}{s + a}\right)^n \tag{16}$$

where s is the complex frequency and a is the corner frequency expressed in radians/second.

Referring again to Figure 1, it is apparent that in every case, it is not necessary to match filter responses exactly because the cutoff frequencies fall well outside of any frequencies useable on a plotted record section. For instance, the low-cut filter section of the MEQ 800 does not introduce significant phase or amplitude changes until frequencies are less than 0.5 Hz, and high-cut filter section of the USGS instrument does not affect frequencies lower than 30 Hz, hence these filter sections will be ignored in the instrument normalization.

One serious difficulty has been found in attempting to match the low-frequency response of the recording instruments. An instability in the seismograph filter transfer function arises because of the phase response of the low-cut filter in the desired instrument response (in this case a 0.25 Hz low-cut filter in the MEQ 800 reference instrument). Hence, if complete instrument normalization is desired, a low-cut filter should be applied to the records not having 0.25 hertz low-cut filters.

An additional example of application of the method is illustrated in Figure 2B in which the inverse filter for the European MARS seismograph system was derived. For the inverse

instrument filter for the MARS system, the problem reduces to converting a two-stage 17-Hz Butterworth filter to a two-stage 5-Hz Butterworth filter. Once again, the bilinear z-transform is applied to equation (15) for a two-stage filter and equation (17) results, again ignoring the constant gain factor.

$$F(z) = \frac{1 + 2z + z^2}{1 - \left(\frac{2(n^2 - a^2)}{n^2 + 2an + a^2}\right) z + \left(\frac{n^2 - 2an + a^2}{n^2 + 2an + a^2}\right) z^2} \qquad (17)$$

In order to determine the coefficients for the cutoff frequencies when these frequencies are a significant fraction of the Nyquist, it is necessary to pre-warp the filter poles because of utilization of the bilinear z-transform (Golden and Kaiser, 1964). For the MARS system with a sample interval of 0.01 seconds and a cutoff of 17 Hz, the pre-warped frequency becomes 18.8 Hz and the 5 Hz cutoff becomes 5.04 Hz. Substituting these frequencies into equation (17) and taking the ratio of the desired to the input response results in the recursion filter, equation (18).

$$F(z) = \frac{F_{800}(z)}{F_{MARS}(z)} = \frac{1. - 0.5147z + 0.0662z^2}{1. - 1.4570z + 0.5407z^2} \qquad (18)$$

The final filter for the seismometer-filter system may be obtained by multiplying the two filters together, which is equivalent to the convolution of the numerators divided by the convolution of the denominators, resulting in a ratio of fourth order polynomials. For the MARS system, these two polynomials are as given in equation (19).

$$F(z) = \frac{1. - 2.617z + 2.407z^2 - 0.900z^3 + 0.117z^4}{1. - 3.336z + 4.152z^2 - 2.284z^3 + 0.468z^4} \qquad (19)$$

When this filter is applied to the MARS system calibration pulse, the 'normalized' calibration pulse shown at the bottom of Figure 2B results. This pulse shows a rather good match to the MEQ 800, S-7000 calibration pulse. Once again, noise is introduced in the digitization process which shows as the 'hump' in the decay portion of the curve.

Application of the filters derived by the methods described above is a simple matter of recursive (or convolution) filtering of the seismograms recorded by a given instrument type. The filtered seismograms are then approximations to the records which would have been recorded by the reference seismograph. One additional factor is required - the relative gain of the two seismograph systems. This can best be determined by the simultaneous recording of a signal on the non-standard and the reference seismographs at the same location (often called a 'huddle test'). After application of the normalization filter, it is a simple matter to compare the relative gains to obtain this scale factor. An example of the application is illustrated for the data in Figure 3 in which an actual recording with the reference instrument at the same site is available as a check on the normalization filter procedure. The top two seismograms of Figure 3 were recorded near the Bingham Copper Mine in Utah for the same shot along with eight other instruments to use for comparison purposes. When the filter of equation (19) was applied to the seismogram from the ETH (MARS) instrument and gain scaled to match the MEQ 800 record, the overall gain of the filter is

determined by this scaling factor. An additional example of the effectiveness of the amplitude normalization procedure is shown in Figure 4 in which a filtered (normalized) seismogram recorded on a LASL seismograph (Figure 1) is compared to the seismogram recorded on the reference instrument for the same source (shotpoint 8) at the same location. Note that although the filter responses of the two recording instruments are quite different, the normalization procedure has produced an excellent correlation between the seismograms.

Filters were derived for each of the seismometer/recorder systems utilized in the Y-SRP experiment using the methods described above. The filters work quite well in matching the frequency responses of the system and operate in a stable manner as long as the bandwidth of the reference system is not increased substantially. Application of the filters results in a reasonably good correction of phase differences although improvement of the ease of picking the onset of arrivals is marginal. The most significant improvement lies in the consistent amplitude spectrum response and the 'stability' of the amplitude-distance data. One factor which was not considered in this development, and could not be treated by any of the other approaches attempted to date, is the degree of coupling between the ground and seismometer. Theoretically this coupling should also be measurable from the impluse response, assuming the seismometer behavior with near perfect coupling for a calibration signal is well known.

The method of synthesis of seismometer filter coefficients is not generalized, much being left to judgement and prejudice. A generalized approach could use either inversion of the individual calibration pulse for system parameters or use a non-linear inversion technique to go directly from input to desired waveform, optimizing the seismometer parameters, which are generally not well know.

Additional details, a listing of a computer program to apply the recursive filter and the filter coefficients for the various seismographs utilized in the Y-SRP seismic experiment are given by Baker (1979).

AMPLITUDE NORMALIZATION OF THE Y-SRP RECORD SECTIONS

The amplitude normalization procedure was applied to each seismogram for the record sections recorded during the Y-SRP project. A more detailed amplitude interpretation is presented by Braile et al., (this volume) and thus only a few comments on the adequacy of the normalization, the improvement in the lateral coherency of phases on the record sections, and the sources of scatter on an amplitude-distance plot for one of the observed record sections will be presented here.

A trace-normalized record section of vertical component seismograms for shotpoint 2 recorded southwest (Braile et al., this volume) is shown in Figure 5. After amplitude normalization the same record section is shown in Figure 6. The seismograms are coded according to their recording instrument type in order to identify any systematic amplitude effects which might be associated with a given instrument type. The amplitude-corrected data are also scaled according to the source-receiver distance in order to provide for convenient visualization of the seismograms at all distances. This scaling is performed by multiplying the amplitudes of the seismograms by distance to the 1.5 power in order to amplify distant records sufficiently to see the arrivals. Seismograms in both record sections are bandpass filtered from 1-8 hertz. In addition, theoretical travel-time lines for inferred arrivals are

indicated on Figure 6 (Braile et al., this volume). The seismograph response of the seismograms shown in Figure 6 (both the reference instrument records and the normalized records) is shown in Figure 7. Comparison of the record sections (Figures 5 and 6), identifies several interesting characteristics of the amplitude-corrected data. Phase correlation of the P_5P arrival in the distance range of 90 to 180 km is improved by the normalization. Correct amplitude scaling for the P_mP phase near the critical distance (110 to 150 km) more accurately reflects the character of this phase on the amplitude corrected record section. Finally, the variation with distance in the amplitudes of arrivals is generally smooth and shows no indication of abrupt changes at distances corresponding to changes in recording instrument types. This latter observation is confirmed by plotting the amplitudes of three arrivals as a function of distance (Figure 8). Amplitudes for the individual arrivals show some scatter but generally display consistent trends. A few erratic points are also evident. Examination of the amplitude distance variations and the locations of the various instrument types indicates that as much variance in the amplitudes is present within groups of the same instrument type as that observed between instrument types. We conclude that the trends in the amplitude-distance curves for the various arrivals are representative of wave-propagation effects through the crust and upper mantle of the eastern Snake River Plain. The remaining scatter in the amplitude observations shown in Figure 8 is probably due

to local site response characteristics of the seismograph recording stations, inaccuracy of the amplitude normalization procedure and imprecise knowledge of the instrument parameters.

CONCLUSIONS

A simple and efficient method is described for normalizing the amplitude responses of various seismometer-recording instrument types to a reference instrument. The method requires trial-and-error modeling of the z-polynomial description of relative responses of both the seismometers and the recording instrument filters of the input and reference instrument responses. The normalization is then performed by recursive filtering. Application of the normalization procedure to seismic record sections recorded during the 1978 Yellowstone-Snake River Plain experiment improves the lateral coherency of the seismic arrivals and the ability to interpret the seismograms and allows modeling of the amplitude-distance variations of the observed data to infer velocity structure and anelasticity.

ACKNOWLEDGEMENTS

We would like to acknowledge the significant efforts of all of the participants (indicated in the acknowledgements of the papers by Smith et al., this volume and Braile et al., this volume) in the 1978 Yellowstone-Snake River Plain seismic experiment. Jack Healy, Will Koller, Mike Schilly, Tom Owens, W.J. Hinze, J.L. Sexton, Nicholas Deichmann and Mark Sparlin provided assistance in processing of the data and helpful discussions concerning this research. This work was supported by National Science Foundation Grant No. EAR77-23357 and United States Geological Survey Geothermal Research Program Grant No. 14-08-0001-G-532.

REFERENCES

Baker, M.R., Application of Time Series Analysis to the Enhancement of Seismic Refraction Data Interpretation, Unpublished M.S. Thesis, Purdue University, 1979.

Braile, L.W., R.B. Smith, J. Ansorge, M.R. Baker, M.A Sparlin, C. Prodehl, M.M. Schilly, J.H. Healy, St. Mueller and K.H. Olsen, The Yellowstone-Snake River Plain Seismic Profiling Experiment: Crustal Structure of the Eastern Snake River Plain, submitted to J. Geophys. Res., 1981.

Claerbout, J.F., Fundamentals of Geophysical Data Processing, 274 p., McGraw Hill Book Company, New York, 1976.

Golden, R.M. and J.F. Kaiser, Design of Wideband Sampled Data Filters, Bell System Tech. J., 43, 1533-1548, 1964.

Robinson, Enders A., Multichannel Time Series Analysis with Digital Computer Programs, 298 p., Holden Day, San Francisco, 1976.

Schilly, M.M., Interpretation of Crustal Seismic Refraction and Reflection Profiles from Yellowstone-and the Eastern Snake River Plain, Unpublished M.S. Thesis, U. of Utah, 1979.

Smith, R.B., L.W. Braile, M.M. Schilly, J. Ansorge, C. Prodehl, J.H. Healy, J.R. Pelton, St. Mueller and M.R. Baker, The Yellowstone-Snake River Plain seismic Profiling Experiment: Yellowstone, submitted to J. Geophys. Res., 1981.

FIGURE CAPTIONS

Figure 1. Frequency response curves for five of the seismograph amplifier-filter systems used in the Yellowstone-Snake River Plain seismic experiment. The effects of various seismometer types has not been included.

Figure 2. Calibration pulses (from a step function in current) corresponding to various seismometer/recorder systems. (A) Upper plot is the calibration pulse for an MEQ-800 seismograph with an underdamped seismometer. Middle plot shows the calibration pulse for the reference system (MEQ-800, 1-hz seismometer and 0-5 hz filter settings). Lower plot shows the calibration pulse for the underdamped system (upper plot) after application of the amplitude normalization filter. (B) Upper plot is the calibration pulse for a MARS seismograph system. Middle plot is the calibration pulse for the reference instrument. Lower plot shows the calibration pulse for the MARS system (upper plot) after application of the amplitude normalization filter.

Figure 3. Comparison of seismograms for two different recording systems (upper and middle plots) recorded at the same location for the same source. Lower figure is the ETH (MARS) seismogram (upper plot) after application of the amplitude normalization filter.

Figure 4. Comparison of an MEQ-800 (reference instrument) and a LASL seismogram recorded at the same location for shotpoint 8. Seismograms are plotted at true relative amplitudes. The LASL seismogram has been filtered with the appropriate amplitude normalization filter.

Figure 5. Vertical component seismograms recorded on various instrument types for shotpoint 2 to the southwest. Amplitude normalization filters have not been applied. All seismograms are trace-normalized - that is plotted with the same maximum amplitude within the time window of the record section. A 1 to 8 hz bandpass filter has been applied. Note the apparent loss of energy on the seismograms from 120-140 km in the reduced time range of approximately 0 to 2 seconds caused by the trace-normalization of the large amplitude PmP phase on the seismograms.

Figure 6. Seismic record section for shotpoint 2 to the southwest after application of the trace normalization filters. In addition, the amplitudes of each seismogram have been multiplied by the source-receiver distance to the 1.5 power to provide for convenient plot scaling. The seismograms are coded by the symbols as to the seismograph system used to record them. Theoretical travel-times for a simple dipping layer velocity model (Braile et al., this volume) are also shown.

Figure 7. Frequency response curve for the reference seismograph (and, ideally, all seismographs after the application of the amplitude normalization filters) for the Y-SRP experiment including the seismograms shown in Figure 6. Response curve for the 0-5 hz instrument filter settings (solid line) and an additional 1-8 hz digital bandpass filter (dashed line) are shown.

Figure 8. Amplitude versus distance data for three phases for the seismograms shown in Figure 6. Inset illustrates the manner in which the amplitudes of the phases were measured.

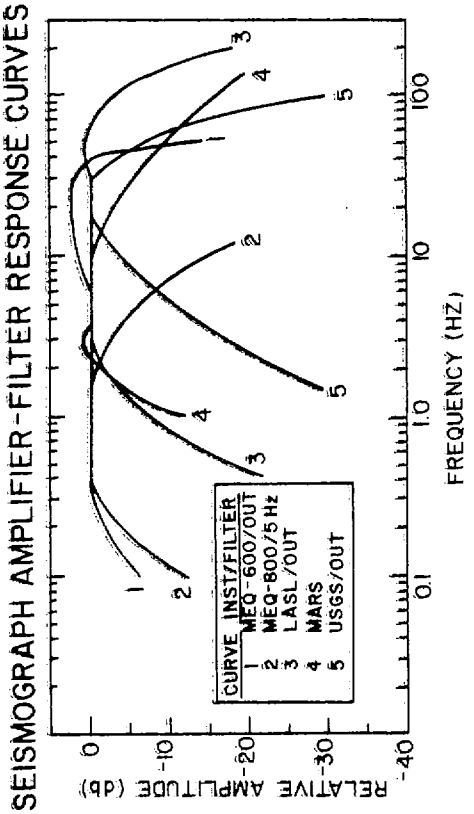
1978 Y-SRP SEISMIC EXPERIMENT
SEISMOGRAPH AMPLIFIER-FILTER RESPONSE CURVES
RELATIVE AMPLITUDE (db)
0
-10
-20
-30
-40
0.1
1.0
10
100
FREQUENCY (HZ)
CURVE INST/FILTER
1 MEQ-600/OUT
2 MEQ-800/5 Hz
3 LASL/OUT
4 MARS
5 USGS/OUT

Figure 1

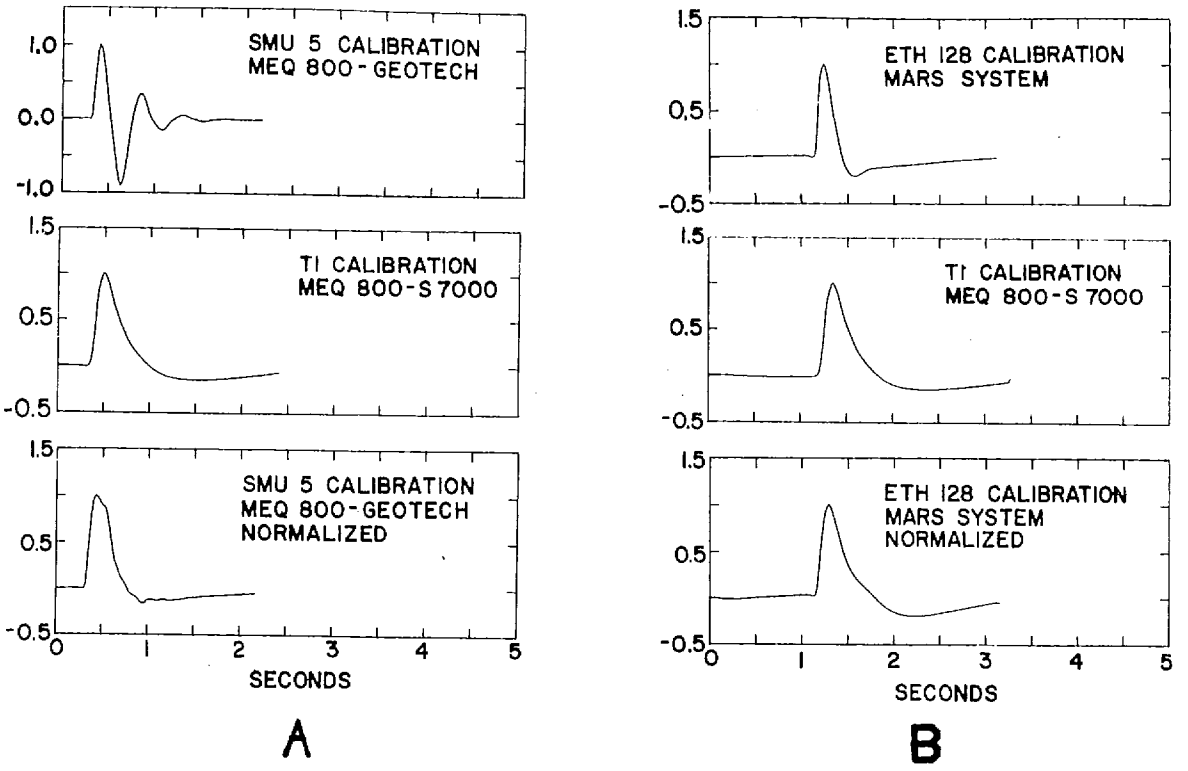

Figure 2

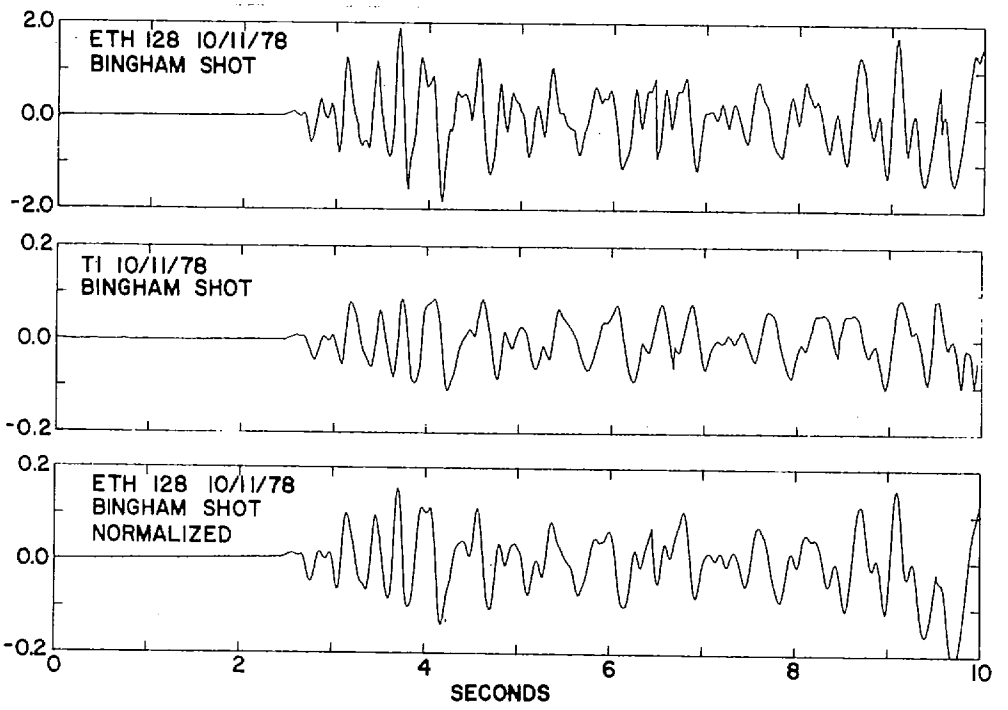

Figure 3

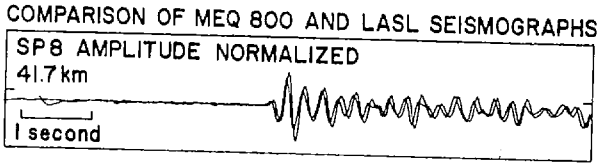
COMPARISON OF MEQ 800 AND LASL SEISMOGRAPHS
SP 8 AMPLITUDE NORMALIZED
41.7 km
1 second

Figure 4

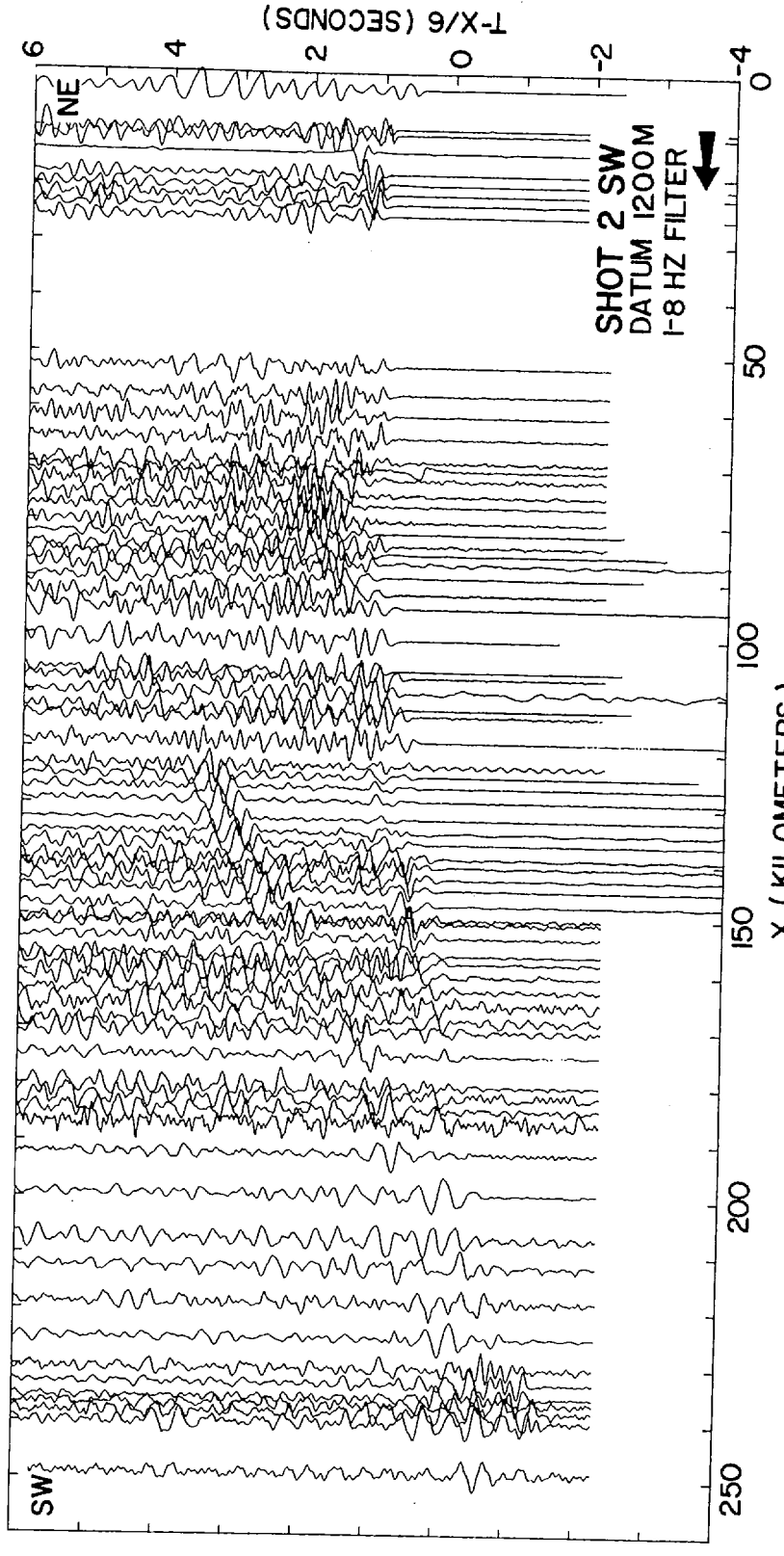
T-X/6 (SECONDS)
6
4
2
0
-2
-4
NE
SW
SHOT 2 SW
DATUM 1200M
1-8 HZ FILTER
0
50
100
150
200
250
X (KILOMETERS)

Figure 5

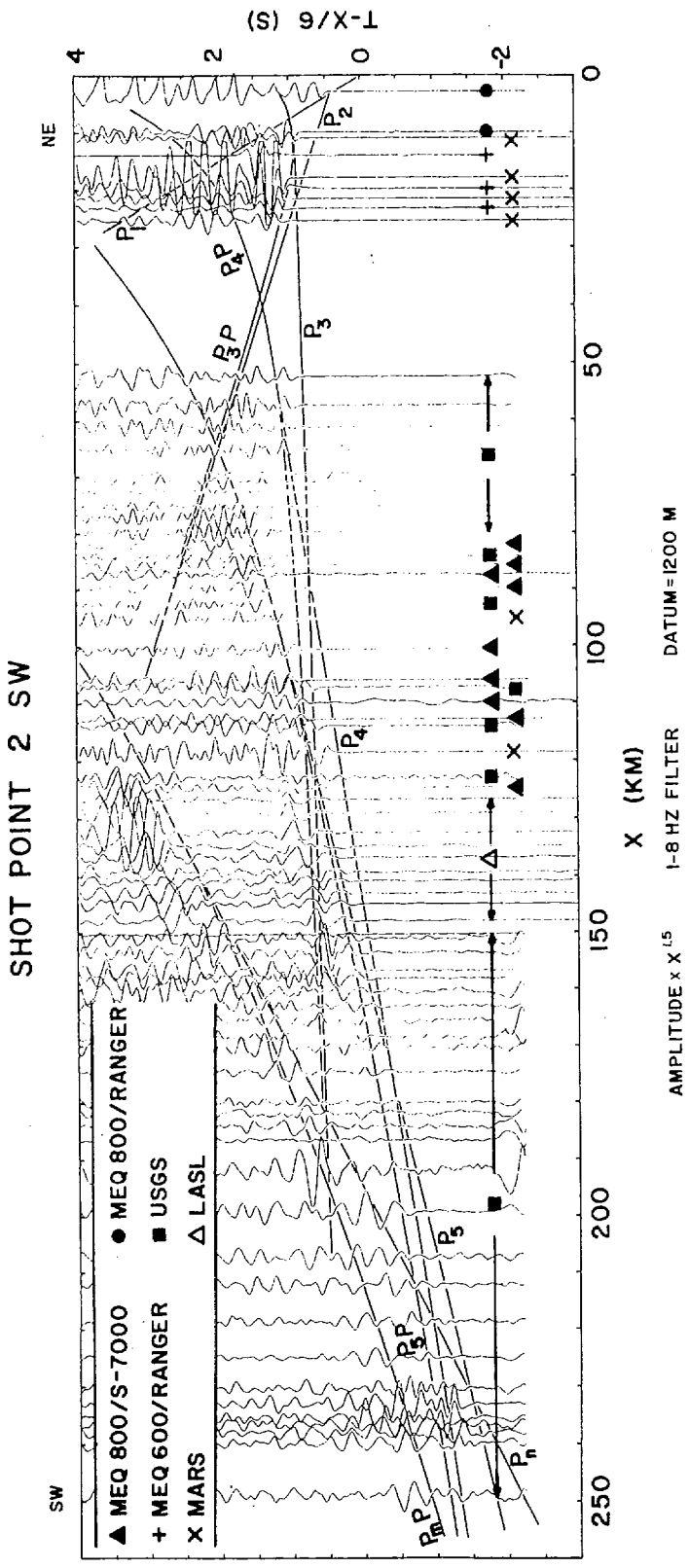
SHOT POINT 2 SW
T-X/6 (S)
4
2
0
-2
NE
SW
0
50
100
150
200
250
X (KM)
AMPLITUDE x X^1.5
1-8 HZ FILTER
DATUM=1200 M
▲ MEQ 800/S-7000
+ MEQ 600/RANGER
X MARS
● MEQ 800/RANGER
■ USGS
Δ LASL
P1
P2
P3
P4
P5
Pn
P2P
P3P
P4P
P5P
PmP

Figure 6

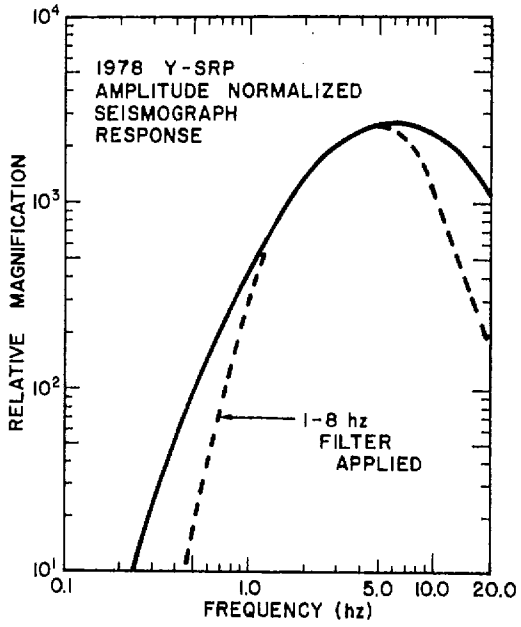
1978 Y-SRP
AMPLITUDE NORMALIZED
SEISMOGRAPH
RESPONSE
RELATIVE MAGNIFICATION
10^4
10^3
10^2
10^1
1-8 hz
FILTER
APPLIED
0.1
1.0
5.0
10.0
20.0
FREQUENCY (hz)

Figure 7

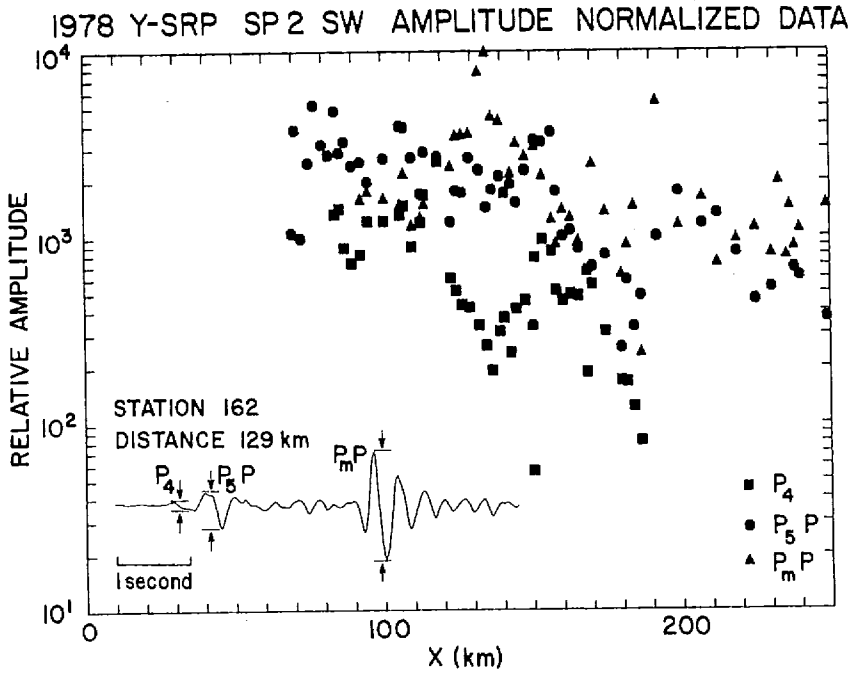
1978 Y-SRP SP 2 SW AMPLITUDE NORMALIZED DATA
RELATIVE AMPLITUDE
10^4
10^3
10^2
10^1
0
100
200
X (km)
STATION 162
DISTANCE 129 km
P_4
P_5P
P_mP
1 second
P_4
P_5P
P_mP

Figure 8

CRUSTAL STRUCTURE OF THE EASTERN SNAKE RIVER PLAIN DETERMINED FROM RAY-TRACE MODELING OF SEISMIC REFRACTION DATA

M.A. Sparlin[1]
L.W. Braile

Department of Geosciences
Purdue University
West Lafayette, Indiana 47907

R.B. Smith

Department of Geology and Geophysics
University of Utah
Salt Lake City, Utah 84112

February 1, 1981

1) Now at: Arco Oil & Gas Company, PO Box 2819, ARB 2615, Dallas, TX 75221

ABSTRACT

Ray-trace travel-time modeling of the seismic refraction record sections for a profile across the eastern Snake River Plain (ESRP) was used to derive a crustal model of the eastern Snake River Plain. The derived crustal model is consistent with the velocity structure interpreted from a profile along the axis of the ESRP. The interpretation also indicates that significant lateral inhomogeneities in the upper crust exist beneath the ESRP when compared with the upper crust beneath the adjoining Northern Rocky Mountain and Basin and Range provinces.

The most prominent features of the crustal structure inferred by the ray-trace modeling are as follows:

(1) The northwest margin of the eastern SRP was modeled as a fault structure downthrown on the SRP side (SE) with an offset of greater than 4 km. The southeast margin conversely, appears to be downwarped with possible minor faulting. The Paleozoic sedimentary rocks, thus were indicated to exist beneath the SRP volcanics possibly to and beyond 40 km from this margin of the SRP.

(2) The modeling indicates no abrupt variation in the depth to the top of the lower crustal layer in the proximity of either of the eastern SRP margins. Rather, this interface was indicated to occur at approximately 19 ± 1 km beneath the SRP and the adjacent regions.

(3) An "intermediate" 6.53 km/sec layer occurring beneath the eastern SRP indicated on the axial profile was found to be localized within the SRP margins and appears to be a pervasive intrusion of higher velocity material from the upper mantle into the highly fractured upper crustal layer in this region.

(4) A density model of the crust across the eastern SRP was prepared with the appropriate densities being selected using the interpreted seismic velocities as a constraint. The gravity field calculated from this model resulted in a good match to the observed gravity field over the eastern SRP.

INTRODUCTION

During the 1978 Yellowstone-Snake River Plain (Y-SRP) seismic profiling experiment, a partially reversed seismic refraction profile was recorded along a northwest-southeast line across the axis of the eastern Snake River Plain (ESRP). Four shotpoints located along this profile resulted in refracted and reflected arrival phases which have been interpreted in order to infer the crustal structure beneath the ESRP and the transition in crustal models between the ESRP and adjacent provinces. The objective of this paper is to describe ray-trace travel-time modeling applied to the seismic data recorded along this northwest-southeast line. In addition, the anomalous gravity field of the derived crustal model is compared with observed gravity data across the ESRP in order to confirm and further constrain the crustal model. The details of the 1978 Y-SRP seismic profiling experiment and shotpoint and seismograph information are presented by Smith *et al.* (this volume) and Braile *et al.* (this volume).

DATA ACQUISITION AND PRESENTATION

Seismograph stations and shot locations for the eastern SRP phase of the Y-SRP seismic experiment are shown in Figure 1. Four shotpoints were recorded along the axis of the plain; SP5, SP8, SP4 and SP2, and four shotpoints along a profile approximately perpendicular to the SRP axis; SP7, SP8, Gay Mine and Conda Mine. Shotpoint 8 was recorded both transverse (NW-SE) and parallel (NE-SW) to the axis of the ESRP. Shotpoint locations, origin times, sizes and other relevant information for these sources are given in Braile et al. (this volume). The 196 km seismic refraction line oriented roughly perpendicular to the axis of the ESRP and intersecting both the northwest and southeast boundaries of the SRP near Arco and Pocatello, Idaho, respectively, has been interpreted using ray-trace modeling. This refraction profile will be termed the Conda-SP7 line or the 'crossline'. The interpretation procedure and the derived crustal model along this profile are the principal topics of this paper. In addition, a 47 km long reversed profile from shotpoint 8 to shotpoint 4 (Figure 1) is interpreted. This profile is particularly relevant to the Conda-SP7 interpretation because the two profiles intersect near the axis of the ESRP.

As described in detail by Smith et al. (this volume) and Braile et al. (this volume), seismic data were recorded along

the Conda-SP7 profile utilizing portable seismographs with timing referenced to crystal clocks and radio signal WWV or the radio broadcast time standard WWVB. Seismograms recorded on FM tape or analog records (240 mm/min or 480 mm/min fast rotation smoked paper drum recordings) were subsequently digitized for plotting as reduced time record sections. Data reduction and editing procedures are described by Schilly (1979).

In order to standardize the response of the seismograms on the plotted record sections to facilitate correlation of phases and reading travel-times, all seismograms were normalized to a reference instrument, in this case a Sprengnether MEQ-800 seismograph with 0-5 Hz filter settings and an S-7000 seismometer set for a 1 Hz resonant frequence. Thus, the variations in response between the many recording systems utilized in the experiment were minimized and allowed for amplitude control and coherency of arrival character between seismograms. The amplitude normalization procedure is described by Baker et al. (this volume).

All of the seismograms presented here are vertical component records which have been plotted with a reducing velocity of 6 km/sec and corrected to a 1200 m elevation datum utilizing an average velocity for the surface material of 4.50 km/sec. Amplitude scaling of the seismograms was performed during plotting by multiplying the seismogram amplitude by the source-receiver distance raised to the 1.5 power. In addition, a recursive band-pass filter was applied to each seismogram to pass frequencies from 1 to 8 Hz (Baker, 1979).

SEISMIC MODELING

The procedure utilized in the interpretation of the Conda-SP7 refraction profile was to identify the travel-times of principal refracted and reflected phases by their lateral coherency of amplitude and phase character of the seismograms. Because of the seismogram normalization procedure, phase correlation was usually significant except for (generally) small travel time shifts due to local velocity anomalies, elevation or timing errors. A comment is appropriate here as to the identification of the arrival time of a phase on the observed record sections. We have consistently selected the onset of a phase, recognized by amplitude or frequency character, to be the earliest time consistent with the data. Considering the band-limited source and recording instruments this is the most appropriate travel-time convention. Also, calculated arrival times were compared with expanded-amplitude (large scale) seismic record sections during the ray-trace modeling. Examples of expanded-amplitude record sections are shown by Braile et al. (this volume). These large-scale record sections were important in recognizing the true arrival times of several of the emergent phases which were observed. The seismic record sections shown here are designed to display the character of the seismograms for all phases and thus the amplitudes are sometimes 'scaled down' such that onset times

may not be apparent. Modeling of the correlated phases was initially performed using one-dimensional velocity models (travel-times of reflected and refracted head-wave arrivals for a stack of plane, homogeneous layers). This provided an approximate starting model beneath each shotpoint location from which to begin more complex travel-time modeling. Subsequently, travel-time calculations were performed by ray-trace modeling (Cerveny et al., 1977) for each shotpoint and refraction profile. These models were then refined and integrated iteratively until a single crustal velocity model was determined which was consistent with all of the seismic record sections. Although this procedure is somewhat subjective and the models derived must be considered to be non-unique, the extensive modeling effort, as measured by the number of trial models utilized and the degree of structural pertubation of the various trial velocity models, produces confidence in the interpretation. In addition, many regions of the crustal model are traversed by ray-paths from more than one shotpoint or for two or more ray types and thus the derived model is subjected to a large number of travel-time comparisons which are met in the successful velocity model.

The advantage of the application of the ray-trace theory in this case is the ability to simulate the propagation of various seismic wave types through discontinuous bodies and layers. In geometric ray theory a true head wave cannot be generated. For our travel-time modeling, critical refractions were simulated by introducing a velocity gradient of

0.01 km/sec per one km increase in depth. These small velocity gradients were parallel to the interface along which the critical refractions were being calculated. Thus, with the extremely small curvature introduced into the ray as it traveled in the medium below the interface, quite accurate approximations to head-wave arrivals could be obtained. The refractions simulated in this manner did not differ by more than 0.005 sec in travel-time when compared with travel-times for plane-homogeneous layered models computed using standard Snell's law methods.

In the diagrams to follow, the crustal velocity models are idealized, utilizing simple linear or curvilinear boundaries and are thus approximations to a geological model. When more than one refracted phase appears on a plot, each phase was calculated separately with the velocity gradient introduced only in the layer in which the head-wave was generated. The layers above and below were seismically homogeneous. The reflected phases were calculated with all layers homogeneous, no velocity-depth gradients were introduced during calculation of any of these phases.

In addition to the interpretation of the Conda-SP7 profile, the seismic refraction profile recorded along the axis of the ESRP (shotpoints 5, 8, 4 and 2; Figure 1) was used to provide important constraints on the crustal model across the plain (Braile et al., this volume). The 252 km reversed profile from shotpoint 2 to shotpoint 5 provided detailed information less complicated by lateral velocity

structure variations. Because of the length of the SP2-SP5 profile and the shotpoint locations, this profile was particularly useful in determining the velocity-depth relations for the deeper layers beneath the ESRP.

Utilizing the interpretation of the SP2-SP5 profile (Braile et al., this volume) the following constraints were applied to the crustal model beneath the central area of the ESRP.

The upper crustal layer (velocity ≈ 6.15 km/sec) is interpreted to thicken towards shotpoint 2. This layer may be discontinuous in places. However, satisfactory results were obtained utilizing a continuous upper crustal layer. The interpretation of the axial profile (shotpoints 5, 8, 4 and 2; Braile et al., this volume) indicated an apparent velocity of the upper crustal layer of between 6.08 and 6.19 km/sec. A value of 6.15 km/sec was utilized in the idealized model of the crossline presented here. Below the upper crustal layer and extending down to approximately 19 ± 1 km is an intermediate layer with a velocity of approximately 6.53 km/sec. The velocity of this layer is well defined from the interpretation of the shotpoint 2 to 5 data. The lower crust extends from the base of the intermediate layer to a depth of approximately 42 ± 2 km with a velocity of 6.80 km/sec.

For the near surface volcanic structure, we relied heavily upon the interpretation of the INEL-1 well, 15 km from the north boundary of the plain, east of Arco (Doherty

et al., 1979). This well penetrated to a depth of 3.16 km and intersected three general lithologies. Basalt interbedded with lacustrine and fluvial deposits were encountered from the surface to a depth of approximately 700 m. Below the surficial basalt, to a depth of 2400 m, a sequence of welded tuff was penetrated and then from this level to the bottom of the well, recrystallized, hydrothermally-altered rhyodacite was the predominant lithology (Doherty et al., 1979). We utilized a velocity of 3.33 km/sec in the idealized model for the surficial basalts and sedimentary deposits. This velocity is between the values of 3.40 km/sec indicated by Ackermann (1979) and 3.02 km/sec indicated by Perkins et al. (1947) for these strata. Our smoothed velocity log from the INEL-1 well (Figure 2) indicates velocities of 4.9 km/sec for the welded tuffs and 5.3 km/sec for the recrystallized rhyodacite. The thicknesses of these layers were extrapolated from the well, this being the only lithologic reference point with velocity information near the intersection of the two seismic profiles.

Initially, the 136 km reversed seismic line from shotpoint 7 in the Northern Rocky Mountain (NRM) Province to the Gay phosphate mine located in the Basin and Range (BR) Province was interpreted. Shotpoint 7 was located 30 km northwest of the inferred SRP boundary on the north side of Antelope Valley while the Gay Mine was located 20 km southeast of the southern margin of the SRP near Blackfoot, Idaho (Figure 1).

The data from both of these shotpoints were modeled iteratively. Figures 3 and 5 show the idealized crustal velocity models, to a distance of 70 km from the respective shotpoints, which provided appropriate fits to the arrivals on the seismic data. Also shown are representative computer-drawn raypaths used in generatnng the various calculated travel-time curves utilized during the modeling. A complete model of the crustal structure across the ESRP was formed from the combination of the 70 km segments. Representative refracted and reflected phases from the top of the 6.53 km/sec layer and the lower crustal 6.80 km/sec layer are shown in the 136 km long crustal model in Figures 4 and 6. The Conda Mine data were then used to extend this crustal model into the Basin and Range Province southeast of the ESRP.

Because of the complexity of the inferred structure, the various groups of modeled rays are referred to as wave types or phases and denoted alphabetically. This provides a simple means of indexing the different phases with their respective arrivals on the seismograms. Figures 4 and 6 display the theoretical travel-time curves superimposed on the observed seismic sections recorded from shotpoint 7 and the Gay Mine, respectively.

Shotpoint 7

Phase A in Figures 3 and 4 has an apparent velocity of 5.56 km/sec to a distance of 30 km and was modeled essentially as a direct wave. Theoretically the travel-time curve for this phase should pass through the origin on the seismic

data, but instead it exhibits a delay in intercept time of approximately 0.3 sec. This delay is accounted for by 450 m of 1.5 km/sec low velocity material below the shotpoint located in Antelope Valley.

At a distance of 30 km from the shotpoint, the SRP boundary is encountered and phase A from 30 to 45 km displays an apparent velocity of 4.84 km/sec. This lower velocity segment was modeled by abruptly terminating the 5.56 km/sec Paleozoic sedimentary strata and passing the rays into the 4.90 km/sec welded tuffs of the SRP. It also was necessary to thin the 3.33 km/sec basalt and fluvial deposits overlying the tuffaceous strata from their 700 m thickness at the INEL-1 well location to 430 m at the SRP margin. (This thinning is also consistent with the fact that a time correction to a 1200 m elevation datum was employed and thus approximately 300 m of surficial material was 'stripped off' by the datum correction).

The thickness of the 5.56 km/sec sedimentary strata directly adjacent to the north side of the ESRP is not well known. However, a review of the stratigraphic work done by Ross (1962) and Skipp and Hall (1980) indicates the thickness is quite substantial. We regard the 3 km thickness indicated by the velocity model (Figures 3 and 4) for these strata as a conservative value. In actuality, some of the Precambrian and Lower Paleozoic quartzites which Ross describes, conceivably could propagate seismic energy with a velocity of approximately 6 km/sec. It would be difficult to distinguish between these strata and the upper crustal crystalline layer, thus resulting in a shallower interpreted depth to this interface.

A very prominent feature of the shotpoint 7 seismograms displayed in Figure 4 is the absence of a well developed arrival with an apparent velocity of 6.15 km/sec extending in the SRP. However, phase C in Figure 3, the critical refraction from the top of the upper crust northwest of the SRP margin, models the first arrivals on the seismograms between 43 and 53 km quite well. We assumed the simplest structural model in generating this interpretation. The 2400 m depth to the interface between the 4.90 km/sec and 5.30 km/sec volcanics was projected to the margin of the SRP and terminated. Thus, rays incident upon the 6.15 km/sec layer just under the critical angle refracted through this upper crustal layer and then traversed the near-vertical boundary into the 5.30 km/sec recrystallized rhyodacite of the SRP, producing arrivals corresponding to the observed seismic data. Phase C is not developed at all from 30 to 43 km, but is a strong first arrival from 43 to 53 km along this profile.

The seismic data available for the crossline do not provide definitive resolution on the depth to the bottom of the 5.30 km/sec volcanics. The depth of approximately 5 km was derived by modeling of the crossline data while requiring reasonable consistency with the interpretation of the axial profile (Braile et al., this volume).

Phases D and E, reflections and refractions respectively from the top of the 6.53 km/sec layer, indicate this boundary slopes to the northwest with a dip of approximately 10°, as

shown in Figures 3 and 4. The model indicates a depth of 7 km near the center of the plain and a depth of 17 km under shotpoint 7 to the top of this layer. However, phase D is only well developed from 27 to 70 km on the seismic record sections, and therefore, the configuration of this interface beneath shotpoint 7 is only inferred. These two phases produce the prominent first arrivals between 60 and 70 km with reflected phase D attenuating drastically in amplitude beyond 70 km. The top ray-diagram in Figure 4 shows phase E calculated to a distance of 110 km, however, there is very little energy from this refracted phase apparent in the observed seismic data beyond 70 km.

The attenuation of Phase D can be interpreted in two ways. Figure 4 shows the ray paths for this phase with the reflections incident near the crest of the 6.53 km/sec layer. The rapid spreading of the wave-front as the angle of incidence increases along this portion of the interface could account for the rapid loss of energy. Also, much of the energy carried by phase D could be diminished by propagation through the inferred fault zone at the margin of the SRP as the angle of incidence upon the 6.53 km/sec layer increased beyond that shown in Figure 4.

Finally, Phase F, which is well developed from 70 to 110 km was satisfactorily modeled as a reflection from the top of the 6.80 km/sec layer. This interface dips slightly to the southeast from a depth of 18 km under shotpoint 7 to 19 km under the Gay Mine shotpoint. The calculated

travel-time curve for phase G, the theoretical head-wave from this boundary, is also shown in Figure 4.

Gay Mine Shotpoint

The procedure used in the interpretation and the discussion of the Gay Mine data in this section is analogous to the presentation of the shotpoint 7 data. Figure 5 shows the derived crustal model from the shot origin to a distance of 70 km while Figure 6 displays the seismograms recorded from the mine blast and the calculated travel-time curves superimposed above the 136 km velocity model of the ESRP. This model in Figure 6 is identical to that utilized in Figure 4. However, the corresponding phases have different expression in the seismic data recorded from the Gay Mine and thus qualitatively indicate the structural differences between the northwest and southeast margins of the ESRP.

The station spacing and data recovery beyond 35 km for this shot were quite good. However, the inability to locate adequate seismograph sites in the area of the Snake River and Blackfoot, Idaho caused the lack of coverage in the distance range of 20 to 35 km. Also, it was not possible to obtain data between the Gay Mine shotpoint and the margin of the ESRP because of permitting difficulties. Thus, the velocity of the Paleozoic strata on the southeast side of the SRP is poorly defined. The velocity of 5.56 km/sec was used for these rocks because it was consistent with the seismic data recorded from this shot and because it is the velocity associated with the corresponding rocks on the northwest side of the SRP.

Phase A in Figure 5 and 6 was modeled as a direct wave through the 5.56 km/sec material to the ESRP boundary. At the margin, to allow for the fluvial deposits associated with the Snake River and the surficial basalts, a small fault of 500 m throw was modeled with the Paleozoic strata then dipping under the plain from this depth to a depth of 3.40 km at 70 km from the shot location. However, the location and throw of this fault is not well defined by the seismic data. Phase A then accounted for the 5.40 km/sec apparent velocity arrival which is prominent on the seismograms extending across the plain from 35 to 53 km from the shotpoint.

The most striking difference between the shotpoint 7 and Gay Mine data is the presence of a first arrival with an apparent velocity of approximately 6 km/sec on the Gay Mine record section. This arrival extends across the ESRP from approximately 35 to 80 km from the shot location. An arrival analogous to this is totally absent in the shotpoint 7 data on the north side of the SRP and thus implies that the upper crustal layer extends under the southeast side of the plain relatively undisturbed.

The boundary between the 5.56 km/sec material and the 6.15 km/sec material was modeled as an interface dipping to the northwest from a depth of approximately 3.20 km under the Gay Mine in the Basin and Range Province to a depth of 5 km near the center of the plain. Phases B and C in Figures 5 and 6 are the reflected and refracted energy from this interface respectively.

Another very prominent arrival in the Gay Mine data is the large amplitude reflected phase D, from the top of the 6.53 km/sec layer. This phase provided substantial evidence for a sharp velocity contrast between the upper crustal layer and the 6.53 km/sec material and the observations of this phase allowed accurate delineation of this interface. The interface modeled as approximately 7 km in depth near the center of the plain and dips to the southeast at 12° to approximately 19 km in depth beneath the Gay Mine.

The lower amplitude arrival approximately 0.5 seconds later than phase D was modeled as the reflected energy, phase F, from the top of the 6.80 km/sec lower crust as illustrated in Figure 6. Wave type G, the refraction from this boundary, was calculated and the travel-time curve shown, but does not appear to be present as a strong arrival in the observed data. Also present in the seismic data for the Gay Mine shot is a large amplitude arrival approximately 1 second later than phase D between 53 and 90 km. Several attempts were made to adequately model this phase as a multiple, but were unsuccessful. It is possible that this phase is a P to S wave conversion originating at the top of the 6.53 km/sec layer.

It should be added here, that the available seismic data from shotpoint 7 and the Gay Mine do not allow definite resolution on the nature of the interface between the extension of the Paleozoic rocks under the ESRP and the 5.30 km/sec volcanics in the region near the center of the plain. Modeling

of record sections along the axis of the SRP (Braile et al., this volume) did not require the 5.56 km/sec material to be present. Thus, the absence of the 5.56 km/sec Paleozoic sedimentary rocks beneath the central and northeastern region of the SRP is reflected in our velocity model, but cannot be inferred with certainty at this time. Figure 7 presents a record section from shotpoint 8 recorded transverse to the axis of the plain. A high velocity (apparent velocity ≈ 6 km/sec) first-arrival is present on the record section beginning at about a distance of 30 km to the southeast. As can be seen by the rays calculated in the SRP model (Figure 7), refractions from the top of the 5.56 km/sec material under the plain provide a reasonable match to the observed arrivals. Due to the small number of records available, the seismograms recorded to the northwest from shotpoint 8 were not interpreted. Also, the first seven seismograms plotted on this record section to the southeast of the shotpoint were actually located parallel to the axis of the plain northeast of the shotpoint (Figure 1) and were not modeled here.

Conda Mine Shotpoint

The Conda Phosphate Mine is located approximately 59 km southeast of the Gay Phosphate Mine and 79 km southeast of the inferred SRP margin (Figure 1). As the Conda Mine shotpoint was not located in close proximity to the boundary of the SRP, the data obtained from this blast was used primarily to determine the transition of deeper crustal layers between the Basin and Range Province and the ESRP. Interpretation of

the data for this line provided a model consistent with the shotpoint 7 to Gay Mine profile. However, the data were not useful in direct interpretation of the near-surface structure of the ESRP.

The seismograms recorded from the Conda shotpoint and the derived model to a depth of 50 km, are shown in Figures 8 and 9 respectively. The raypaths of the interpreted refracted phases are plotted on the idealized crustal model and the associated travel-time curves are shown on the seismic record sections in Figure 8. The ray-paths calculated for the various reflected phases are presented in Figure 9.

The crustal model shown in Figures 8 and 9, beyond a distance of 70 km from the Conda shotpoint, is exactly the model derived from the shotpoint 7 to Gay Mine profile. A low-velocity surface layer of 4.50 km/sec dipping southeast near the Conda Mine was introduced to account for delay times of the arrivals. The calculated travel-time curves for the direct wave through this layer and the reflected phase from the base of this material are shown on the seismograms in Figure 8, but they are not coded according to wave type. Thus, proceeding with phase A, the coding of the wave types is generally analogous to that previously discussed.

Phase A in Figure 8 has an apparent velocity of 5.78 km/sec to a distance of 30 km from the origin. Then from a distance of 30 km to the boundary of the SRP, the apparent velocity of this phase is 5.56 km/sec. Thus, in this distance range, phase A and the reflected energy from the top

of the upper crustal layer, phase B, account for the arrivals on the seismic data quite adequately. The three seismograms between the distances of 18 to 23 km from the shotpoint exhibit first arrivals that are approximately 0.25 seconds late compared to the calculated travel-times for phase A. These stations were located on the Blackfoot Lava Field, located directly northwest of the mine, and thus it is possible that these delays are attributable to the near-surface velocity structure associated with the volcanic rocks.

From a distance of 40 km from the Conda shotpoint to the ESRP boundary the seismic data exhibit a first-arrival with an apparent velocity somewhat higher than 6.15 km/sec. By sloping the top of the upper crustal layer from 3.85 km in depth at a distance of 60 km to a depth of 6.35 km beneath the Conda Mine, phase C modeled these arrivals quite well with an apparent velocity of 6.25 km/sec. Beyond the SRP margin phase C attenuates rapidly. The calculated apparent velocity of this phase extending into the SRP is 5.96 km/sec.

There is no evidence in the Conda Mine data that suggests the 6.53 km/sec intermediate layer extends into the Basin and Range Province for any appreciable distance. This interpretation of the crustal structure beneath the Basin and Range Province, directly southeast of the SRP margin, is consistent with the interpretation of the American Falls Reservoir - Bear Lake - Flaming Gorge Reservoir seismic refraction data discussed by Wilden (1965). His interpretation of the reversed profile, American Falls Reservoir - Bear Lake, also

did not require the presence of a layer with a velocity intermediate to the velocities of the upper and lower crust in this region.

Phase D, illustrated in raypaths and the travel-time curve in Figure 8, is initially a reflection from the top of the lower crust and then becomes a reflection from the top of the 6.53 km/sec layer. Although the travel-time curve associated with phase D is rather complex, the seismic data were modeled quite satisfactorily by these calculated arrival times.

Phases E and G are refractions from the top of the intermediate and lower crustal layers respectively, and are shown in Figure 8. Phase G from the critical point to approximately 105 km has an apparent velocity of 6,80 km/sec. Then from 105 km, the apparent velocity of this phase increases as the rays intersect the updip portion of the intermediate layer and then the apparent velocity decreases as the rays intersect the crest. Beyond 132 km, the apparent velocity is again approximately 6.80 km/sec. The calculated travel-time curve for phase E is shown in Figure 8. The excellent correlation between the calculated arrivals of phase G and the actual seismic data from 110 to 160 km, substantiates the configuration of the interface between the 6.53 km/sec material and the lower crustal (6.80 km/sec) layer beneath the ESRP. Thus, the Conda Mine data are in agreement with the shotpoint 7 and Gay Mine interpretation of this interface and are also consistent with the configuration of the 6.53 km/sec layer as indicated by the shotpoint 7 to Gay Mine profile.

Finally, the reflected energy from the crust-mantle interface, indicated conventionally herein as PmP, is apparent in the seismic data beyond 110 km. This phase was modeled adequately with the Moho occurring at 40 km in depth. This depth to the Moho is consistent with the interpretation of the PmP arrivals for the axial profile (Braile et al., this volume). Although the model shown in Figure 9 indicates the interface is planar, reflections from this interface were obtained over only approximately a 30 km distance and, therefore, the possibility of structure on this interface cannot be eliminated.

Shotpoint 8 NE and Shotpoint 4 SW

Shotpoint 8 NE and shotpoint 4 SW were recorded along the axis of the ESRP and provided a 47 km reversed profile which was utilized in the interpretation of the shallow crustal structure of the ESRP in this area. Figures 10 and 11 show the seismic record sections from these two shotpoints to a distance of 50 km from their respective origins. The intersection of the shotpoint 7 to Gay Mine crossline with this profile is located approximately 15 km from shotpoint 8 (Figure 10) and approximately 32 km from shotpoint 4 (Figure 11).

Because a simple layered crustal model was used to model the shotpoint 8 NE and shotpoint 4 SW data, the phase nomenclature that is used in Figures 10 and 11 describes the reflected and refracted arrivals by the layer number from which the phase originates. Specifically, the refractions

from the top of the ith layer are identified as P_i while the reflections from the top of this layer are identified as P_iP. Because of the short distances involved, only the travel-time curves associated with the first three layers are indicated on the seismic record sections, and only the P_3 phase is represented by ray-paths in the crustal model in both figures. The depths to the fourth and fifth layers were derived from the Conda-SP7 interpretation at the intersection with this profile. The interface between the 5.30 km/sec material and the 6.15 km/sec upper crustal layer may be highly irregular if not gradational due to the nature of the volcanic processes which have produced this structure. There is also the possibility of the occurrence of ≈ 5.56 km/sec Paleozoic sedimentary rocks beneath the 5.3 km/sec volcanic rocks as discussed previously. However, this layer was not required in the modeling of the axial line and could not be resolved with the 2 to 3 km station spacing used during data collection.

Computer modeling of this reversed profile yielded a velocity versus depth model of the crust which generally was in good agreement with the INEL-1 well interpretation (Figure 2 and Doherty et al., 1979). However, the modeling also indicated that significant relief existed in the interface between the 4.90 km/sec and 5.30 km/sec material from approximately the mid-point of the profile to and beyond shotpoint 4. The surficial 3.33 km/sec layer was modeled as 0.9 km in thickness beneath shotpoint 8 and sloped very gently to a depth

of 1.1 km beneath shotpoint 4. Layer 2, the 4.90 km/sec material, was determined to be 2.7 km in thickness below shotpoint 8 and is essentially horizontal at this depth to a distance of 23 km from the shotpoint 8 location. For the next 24 km, this interface was modeled successfully as dipping 4.5° to a depth of 4.5 km beneath shotpoint 4. Preliminary modeling of shotpoint 4 NE, which is not presented in this text, suggests that the dip on this interface persists at least 30 km northeast of shotpoint 4 location although with a somewhat lesser slope.

The P_2 phase, which are refractions from the top of the 4.90 km/sec welded-tuff layer, attenuate very rapidly in amplitude, and energy from this arrival was essentially nonexistent in the seismic records beyond about 7 km from both of the shotpoint 8 and 4 locations. Thus, the Q value of this material is extremely low (Braile et al., this volume).

The reflections and refractions from the top of the 5.30 km/sec material, phases P_3P and P_3 respectively, account for the large amplitude early arrivals beyond about 10 km in both data sets. The P_3 phase beyond approximately 27 km from shotpoint 4 (Figure 11) has an apparent velocity of approximately 5.30 km/sec as does the P_3 phase between the critical point and 23 km from shotpoint 8 in Figure 10. Between the critical point for this phase to 27 km from shotpoint 4, the apparent velocity is greater than 5.30 km/sec while this phase exhibits an apparent velocity less than 5.30 km/sec beyond 23 km from shotpoint 8. Thus the structure on the top of the 5.30 km/sec material is inferred from these apparent velocity anomalies in the P_3 phase.

GRAVITY MODELING

Several investigators have previously studied the gravity field associated with the ESRP and generally characterize the gravity field as an asymmetric positive anomaly roughly parallel to the axis of the ESRP (LaFehr and Pakiser, 1962; Mabey, 1976 and 1978). We calculated the gravitational field over the crustal model derived from the seismic interpretation and compared this field with observed gravity data to further constrain and refine the seismic modeling.

Three gravity profiles were constructed from a simple Bouguer gravity map provided by G.R. Keller (written communication, 1979) which was compiled from the gravity data file of the U.S. Defense Mapping Agency. The first profile was coincident with the Conda-SP7 seismic profile and extended 50 km northwest of shotpoint 7 to 44°N latitude and 114°W longitude. This profile also extended 51 km southeast of the Conda Mine to $42^{\circ}30"$N latitude and 111°W longitude. The two other observed gravity profiles were of the same length (297 km) and parallel to the first one, however, they were located 20 km northeast and southwest respectively of the Conda-SP7 profile. By utilizing the three observed profiles, characteristic trends of the observed gravity field in this region could be compared to the calculated gravity anomalies.

The densities utilized in the modeling of the ESRP

volcanics were derived from an averaged, compensated density log recorded in the INEL-1 well. The remaining densities were assigned by utilizing the appropriate velocity versus density curves for various rock types compiled by Woollard (1962). The densities were assigned by selecting, from Woollard's velocity-density data, the average density value which corresponded to the seismic velocity for each layer. The velocity-density relation which resulted from this procedure is graphed in Figure 12. Although these densities were derived from various sources, this relation indicates that the velocity-density curve deviates very little from an almost linear relationship.

Figure 13 shows the topographic and gravity profiles above the final inferred geological model. The densities utilized in the calculation of the theoretical gravity curve are indicated in parentheses beside the corresponding seismic velocities. The general characteristics of the observed gravity profiles are matched quite well by the calculated profile although no attempt was made to model the shorter-wavelength anomalies on these profiles. The fault structure on the northwest side of the SRP yields a characteristic signature local anomaly which is recognizable on the three observed gravity profiles although the amplitudes are slightly different.

It was necessary to thicken the lower crustal layer in the idealized model from 10 km under the SRP to approximately 18 km beneath the Idaho Batholith, northwest of the SRP margin. It also was necessary to decrease the distance that the 6.53 km/sec

intermediate layer extends beyond the northwest boundary of the plain to satisfactorily model the steep gravity gradient which occurs on this side of the plain. This configuration of the intermediate 6.53 km/sec layer did not violate the seismic data as there are no significant reflections observed from this region of the interface on the shotpoint 7 data. Also, the inferred crustal thickening to the northwest of the SRP is not constrained by the seismic data and thus the gravity data could have equally well been modeled by a lower density crust rather than a variation in the depth to the Moho. However, the increased depth to the Moho in this area was the simplest structural assumption and is also consistent with isostatic compensation beneath the large topographic elevations associated with the Idaho Batholith and, therefore, was considered a reasonable assumption. The interfaces in Figure 13 are dashed where inferred and are solid where the seismic data were deemed sufficient to resolve them.

CONCLUSIONS

Use of the ray-trace method to model the seismic refraction data presented here was invaluable in defining the crustal structure beneath the ESRP. It is essentially the only method by which such complex structure could adequately be modeled utilizing the seismic data. The interpreted structural profile presented in Figure 13 is consistent with the average crustal model parallel to the axis of the ESRP at their point of intersection (Braile et al., this volume). However, we utilized simple, dipping, planar and homogeneous crustal layering in the modeling of the latter profiles whereas the ray-trace method utilized for the crossline provided information on the lateral variations of these layers and the structure associated with the margins of the ESRP.

The ray-trace modeling of the seismic refraction profiles and subsequent gravity modeling has substantiated a 3-dimensional idealized model of the crust beneath the ESRP and indicated the structure, especially in the upper crust, to be highly anomalous. An asymmetric graben-like structure is indicated, with greater throw along the fault at the northwest margin of the SRP. This structure was subsequently infilled by a thick sequence of volcanic rocks. The 6.15 km/sec upper crustal layer is greatly thinned in comparison with the surrounding regions.

The fault structure inferred at the northwest boundary of the SRP, with the sedimentary strata terminating there, is a significant feature which was indicated by both the seismic and gravity data. However, it appears that along the southeast margin of the SRP the Paleozoic sedimentary rocks extend under the SRP volcanics for a distance of at least 40 km. If there is a fault present along the southeast margin of the SRP, then it is of much less magnitude than that along the northwest boundary.

The modeling of the 6.53 km/sec intermediate layer indicates that it is localized within the SRP margins and has a minimum relief of 10 km above the contact with the lower crust beneath the center of the plain. This anomalous body may have been generated by the intrusion of mafic material from the upper mantle into the highly fractured upper crust beneath the ESRP. Figure 14 depicts this schematically. The prominent reflections from the flanks of this body as well as from the interface between this layer and the lower crust suggest that the 6.53 km/sec velocity is due to intrusion of higher velocity material into the upper crust rather than a metamorphic effect caused by heat conduction from below. If the latter were the case, the velocity contrasts at these interfaces would likely be gradational. The gravity modeling indicates that an anomalously high density upper crust could adequately provide for the long wavelength gravity high observed over the ESRP.

The lower crust appears to be relatively undisturbed beneath the ESRP and is a continuous layer which extends into

the adjacent geological provinces. The interpreted depth to the interface between the upper and lower crust (19 ± 1 km) extending into the Basin and Range is consistent with the interpretation of the seismic-refraction data between American Falls, Idaho and Flaming Gorge, Utah discussed by Wilden (1965). He found the depth to this interface from American Falls to Bear Lake to be 18.1 km while the reversal of this segment of the profile indicated a depth of 19.4 km. Hill and Pakiser (1966) also interpreted the depth to the lower crust as ≈ 19 km beneath the Basin and Range Province, south of the western SRP.

Combined gravity and ray-trace travel-time modeling has proven to be a powerful interpretation procedure for investigation of the crustal structure of the eastern Snake River Plain and the transition to adjacent provinces. A highly anomalous crust is shown to exist beneath the ESRP (Figure 14). A volcanic-filled asymmetric graben at least 5 km deep, overlies an intruded upper crust beneath the ESRP. Although it is beyond the scope of this paper, proposed models for the geologic and tectonic evolution of the Snake River Plain will require consideration of the crustal model presented here.

ACKNOWLEDGEMENTS

We are grateful to all of the participants in the 1978 Y-SRP seismic refraction profiling experiment. Participants are indicated in the acknowledgements of the papers by Braile et al. (this volume) and Smith et al. (this volume). The interest and hard work of these people in the field was critical to the success of the experiment and the interpretation presented here. We would expecially like to thank the following people for helpful discussions during the course of this research: Mark R. Baker, Mike M. Schilly, Hans D. Ackermann, Jorge Ansorge, David D. Blackwell, Mel A. Kuntz, Roger Greensfelder, Kenneth H. Olsen, David P. Hill, John H. Healy, William J. Hinze, Claus Prodehl, John L. Sexton, S. Thomas Crough and Walter Mooney. G. Randy Keller provided Bouguer gravity data for the eastern Snake River Plain. Walter Mooney provided us with a copy of the ray-tracing program used for the travel-time modeling. The Idaho National Engineering Laboratory, The U.S. Forest Service, the National Park Service, the U.S. Geological Survey and the U.S. Bureau of Land Management were helpful with logistics in the field work. David Blackwell aided with the siting and acquisition of shotpoint 8. Several government agencies and universities provided personnel and instrumentation during the experiment (see Braile et al. and Smith et al., this volume). Personnel at

the Gay and Conda Phosphate Mines were most cooperative in allowing us to record the origin times of quarry blasts. The efforts of David Butler, Roger Bowman and Andy Staatz of Microgeophysics Corporation were important to the success of this experiment. This research was supported by the National Science Foundation Grant No. EAR77-23357 to Purdue University and Grant No. EAR77-23707 to the University of Utah and by the United States Geological Survey Geothermal Research Program Grant No. 14-08-0001-G-532 to Purdue University.

REFERENCES

Ackermann, H.D., Velocity structure to 3000-meter depth at the Idaho National Engineering Laboratory, eastern Snake River Plain (abstract), EOS Trans. AGU, 60, 942, 1979.

Baker, M.R., Application of time series analysis to the enhancement of seismic refraction data interpretation, Unpublished M.S. Thesis, Purdue University, 1979.

Baker, M.R., L.W. Braile and R.B. Smith, Amplitude normalization of seismograms from multiple seismograph recording systems for the Yellowstone-Snake River Plain seismic refraction experiment, submitted to J. Geophys. Res., 1981.

Braile, L.W., R.B. Smith, J. Ansorge, M.R. Baker, M.A. Sparlin, C. Prodehl, M.M. Schilly, J.H. Healy, St. Mueller and K.H. Olsen, The Yellowstone-Snake River Plain seismic profiling experiment: Crustal structure of the eastern Snake River Plain, submitted to J. Geophys. Res., 1981.

Cerveny, V., I.A. Molotkov and I. Psencik, Ray Method in Seismology, Vydala Universita Karlova, Praha, Czechoslovakia, 1977.

Doherty, D.J., L.A. McBroome and M.A. Kuntz, Preliminary geological interpretation and lithologic log of the exploratory geothermal test well (INEL-1), Idaho National Engineering Laboratory, eastern Snake River Plain, Idaho, U.S. Geol. Surv. Open-File Rept. 79-1248, 1979.

Fenneman, N.M. and D.W. Johnson, Physical divisions of the United States: U.S. Geol. Surv. map, scale 1:7,000,000, 1946.

Hill, D.P. and L.C. Pakiser, Crustal structure between the Nevada Test Site and Boise, Idaho, from seismic-refraction measurements, in The Earth Beneath the Continents, Amer. Geophys. Union Mon. 10, 391-419, 1966.

LaFehr, T.R. and L.C. Pakiser, Gravity, volcanism and crustal deformation of the eastern Snake River Plain, U.S. Geol. Surv. Prof. Pap., 450-D, 76-78, 1962.

Mabey, D.R., Interpretation of a gravity profile across the western Snake River Plain, Geology, 4, 53-56, 1976.

Mabey, D.R., Regional gravity and magnetic anomalies in the eastern Snake River Plain, Idaho, J. Res. U.S. Geol. Surv., 6, 553-562, 1978.

Perkins, B., D.S. Gardner, T.H. Pearce and R.M. Patterson, Subsurface structure of Snake River Valley, Idaho, from seismograph records of ammunition explosions (abstract), Geophysics, 12, 496, 1947.

Ross, C.P., Stratified rocks in south-central Idaho, Idaho Bur. of Mines and Geol. Pamph., 125, 126 pp., 1962.

Schilly, M.M., Interpretation of crustal seismic refraction and reflection profiles from Yellowstone and the eastern Snake River Plain, Unpublished M.S. Thesis, U. of Utah, 1979.

Skipp, B. and W.E. Hall, Upper Paleozoic paleotectonics and paleogeography of Idaho, in Paleozoic Paleogeography of West-Central United States, edited by T.D. Fouch and E.R. Magathan, Rocky Mtn. Sec. Soc. Econ. Paleon. Min., 387-442, 1980.

Smith , R.B., L.W. Braile, M.M. Schilly, J. Ansorge, C. Prodehl, J.H. Healy, J.R. Pelton, St. Mueller and M.R. Baker, The Yellowstone-Snake River Plain seismic profiling experiment: Yellowstone, submitted to J. Geophys. Res., 1981.

Wilden, R., Seismic-refraction measurements of crustal structure between American Falls Reservoir, Idaho and Flaming Gorge Reservoir, Utah, U.S. Geol. Surv. Prof. Pap., 525-C, 44-50, 1965.

Woollard, G.P., The relation of gravity anomalies to surface elevation, crustal structure and geology, U.S.A.F. Res. Rept. Ser. No. 62-9, Aeron. Chart and Inform. Center, St. Louis, Missouri, 1962.

FIGURE CAPTIONS

Figure 1. Index map of southeastern Idaho showing locations of shotpoints (large circles) and seismograph stations (small triangles) utilized during the eastern Snake River Plain phase of the refraction experiment. Province boundaries (dashed lines) are from Fenneman and Johnson (1946).

Figure 2. Compressional velocity versus depth profile inferred for the shallow structure of the ESRP from the smoothed interval velocity log observed in drill hole INEL-1. A generalized lithologic log from drill cuttings and cores (Doherty et al., 1979) is also shown. The interval velocity data were available between the bottom of the drill casing and the bottom of the hole. However, the velocity data were highly erratic in the depth range of 500-800 m corresponding to a depth interval characterized by alternating layers of high-velocity altered basalts and low-velocity sedimentary rocks. The velocity data in this interval are shown schematically by the dashed line. The velocity profile for the upper 700 m which was used for interpretation (dotted line) is more consistent with the observed refraction data and the interpretations of Ackermann (1979) and Perkins et al. (1947).

Figure 3. Velocity model for the ESRP from shotpoint 7 to the southeast showing the compressional wave velocities, interfaces (heavy solid lines) and computed raypaths (thin lines) for selected angle-of-incidence ranges for refracted (upper plot) and reflected (lower plot) ray types. The phase names correspond to calculated ray-trace travel-times shown in the record section in Figure 4.

Figure 4. Velocity model and calculated raypaths for larger distance range for shotpoint 7 to the southeast. Reduced velocity seismic record section (top figure) shows the vertical component seismograms, amplitude normalized and plotted with an amplitude scaling factor of distance to the 1.5 power. Theoretical travel-time curves for the phases illustrated in the velocity model (and from Figure 3) are also shown.

Figure 5. Velocity model and raypaths for Gay Mine shotpoint to the northwest. Travel times for the refracted arrivals (upper figure) and reflected arrivals (lower figure) are shown in Figure 6.

Figure 6. Velocity model, raypaths and seismic record section for larger distance range arrivals from the Gay Mine shotpoint. Record section shows vertical component, amplitude normalized seismograms with an amplitude scale factor of distance to the 1.5 power for plot scaling. Theoretical travel-times are shown on the record section for the phases illustrated by the raypaths shown here and in Figure 5.

Figure 7. Velocity model, raypaths and seismic record section recorded from shotpoint 8 to the northwest and southeast. Theoretical travel-times for the raypaths shown are drawn on the record section. The third through the seventh seismograms plotted to the right of the zero distance correspond to stations 2105, 2104, 2102, 2101, and 2652 (Figure 1) which are actually located northeast or east of the shotpoint and are modeled in Figure 10.

Figure 8. Velocity model, raypaths for refracted phases and seismic record section for the Conda Mine shotpoint. Record section shows vertical component, amplitude-normalized seismograms with an amplitude scale factor of distance to the 1.5 power for plot scaling. Theoretical travel-times are shown on the record section for the phases illustrated by the raypaths shown here and in Figure 9.

Figure 9. Velocity model and raypaths for reflected phases for the Conda Mine shotpoint to the northwest. Travel times for these phases are plotted on the record section shown in Figure 8.

Figure 10. Velocity model, raypaths (for the P_3 arrival only) and seismic record section for shotpoint 8 to the northeast. Seismograms are vertical component, amplitude normalized with an amplitude scale factor of distance to the 1.5 power for plot scaling. Theoretical travel-times for the velocity model are shown on the record section.

Figure 11. Velocity model, raypaths (for the P_3 arrival only) and seismic record section for shotpoint 4 to the southwest. Seismograms are vertical component, amplitude normalized with an amplitude scale factor of distance to the 1.5 power for plot scaling. Theoretical traveltimes for the velocity model are shown on the record section.

Figure 12. Plot of velocity-density relation for the crustal model shown in Figure 13.

Figure 13. Inferred crustal model across the eastern Snake River Plain. Interfaces are dashed where no seismic control is available. Elevation and gravity profiles are also shown. Three observed simple Bouguer gravity profiles are shown. One is located along the Conda-SP7 profile, and the other two are oriented parallel to the Conda-SP7 profile but are shifted 20 km northeast and 20 km southwest. The gravity anomaly calculated from the two-dimensional density model (densities are values shown in parentheses) is also illustrated.

Figure 14. Schematic diagram illustrating the inferred crustal model beneath the eastern Snake River Plain and adjacent provinces.

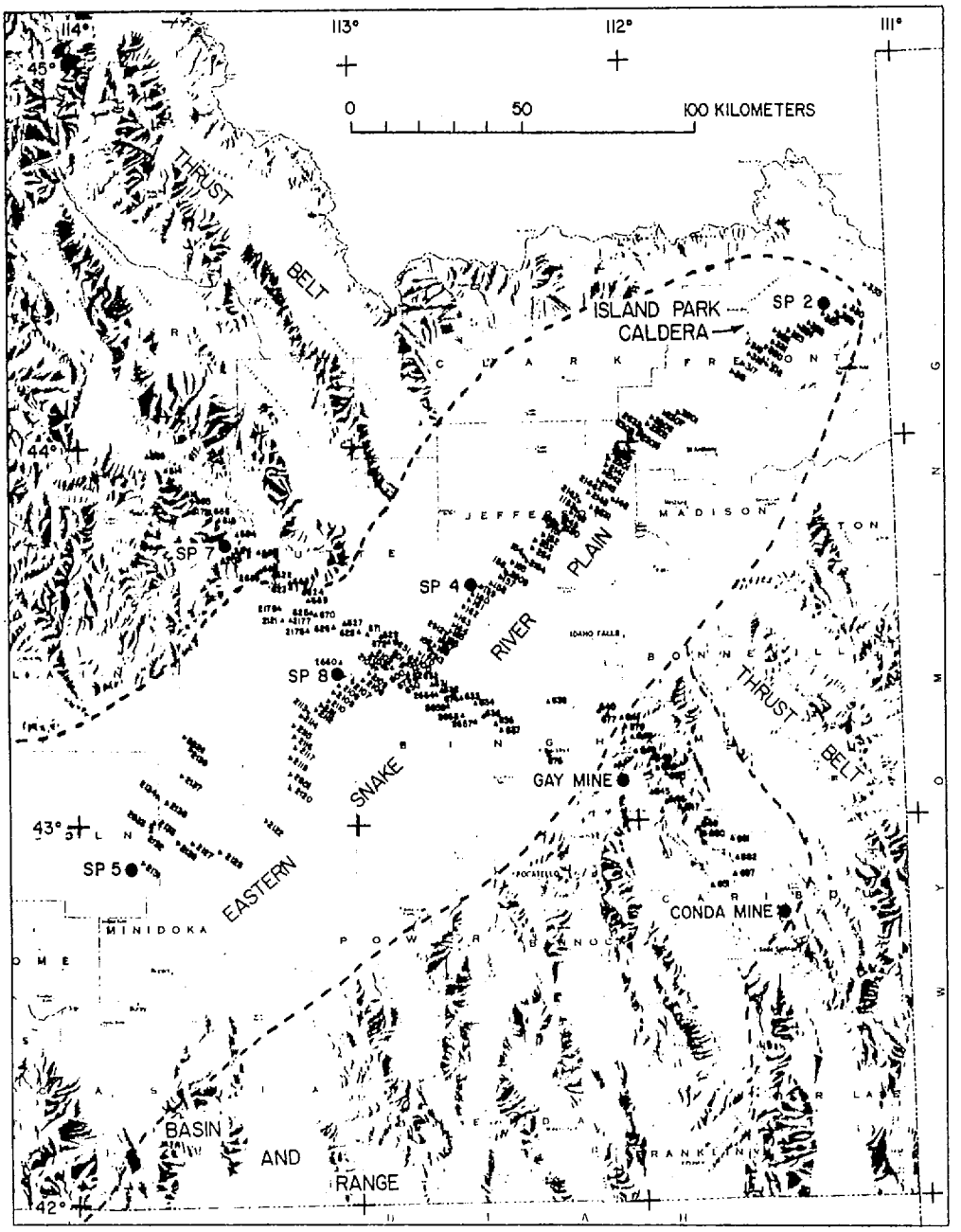
114°
113°
112°
111°
45°
44°
43°
42°
0
50
100 KILOMETERS
THRUST
BELT
ISLAND PARK
CALDERA
SP 2
SP 7
SP 4
SP 8
SP 5
RIVER
PLAIN
SNAKE
EASTERN
GAY MINE
CONDA MINE
THRUST
BELT
BASIN
AND
RANGE
JEFFERSON
MADISON
MINIDOKA
POWER
BINGHAM
CARIBOU
FRANKLIN

Figure 1

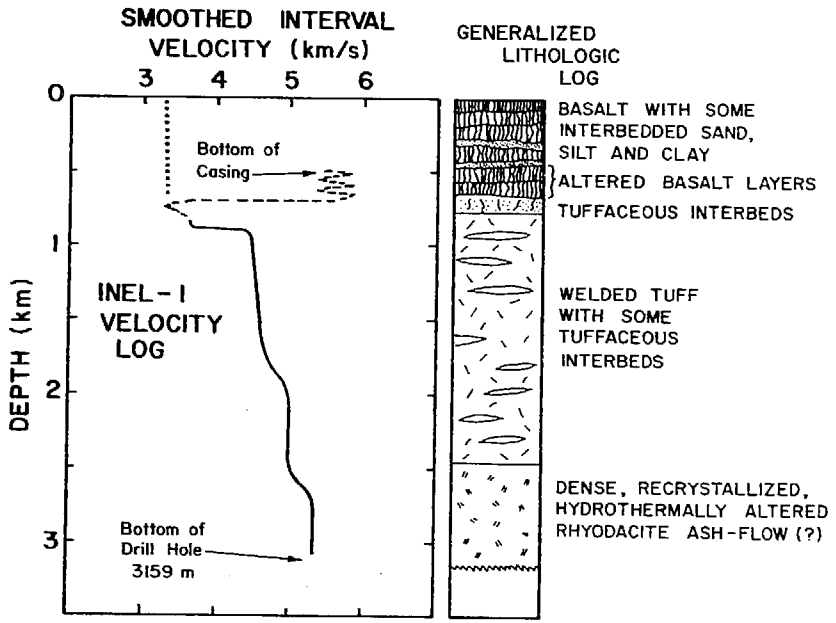
SMOOTHED INTERVAL VELOCITY (km/s)
3
4
5
6
0
1
2
3
DEPTH (km)
Bottom of Casing
INEL-1 VELOCITY LOG
Bottom of Drill Hole
3159 m
GENERALIZED LITHOLOGIC LOG
BASALT WITH SOME INTERBEDDED SAND, SILT AND CLAY
ALTERED BASALT LAYERS
TUFFACEOUS INTERBEDS
WELDED TUFF WITH SOME TUFFACEOUS INTERBEDS
DENSE, RECRYSTALLIZED, HYDROTHERMALLY ALTERED RHYODACITE ASH-FLOW (?)

Figure 2

SHOT POINT 7

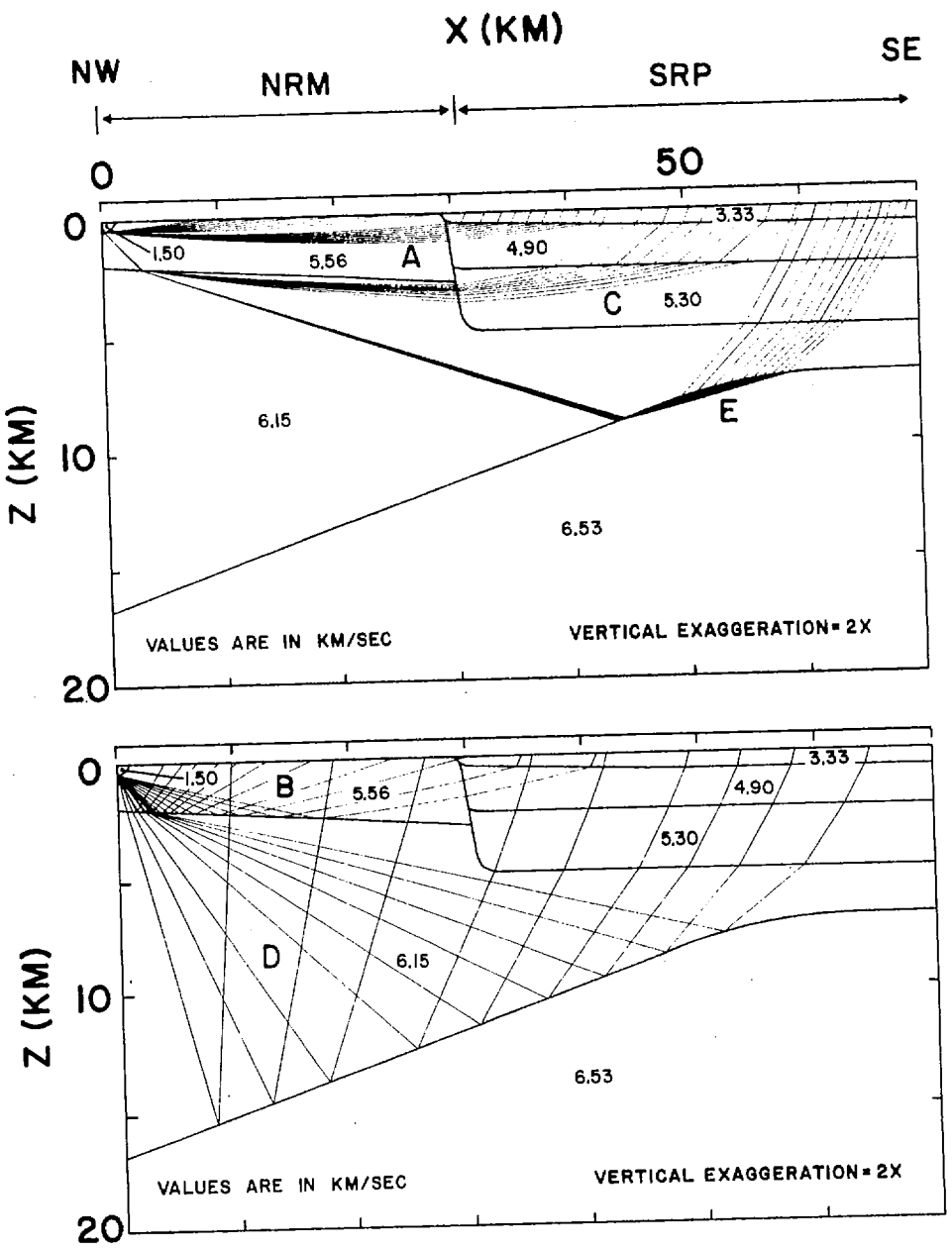

Figure 3

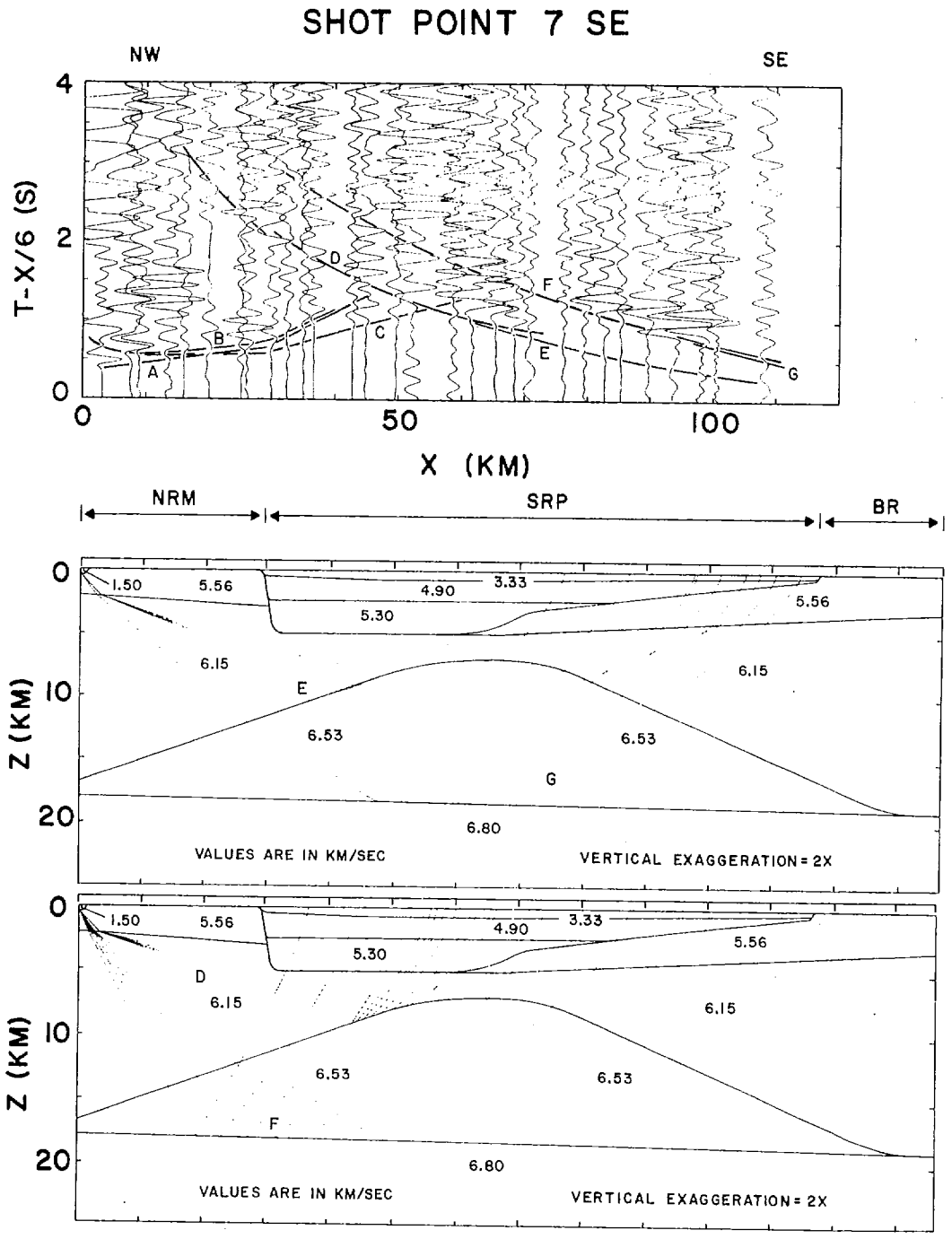
SHOT POINT 7 SE
NW
SE
T-X/6 (S)
X (KM)
A
B
C
D
E
F
G
NRM
SRP
BR
Z (KM)
1.50
5.56
4.90
3.33
5.30
6.15
6.53
6.80
VALUES ARE IN KM/SEC
VERTICAL EXAGGERATION = 2X

Figure 4

GAY MINE

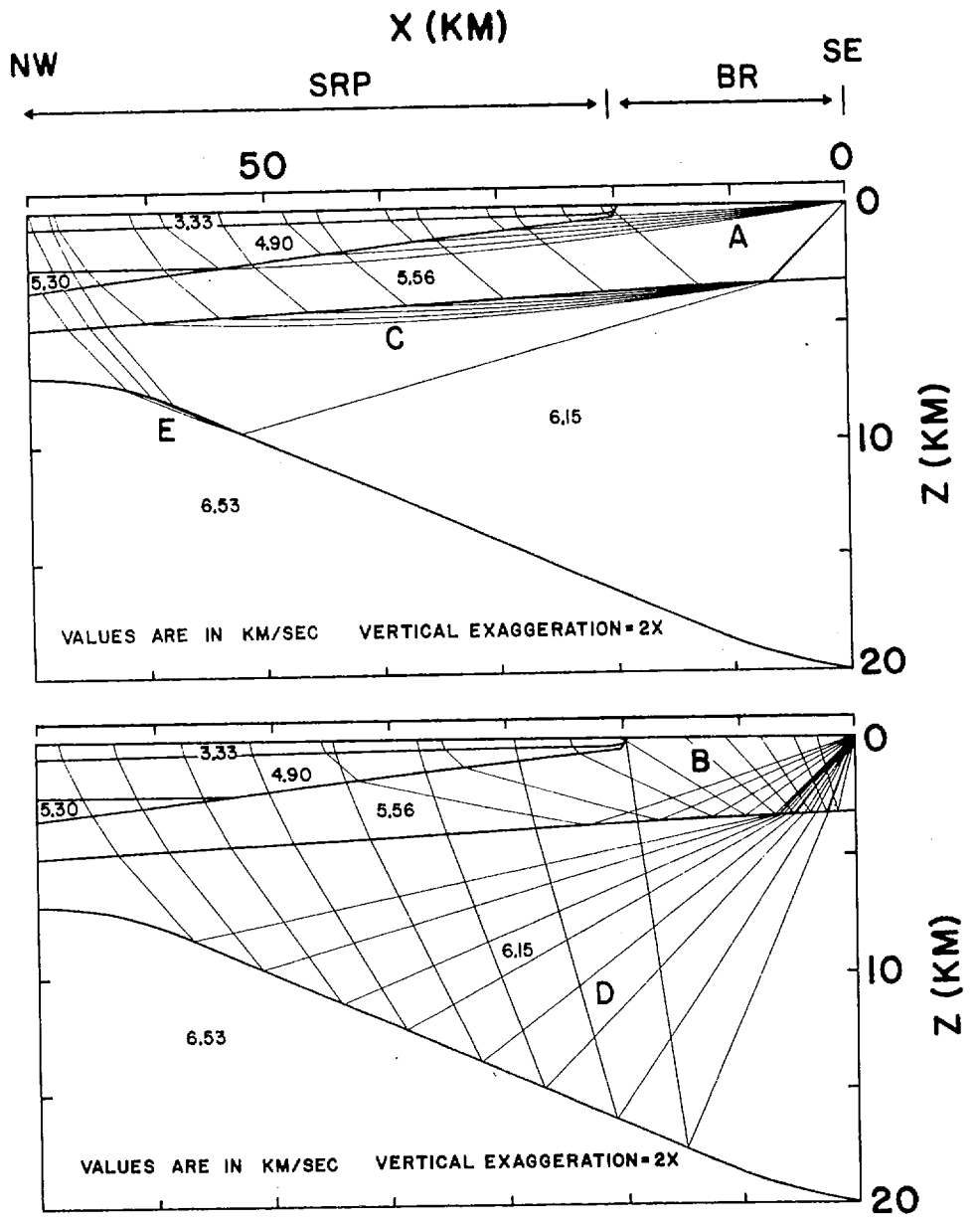

Figure 5

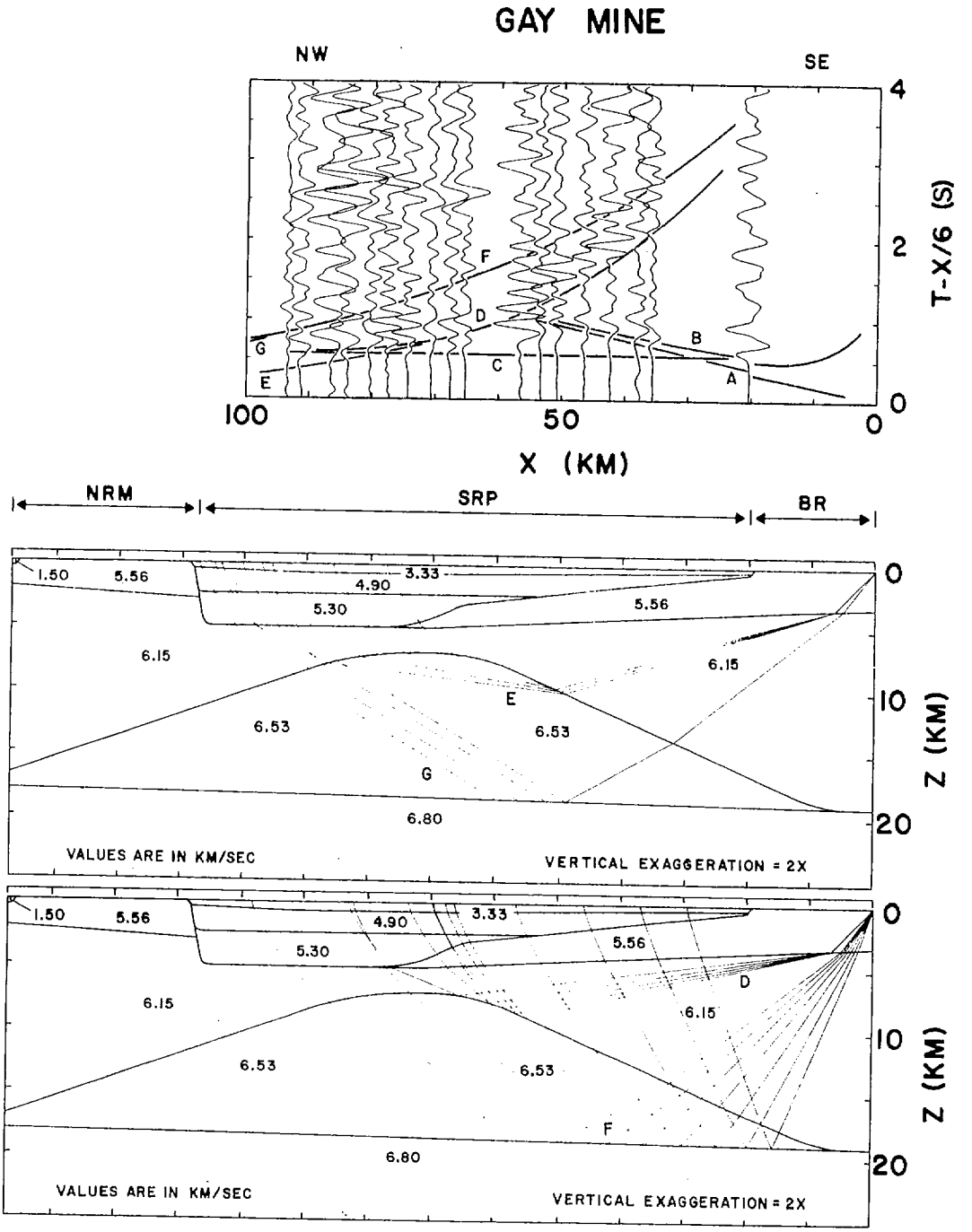
GAY MINE
NW
SE
4
2
0
T-X/6 (S)
F
D
B
G
C
E
A
100
50
0
X (KM)
NRM
SRP
BR
1.50
5.56
3.33
4.90
5.30
5.56
6.15
6.15
E
6.53
6.53
G
6.80
VALUES ARE IN KM/SEC
VERTICAL EXAGGERATION = 2X
0
10
20
Z (KM)
1.50
5.56
4.90
3.33
5.30
5.56
D
6.15
6.15
6.53
6.53
F
6.80
VALUES ARE IN KM/SEC
VERTICAL EXAGGERATION = 2X
0
10
20
Z (KM)

Figure 6

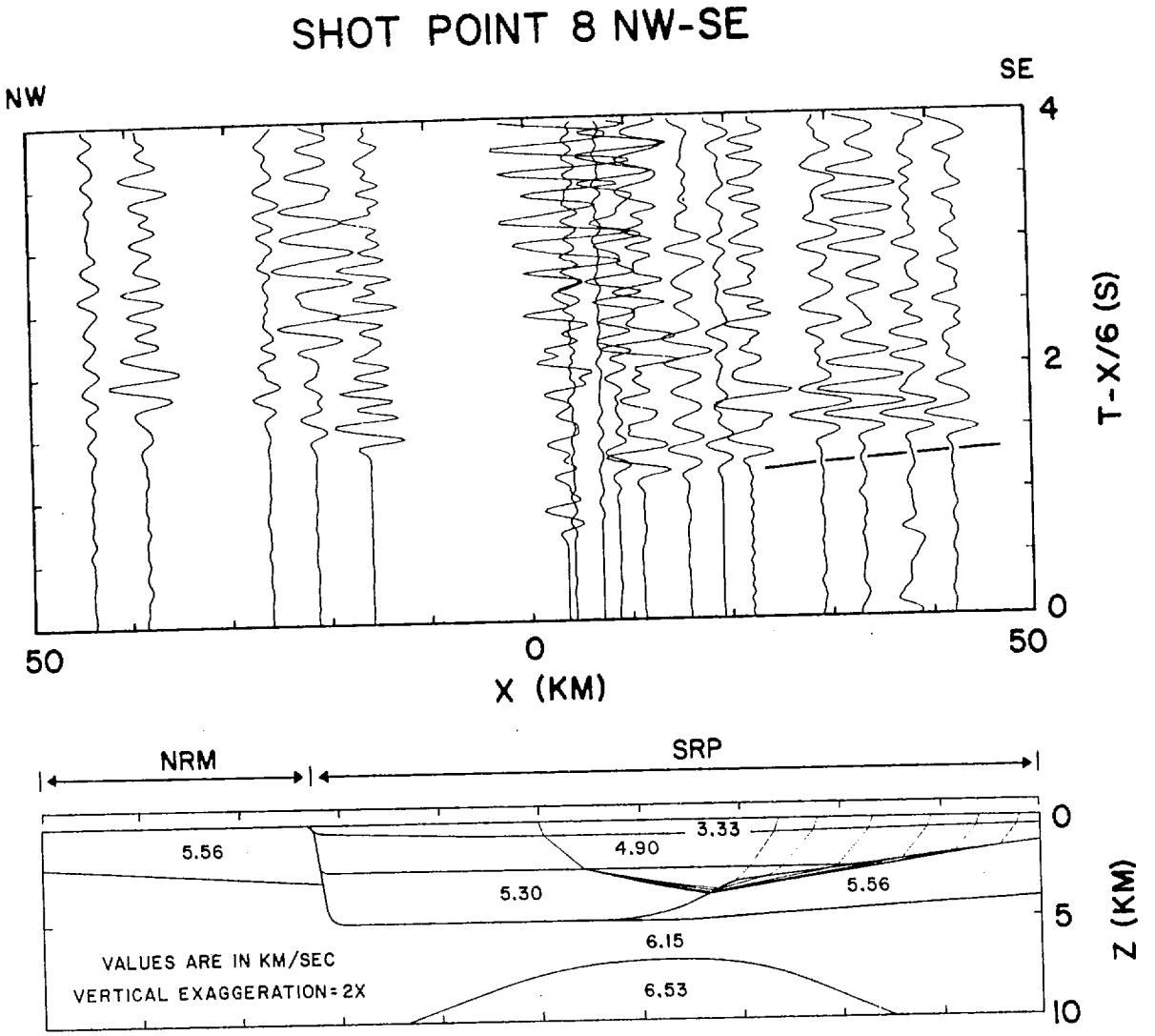
SHOT POINT 8 NW-SE
NW
SE
4
2
0
T-X/6 (S)
50
0
50
X (KM)
NRM
SRP
5.56
3.33
4.90
5.30
5.56
6.15
6.53
VALUES ARE IN KM/SEC
VERTICAL EXAGGERATION=2X
0
5
10
Z (KM)

Figure 7

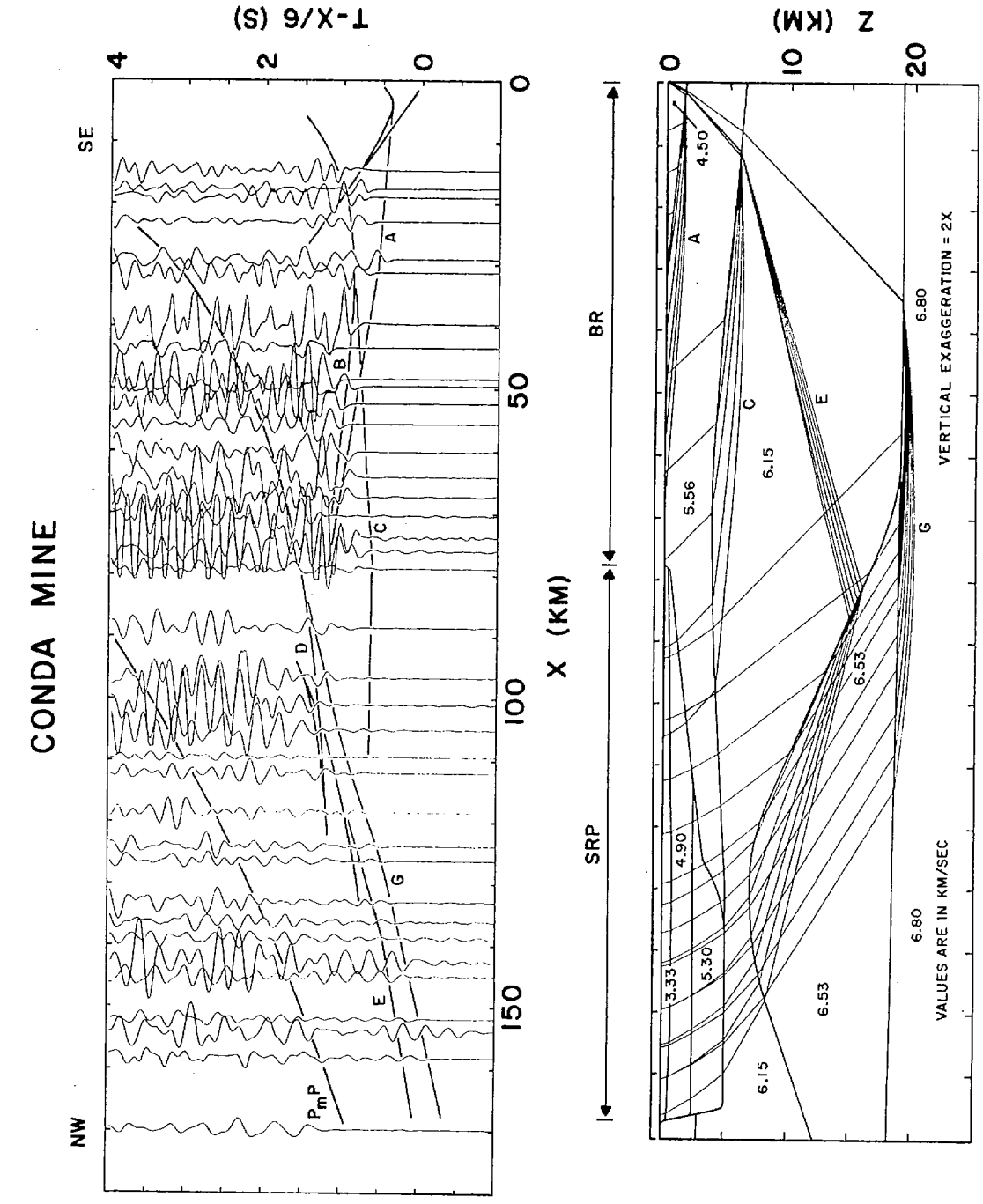
CONDA MINE
T-X/6 (S)
SE
NW
A
B
C
D
E
G
P_mP
X (KM)
BR
SRP
Z (KM)
VERTICAL EXAGGERATION = 2X
VALUES ARE IN KM/SEC
4.50
5.56
6.15
6.80
4.90
5.30
3.33
6.53

Figure 8

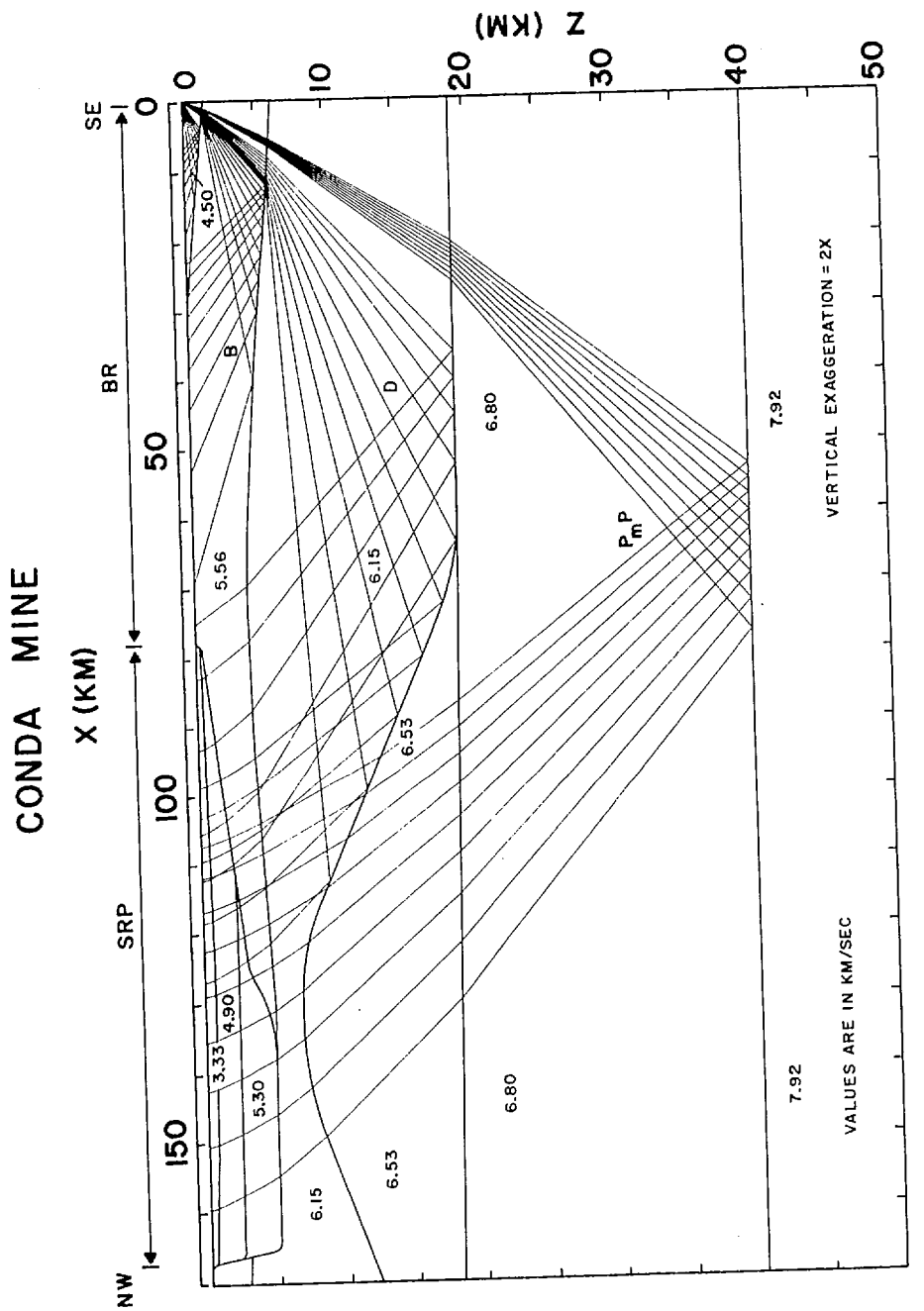
CONDA MINE
X (KM)
Z (KM)
SE
BR
SRP
NW
0
50
100
150
0
10
20
30
40
50
4.50
B
D
5.56
6.15
6.53
6.80
7.92
$P_m P$
3.33
4.90
5.30
VERTICAL EXAGGERATION = 2X
VALUES ARE IN KM/SEC

Figure 9

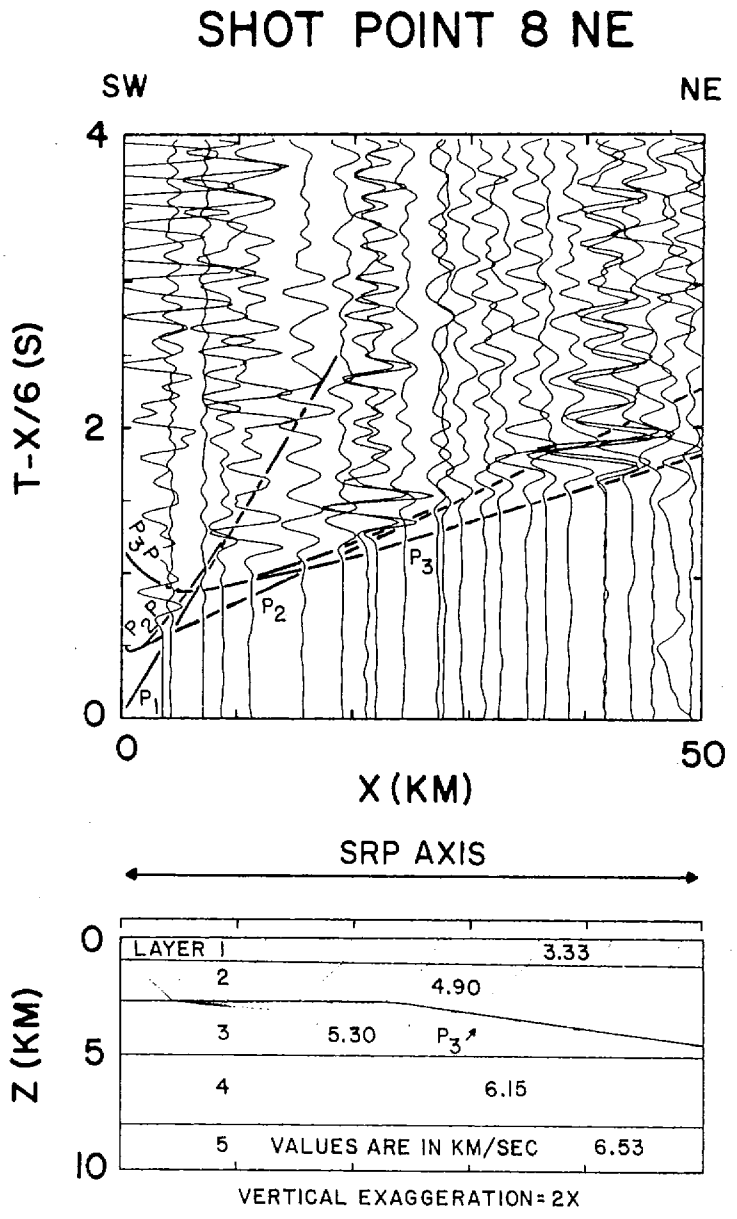
SHOT POINT 8 NE
SW
NE
4
2
0
T-X/6 (S)
0
50
X (KM)
P1
P2
P2P
P3P
P3
SRP AXIS
0
5
10
Z (KM)
LAYER 1
3.33
2
4.90
3
5.30
P3
4
6.15
5
VALUES ARE IN KM/SEC
6.53
VERTICAL EXAGGERATION= 2X

Figure 10

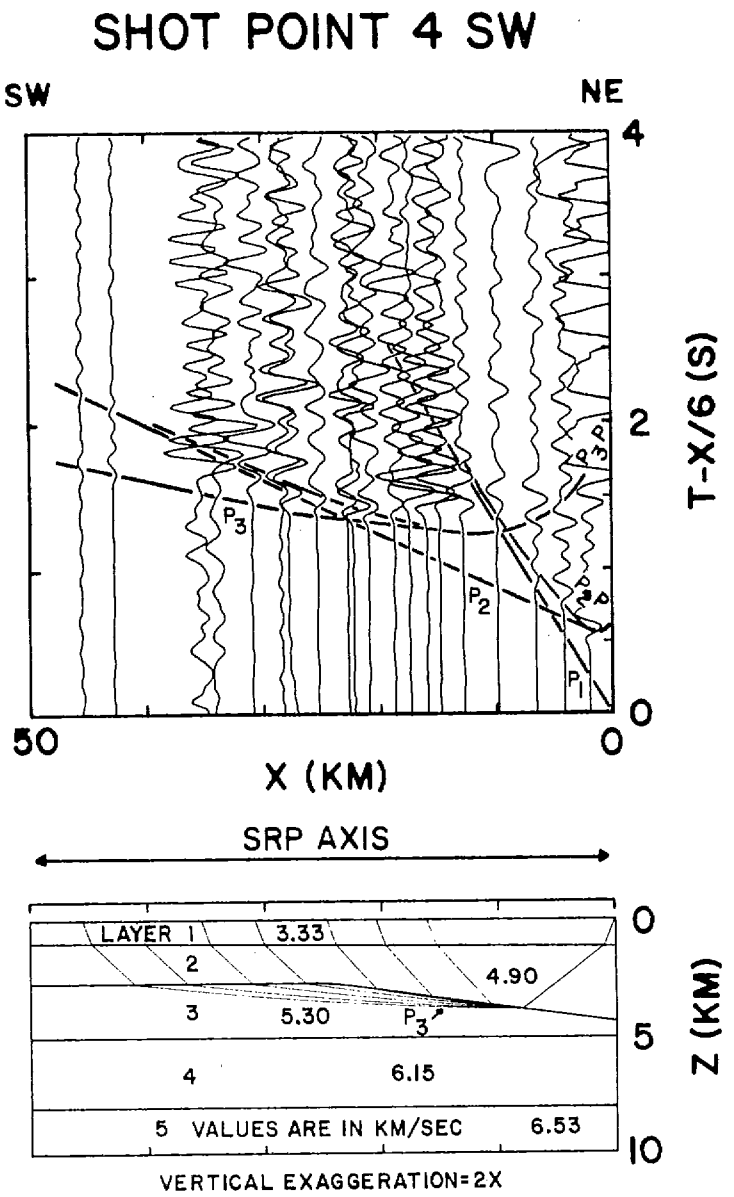
SHOT POINT 4 SW
SW
NE
4
2
0
T-X/6 (S)
50
0
X (KM)
P3
P2
P1
SRP AXIS
LAYER 1
3.33
2
4.90
3
5.30
P3
4
6.15
5 VALUES ARE IN KM/SEC
6.53
0
5
10
Z (KM)
VERTICAL EXAGGERATION=2X

Figure 11

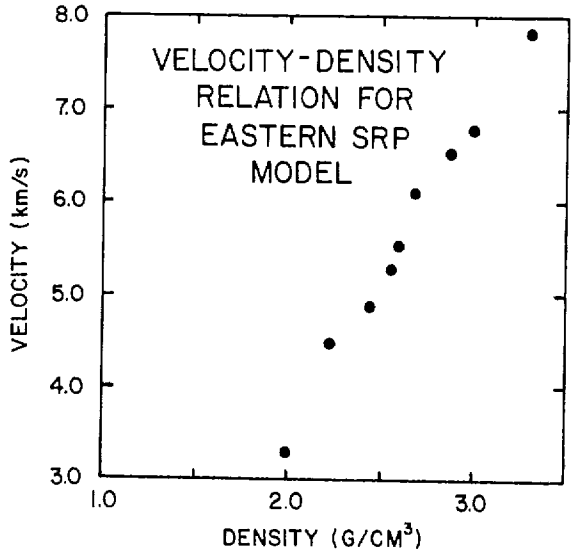
VELOCITY-DENSITY
RELATION FOR
EASTERN SRP
MODEL
VELOCITY (km/s)
8.0
7.0
6.0
5.0
4.0
3.0
1.0
2.0
3.0
DENSITY (G/CM³)

Figure 12

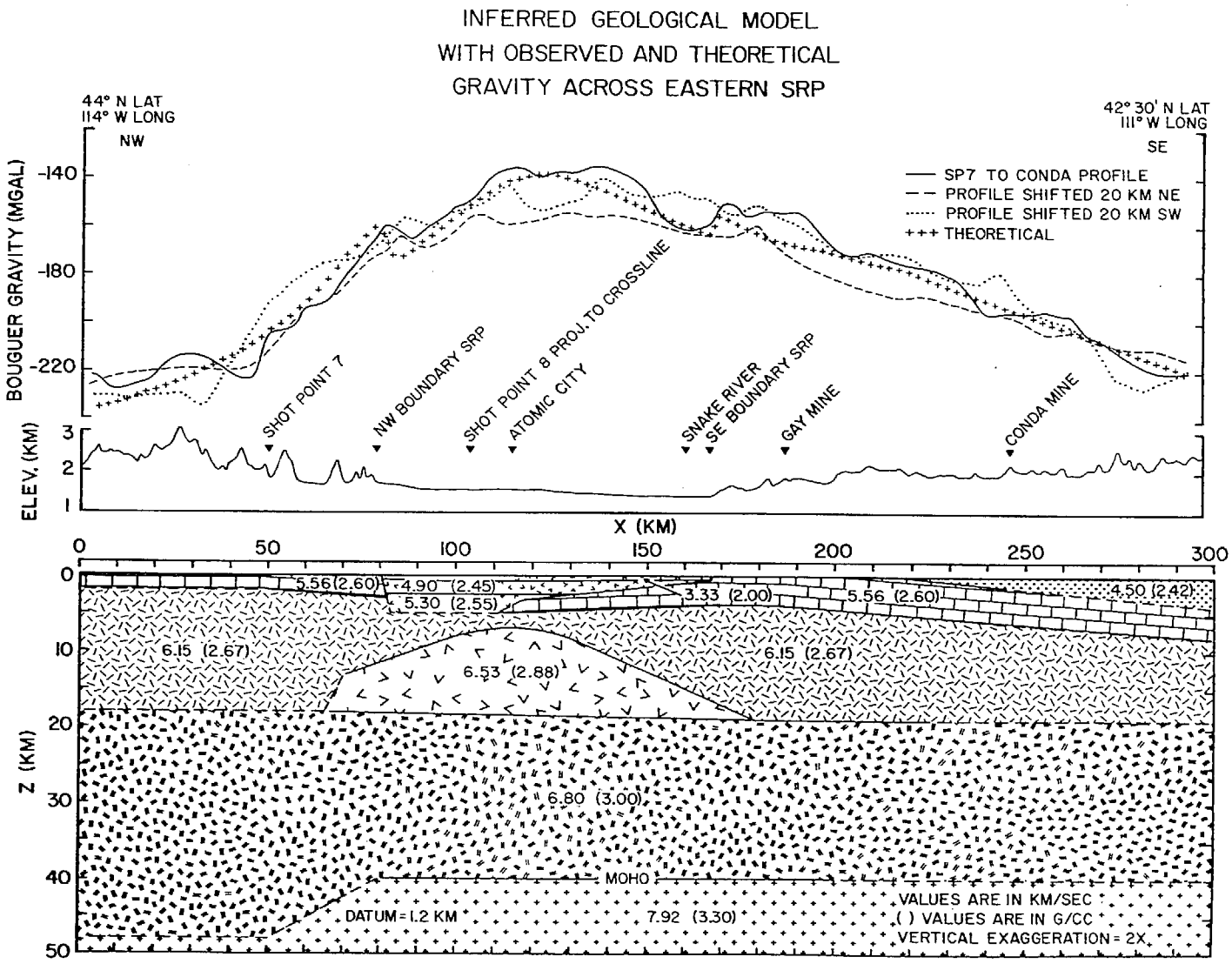
INFERRED GEOLOGICAL MODEL
WITH OBSERVED AND THEORETICAL
GRAVITY ACROSS EASTERN SRP
44° N LAT
114° W LONG
NW
42° 30' N LAT
111° W LONG
SE
SP7 TO CONDA PROFILE
PROFILE SHIFTED 20 KM NE
PROFILE SHIFTED 20 KM SW
+++ THEORETICAL
BOUGUER GRAVITY (MGAL)
-140
-180
-220
ELEV. (KM)
3
2
1
SHOT POINT 7
NW BOUNDARY SRP
SHOT POINT 8 PROJ. TO CROSSLINE
ATOMIC CITY
SNAKE RIVER
SE BOUNDARY SRP
GAY MINE
CONDA MINE
X (KM)
0
50
100
150
200
250
300
Z (KM)
0
10
20
30
40
50
5.56 (2.60)
4.90 (2.45)
5.30 (2.55)
3.33 (2.00)
5.56 (2.60)
4.50 (2.42)
6.15 (2.67)
6.53 (2.88)
6.15 (2.67)
6.80 (3.00)
MOHO
DATUM = 1.2 KM
7.92 (3.30)
VALUES ARE IN KM/SEC
( ) VALUES ARE IN G/CC
VERTICAL EXAGGERATION = 2X

Figure 13

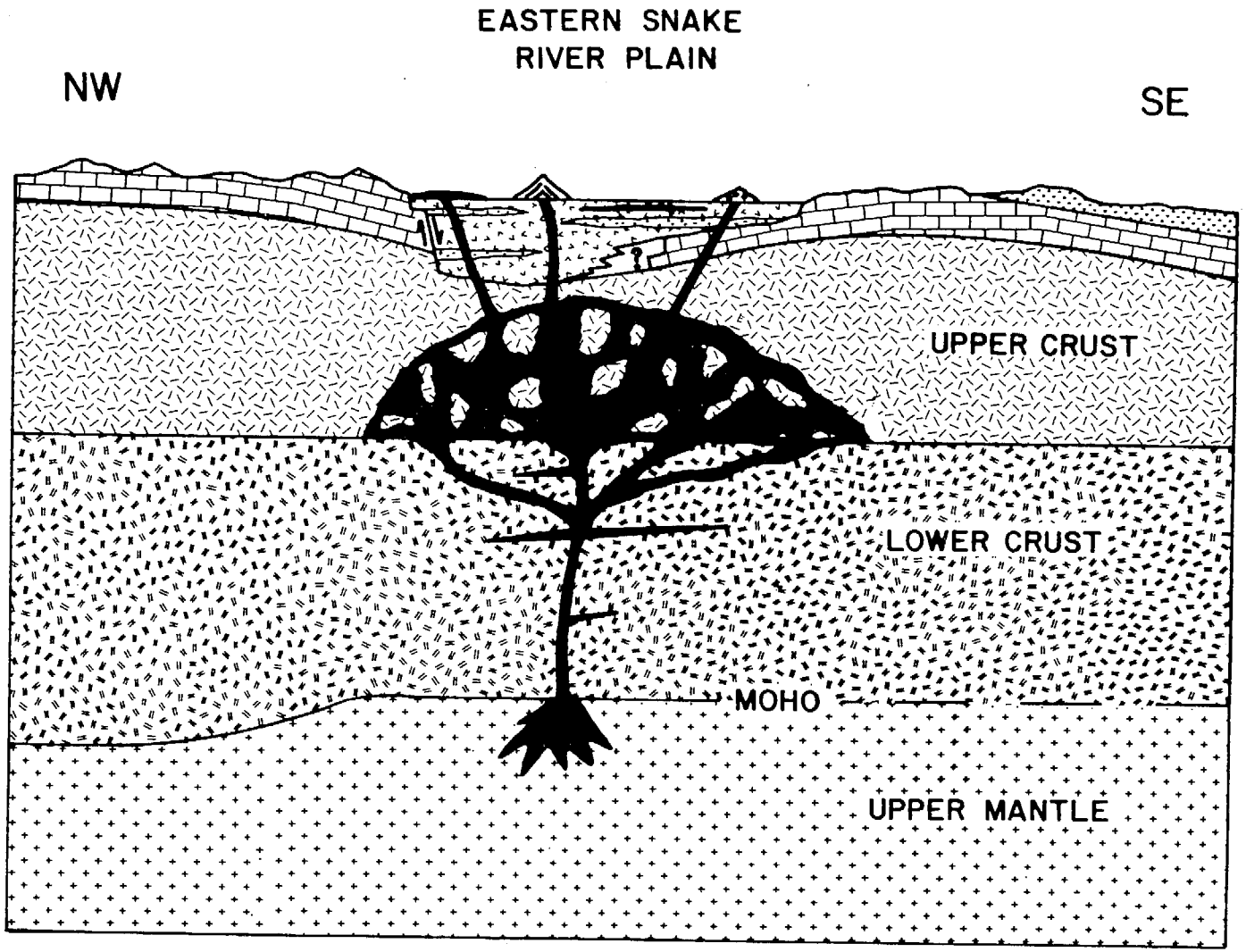
EASTERN SNAKE
RIVER PLAIN
NW
SE
UPPER CRUST
LOWER CRUST
MOHO
UPPER MANTLE

Figure 14

THE 1978 YELLOWSTONE-EASTERN SNAKE RIVER PLAIN SEISMIC PROFILING EXPERIMENT: DATA AND DETAILED CRUSTAL STRUCTURE OF THE YELLOWSTONE REGION

M. M. Schilly[1] (Department of Geology and Geophysics, University of Utah, Salt Lake City, Utah 84112)

R. B. Smith (Department of Geology and Geophysics, University of Utah, Salt Lake City, Utah 84112)

J. A. Lehman[2] (Department of Geology and Geophysics, University of Utah, Salt Lake City, Utah 84112)

L. W. Braile (Department of Geosciences, Purdue University, West Lafayette, Indiana 47907)

J. Ansorge (Geophysics Institute, Swiss Federal Institute of Technology, CH-8093, Zurich, Switzerland)

[1]Now at the Amoco Prod. Co., Security Life Bldg., Denver, Colorado 80202
[2]Now at ARCO Oil Co., Anchorage, Alaska 99504

ABSTRACT

Eleven in-line seismic profiles and one azimuthal fan plot were constructed from data recorded within the Yellowstone National Park area during the 1978 Yellowstone-Snake River Plain seismic experiment. Interpretations of these data suggest that the regional Yellowstone velocity model is characterized by: (1) an averaged 10 km "granitic" layer, V_p ~6.0 km/s; (2) a 30 km thick lower crustal layer, V_p ~6.8 km/s; (3) a total crustal thickness of 44 km; and (4) an upper-mantle, Moho velocity of 7.9 to 8.0 km/s. Velocity models are presented for several profiles throughout the Yellowstone Plateau that show: (1) a decrease in the thickness of the upper-mantle "granitic" layer from 5 km at the southwest near Island Park to 1 km at the northeast side of the Yellowstone Plateau in the vicinity of exposed Precambrian granitic gneiss; (2) a decrease in depth of 4 km to 2 km to the top of the "granitic" layer south of Jackson Lake, Wyoming; and (3) an upper-crustal low-velocity body with a velocity decrease of at least 10% that coincides with a 30 mgal residual gravity anomaly located in the northeast corner of the Yellowstone Plateau. This low-velocity zone is coincident with the location of the Hot Springs Basin, the largest hydrothermal system in Yellowstone. The low-velocity body appears to have a maximum depth to the top of 3 km and a minimum depth of 9 km to the bottom. Based on interpretations of well developed P* refracted branches and P_mP reflection from the Moho, the lower crust beneath Yellowstone is a homogeneous, 30 km thick layer, V_p = 6.8 km/s, that shows little evidence of travel-time delays or lateral heterogenieties. Thus the Yellowstone crustal section consists of a laterally

inhomogeneous upper-crust underlain by a homogeneous lower-crustal layer that is continuous with the same unit as mapped beneath the eastern Snake River Plain. This generalized velocity model is consistent with a hypothesis that suggests that the source of the high heat flow at Yellowstone is produced by basaltic magma derived from the upper-mantle that apparently migrates through the lower crust without significant metamorphic reactions, to the upper crust where partial differentiation and convective mixing produce the bimodal rhyolite-basaltic melts that are then extruded to the surface.

INTRODUCTION

In recent years, Yellowstone National Park has been the subject of several geologic and geophysical investigations that were designed to understand the origin and properties of this large hydrothermal system. These studies indicated that Yellowstone has been subjected to intense silicic volcanism beginning 2.2 million years ago and that may have only temporarily ended as recently as 150,000 to 70,000 years ago (Christiansen, 1978, personal communication; Smith and Christiansen, 1980). Widespread hydrothermal activity (Fournier et al., 1976) and high heat flow (Morgan et al., 1977) argue for the presence of shallow crustal heat sources that until at least 70,000 years ago may have been in the form of magma or partial melts within the crust. High rates of crustal uplift, as large as 14 mm/yr (Pelton and Smith, 1979, 1981), and intense seismicity (Trimble and Smith, 1975; Smith et al., 1977) support the view that Yellowstone is still tectonically active. In a regional framework bimodal rhyolite/basaltic volcanism along the eastern Snake River Plain, to the southwest, has shown a progression of silicic centers at $\sim$3.5 cm/yr (Armstrong et al., 1975) along the Snake River Plain to it's present location at Yellowstone and suggests that Yellowstone's volcanism and hydrothermal features are closely related to the propagating silicic volcanic centers.

Recognizing the important relationship between Yellowstone and the eastern Snake River Plain (Y-SRP, 1978), a large-scale seismic refraction, wide-angle reflection experiment was conduced in this area in September, 1978 by a U.S.-European cooperative research group (described by

Smith et al., 1981; Braile et al., 1981, this vol.). The primary objective of this experiment was to determine the lithospheric velocity structure of this continental volcanic province.

This paper will focus on the data and detailed P-wave velocity models of the Yellowstone region. The discussion compliments the papers by Smith et al. (1981) that focuses on the experiment design and generalized crustal structure of Yellowstone and by Lehman et al. (1981) that describes the lateral velocity structure of the upper-crust in Yellowstone using delay-time analysis.

DATA PRESENTATION AND ANALYSIS

Figure 1 shows the major tectonic features of the Yellowstone National Park area and the locations of the more than 150 recording sites and shotpoints, nos. 1, 6, G9, and 2A2B, used in this analysis. The details of field recording and compilation of the data are documented in Schilly (1979) and Smith et al. (1981). Individual seismograms recorded from the four sources were plotted into eleven azimuthically-corrected, straight-line profiles. Figure 2 shows the shot and station locations and configuration of ten of the profiles. The eleventh profile, G9S, was recorded on a N-S line south of the Park and its location can be inferred from the shotpoint reference map in Smith et al (1981). Note that the title of each profile refers to the source point and direction of the profile. The pertinent profile information is tabulated in Table 1.

Record sections for the eleven profiles (shown in Figures 3a through 3k) are presented in an unfiltered form to emphasize high-frequency arrivals. To facilitate phase correlations the seismograms for the same profiles were bandpass filtered from 3.1 hz to 10.9 hz but are not shown here. All data were elevation corrected and migrated to a datum plane of 2,200 m above sea level (Schilly, 1979). Trace amplitudes have been scaled by a constant that was calculated by determining the range between the largest and smallest signal. Instrument and station numbers are listed above the seismic section for reference to Figure 2.

From the Yellowstone profiles, first and later refracted arrivals and wide-angle reflections were correlated across the sections to provide the apparent velocities and intercept times. Several distinct P-wave

branches were observed and classified according to the notation discussed in Smith et al. (1981, Figure 3).

Time picks for first-arrivals were made to ±0.005 s (in the best cases) with a repeatability of ±0.01 s. Timing errors due to imprecision in determining location coordinates were estimated to be no greater than ±0.02 s (Schilly, 1979).

Once the phase identifications and time picks were made, reverse and cross-profiles were compared to check similarities in phases, arrival times, apparent velocities, and reciprocity. For this initial phase of the interpretation, linear least-squares fits of the first arrivals were made assuming an averaged flat-lying velocity structure. The interpreted phases are labelled on the profiles and are drawn with a solid line when observed and a dashed line where inferred. Table 2 lists the interpreted phases, apparent velocities, and intercept times for each of the refracted branches drawn on the profiles. In addition, Table 2 lists, the number of picks (N), the mean (μ), and the standard deviation (σ) of the observed phase arrival-time minus the theoretical time (calculated using the interpreted apparent velocity and intercept time). Using these slopes and intercept times, layer thicknesses (Z) were calculated assuming horizontal, homogeneous layers. For a phase that had delayed branches (e.g. P_2, P_2', P_2''), the preferred velocity and calculated thicknesses are noted. These preferences were based on the consistency of the interpretation with other profiles (i.e.- reversed and cross-profiles) and with local geology (surface variations may cause a branch to be time-shifted and the branch is not representative of the velocity structure at depth).

There is some evidence for dipping layers, so that the horizontal

layer-assumption was not always correct. For example on profile 1SW (Figure 3b) the calculated thicknesses and apparent velocities suggest dips of 2° on the P_2, P*, and P_n refracting horizons. Because these dips are so small, in relation to the total length of the profile, the calculated thicknesses serve as a good approximation to the dip within the error of the data. However profiles G9N and G9S (Figure 3f, 3g) show evidence for a dip up to 3.6° on the interface between the first and second layers and a corrected thickness of the first layer is 1.04 km. This information is included in the velocity model for this layer but is not shown in Table 2. It was not possible to make any other calculations of dip and true thicknesses for profiles G9N and G9S because the data were insufficient for a more complete reversed interpretation.

UPPER-CRUSTAL INTERPRETATION

The upper-crustal structure of Yellowstone was based upon interpretation of shallow phases: P_0, P_1, P_2 (P_g) recorded from both single and reversed profiles at various azimuths. However because of high ambient noise, high attenuation, low Q's of 30-300 (Smith et al. 1981), and cultural noise these data were not as detailed and for most profiles were only recorded to maximum distances of ~80 km. Also for the shorter profiles it was not always possible to obtain a thickness for the upper-crustal "granite" layer because the deeper P*-phases from the bottom of the layer were not always observed.

Four velocity models corresponding to different locations are presented for the Yellowstone area (Figure 4, 5, 6, 7). Figure 4 represents the model for the northeast portion of the regional Y-SRP refraction line that was recorded in parts from shotpoint 2 in Island Park to Red Lodge, Montana. A N-S averaged model including the area south of Yellowstone in the Jackson Lake-Teton area (Figure 5) is based upon reversed profiles 6S-G9N (Figure 3e, 3f). Figure 6 shows the model for a SSW-NNE line across the Yellowstone Plateau from reversed profiles 1SSW and G9NNE (Figure 3c, 3d), including the northeastern part of the Yellowstone caldera; and Figure 7 represents the model for reversed profiles 1W-6E (Figure 3i, 3h) in the northern part of Yellowstone including Paleozoic and Precambrian outcrops outside the caldera. These models also take into account dip on the P_1-interface observed on profiles from shotpoint G9 and include results from cross-lines (e.g. 2A2BNE-1SW) and unreversed profiles 6SE (Figure 3k) and 2A2BENE (Figure 3j). In these models a

velocity interface determined from a reversed profile is shown as a solid line and an interface from an unreversed or ambiguous phase is shown as a dashed line.

From these models an important characteristic of the Yellowstone area was the recording of a well-developed phase P_2 (P_g) from the crystalline upper-crustal "granitic" layer that averaged 10 km thick. Although it was not possible to calculate the thickness for this layer from each profile (because the next deeper ray, P* was not always observed) it is reasonable to assume that this thickness is fairly uniform in the caldera because all the P_2 curves have similar intercept times and/or crossover distances.

However, the near-surface layer above the "granitic" layer shows a wide variation in velocity and thickness, varying from 2 km to 5 km. In general, the first layer, represented by the P_0 phase, has an average velocity of 3.0 km/sec to 3.8 km/sec. This layer is interpreted to be associated with alluvium, weathered volcanics, caldera fill, lake sediments, and landslide debris. However in the northern part of Yellowstone, a 0.5 km thick layer with a much higher velocity of 4.8 km/sec suggests that it is representative of consolidated sediments at shotpoint 1. The velocity of the P_1 layer also varies laterally within Yellowstone from 4.6 km/sec to 5.5 km/sec. Velocities of 4.6 km/sec to 5.0 km/sec were attributed to Yellowstone Plateau volcanics (rhyolites and ash flow tuffs) and are confirmed by the surface geology. The velocity of 5.5 km/sec for P_1 at shotpoint 1 is thought to be representative of the Paleozoic sedimentary rocks and underlying weathered granitic

gneiss that outcrop near the shotpoint. Thus, the first two layers represented by P_0 and P_1 are variable in thickness and velocity throughout Yellowstone, but seem to be thinnest and have the highest velocities in northeastern Yellowstone National Park near shotpoint 1 near exposed Precambrian granitic gneiss.

One of the most interesting features of the Yellowstone data is the evidence for lateral velocity variations in the upper-crustal crystalline layer. For example on profiles 1SW, 1SSW, and 1W from 18 to 32 km (Figure 3b, 3c, and 3i), P_2 is seen as an early arrival relative to other profiles. On these profiles there is also a later branch, P_2', that is more representative of the P_2 branch seen elsewhere in Yellowstone. The P_2 branch observed in profiles from shotpoint 1 can be attributed to the near-surface Precambrian granitic gneiss that outcrops near station 505, but become deeper 30 km to the west and southwest of shotpoint 1. In addition, the P_0 and P_1 branches have much higher velocities than those observed on other profiles in Yellowstone. Thus, the effect on the data is to produce two P_2 branches; the short-distance P_2 curve is representative of the high velocity Precambrian and Paleozoic rocks immediately around shot 1 while the later P_2' curve is more characteristic of the Yellowstone Plateau.

Another lateral velocity variation can be seen on profile G9S (Figure 3g) south of Yellowstone where a "normal" P_2 phase (relative to other P_2 curves in Yellowstone) is replaced by a much earlier P_2 phase (P_2') which has the same apparent velocity. This change occurs at the south end of Jackson Lake and is most likely due to a shallow block of Precambrian crystalline crust that results in a decrease in the depth to the P_2 refractor.

Delays of up to 0.3 seconds were noted on the P_2 branches recorded in both directions from shots 2A and 2B in Island Park; for example the arrivals at 12 km on 2A2BNE (Figure 3j). These delays are recorded by stations outside the caldera rim and may be a direct result of crossing the boundary between inner- and outer-caldera structure. An alternative interpretation is that the delay may be due to a low-velocity layer.

The largest lateral velocity variation seen in the Yellowstone data was observed on profile 1SSW (Figure 3c). This profile shows three distinct P_2 branches labeled P_2, P_2', and P_2''. As discussed earlier, P_2' is interpreted as the "normal" curve with P_2 representing the propogation of waves through near-surface Precambrian rocks. P_2'', however, is substantially delayed up to 1.5 seconds relative to P_2 and its cause is not obvious from the surface geology. In addition, similar delays were noted for stations 411 and 412 on the profile 1SW (Figure 3b) relative to the P_2' curve for profile 1SW.

In order to investigate this further, a filtered fan profile was constructed (Figure 8). For this profile, seismograms were plotted by azimuth rather than by distance. Stations within a distance range of 50 km to 82 km and an azimuth range of 180° to 270° were selected for display. These stations were reduced using the travel-time equation for the P_2' curve for profile 1SSW, $T_r = X/5.95 + 0.7$, that was interpreted as "representative" of the region. If the structure was laterally homogeneous, the first arrivals for each of the seismograms on the fan plot would occur on the reduced time line, $T_r = 0.7$. From Figure 8, several observations can be made. The first is that in the range of 232° to 265°, the first arrivals are consistently 0.2 seconds earlier than the

T_r = 0.7 line, implying that the reducing velocity (V = 5.95 km/sec) is correct but that a more reasonable intercept time would be 0.5 seconds. Arrivals from stations from 180° and 195° are about 0.3 to 0.4 seconds early and by the same argument a more reasonable intercept time would be 0.4 seconds. A possible explanation for the arrivals that were observed earlier, from 180° to 195° when compared to those from 232° to 265°, is that the rays returning to the surface at stations immediately south of shotpoint 1 have traveled through higher velocity Paleozoic rocks than the rays returning to the surface at stations southwest and west of the shotpoint. The latter raypaths have traveled upward through lower velocity caldera infill and volcanic rocks. An alternative interpretation is that the depth to the 5.95 km/sec layer may be less to the south of shotpoint 1 than to the west.

The most important features of the fan plot are the large first-arrival delays, up to 1.5 seconds, relative to the zero line in the azimuth range of 209° to 227°. The first few cycles of the delayed waveforms appear to be of lower frequency and attenuated when compared to adjacent traces. Based on this evidence all the other profiles were examined but no delays of similar magnitude were detected. Profile G9NNE (Figure 3d), from 80 km to 120 km, shows attenuated signals and a possible delay. However, the attenuation may be due to the high ambient noise levels at the recording sites. Profile 6SE (Figure 3k) shows little evidence of the delays as seen on Profile 1SSW but there is a definite change in the character for the first few cycles of the seismogram recorded at station 433. Finally, profile 2A2BNE was examined in the range of 110 km to 200 km but no delays were noted.

The large delays seen on the fan plot (Figure 8) are interpreted to be due to lateral variations of velocity in the upper-crust. The lateral variation may be due to down-faulting of the 5.95 km/sec layer or a low-velocity zone. If it is produced by a fault, the 5.95 km/sec layer would have to drop more than 8 km to account for the large delays which is unrealistic geologically. However, if this were the only effect, the P_2'' branch would not be seen as a first arrival because there is a shorter time path nearer the surface. Thus, a low-velocity zone, possibly coincident with a zone of high attenuation, is required to explain the magnitude and character of the observed delays. If the effect is attributed to a LVZ at 5 km (depth based on calculation of thicknesses for the first two layers of 1SSW), then a 10% decrease in velocity to 5.3 km/sec requires a body of minimum dimensions 30 km in a northeast-southwest direction; a 20% decrease to 4.8 km/sec requires a body 20 km long, and a 30% decrease to 4.2 km/sec requires a body 10 km long.

The lateral extent of the anomalous velocity body is shown in Figure 9 but could be located anywhere within the outlined zone depending on the velocity contrast. More information than is available here is required to accurately outline the low velocity zone. However from this interpretation the body is centered at least 5 km beneath the surface and must extend to at least 3 km beneath the surface or the rays would travel over the body without receiving a delay. Also the body must extend to at least 9 km below the surface or the rays would propagate undisturbed beneath it. Since profile 2A2BNE shows no delays on the P*' branch that passes directly beneath the body it apparently does not extend to the depths of the lower crust. In a companion paper by Lehman et al., 1981,

this low velocity distribution is examined in detail using time-term analyses and gravity data. Their findings corroborate this interpretation but place constraints on the size and velocity of this anomalous body.

LOWER-CRUSTAL INTERPRETATION

Interpretation of the lower-crustal structure for the Yellowstone region was based upon the analyses of well recorded branches of the mid-crustal refractor, P*, and from wide-angle reflections from the Moho, P_mP. In addition travel-times of P* phases were used to limit the depth to the bottom of the upper-crustal, P_g-layer, and to provide an interpretation of the lateral-variation of the lower crust. Using corrections for the configuration and velocities of the laterally-variable upper-crustal P_g-velocity structure (Lehman et al., 1981) depths to the top of the P*-layer were then computed for the Yellowstone region based upon the intercept times given in Table 2. Depths to the top of the P* refractor ranged from 16 km to 19 km throughout the region and averaged 16.5 km beneath the Yellowstone caldera. The migrated locations of the refraction sub-surface coverage and corresponding depths of the layer are shown in Figure 10 with the apparent P*-velocities.

Comparison of the P*-branches (e.g. Profiles 2A2BNE, 1SW, etc.) showed remarkable similarities in intercept time and waveform except where the lateral variations in the upper-crust (Lehman et al., 1981) introduced delay times that were corrected for. For example, on profile 1SSW (Figure 3c) a 0.55 sec offset is indicated at 100 km that was accounted for by an overlying low-velocity 5.7 km/s upper-crustal layer (Lehman et al., 1981) that extends to the top of the P*-layer beneath the caldera.

A map of the migrated P* refracting paths (Figure 10) shows that raypaths for profile 1SSW between West Thumb and Pitchstone Plateau

are located well within the Yellowstone caldera. This raypath geometry provides evidence that the P*-velocity of 6.8 km/s for the caldera is the same as that observed outside the caldera including the surrounding region of Island Park, the Beartooth Mountains, and the Grand Teton area. The consistency of the 6.8 km/s velocity implies a seismically homogeneous lower-crust; perhaps different from that expected on the basis of the widespread occurrence of major hydrothermal systems and the complex volcanic-tectonic features of the Yellowstone region.

Further evidence for a homogeneous lower-crust is from P*-branches recorded along the eastern Snake River Plain for raypaths that pass beneath Yellowstone for shotpoints 1 and 6. Ten stations were located along the eastern Snake River Plain, southwest of the Island Park area, that recorded data from shotpoints 1 and 6 at distances of 170 km to 300 km. Seismic traces from both shots were plotted on the same profile for comparison (Figure 11) with overlap between 220 km and 240 km. To preserve the raypath reciprocity no elevation corrections are made and each trace was filtered between 3.1 and 10.9 Hz to enhance P* arrivals. While a distinct cross-over distance between the P* and the P_n branches is not obvious, it is clear that rays passing through the lower-crust beneath the Yellowstone caldera from shotpoint 1 have almost identical travel-times and waveforms as those that propagated to the northwest of the caldera from shotpoint 6, suggesting little lateral variation along their raypaths.

A depth of 19 km to the P*-refractor northeast and south of the Yellowstone caldera corresponds to depths of the same mid-crustal refractor determined from areas outside the Yellowstone and eastern Snake River

Plain. Prodehl (1970) calculated a depth to the P*-layer of 20 km from a line located about 220 km southwest of Yellowstone between American Falls, Idaho and Flaming Gorge, Utah. In southern Montana, 70 km north of Yellowstone, McCamy and Meyer (1964) calculated a depth of 20 km to the top of the P*-layer. Furthermore, data recorded along the east side of the Teton Range, just 50 km south of Yellowstone, from our shot-point 2A2B showed no evidence of the P*-branch at distances up to 105 km, the maximum recording range. Assuming a P*-velocity of 6.8 km/s for a minimum crossover distance of 105 km implies a depth to the P*-layer of at least 18.9 km for the Teton area. Therefore the lower-crust of the eastern Snake River Plain-Yellowstone system appears to be characterized by a homogeneous 6.8 km/s, P*-layer, with an average depth to the top of the layer of 16.5 km beneath the Yellowstone caldera, somewhat shallower than in areas outside the thermally disturbed region.

Additional evidence for the homogeniety of the lower-crust is from the character of the Moho reflector, P_mP, that appears to be produced by a sharp discontinuity between the 6.8 km/s lower-crustal layer and the 7.8-7.9 km/s upper-mantle layer beneath the Yellowstone-Snake River Plain region (Smith et al., 1981; Braile et al., 1981). Figure 12 shows the location of the migrated reflecting points of the observed P_mP branches on profiles 2A2BSW (shown in Braile et al., 1981) from the eastern Snake River Plain and 2A2BNE (Figure 3a) from the Yellowstone area. These reflectors have nearly identical travel-times suggesting little variation in the average crustal velocity beneath the Yellowstone caldera relative to the eastern Snake River Plain.

These data thus demonstrate that the lower crust of the Yellowstone Plateau, the Island Park area, and the nearby eastern Snake River Plain

appear to have a relatively shallow, 6.8 km/s, lower-crustal layer at a depth of 16 km to 17 km, about 5 km shallower than the surrounding thermally undisturbed region. The homogeneous nature of the lower-crust, at spatial scales resolved by the seismic frequencies of 3 hz to 15 hz, suggests that the thermal perturbations implied by the presence of the Quaternary volcanism and the high heat flow at Yellowstone have either uniformally perturbed the lower-crust or have left it undisturbed compared to the upper-crust.

CONCLUSIONS

The crustal structure of the Yellowstone Plateau and surrounding areas to the northeast, the crystalline Beartooth Mountains; and to the south, the block-faulted Teton region has been derived from eleven in-line seismic profiles and one fan profile recorded in the 1978 Yellowstone-Snake River Plain seismic experiment. The interpretation of these data leads to several important conclusions. The first is that the regional velocity structure of Yellowstone is similar to that of the eastern Snake River Plain (compare with Braile et al., 1981), i.e. a crustal thickness of 44 km characterizes the entire eastern Snake River Plain, Island Park, and Yellowstone region (also see Smith et al., 1981). However differences in the crustal structure between Yellowstone and the eastern Snake River Plain include evidence for large lateral velocity variations in the upper-crust not seen in longitudinal sections along the eastern Snake River Plain.

Lack of detailed data at distances greater than 80 km on several of the Yellowstone profiles precluded the delineation of a complete crustal velocity model for the entire area. However, several velocity models for both upper- and lower-crustal layering have been determined. The large lateral velocity variations in the upper-crust of Yellowstone suggest direct evidence for compositional and structural variations beneath the Yellowstone hydrothermal system consisting of: (1) a decrease in depth from SW to NE across Yellowstone to the top of the "granitic" layer from 5 km to 1 km; (2) a decrease in depth to the top of the "granitic" layer from 4 km to 2 km south of Jackson Lake, and (3) a major low-velocity body with a decrease of at least 10%, coincident

with a 30 mgal gravity anomaly in the northeast part of the Yellowstone Plateau, with a maximum depth to the top of the body of 3 km and a minimum depth of 9 km to the bottom.

The significance of the upper-crustal low velocity body is shown in Figure 9; the length of the body is 30 km from NE to SW for a 10% decrease in velocity. Blank and Gettings (1974) showed a gravity residual anomaly of 30 mgal that coincides in part with the outline of the anomalous low-velocity body (see Figure 9, complete Bouguer gravity contours modified from Blank and Gettings, 1974). Thus, this area exhibits not only a decrease in P-wave velocity of at least 10% but also a decrease in density. In addition, the area above the low velocity body coincides with the Hot Springs basin; the largest hydrothermal system in Yellowstone and suggests the correlation of the anomalous body with a zone of very high heat flow. Thus the high heat flow, a mass deficiency, at least a 10% decrease in velocity, and the spatial correlation of Yellowstone's Quaternary volcanic activity suggests that the low-velocity anomaly in the northeast Yellowstone Plateau may represent a molten or partially molten body.

Eaton et al. (1975) modeled the gravity anomaly in this part of Yellowstone by a density contrast of up to 0.5 gm/cm^3 produced by a rhyolitic magma. Murase and McBirney (1973) showed that up to a 0.1 gm/cm^3 difference in density can be produced by complete melting of igneous rocks with a corresponding decrease in velocity of up to 60%. Thus, only part of the gravity anomaly may be attributed to a molten material. The remainder can be explained as due to the compositional contrast between rhyolite (2.3 gm/cm^3) and the surrounding country rock (2.7 gm/cm^3). If this model is correct, then time delays representing velocity

decreases of up to 60% can be hypothesized due to the molten material (not including pressure and pore fluid effects). Additional velocity variations can be expected if the change is also compositional. A detailed evaluation by Lehman et al. (1981, this vol.) of time-term delays from the 1978 Yellowstone seismic data have shown a smaller but better defined velocity reduction of 40%.

The lower crustal structure of the Yellowstone region shows spatial homogeneity between the eastern Snake River Plain and the Yellowstone Plateau as demonstrated by the continuous refracted phase from the lower crust, P*, that showed no significant delays. The average velocity of the lower crust is 6.8 km/s and has an average depth to the top of 16.5 km beneath the Yellowstone Plateau. Additional evidence for homogeniety of the lower crust is from the continuity and equivalent travel times for the Moho reflector, P_mP, for ray paths that pass beneath the Yellowstone caldera from shotpoints to the northeast, shotpoint 1, and for ray paths from a shotpoint external to the Yellowstone caldera, shotpoint 6, that were recorded along the eastern Snake River Plain. These data showed identical travel times for the wide-angle reflections and thus provide evidence for the continuity of the lower crust. There is a suggestion that the top of the 6.8 km/s layer is about 5 km shallower beneath the volcanic system than the surrounding undisturbed Archean crust of the Rocky Mountains. But in general the interpretation of the homogeneous nature of the thick lower crustal layer suggests that the thermal perturbations that have produced the large lateral-velocity variations in the upper crust have had minor effects at depths greater than 16 km. This argues that the high heat flow of the Yellowstone hydrothermal

system apparently is derived from the upper mantle and has either uniformily perturbed and thickened the lower crust or has left the lower crust undisturbed by rather rapid passage of basaltic magma into the upper-crust.

Recent work by Iyer (1975), Iyer and Stewart (1976), and Zandt (1978) suggests a large velocity decrease of up to 15% in the upper-crust and up to 5% at mantle depth's of up to 250 km based on teleseismic P-wave delays. None of the Yellowstone profiles, except for possibly the P* and P*' branches on 2A2BNE, show any significant evidence for these large teleseismic delays. On profile 2A2BNE the delay between the P* and P*' branches of 0.4 seconds is much less than the teleseismic delay of up to 1.5 seconds noted by Iyer (1975). However the character of the P_mP reflections on profile 2A2BNE is different from those on profile 2SW (Braile et al., 1981) even though both data sets originated from the same shotpoint. The multiple P_mP-waveform on profile 2A2BNE imply that the Moho boundary may not be as distinct beneath Yellowstone as it is beneath the eastern Snake River Plain. The multiple cycles may represent layering at the Moho similar to that modeled by Meissner (1973). This layering may reflect zones of partial melting at the Moho and would add support to Iyer and Stewart's (1978) hypothesis of partial melting in the upper-mantle that they use to explain the observed teleseismic delays. In any case, the absence of definitive data on major P-wave delays in the crust do not imply that the reported teleseismic delays are not absent but rather that the delays are produced by a deeper, upper-mantle low-velocity zone.

ACKNOWLEDGMENTS

The Yellowstone portion of the 1978 Yellowstone-Snake River Plain seismic experiment was a major component of a U.S.-European cooperative project that brought together many individuals, universities, and research organizations. An extended list of participants and supporting personnel is listed in the accompanying paper by Smith et al. (1981). In addition, several individuals deserve an additional acknowledgment for their valuable suggestions, help in data compilation and in review of the interpretations. These include: George Zandt, Debbie Wechsler, Mark Baker, Kevin Furlong, Tom Owens, Steve Clawson, and Nicholas Diechmann. We also acknowledge the excellent cooperation of the National Park Service, Yellowstone National Park; John Townsley-Superintendent, Jerry Phillips, Alan Mebane, Mary Meagher, and Rick Hutchinson. The Microgeophysics Corporation of Golden, Colorado provided shotpoint operations and explosives management and we are indeed grateful to Roger Bowman, David Butler, Roger Grette, and Andy Staatz for their services. J. H. Healy, David P. Hill, Mitch Pitt and Craig Weaver of the U.S. Geological Survey kindly provided a major compliment of instruments and personnel that assisted in the Yellowstone recording and of data from their permanent seismograph network. Funding for this research was provided by the National Science Foundation grant #EAR-77-23707 and from the Geothermal Research Program of the U.S. Geological Survey grant no. 14-08-0001-6674.

REFERENCES

Armstrong, R. L., W. P. Leeman, and H. E. Malde, K-AR dating, Quaternary and Neogene volcanic rocks in the Snake River Plain, Idaho, Am. J. of Science, 275, 225-251, 1975.

Blank, H. R., Jr. and Gettings, M. E., Complete Bouguer Gravity Map: Yellowstone-Island Park Region, U.S. Geological Survey Open-file Map 74-22, 1974.

Braile, L. W., R. B. Smith, J. Ansorge, M. R. Baker, M. A. Sparlin, C. Prodehl, M. M. Schilly, J. H. Healy, St. Mueller, and K. H. Olsen, The Yellowstone-Snake River Plain seismic profiling experiment: Crustal structure of the eastern Snake River Plain, J. Geophys. Res., 1981, (this volume).

Eaton, G. P., R. L. Christiansen, H. M. Iyer, A. M. Pitt, D. R. Mabey, H. R. Blank, Jr., I. Zietz, and M. E. Gettings, Magma beneath Yellowstone National Park, Science, 188, 787-796, 1975.

Fournier, R. O., D. E. White, and A. H. Truesdell, Convective heat flow in Yellowstone National Park, in Proceedings of the Second U.N. Symposium on Development and Use of Geothermal Resources, I, 731-739, U.S. Government Printing Office, Washington, D. C., 1976.

Iyer, H. M., Anomalous delays of teleseismic P-waves in Yellowstone National Park, Nature, 253, 425-427, 1975.

Iyer, H. M. and R. M. Stewart, Teleseismic technique to locate magma in the crust and upper mantle, paper presented at the Chapman Conference on Partial Melting in the Upper Mantle, Brookings, Oregon, 1976.

Lehman, J. A., R. B. Smith, M. M. Schilly, and L. W. Braile, Upper-crustal structure of Yellowstone from seismic and gravity observations, J. Geophys. Res., 1981, (this vol.).

McCamy, K., and R. P. Meyer, A correlation method of apparent velocity measurements, J. Geophys. Res., 69, 691-699, 1964.

Meissner, R., The "Moho" as a transition zone, Geophys. Survey, s, 1, 195-216, 1973.

Morgan, P., D. D. Blackwell, R. E. Spafford, and R. B. Smith, Heat flow measurements in Yellowstone Lake and thermal structure of the Yellowstone caldera, J. Geophys. Res., 82, 3710-3732, 1977.

Murase, T., and A. R. McBirney, Properties of some common igneous rocks and their melts at high temperatures, Geol. Soc. Am. Bull., 84, 3563-3592, 1973.

Pelton, J. R. and R. B. Smith, Recent crustal uplift in Yellowstone National Park, Science, 206, 1179-1182, 1979.

Pelton, J. R. and R. B. Smith, Contemporary vertical surface displacements in Yellowstone National Park, J. Geophys. Res., 1981, (this vol.).

Prodehl, C., Seismic refraction study of crustal structure in the western United States, Geol. Soc. Am. Bull., 81, 2629-2646, 1970.

Schilly, M. M., Interpretation of crustal seismic refraction and reflection profiles from Yellowstone and the eastern Snake River Plain, M.S. thesis, Univ. of Utah, Salt Lake City, Utah, 170 p.

Smith, R. B., R. T. Shuey, J. R. Pelton, and J. P. Bailey, Yellowstone hot spot: Contemporary tectonics and crustal properties from earthquake and magnetic data, J. Geophys. Res., 82, 3665-3676, 1977.

Smith, R. B. and R. L. Christiansen, Yellowstone Park as a window on the earth's interior, Sci. Am., 242, 104-117, 1980.

Smith, R. B., M. M. Schilly, L. W. Braile, J. Ansorge, M. R. Baker, C. Prodehl, J. H. Healy, St. Mueller, and R. W. Greensfelder, The 1978 Yellowstone-eastern Snake River Plain seismic profiling experiment: Crustal structure of the Yellowstone region and experiment design, J. Geophys. Res., 1981, (this vol.).

Trimble, A. B., and R. B. Smith, Seismicity and contemporary tectonics of the Hebgen Lake-Yellowstone Park region, J. Geophys. Res., 80, 733-741, 1975.

Zandt, G., Study of three-dimensional heterogeneity beneath seismic arrays in central California and Yellowstone, Wyoming, Ph.D. thesis, Massachusetts Institute of Technology, Massachusetts, 1978.

TABLE 1

Geographic Coverage of Seismic Profiles (Reversed Or Unreversed And Corresponding Figure Reference).

Profile Identification	Directional Coverage	Geographic Coverage	Figure Reference Number
2A2BNE-1SW	Reversed	Island Park - northeastern Yellowstone	3a,3b
1SSW-G9NNE	Reversed	northeastern Yellowstone - southern Yellowstone - Jackson, Wyoming	3c,3d
6S	Reversed	Mammoth - Jackson, Wyoming	3e
G9N	Reversed	southern Yellowstone - Mammoth	3f
G9S	Unreversed	southern Yellowstone - Jackson, Wyoming	3g
6E-1W	Reversed	Mammoth - Cooke City	3h,3i
2A2ENE	Unreversed	Island Park - eastern Yellowstone	3j
6SE	Unreversed	Mammoth - eastern Yellowstone	3k

TABLE 2

Observed P-Wave Branches Listing the Phase, P-Wave Velocity (km/s), T_i (intercept time in s), N (number of observations for the phase), μ (mean in s), σ (standard deviation in s), and Z (thickness in km). μ and σ are calculated for the difference of the observed arrival times minus the theoretical time.

Phase	V_p (km/s)	T_i (s)	N	μ (s)	σ (s)	Z (km)
Profile 2A2BNE						
P_0	3.00	0.00	3	-	-	1.01
P_1	4.90	0.53	4	0.02	0.04	2.53
P_2	5.70	1.10	4	-0.01	0.01	6.95, 9.04[1]
P^*	6.80	2.65	8	-0.02	0.07	
$P^{*'2}$	6.80	3.05	22	0.03	0.07	
					Total	12.58 km
Profile 1SW						
P_0	4.80	0.00	1	-	-	0.45
P_1	5.47	0.09	3	0.00	0.00	0.48. 4.57[4]
P_2	5.95	0.18	5	0.00	0.02	
$P_2'^4$	6.06	0.83	21	-0.02	0.05	9.81
P^{*5}	6.50	2.20	12	0.02	0.00	30.49
P_n^5	8.00	8.95	8	0.02	0.05	
					Total	45.32 km
Profile 6S						
P_0	3.70	0.00	1	-	-	1.24
P_2	5.70	0.51	16	-0.02	0.06	15.50
P^*	6.95	3.68	5	0.02	0.09	
					Total	16.74 km
Profile G9N						
P_0	3.80	0.00	1	-	-	0.97
P_1	5.22	0.35	6	0.00	0.05	3.86
P_2	6.05	1.15	5	0.01	0.04	
					Total	4.83 km
Profile G9S						
P_0	3.80	0.00	1	-	-	1.13
P_1	4.70	0.35	3	0.00	0.03	3.48[6], 1.05
P_2^4	6.05	1.40	4	0.00	0.02	
P_2'	6.10	0.75	6	0.00	0.02	
					Total	4.61 km

TABLE 2 (Continued)

Phase	V_p (km/s)	T_i (s)	N	μ (s)	σ (s)	Z (km)
Profile G9NNE						
P_0	3.80	0.00	1	-	-	0.97
P_1	5.22	0.35	6	0.00	0.05	3.86
P_2	6.10	1.17	9	0.00	0.01	
					Total	4.83 km
Profile 1SSW						
P_0	4.80	0.00	1	-	-	0.45
P_1	5.47	0.09	3	0.00	0.00	0.48, 4.1[7], 12.89
P_2	5.95	0.18	5	0.00	0.02	
P_2'[4]	5.95	0.70	7	0.00	0.03	13.20
P_2''	6.25	2.40	7	0.00	0.03	
P*	6.80	3.17	8	0.00	0.07	
					Total	17.75 km
Profile 6E						
P_0	3.70	0.00	1	-	-	0.23
P_1	4.60	0.07	3	0.00	0.01	2.81
P_2	6.20	0.92	7	0.01	0.04	
					Total	3.04 km
Profile 1W						
P_0	4.80	0.00	1	-	-	0.45
P_1	5.47	0.09	3	0.00	0.00	0.48, 3.32[8]
P_2	5.95	0.18	5	0.00	0.02	
P_2'[4]	5.95	0.55	6	0.00	0.03	
					Total	3.77 km
Profile 6SE						
P_0	3.70	0.00	1	-	-	1.24
P_2	5.70	0.51	12	-0.01	0.05	
					Total	1.24 km
Profile 2A2BENE						
P_0	3.00	0.00	3	-	-	1.01
P_1	4.90	0.53	4	0.03	0.04	2.53
P_2	5.70	1.10	4	-0.01	0.01	9.04
P*	6.80	3.01	6	-0.01	0.03	
					Total	12.58 km

TABLE 2 (Continued)

[1]Preferred P_2 thickness based on P*'. Total thickness is based on this calculation.
[2]Preferred P* phase.
[3]Preferred P_1 thickness based on P_2'. Subsequent thickness calculations are based on this.
[4]Preferred P_2 phase.
[5]Not all of the data for the P* and P_n phases are presented in this paper. For more information, see Schilly [n](1979).
[6]Preferred P_1 thickness based on P_2. Total thickness based on this calculation.
[7]Preferred P_1 thickness. All subsequent thickness calculations are based on this.
[8]Preferred P_1 thickness. Total thickness based on this calculation.

TABLE 3

Table of Lower Crustal P* Branch Velocities Intercept Times and Number of P* Observations for the Yellowstone Region.

Profile No.	Geographic Area	V_p (km/s)	Intercept Time T_i (sec)	Number of Observations
2A2BNE	Beartooth Plateau	6.8	3.05	22
1SW	Island Park	6.8	3.05	6
1SSW	West Thumb-southern Yellowstone	6.8	3.55	7
1SSW	southern Yellowstone-Jackson, Wyoming	6.8	3.00	6
2A2BNNE	Norris-Mammoth	6.7	2.70	4

ILLUSTRATION CAPTIONS

Figure 1 Generalized tectonic map including Yellowstone National Park showing major geologic features, locations of seismograph stations, and shotpoint locations occupied in 1978.

Figure 2 Map showing locations of stations, profiles, and shotpoint locations. Stations were projected onto in-line profiles for plotting.

Figure 3a Profile 2A2BNE, seismic record section from Island Park across Yellowstone Plateau to Beartooth Mountain. The travel time has been reduced by an amount of time of the distance divided by 6 km/s. Phases correspond to notation of Smith et al., (1981) and follows the notation given in Table 2. Insert map shows general locations of stations by black does and shotpoints by stars. Surface geology beneath each profile is taken from generalized geologic maps.

Figure 3b Profile 1SW, seismic record section from northeast corner of Yellowstone National Park to the southwest acrOss Island Park area to eastern Snake River Plain. Notation follows that of Figure 3a.

Figure 3c Profile 1SSW, seismic record section from northeastern Yellowstone area southward across Yellowstone Plteau to Jackson, Wyoming.

Figure 3d Profile G9NNE, seismic record section from southern Yellowstone northward across Yellowstone Plteau to northeastern Yellowstone National Park.

Figure 3e Profile 6S, seismic record section from northwestern Yellowstone Park near Mammoth and recorded southward around western edge of Yellowstone cadera to Jackson, Wyoming.

Figure 3f Profile G9N, seismic record section from southern Yellowstone National Park recorded northward around the western edge of the Yellowstone caldera to the Mammoth Hot Springs area.

Figure 3g Profile G9S, seismic record section from south of Yellowstone National Park, recorded southward to Jackson, Wyoming.

Figure 3h Profile 6E, seismic record section recorded from Mammoth eastward across northern portion of Yellowstone National Park.

Figure 3i Profile 1W, seismic record section recorded from northeastern corner of Yellowstone National Park westward to Mammoth.

Figure 3j Profile 2A2BENE, seismic record section recorded eastward from Island Park across southern area of the Yellowstone Plateau.

Figure 3k Profile 6SE, seismic record section from northwestern Yellowstone National Park recorded southeastward across central portion of Yellowstone caldera to the East Entrance.

Figure 4 Crustal P-wave velocity model from shotpoint 2A2B northeastward across the Yellowstone Plateau to Red Lodge, Montana. Numerical values are in km/s and the datum is 2,200 m above sea level. Layer boundaries are dashed where inferred.

Figure 5 Crustal P-wave velocity model from Jackson, Wyoming northward across the Yellowstone Plateau to shotpoint 6 in northwestern Yellowstone National Park. Notations are the same as in Figure 4.

Figure 6 Crustal P-wave velocity model from Jackson, Wyoming north-northeastward across the Yellowstone Plateau to shotpoint 1 in the northeastern corner of Yellowstone National Park. Notations are the same as in Figure 4.

Figure 7 Crustal P-wave velocity model from shotpoint 6 at northwestern corner of Yellowstone National Park eastward to shotpoint 1. Notations are the same as in Figure 4.

Figure 8 Seismic record section plotted in a fan form, i.e. the seismograms are plotted in reduced travel-time versus azimuth from 180° to 264° from shotpoint 1. Data correspond to distance ranges of 50 km to 82 km and are all interpreted to lie along the P_2 (P_g) branch. Seismograms have been bandpass filtered with a 3.1 Hz to a 10.9 Hz pass band.

Figure 9 Map of Yellowstone region showing geographic distribution of P-wave delays from shotpoint 1 corresponding to the fan profile in Figure 8 and from shotpoint 6SE profile (Figure 3k). Map shows the possible extent of the low-velocity body and is superimposed upon the complete Bouguer gravity map modified from Blank and Gettings (1974).

Figure 10 Map of depths (in km) to the top of the mid-crustal, P*-layer for the Yellowstone region. P-wave velocities for the layer (shown in parentheses) are in km/s.

Figure 11 Composite record section of P*-branches recorded along the eastern Snake River Plain from shotpoints in Yellowstone. Data from shotpoint 1 pass directly beneath the Yellowstone caldera and data from shotpoint 6 propagate to the northwest of the Yellowstone caldera. Individual seismograms are labeled according to their shotpoint; 1 or 6.

Figure 12 Map showing locations of subsurface reflecting paths from the Moho reflector P_mP. Data from profiles 2A2BSW and 5NE are included in the paper by Braile et al. (1981). Profile G9WSW is not shown in this paper.

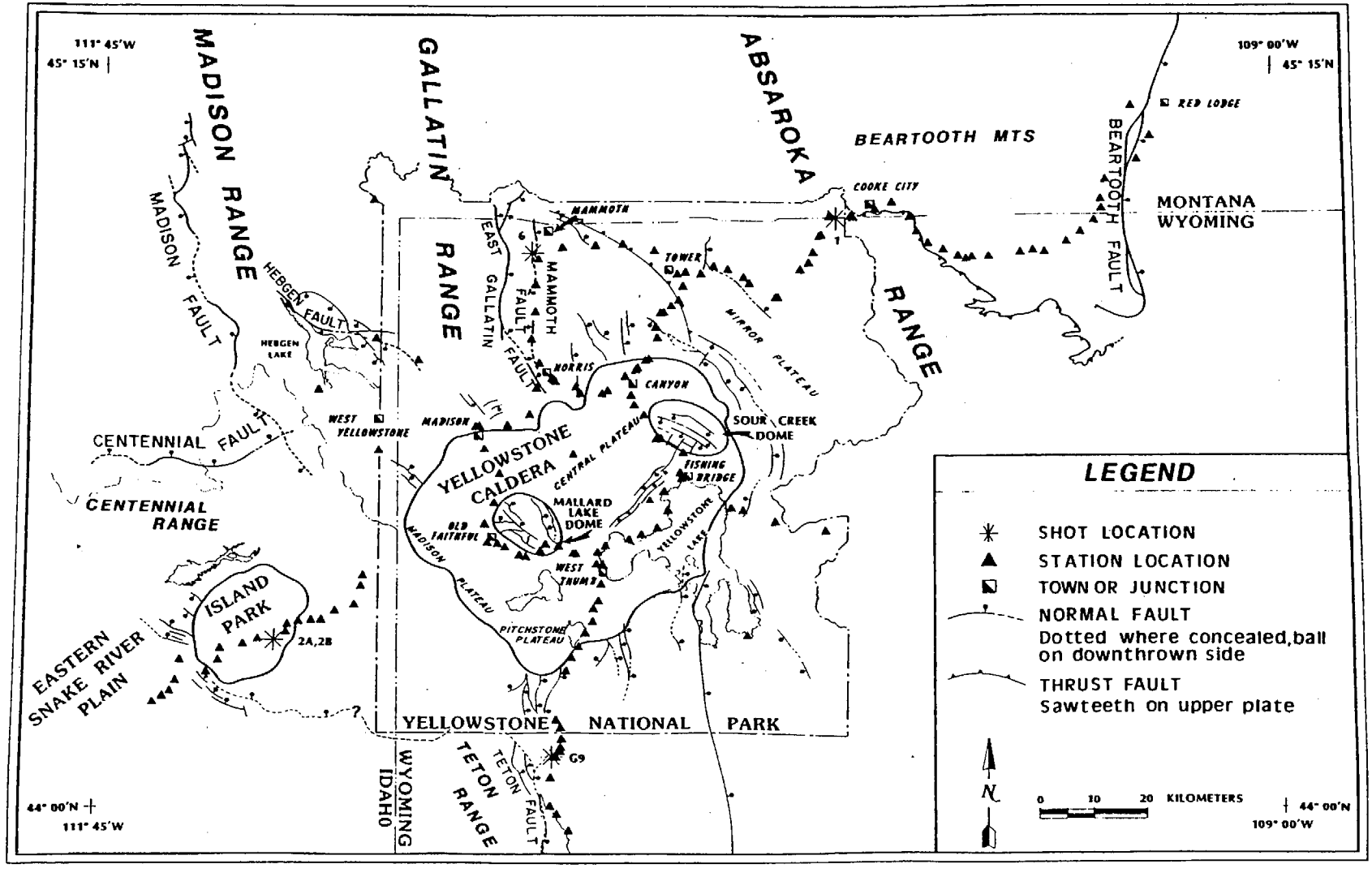
111° 45'W
45° 15'N
109° 00'W
45° 15'N
MADISON RANGE
GALLATIN RANGE
ABSAROKA RANGE
BEARTOOTH MTS
BEARTOOTH FAULT
RED LODGE
COOKE CITY
MONTANA
WYOMING
MADISON FAULT
HEBGEN FAULT
HEBGEN LAKE
EAST GALLATIN FAULT
MAMMOTH
TOWER
MIRROR PLATEAU
HORRIS
CANYON
WEST YELLOWSTONE
MADISON
SOUR CREEK DOME
CENTENNIAL FAULT
YELLOWSTONE CALDERA
CENTRAL PLATEAU
FISHING BRIDGE
CENTENNIAL RANGE
MALLARD LAKE DOME
OLD FAITHFUL
YELLOWSTONE LAKE
MADISON PLATEAU
WEST THUMB
ISLAND PARK
2A,2B
PITCHSTONE PLATEAU
EASTERN SNAKE RIVER PLAIN
YELLOWSTONE NATIONAL PARK
G9
WYOMING
IDAHO
TETON RANGE
TETON FAULT
44° 00'N
111° 45'W
LEGEND
SHOT LOCATION
STATION LOCATION
TOWN OR JUNCTION
NORMAL FAULT
Dotted where concealed, ball on downthrown side
THRUST FAULT
Sawteeth on upper plate
N
0 10 20 KILOMETERS
44° 00'N
109° 00'W

Figure 1

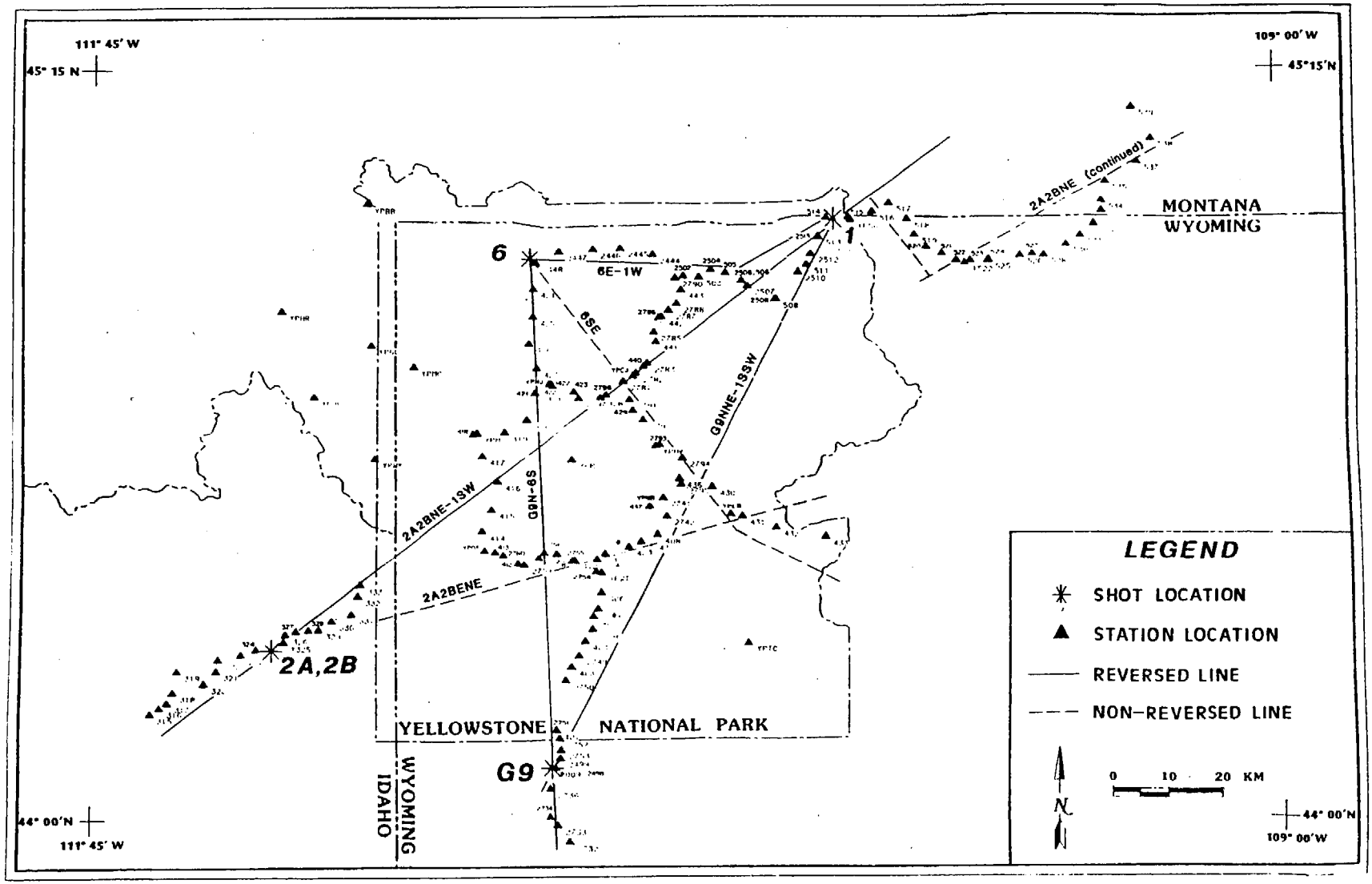
111° 45' W
45° 15 N
109° 00' W
45°15'N
MONTANA
WYOMING
6
6E-1W
1
2A2BNE (continued)
6SE
G9NE-19SW
G9N-6S
2A2BNE-1SW
2A2BNE
2A,2B
YELLOWSTONE NATIONAL PARK
G9
WYOMING
IDAHO
44° 00'N
111° 45' W
44° 00'N
109° 00'W
LEGEND
SHOT LOCATION
STATION LOCATION
REVERSED LINE
NON-REVERSED LINE
0 10 20 KM
N

Figure 2

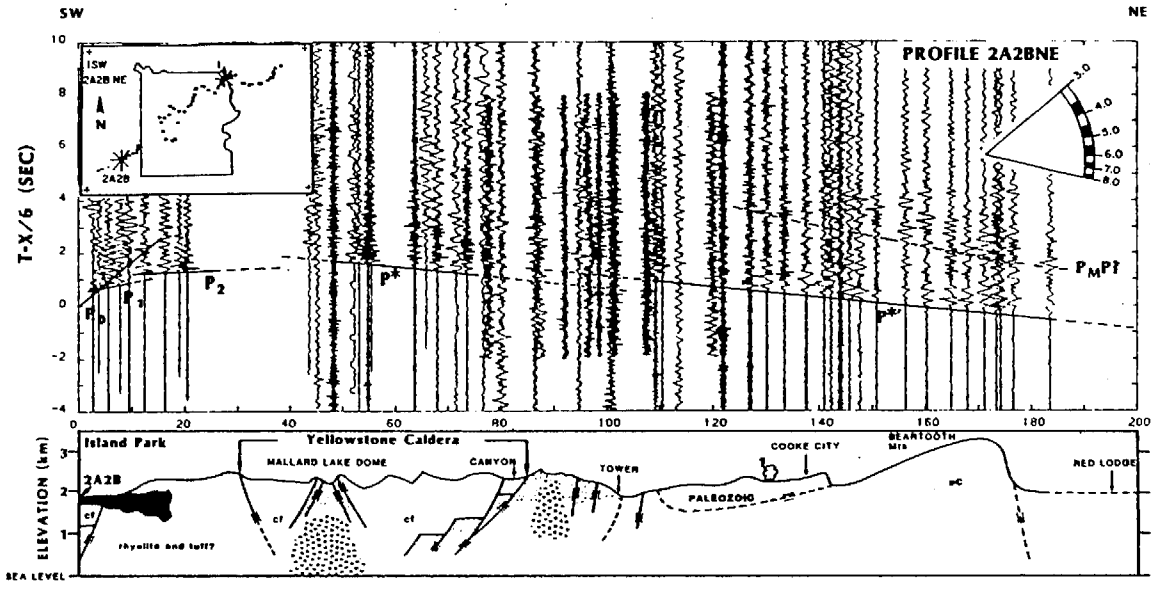

Figure 3a

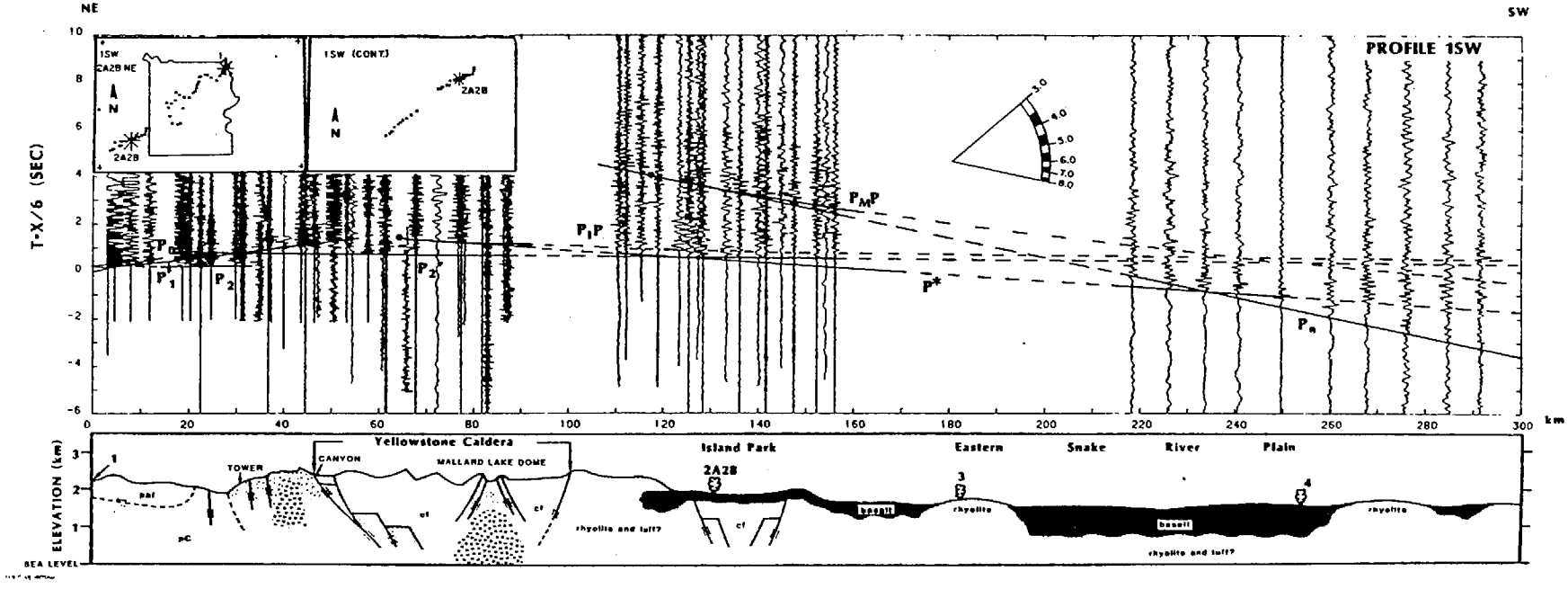

Figure 3b

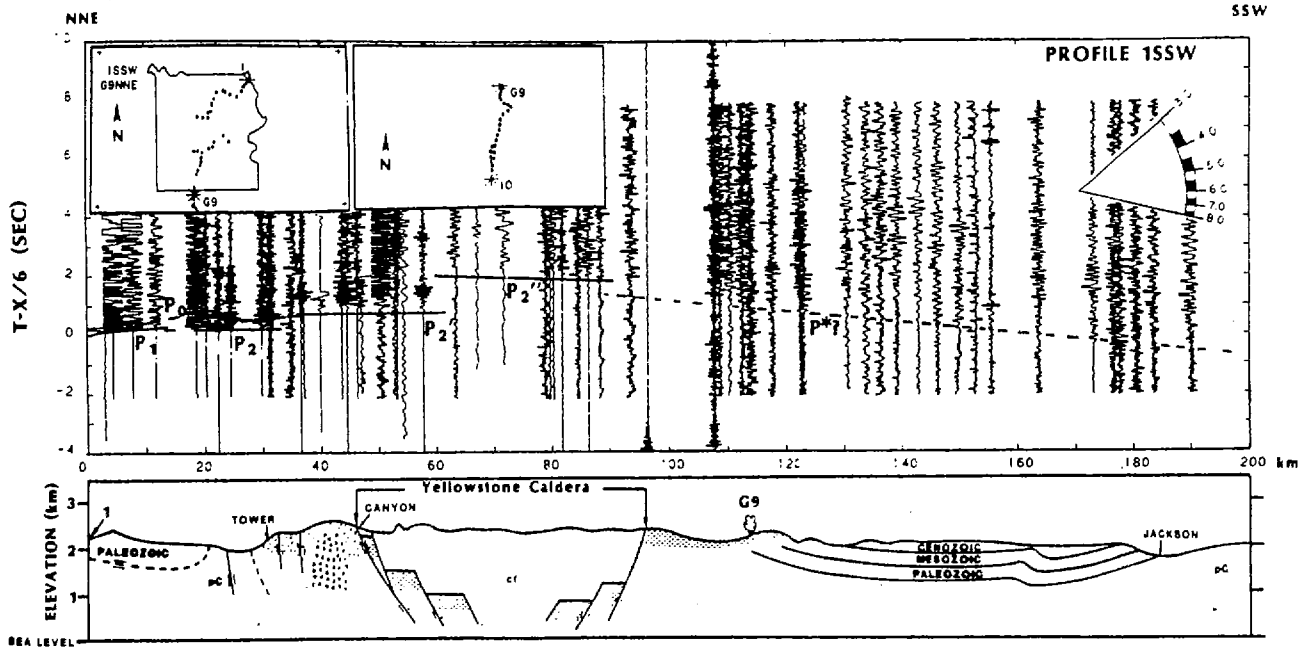

Figure 3c

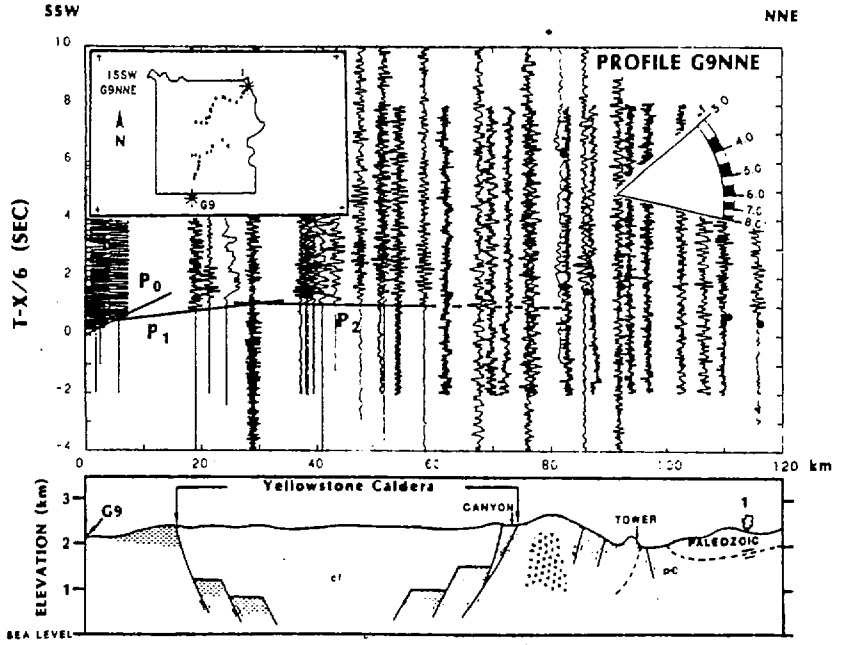

Figure 3d

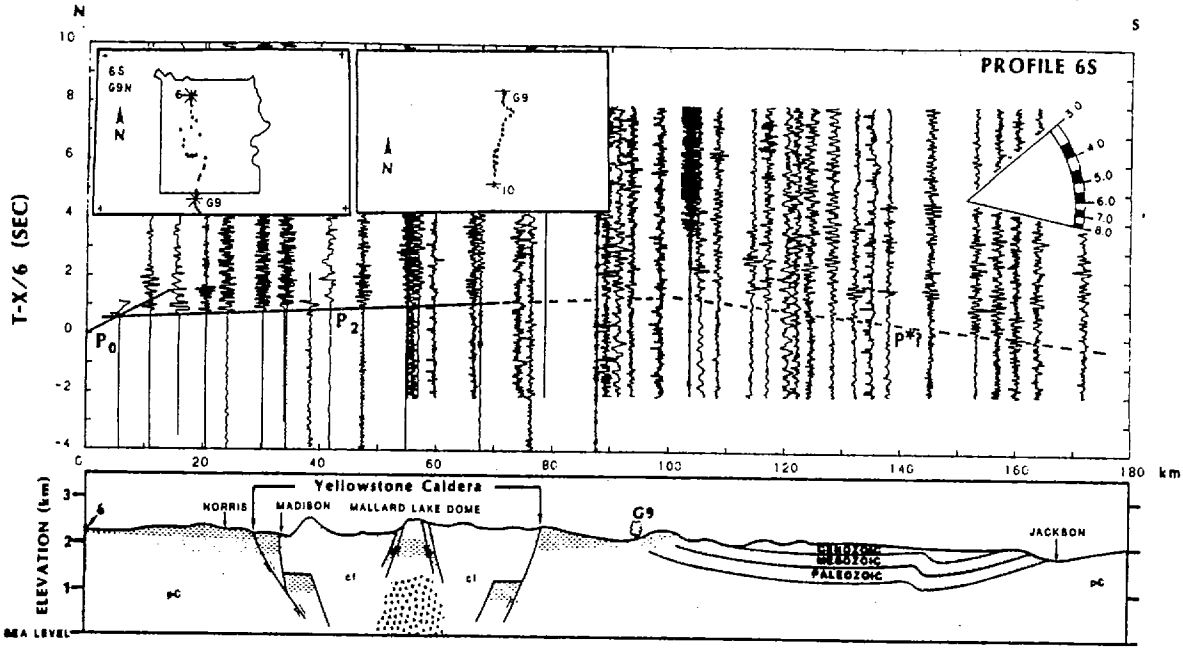

Figure 3e

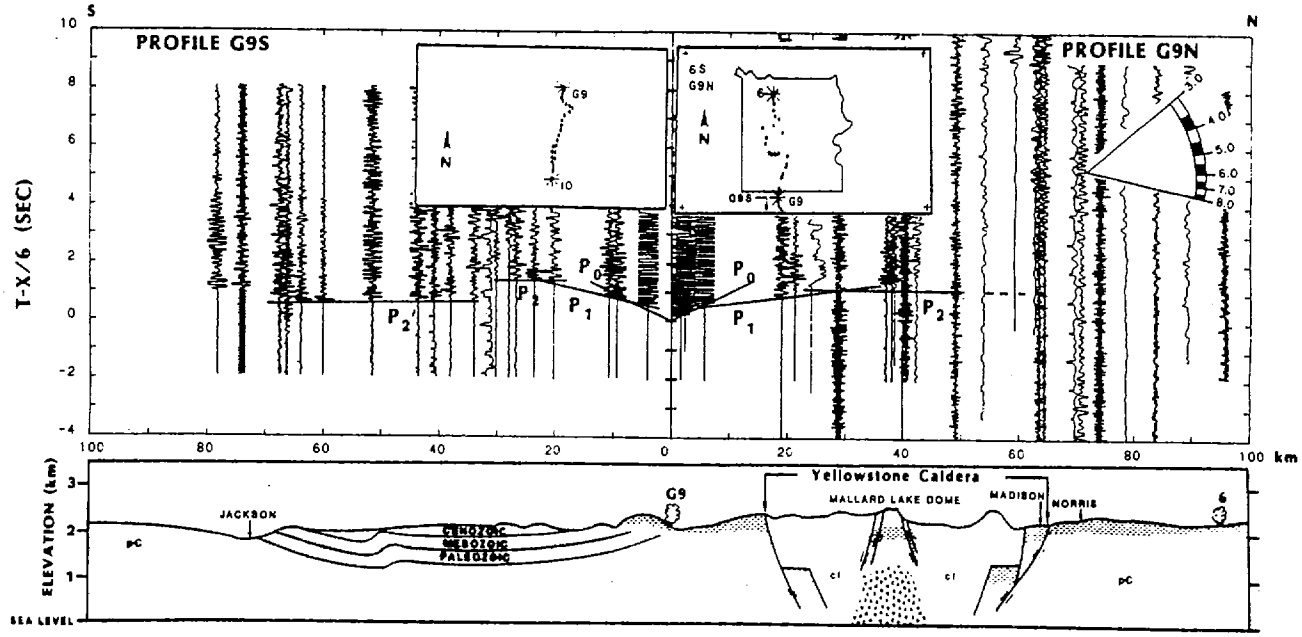

Figure 3f

Figure 3g

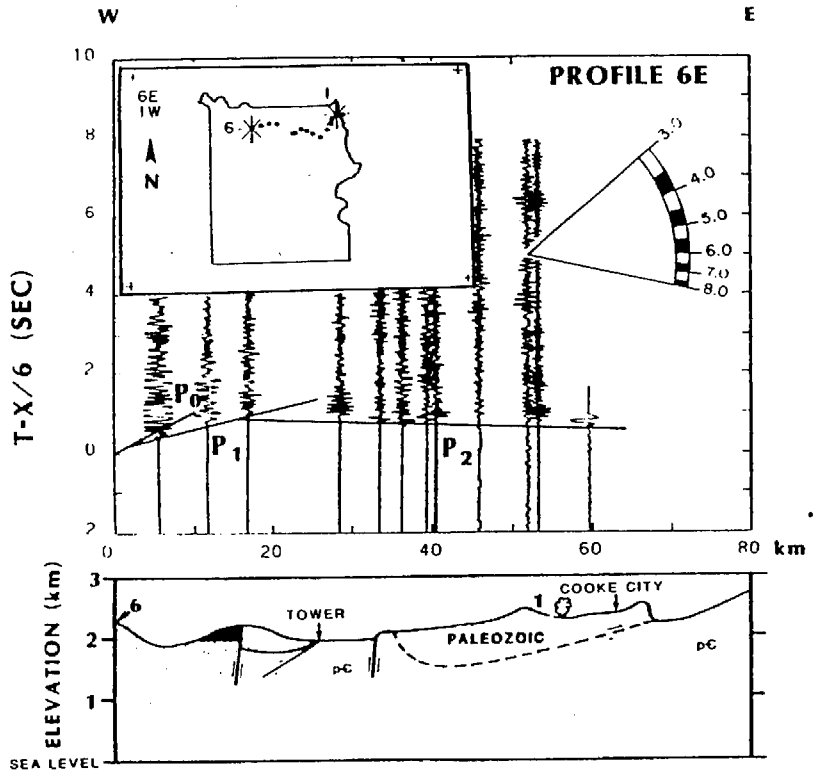

Figure 3h

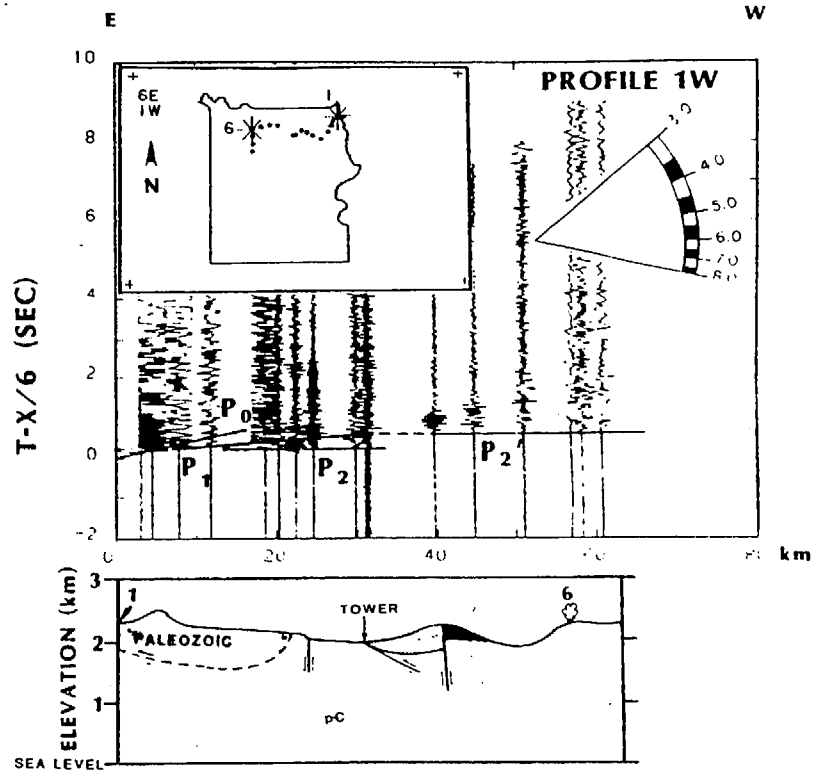

Figure 3i

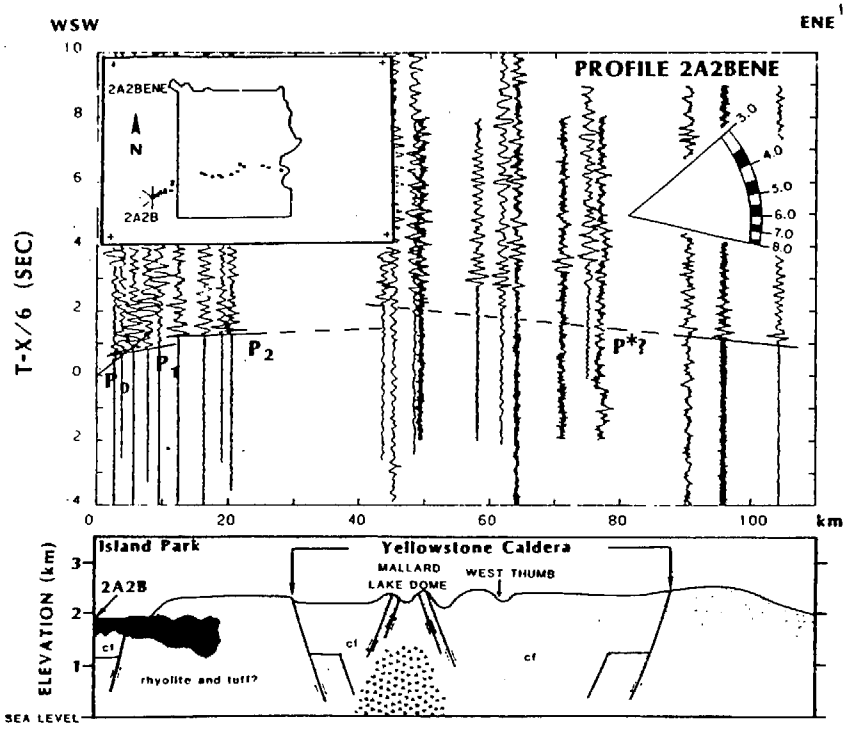

Figure 3j

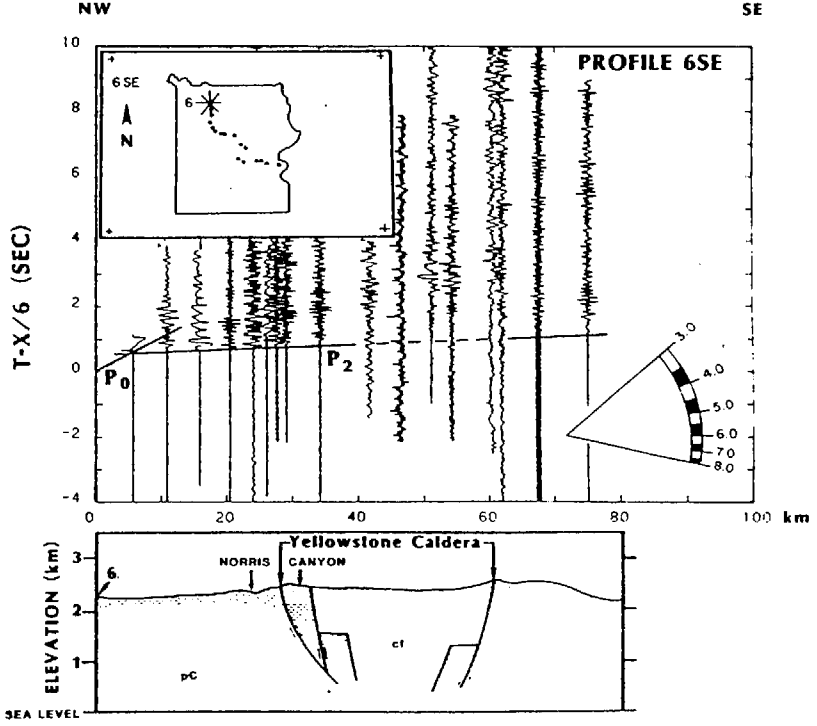

Figure 3k

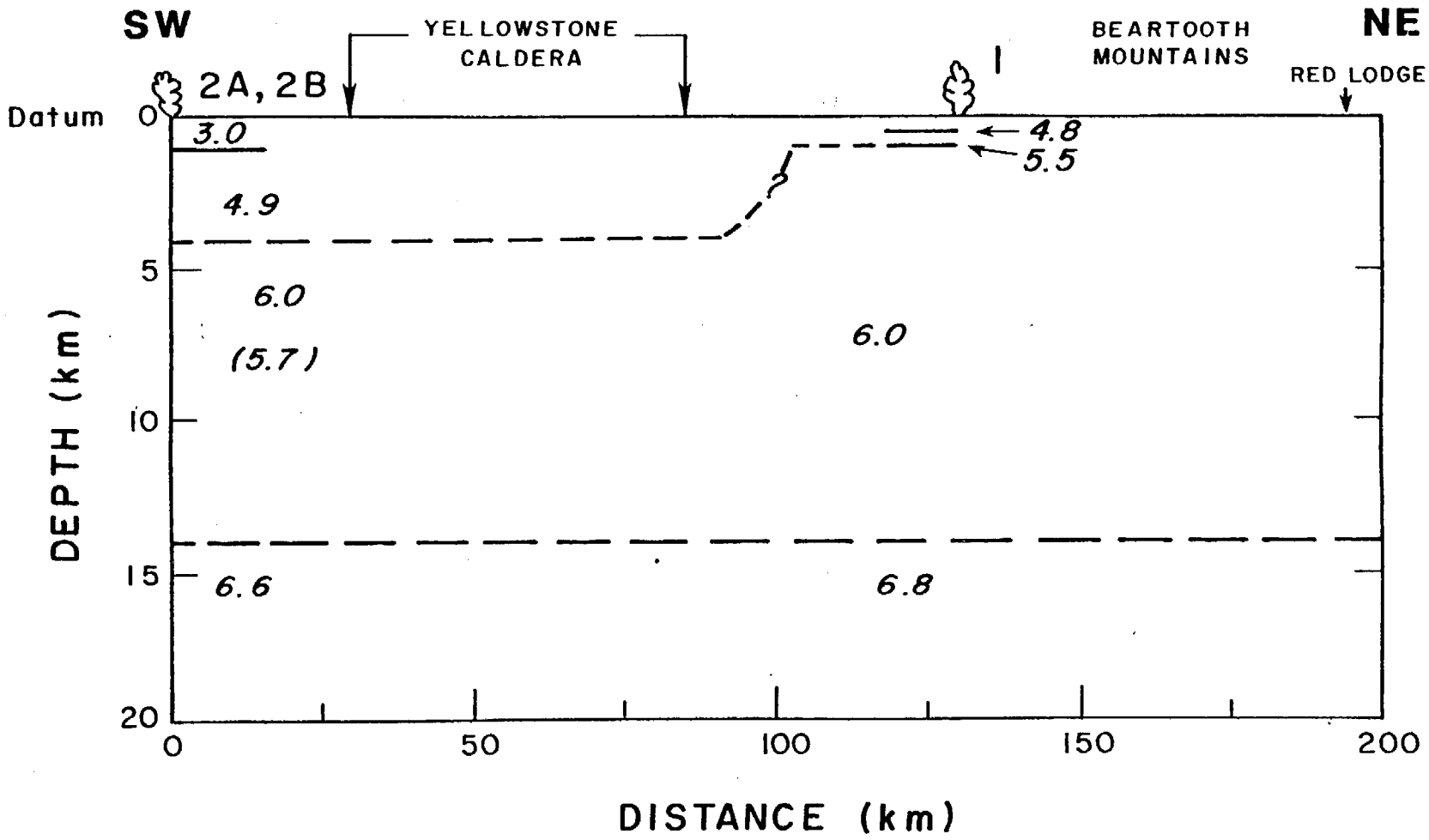
SW
NE
YELLOWSTONE CALDERA
BEARTOOTH MOUNTAINS
RED LODGE
2A, 2B
1
Datum
0
3.0
4.8
5.5
4.9
5
6.0
(5.7)
6.0
10
DEPTH (km)
15
6.6
6.8
20
0
50
100
150
200
DISTANCE (km)

Figure 4

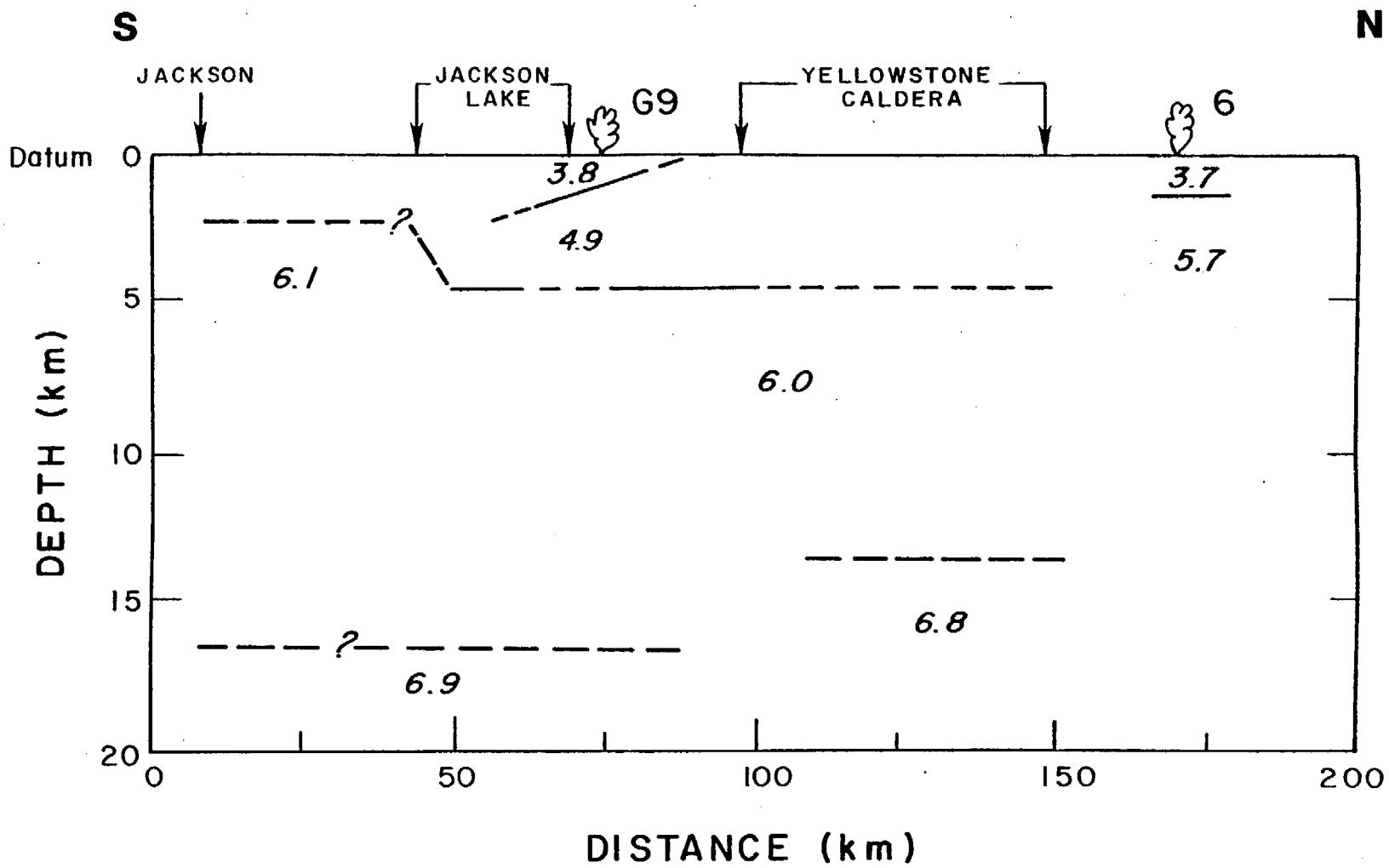
S
N
JACKSON
JACKSON LAKE
G9
YELLOWSTONE CALDERA
6
Datum
0
3.8
3.7
?
4.9
5.7
6.1
5
6.0
10
6.8
15
?
6.9
20
0
50
100
150
200
DEPTH (km)
DISTANCE (km)

Figure 5

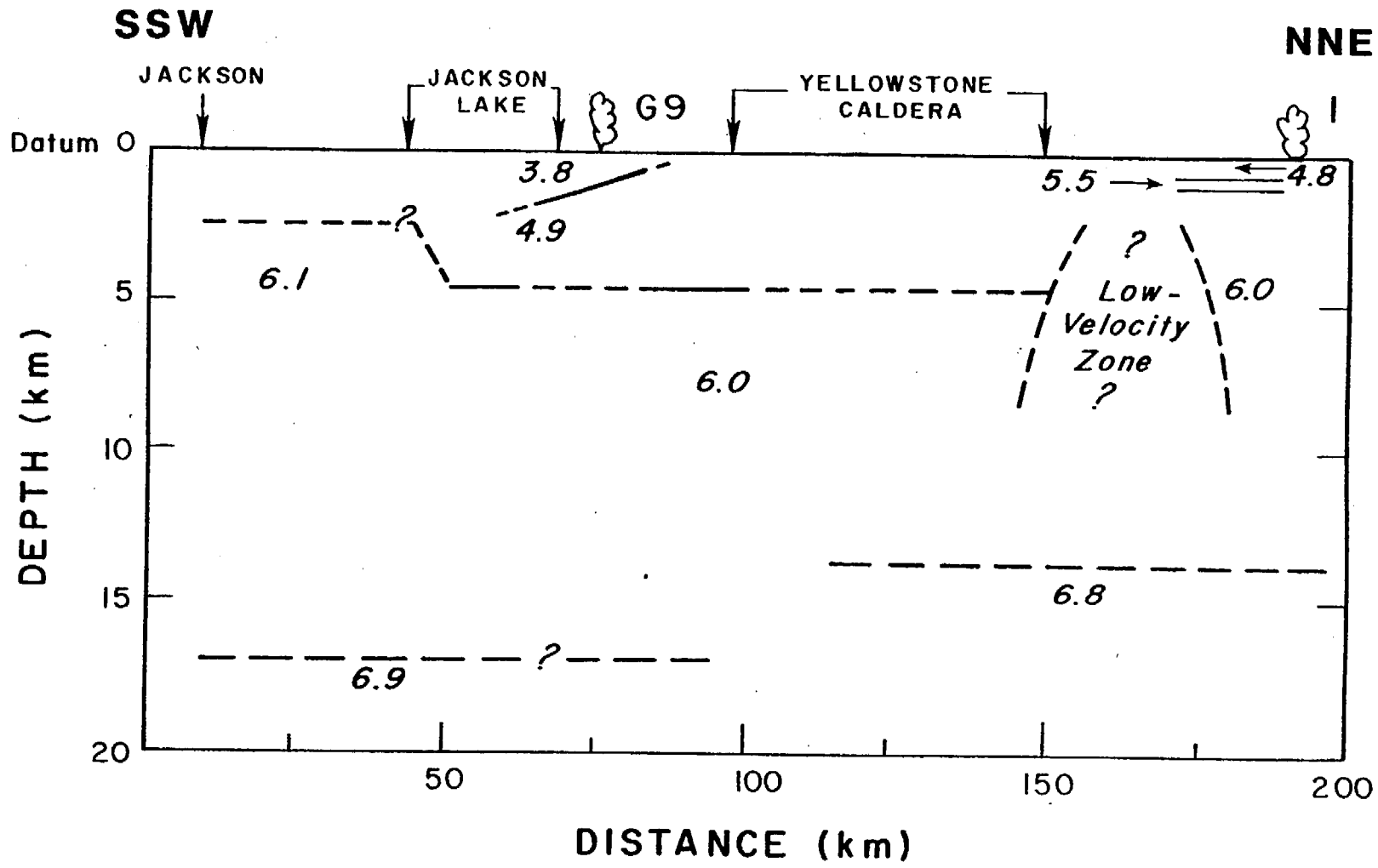
SSW
NNE
JACKSON
JACKSON LAKE
G9
YELLOWSTONE CALDERA
I
Datum 0
3.8
4.9
5.5
4.8
?
6.1
?
Low-Velocity Zone
?
6.0
6.0
6.8
6.9
?
DEPTH (km)
0
5
10
15
20
50
100
150
200
DISTANCE (km)

Figure 6

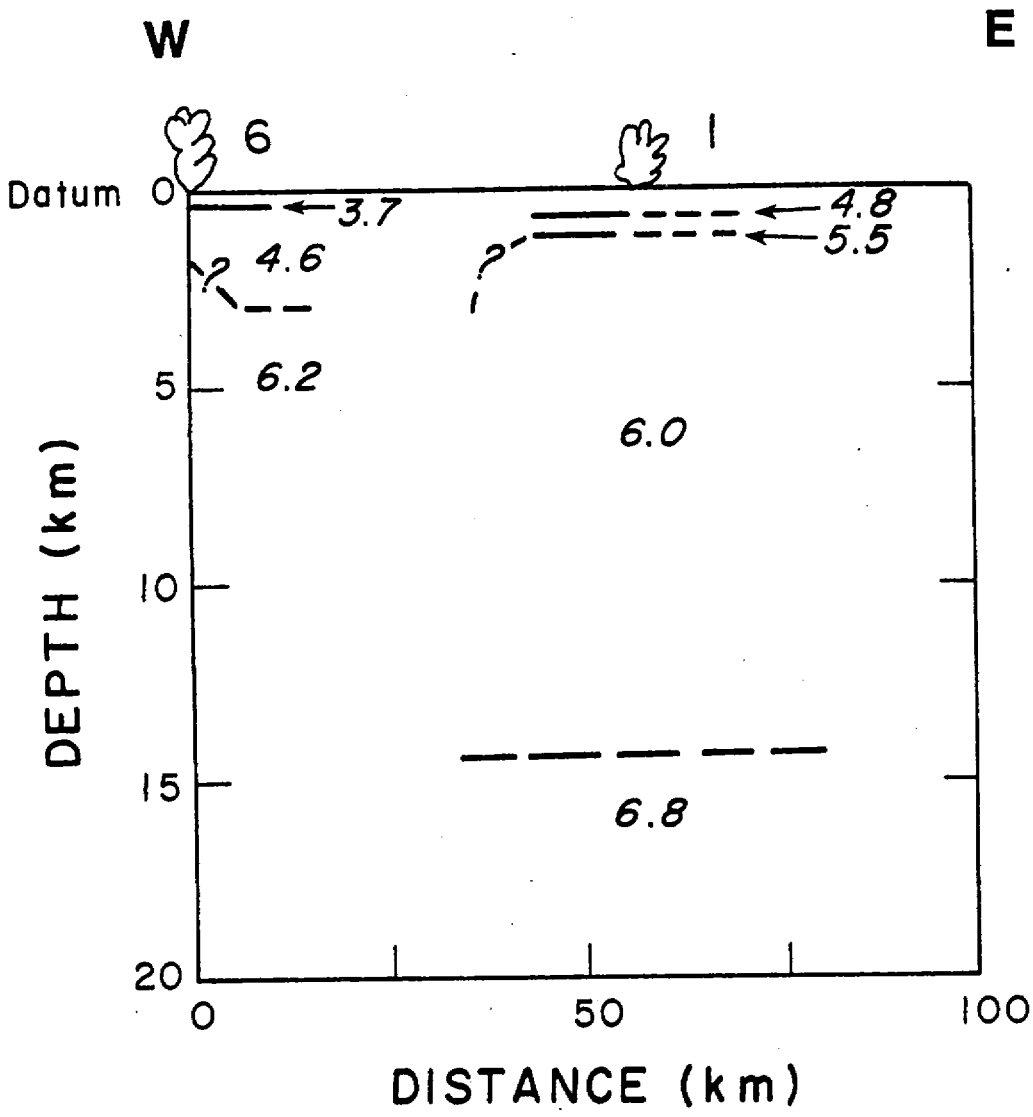
W
E
6
1
Datum
0
3.7
4.8
5.5
?
4.6
?
6.2
5
6.0
10
15
6.8
20
0
50
100
DEPTH (km)
DISTANCE (km)

Figure 7

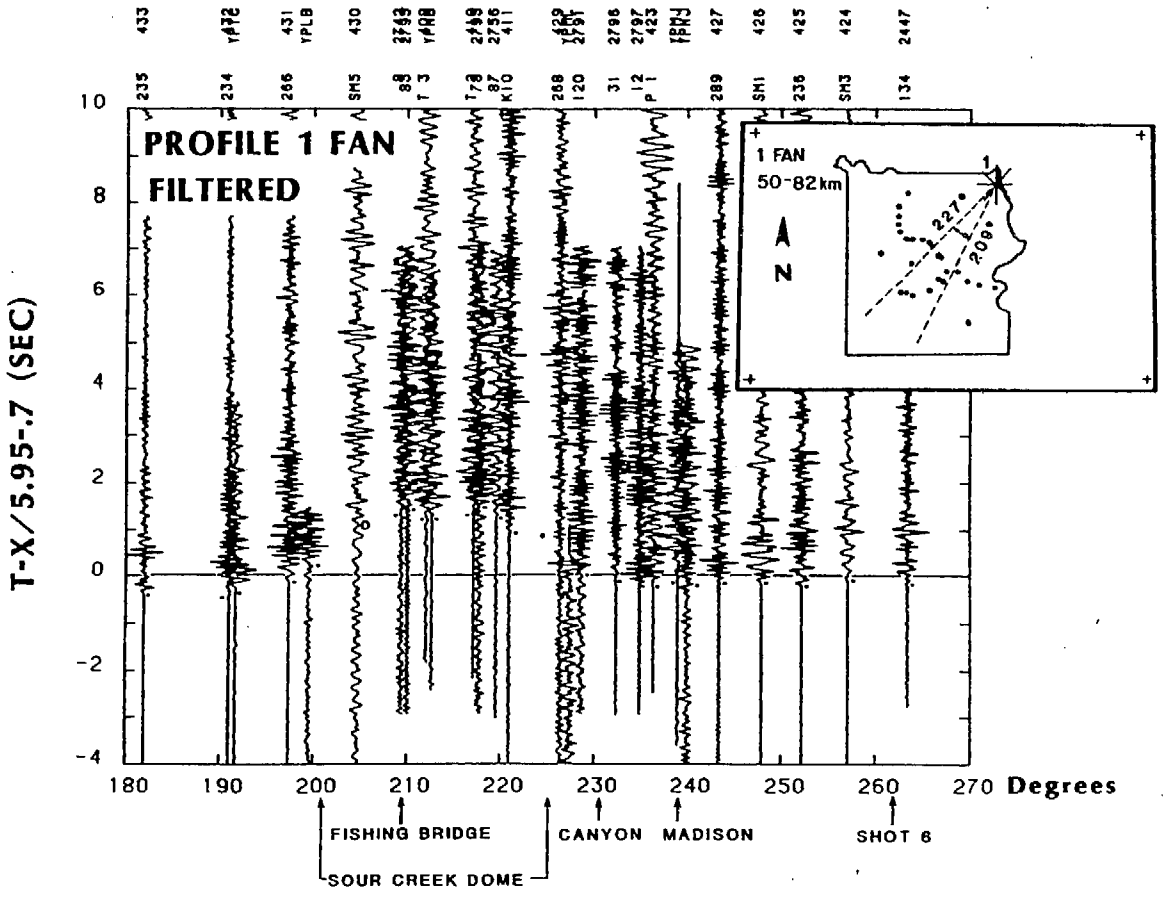
PROFILE 1 FAN
FILTERED
1 FAN
50-82km
227°
209°
N
T-X/5.95-.7 (SEC)
10
8
6
4
2
0
-2
-4
180
190
200
210
220
230
240
250
260
270
Degrees
FISHING BRIDGE
SOUR CREEK DOME
CANYON
MADISON
SHOT 6

Figure 8

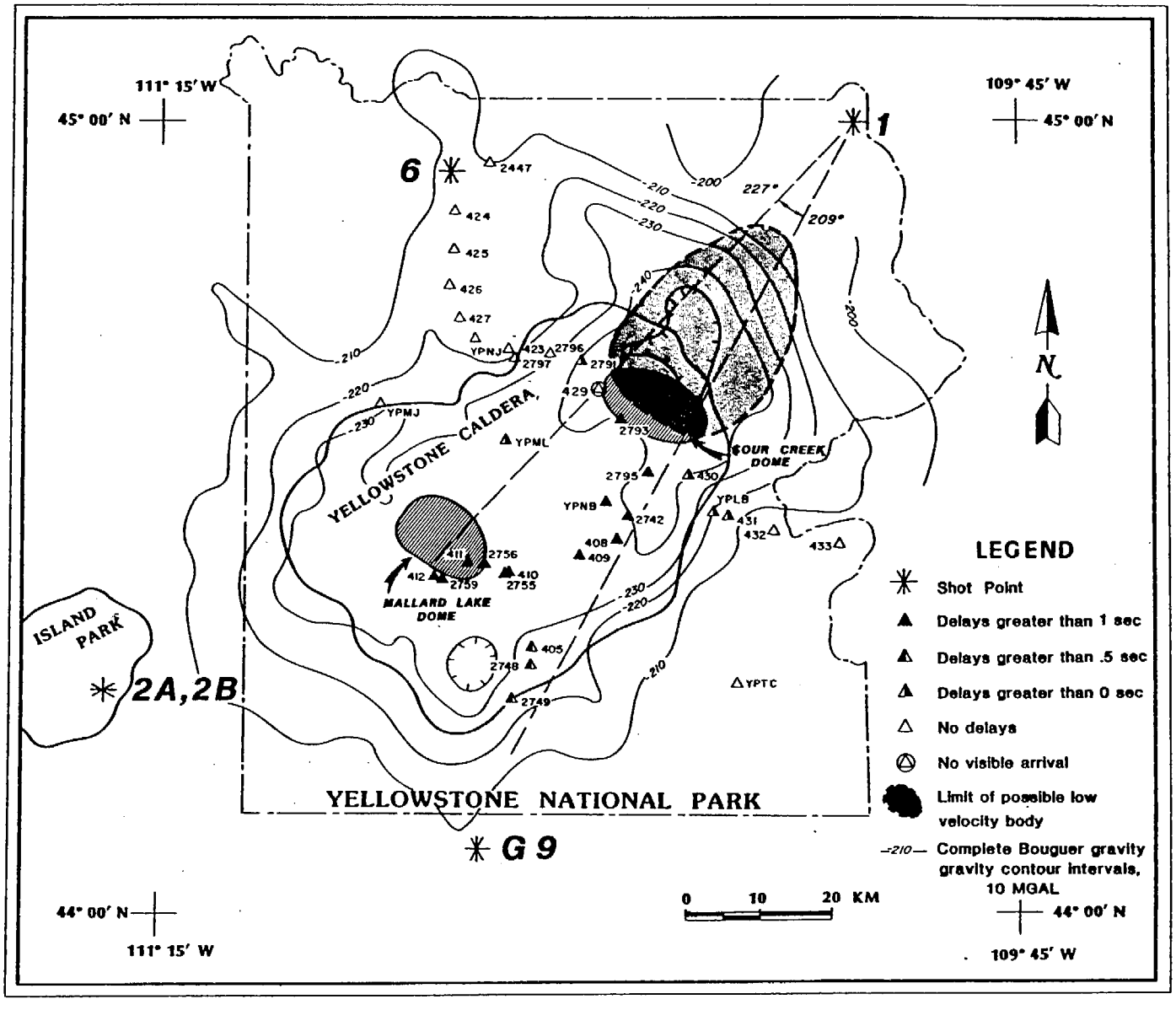
111° 15' W
45° 00' N
109° 45' W
45° 00' N
6
1
2447
424
425
426
427
YPNJ
423
2797
2796
2791
429
2793
YPNJ
YPML
YELLOWSTONE CALDERA
SOUR CREEK DOME
2795
430
YPNB
2742
YPLB
431
432
433
408
409
411
2756
412
2759
410
2755
MALLARD LAKE DOME
405
2748
2749
YPTC
ISLAND PARK
2A,2B
YELLOWSTONE NATIONAL PARK
G 9
210
220
230
200
227°
209°
240
N
LEGEND
Shot Point
Delays greater than 1 sec
Delays greater than .5 sec
Delays greater than 0 sec
No delays
No visible arrival
Limit of possible low velocity body
-210- Complete Bouguer gravity gravity contour intervals, 10 MGAL
0 10 20 KM
44° 00' N
111° 15' W
44° 00' N
109° 45' W

Figure 9

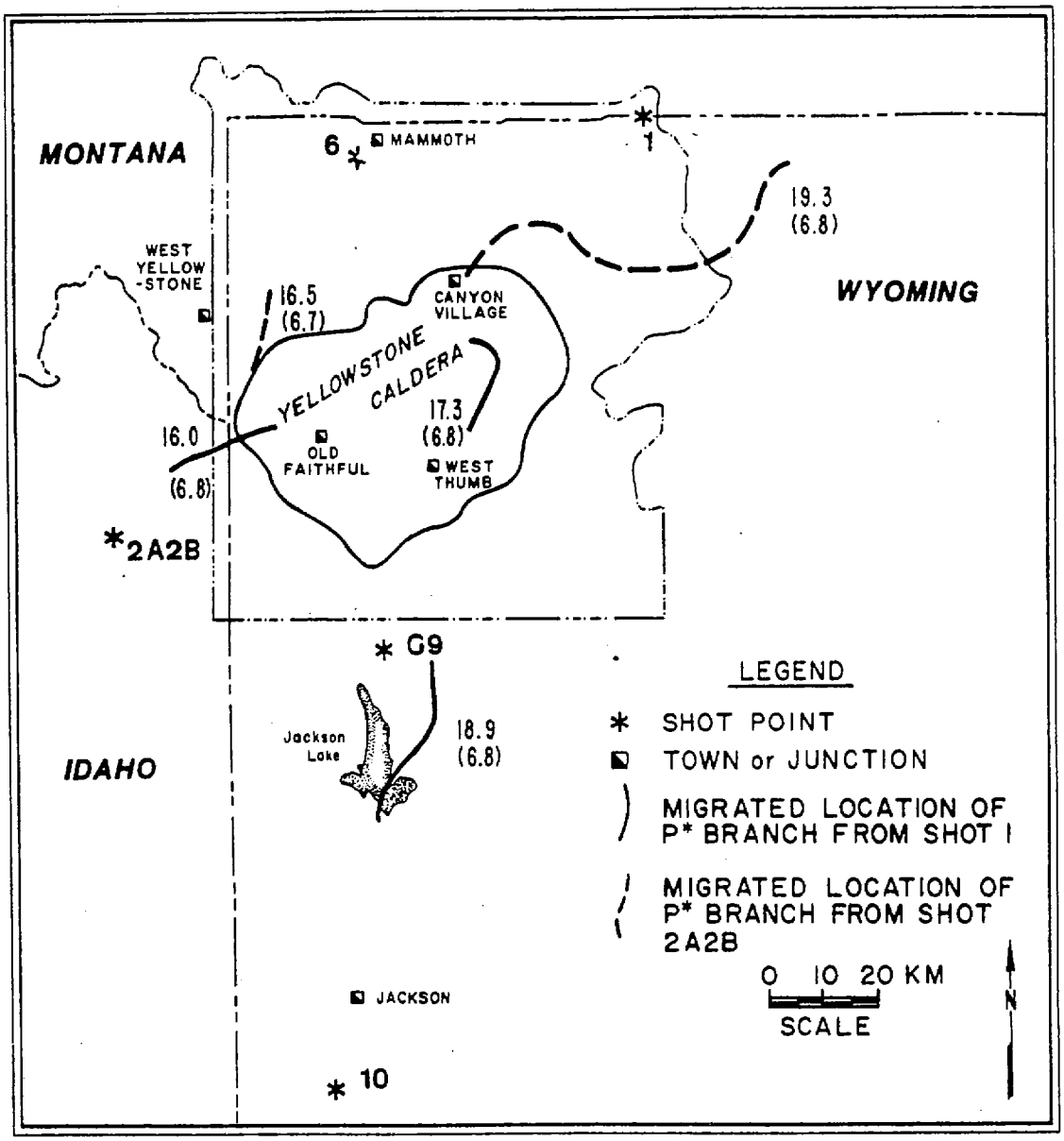
MONTANA
WYOMING
IDAHO
6
MAMMOTH
1
19.3
(6.8)
WEST
YELLOW
-STONE
16.5
(6.7)
CANYON
VILLAGE
YELLOWSTONE
CALDERA
17.3
(6.8)
16.0
(6.8)
OLD
FAITHFUL
WEST
THUMB
2A2B
G9
Jackson
Lake
18.9
(6.8)
JACKSON
10
LEGEND
SHOT POINT
TOWN or JUNCTION
MIGRATED LOCATION OF
P* BRANCH FROM SHOT 1
MIGRATED LOCATION OF
P* BRANCH FROM SHOT
2A2B
0 10 20 KM
SCALE
N

Figure 10

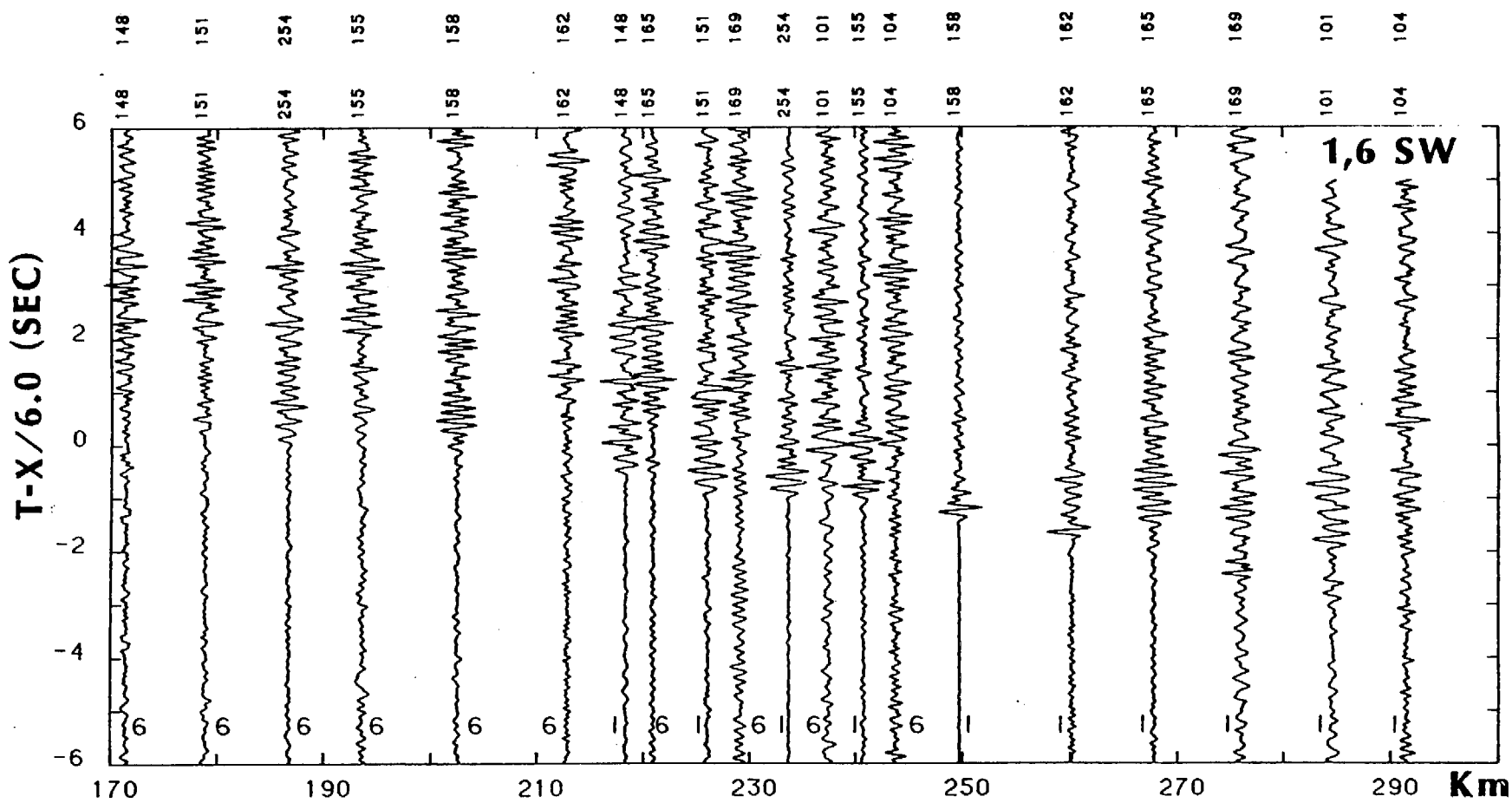
T-X/6.0 (SEC)
6
4
2
0
-2
-4
-6
170
190
210
230
250
270
290
Km
1,6 SW
148 151 254 155 158 162 148 165 151 169 254 101 155 104 158 162 165 169 101 104

Figure 11

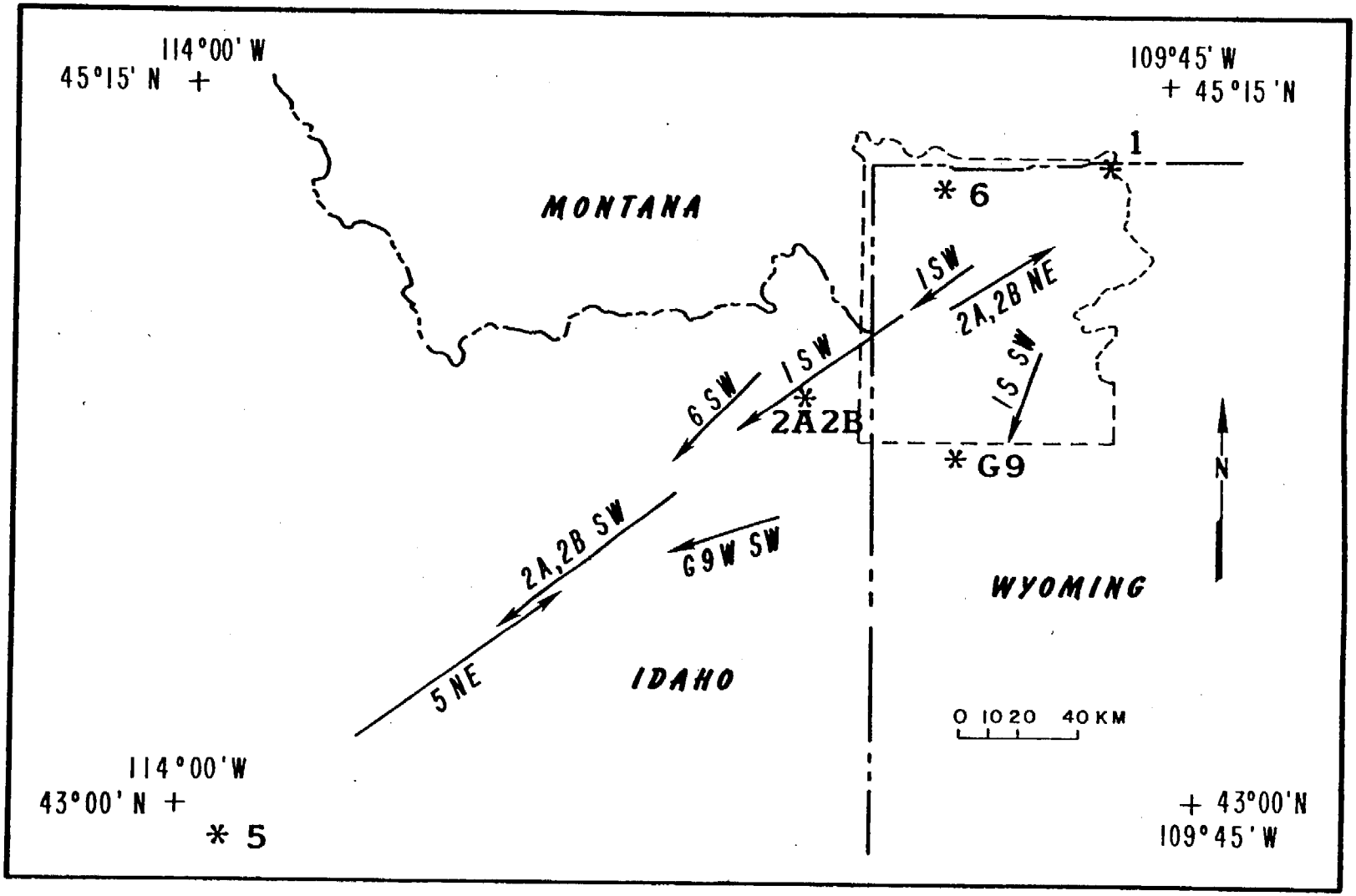
114°00' W
45°15' N +
109°45' W
+ 45°15 'N
MONTANA
1
* 6
1 SW
2A,2B NE
1 SW
6 SW
1 SW
2A2B
* G9
N
2A,2B SW
G9W SW
WYOMING
5 NE
IDAHO
0 10 20 40 KM
114°00'W
43°00' N +
* 5
+ 43°00'N
109°45'W

Figure 12

UPPER-CRUSTAL STRUCTURE OF YELLOWSTONE FROM SEISMIC AND GRAVITY OBSERVATIONS

J. A. Lehman
R. B. Smith
M. M. Schilly
Department of Geology and Geophysics
University of Utah
Salt Lake City, Utah 84112

L. W. Braile
Department of Geosciences
Purdue University
West Lafayette, Indiana 47907

ABSTRACT

The 1978 Yellowstone-Snake River Plain seismic experiment, provided detailed seismic refraction data recorded across a two-dimensional array of seismographs operating in Yellowstone National Park. A delay-time analysis has been applied to 173 P_g-arrivals to determine the three-dimensional distribution of velocity and layer configuration of the upper-crust and was particularly useful in delineating the seismic velocity structure of the Yellowstone caldera. Results indicate that the caldera is characterized by a surface layer of combined sediments and rhyolite flows, 2.8 km/s, that attains thicknesses of 1.5 to 2.0 km. Outside the caldera, the crystalline upper-crustal layer has a P_g-velocity of 6.05 ±0.01 km/s, but decreases by 6 percent to 5.7 ±0.05 km/s

beneath the Yellowstone caldera. Two smaller zones of anomalous low velocity, V_P = 4.0 ±0.5 km/s, occur in the upper-crust beneath the northeastern caldera rim and in the southwest caldera in the vicinity of the Upper Geyser Basin. A three-dimensional gravity interpretation based upon densities derived from the seismic model suggests that the regional gravity low of -60 mgal over the caldera is principally the result of the low-velocity, 5.7 km/s, upper-crustal layer and the low-density surface layer of combined sediments and rhyolite flows. An interpretation of the seismic velocities and densities based on experimental data and theoretical models suggest that the 6.05 km/s, (ρ = 2.70 gm/cm^3), regional P_g-velocity is characteristic of the Precambrian granitic gneissess that form the basement crystallize rocks north and south of Yellowstone. The 5.7 km/s P_g-layer (ρ = 2.65 gm/cm^3) is interpreted to be a 13 to 16 km thick cooling granitic body. The 4.0 km/s low velocity body (ρ = 2.40 gm/cm^3) beneath the northeastern caldera rim is associated with a -20 mgal gravity anomaly and may be interpreted to be a zone of 10 to 50 percent partial gravity melt or large upper dominated/hydrothermal system. The postulated 4.0 km/s low velocity zone in the Upper Geyser Basin does not have a corresponding gravity signature and my reflect an extension of a fractured fault zone that extends north from the Teton fault system beneath the Pleistocene rhyolite flows of the Yellowstone caldera.

ACKNOWLEDGMENTS

We are grateful to Jorg Ansorge, George Zandt, Mark Baker, Steve Clawson, and Harley Benz for their helpful comments and critical discussions. This research is part of the 1978 Yellowstone-Snake River Plain seismic experiment. Many other individuals provided field support and instruments (see Smith, et al. 1981, for lists of names and organizations that participated in the experiment). The National Park Service is gratefully acknowledged for their excellent cooperation and support. Funding for this research was provided by the National Science Foundation grant #EAR-77-23707 and from the Geothermal Research Program of the U.S. Geological Survey grant #14-08-0001-6674.

INTRODUCTION

The most widely known features of Yellowstone National Park are its extensive hydrothermal system, i.e., geysers, hot springs, fumeroles, etc. that owe their origin to elevated temperatures in the crust. The high temperatures are further reflected by the presence of widespread Pleistocene rhyolites and ash flow tuffs. Despite the implication for a large heat source in the crust, postulated early in this century by Daly (1911), it has not been until the last decade that detailed geological and geophysical investigations have been carried out to elucidate the physical properties of the crust and the possible sources of heat. New research has been motivated by the need to understand the hydrothermal systems as well as to understand the contemporary tectonics of the Yellowstone region. In this paper the upper-crustal structure of the Yellowstone region is interpreted from a two-dimensional analysis of seismic refraction data incorporated with regional gravity data.

Geological and Tectonic Setting

Yellowstone National Park has been geologically mapped in detail by the U.S. Geological Survey (1972). Bedrock and surficial geologic maps provide excellent coverage of surface rock types. Much of the northern and eastern portions of the park are covered by early Tertiary andesitic volcanic rocks, with exposures of Precambrian granitic gneisses and Paleozoic carbonate rocks scattered across the northern section of the park. A prominent tectonic-volcanic feature of Yellowstone is a large collapse caldera (75 x 45 km) that was formed during the last of the three major cycles of Quaternary volcanism that began 2.2 million years ago (Smith and Christiansen, 1980).

Each volcanic cycle was climaxed by a violent pyroclastic caldera-forming eruption of rhyolites and ash flow tuffs, the last of which marks the formation of the present caldera 600,000 years ago (R. L. Christiansen, written communication, 1978). Culmulatively, 3500 km^3 of volcanic rock have been erupted during the three cycles attesting to the supposition of major sources of silicic magma that must have resided within the crust. However the present topography is the result of accumulations of numerous Quaternary rhyolite flows (Christiansen and Blank, 1972) that blanket the central and southwestern portions of the Yellowstone Plateau. These widespread flows, that range in age from 600,000 to some as young as 70,000 years (R. L. Christiansen, written communication, 1978) are thought to reflect the presence of large crustal magma sources.

Relation to 1978 Yellowstone-Snake River Plain Experiment

The seismic velocity structure and physical properties of the lithosphere can provide a basis for understanding the volcano-tectonic processes of an active intraplate volcano-tectonic feature such as Yellowstone. These properties were the main target for a cooperative U.S.-European seismic experiment that was implemented in 1978 across the Yellowstone-Snake River Plain volcano-tectonic system (Smith et al., 1981). A description of the Yellowstone portion of this major seismic experiment and general results is given by Smith et al. (1981). Schilly et al. (1981) in a companion paper showed the detailed interpretation of the detailed crustal structure for the Yellowstone region and examined the properties of the lower crust.

Prior to the 1978 experiment, the results of various geophysical and geological investigations (see bibliography, Smith et al., 1981), have inferred the presence of a hot body of low seismic velocity and low density located beneath the Yellwostone caldera. These anomalous properties have

been interpreted to extend from 5 to 250 km below the surface and point out the relationship to a mantle source for the magmatism and heat.

Despite the general agreement that crustal magma bodies must have existed beneath Yellowstone, there is little definition and information on the location of the inferred magma sources. For example, the gravity modeling of Eaton et al. (1975) showed 14 different density models that placed all of the density variations in the upper-16 km of the crust. Thus, a need for a more direct method of measuring the physical properties of the upper-crust was necessary to resolve the source of the heat and the location of possible magma bodies. In response to this objective, a delay-time analysis of the two-dimensional seismic data observed in the 1978 Yellowstone-Snake River Plain experiment was made. The results form the basis of this paper.

Interpretations of the 1978 seismic data by Schilly (1979) and Schilly et al. (1981) demonstrate that the crust beneath Yellowstone appears to be rather homogeneous with an average 6.0 km/s regional upper-crustal layer $\sim$12 km thick and overlying a lower-crustal layer with a velocity of 6.6 to 6.8 km/s and a total crustal thickness of 45 km. The homogeneous nature of the crust led Schilly et al. (1981) to conclude that the large teleseismic P-wave delays reported by Zandt (1978) and Iyer et al. (1980) and attributed to both upper-mantle and crustal levels were more affected by a low-velocity body deeper than previously postulated. While the results of Schilly et al. (1981) are a general interpretation of the velocity structure; the distribution of the 1978 seismic stations, as much as 25° off-line from assumed profiles, spatial gaps of up to 20 km in the data, and scatter due to lateral velocity variations in the first arrivals on the order of 0.1 to 0.4 s require a more refined analysis of the upper-crustal structure.

The primary objective of this paper is to resolve in detail the seismic velocity structure of the upper-crust using information from the two-dimensional distribution of seismographs and by constructing more realistic three-dimensional models of the velocity and density distributions beneath Yellowstone incorporating regional gravity data.

DELAY-TIME INTERPRETATION OF SEISMIC DATA

Five of the shots detonated during the 1978 Y-SRP seismic experiment were recorded across a two-dimensional array of seismographs in the Yellowstone Park area (Figure 1). From these recordings, fifteen profile and fan sections were constructed for the Yellowstone area. Most of the data interpreted here are shown in the companion papers by Schilly et al. (1981), Smith et al. (1981) and Schilly (1979) that describe the general crustal structure of Yellowstone from the 1978 experiment. In this discussion travel-time tabulations were made for the 1978 data assuming a 2.2 km sea level datumn, the same as the companion papers for Yellowstone.

From the profiles apparent velocities were computed for distinct upper-crustal P-wave branches. The principal phases were interpreted as those from the critically refracted rays: P_g from the upper-crustal "granitic" layer; and P* from the lower-crustal layer. Travel-time branches for these phases were identified on the basis of apparent velocity and the names do not necessarily imply material composition. Figure 1 shows the locations of the seismograph stations used to compose the profiles for the Yellowstone area and Figure 2 gives an example of the data taken along a representative profile, 6S.

From eight of the seismic profiles, apparent velocities for the P_g-branch were computed on the basis of straight-line approximations of the first arrivals. Two different groupings of apparent velocities were evident (Table 1). A P_g-velocity of 6.05 km/s fit the average of the profiles located outside the Yellowstone caldera; whereas within the caldera, the apparent velocities were consistently 6 percent lower, averaging 5.70 km/s. For example, profile 6S (Figure 2) shows a decrease in velocity to 5.70 km/s as a clear change in slope of the P_g-branch at 30 km.

Profile 1W (Figure 3) shows another property seen in much of the data; namely, station-to-station travel-time variations greater than 1 sec that were attributed to lateral variations in velocity and variations in depth to the top of the P_g-refractor. Because of these variations it was felt that detailed modeling of the apparent velocities from linear profiles could be misleading. Therefore, a modified delay-time method was used to incorporate, in a three-dimensional interpretation, all the data recorded in Yellowstone in 1978 as a means of a more realistic interpretation.

The initial application of the time-term method to the Yellowstone data required the construction of a station delay-time map. For this analysis the upper-crustal arrivals associated with the P_g-branch were interpreted. Initial arrivals were picked to an accuracy of ±0.01 s for most records. Thirteen additional records from a 1977 seismic refraction line recorded by the University of Utah and the U.S. Geological Survey (shotpoint 9) were timed and added to the 1978 data set giving a total of 173 delay-time measurements.

Following the standard travel-time equation for head-waves:

$$t = X/V_1 + Z_s\cos_i/V_o + Z_d\cos_i/V_o \quad (1)$$

and $$t = X/V_1 + a_s + a_d \quad (2)$$

where source delay times (for each shotpoint), a_s, were computed on the basis of the velocity structure beneath the shotpoint and the depth to the P_g-layer as determined from near-shot arrivals (Figure 4a). Table 2 lists the shotpoint delay times and assoicated velocity models computed from this analysis. In addition, data from a University of Texas-Dallas reflection spread, located in Island Park just west of Yellowstone National Park, were also used in constructing a suitable near-shotpoint model beneath shotpoint 2A2B.

Another step in the data reduction process involved the selection of a refractor velocity, V_1, in equation (1). As noted earlier, apparent velocities for the P_g-branch outside the Yellowstone caldera averaged 6.05 km/s. Since this area was assumed to be less affected by the thermal and volcanic processes of the caldera, V_1 = 6.05 km/s, was assumed "normal" for the undisturbed P_g-layer.

After the shotpoint delay times were computed and a refractor velocity determined, the first two terms of equation (1) were subtracted from the observed total travel time; giving a station delay time, a_d, for each shotpoint-station configuration (Figure 5). At each station in Figure 5, a vector pointing back toward a particular shotpoint is drawn proportional in length to the delay time computed at the station. All station delay times were positive but the most prominent were delays 1.5 to 2.0 s computed from shotpoint 1 as recorded between Fishing Bridge and Old Faithful. Schilly et al. (1981) attributed these large differences to a shallow low-velocity zone located beneath the northeastern caldera.

Another set of anomalous station delay times were computed for shot-point 2B, as recorded from Old Faithful to Fishing Bridge. While not as well defined as the delay times for the northeast caldera, they were as large as 1.5 sec and suggested the presence of strong velocity variations in the southwest caldera boundary area.

Interpretation

In the conventional delay-time analysis, the velocites in equation (1) are fixed and the refractor depth beneath the station can then be solved for. However, this approach was not suitable for the Yellowstone area for several reasons. First (from Table 1), the P_g-velocities demonstrate a strong lateral inhomogeneity from 6.05 km/s to 5.7 km/s, a 6 percent decrease. Second, the assumption of a constant surficial-velocity was considered invalid because of the large variability in rock type exposed at the surface.

A more complete equation that takes into account both refractor and surface velocity variations (Figure 4b) for dips less than 15° is:

$$t = X/V_1 + X'/V_1' - X'/V_1 + Z_s \cos i_s/V_{os} + Z_d \cos i_d/V_{od} \qquad (3)$$

If the velocities in equation (3) are known, the travel-time can be reduced to a function of three unknowns, Z_s, Z_d, and X' (Figure 4). For this study, velocities V_1 and V_1' have been assigned values of 6.05 km/s and 5.70 km/s, respectively, based on the information given in Table 1. The surface velocity distribution, while not as well defined was determined from near-shot (X<15 km) data and surface rock types. Figure 6 shows the velocity structure above the P_g-layer that was used in determining the appropriate terms of equation (3). Surface velocities varied from 2.8 km/s for rhyolites and lake sediments of the inner-caldera; 3.6 km/s

for rhyolites and ash flow tuffs outside the caldera; and 4.8 km/s for the Paleozoic section exposed northeast of the caldera. In cases where more than one layer was present above the P_g-layer, a modified form of equation (3) involved an additional term for the second layer. The depth, Z_s, to the top of the P_g-layer beneath each shotpoint was determined from near-shot data. Thus two unknowns, Z_d and X' remained in equation (3) producing an overdetermined system of equations for which there is no unique solution. However useful results can be obtained as additional constraints are considered. For example, because the depth beneath a particular station is the same for all shots, requires that Z_d be a repeated variable in many cases and help define which portion of the travel time that can be attributed to a P_g-velocity variation. Also, the raypath coverage (Figure 7) provided by the two-dimensional station-shotpoint distribution, provided constraints regarding the lateral extent of discrete velocity zones. For example, if an east-west raypath showed no delay associated with a change in the P_g-velocity (i.e., the depths near the station as determined from more than one shot are equal using the assumption of a constant P_g-velocity), a decrease in P_g-velocity inferred from a crossing north-south raypath must lie to the south or north of the intersection of the raypaths. As more raypaths were analyzed, velocity anomalies can be localized and their boundaries defined. While this approach is somewhat simplistic, the formal mathematical inverse is beyond the scope of our conventional methods because of the complex design of forward raypaths that are constrainted by non-systematic raypath crossings and non-linear functionals. Hence a simple trial-an-error method based upon our knowledge of raypath constraints and realistic geologic models was programed for a simple hand calculator.

Results of Delay-Time Analysis

To initiate the modeling, straight-line approximations of travel-time branches were used to define an appropriate starting velocity model, therefore eliminating a large but unmeasured portion of the non-uniqueness problem. Based on the information in Table 1, the initial P_g-velocity model consisted of an elliptical shaped body of velocity 5.7 km/s, nearly coextensive with the geologically mapped caldera; while the area outside the caldera was assigned a velocity of 6.05 km/s. The depth extent of the 5.7 km/s low-velocity body was considered deep enough such that no rays associated with the P_g-branch would have passed beneath it.

For each station, the distance along which the head wave traversed in the 5.7 km/s layer was measured for the starting model and the refractor depths were computed using equation (3) assuming straight raypaths. When computed depths beneath a particular station were not consistent with respect to measurements from more than one shot, the boundary of the 5.7 km/s layer was adjusted until consistent depth values were obtained. Throughout the analysis, an attempt was made to keep both the depth distribution and the boundary of the 5.7 km/s layer as smooth as possible. This implies that the final velocity model will be one of the simplest possible configurations that can satisfy the seismic refraction data.

Figure 8 shows the configuration of the P_g-velocity distrubtion based on the analyses of the delay times. A "band" representing the precesion of the data indicates the expected error in the boundary location as estimated from the resolution of the individual picks. The most significant change in the 5.7 km/s layer from the starting model was its extension northward into the Tower Junction and Mirror Plateau areas north and east of the Yellowstone caldera. This increase in area was necessary to match the delay times for raypaths from shotpoints 1 and 6. Two additional low-velocity

zones, of V = 4.0 km/s, are also shown in Figure 8. The large delay times observed between Old Faithful and Fishing Bridge for shotpoints 1 and 2B were of such magnitude that velocity reductions greater than 6 percent were necessary to explain them. Once the extent of the 5.7 km/s layer was determined by raypath constraints, additional reductions of the P_g velocity to 4.0 ±0.5 km/s were necessary to satisfy the total travel-times.

As a comparison with other data, Figure 9 shows the computed P_g-velocity distribution superimposed on the Bouguer Gravity Map for Yellowstone Park (Blank and Gettings, 1974). From Figure 9, the boundary of the 5.7 km/s layer is nearly coincident with the -230 mgal gravity contour that represents the limits of the large regional negative anomaly. The configuration of the 4.0 km/s low velocity body in the NE caldera area is suprisingly concident with a pronounced gravity anomaly of an additional -20 mgals closure; suggesting an additional zone of low density as well.

Attempts to define an exact location and P-wave velocity for the southwestern low velocity body near Old Faithful were inconclusive. The clearest evidence for a velocity decrease in this area is the consistent increase in station delay times computed for shotpoint 2B recorded from shotpoint G9 to West Thumb. The large delays observed on profile 2A2BNE showed variations of up to one second but there is no evidence in the gravity data (Figure 9) that this low-velocity zone has an associated low density.

Figure 10 shows the computed depths to the top of the P_g-layer using the previously discussed delay times and modified for the P_g-velocity distribution shown in Figure 8. The depth values are plotted in their ray-path migrated positions for each shotpoint-station combination.

A striking feature of Figure 10 is the consistent depth of ∿1.6 km to the top of the refractor beneath the Yellowstone caldera and the Norris-Mammoth corridor. The top of the P_g-layer is generally deeper outside this region, reaching a maximum of 4.3 km northeast of Canyon. A station 2 km east of Tower Junction, had no station delay and thus was assumed to be located directly on the P_g-layer -- a Precambrian granitic gneiss. This observation suggests that the Precambrian crystalline rock is responsible for the 6.05 km/s P_g-branch in the northeast Yellowstone area.

The sharp increase in depth to the P_g-refractor to the south and west of Tower Jct. could reflect the presence of a buried E-W trending fault. A small travel-time delay (∿0.02 to 0.05 s) has been incorporated in the delay time analysis for raypaths affected by this abrupt change in refractor depth. The interpreted displacement along the top of the P_g-layer here must be older than the Quaternary faults mapped along the Lamar River because these young faults are characterized by downthrown blocks to the north (Brown, 1961; Love, 1961), opposite to that interpreted from the seimsic data.

The northwest trending contours east of the Norris-Mammoth corridor follow the trend of normal faults mapped in this area. The sense of displacement on these faults agrees with the seismic interpretation of a thickening of the near-surface layers to the east of the Norris-Mammoth Corridor but the wide station spacing precluded the detailed resolution of the fault location.

The top of the refractor beneath the Yellowstone caldera appears smooth with respect to the area outside the caldera. This "smoothing" is somewhat artificial and is largely a function of the near-surface velocity. For the surface velocity of the caldera, V = 2.8 km/s, a change of 0.03 seconds in

travel time corresponds to a change in the computed depth of 0.09 km to the top of the refractor while for the northeastern portion of the park, a surface velocity of V = 4.8 km/s, results in a depth change of 0.24 km for the same travel-time change.

Because the surface velocity within the caldera was assumed and not measured, it would be useful to examine the effects of two other surface velocity distributions on the computed refractor depth. The travel-time used to compute a refractor depth of 1.5 km, with a surface velocity of 2.8 km/s would yield a depth of 2.6 km for a surface velocity of 4.0 km/s which is assumed to be a maximum velocity for the caldera material. Furthermore, if we assume a near-surface velocity structure for the caldera equivalent to that measured from Sonobuoy measurements in Yellowstone Lake (Otis et al., 1977), where 0.8 km of 2.8 km/s material overlie a 4.8 km/s layer, this same travel-time gives a depth of 2.7 km. Therefore, the depth to the top of the P_g-refractor, beneath the caldera could extend from 2 to 3 km.

INTEGRATION OF GRAVITY DATA

The Bouguer gravity anomaly map (Figure 11) of the Yellowstone National Park region (Blank and Gettings, 1974) is dominated by a large negative residual anomaly of -60 mgal relative to a regional field of -200 mgal. This gravity low is generally coincident with the Yellowstone caldera but extends beyond its boundary in the northeastern part of the park. Within this large regional anomaly -20 mgal gravity low is located across the northeastern caldera rim. Eaton et al. (1975) presented fourteen, three-dimensional gravity models whose theoretical fields closely matched the observed gravity field of the entire Park with the causitive bodies ranging from thin layers of rhyolite flows and caldera fill to complex combinations of caldera fill, altered basement rock, and rhyolitic magma. Eaton et al. (1975) concluded that the entire source of -55 mgal gravity anomaly was in the upper 16 km of the crust with density contrasts ranging from 0.02 to 0.45 g/cm^3. Evoy (1978) using joint teleseismic P-wave delays and gravity inversions on the other hand, modeled the source as a mass deficiency extending from the surface to a depth of 100 km with average density contrasts of 0.2 to 0.1 g/cm^3. This model was based on the constraint that the velocities derived from teleseismic P-wave delay data fit the density contrasts according to Birch's law (Birch, 1961). In this section, gravity models will be presented that agree with the detailed seismic velocity models derived from the delay-time analysis.

A NE-SW cross-section of the crustal velocity model for Yellowstone (Figure 12) exhibits significant lateral velocity variations within the upper 17 km. If these variations are accompanied by similar density changes, this

model produces a gravity anomaly of similar form and magnitude to that observed. Several three-dimensional gravity models were computed to test this possibility. For the modeling, the boundaries for the layers of P-wave velocity: 2.8, 5.7, and 4.0 km/s were determined from the time-term analysis and different density combinations were modeled in an attempt to match the observed field. It should be noted that the low velocity zone near Old Faithful (Figure 8) was not incorporated in the gravity modeling because, contrary to the northeastern low velocity body, it had no clear gravity anomaly (Figure 9). The three-dimensional gravity modeling program (Plouff, 1975) is based on the formula of Talwani and Ewing (1960) for the gravitational attraction of three-dimensional polygonal prisms.

For the initial models, the contours of the computed gravity field surrounding the maximum gravity low, associated with the northeastern low-velocity body, were located about 5 km southwest of the observed area of closure. This implies that the body responsible for this gravity low is actually located further northeast than postulated on the basis of the seismic refraction data.

Figure 12 shows a cross-section through a three-dimensional gravity model whose thoeretical field matched the observed field within 5 mgal of all long-wavelength anomalies, constrained by velocities and layer configuration results of seismic refraction interpretation. For this model the location of the low velocity body has been moved 5 km to the northeast. Because the location of the northeastern low velocity body in Figures 8 and 9 are based on arrivals from shotpoint 1 recorded between Old Faithful and Fishing Brdige, interpretation of the low velocity zone 5 km to the northeast did not significantly alter the seismic results. Therefore, the location shown in the density model (Figure 12) is preferable for the northeastern low

velocity/low density zone. An interesting feature of this model is the rather low density of 2.40 gm/cc that is necessary to explain the gravity low. The interpretation of this low density and its corresponding velocity in terms of rock composition will be addressed in the next section.

DISCUSSION

The combined interpretation of seismic refraction and gravity data shows that the upper 15 to 17 km of the earth's crust beneath Yellowstone is characterized by significant lateral variations in both P-wave velocity and density. The seismic data suggest that a layer of low velocity, 5.7 km/s (representative of a 6 percent decrease relative to Precambrian basement) extends from depths of 2 to 17 km beneath the Yellowstone caldera; while two smaller zones with a 30% velocity reduction have been identified near the NE and SW areas of the caldera. While the inherent ambiguity associated with the interpretation of the gravity data alone precludes direct density measurements, corresponding density reductions deduced from the velocity information can explain the regional gravity field. Implications from these results that bear on the composition and physical conditions of the upper-crust will be examined here.

Seismic velocities in rocks depend on several factors, the most important of which are: composition, density, temperature, confining pressure, crack density, and pore pressure. The effects of these parameters on seismic velocities in a thermal environment such as Yellowstone have been summarized by Black (1978) and Iyer et al. (1980) based on the experimental and theoretical results of other investigators. These compilations demonstrate that temperature effects on velocities, for typical continental crust with normal heat flow gradients, produced by increasing temperature with depth nearly cancels the effect of increasing pressure. This implies that observed velocity changes within a normal thermal environment are largely a function of compositional and density variations (Black, 1978). However, since Yellowstone's heat flow is very high, averaging 1000 to 1600 mWm^{-2} or

about 60 times the world average (Morgan et al., 1977), demonstrate that the Yellowstone setting is indeed anomalous.

5.7 km/s Low Velocity Body

Velocity decreases as small as 6 percent may be caused by several factors or the combined effect of more than one parameter. For example, the extensive Quaternary volcanism at Yellowstone has led several investigators to suggest that a large magma chamber, of dimensions greater than 20 km x 20 km, must have resided in the upper-crust beneath the caldera within the last 600,000 years (Daly, 1911; Smith and Shaw, 1975; R. L. Christiansen, written communication, 1978). Above a postulated magma body of these dimensions, variations in physical properties of the upper-crust would be expected. In particular if the low-velocity zone is related to a magma, partial melt, or a hot but cooling body, the increased heat could significantly alter the elastic properties and pore fluids of otherwise brittle crystalline rock.

For example, even if a parent silicic magma body has cooled, the resulting granitic batholith would have a different velocity structure than that of the Precambrian granitic gneisses that are thought to form the basement P_g-layer observed outside the caldera. P-wave velocity measurements of 5.6-6.0 km/s are typical for rocks of granite measured both in the field and the laboratory (Smithson and Decker, 1974). Their metamorphic counterparts exhibit slightly larger velocities (Smithson and Ebens, 1971) of 6.1-6.2 km/s for granitic gneiss' of the Wind River Range 100 km SE of Yellowstone. Therefore, a variation in composition between a Precambrian gneiss and a Quaternary granite could be accompanied by a velocity decrease from 6.05 km/s to 5.7 km/s.

A change in composition between granite and a granitic gneiss would most likely be accompanied by a change in density. In the previous section, we showed that the gravity field observed in Yellowstone can be modeled using a change in density of 0.05 gm/cm^3 from 2.70 g/cm^3 for the Precambrian granitic gneiss to 2.65 g/cm^3 for the postulated granitic batholith beneath the caldera. While the ranges of densities measured for granites and gneisses overlap significantly, a density contrast of 0.05 g/cm^3 could be associated with this change in composition. Smithson (1971) reported a mean density of 2.70 g/cm^3 for the granitic gneiss of the Wind River Range. From Birch's Law (Birch, 1961), a velocity decrease of 6 percent should be accompanied by a density decrease of 0.15 g/cm^3. Since this large of a density contrast is not consistent with the gravity data, it appears that at least part of the 6 percent velocity decrease may be associated with an additional temperature effect that limits the application of Birch's law to this domain.

Yellowstone's high heat flow and surface geothermal phenomena imply that temperatures are much higher beneath the Yellowstone caldera than the rest of the region (Morgan et al., 1977). For example heat flow measurements taken in Yellowstone Lake showed an increase from 120 mWm^{-2} to 700 mWm^{-2} between the south end of the lake (outside the caldera) and the central portion of the lake 5 km inside the caldera boundary (Morgan et al., 1977; Smith and Christiansen, 1980). This major gradient in heat flow coincides, within 3 km of the boundary between the 6.0 km/s and the 5.7 km/s low velocity zone. If the heat flow transition corresponds to the lateral extent of high-temperature material, the 5.7 km/s low velocity body

may be the corresponding body responsible for much of the heat flow anomaly observed within the Yellowstone caldera. Morgan et al. (1977) estimate a temperature increase from 80°C to 275°C at the top of the crystalline basement at ∿1 km depth. Their model of the thermal structure of the caldera suggests even higher temperatures (340-900°C) at depths of ∿5 km.

Velocity reductions of 6 percent have been measured for granites that were heated from temperatures of 25°C to 100°C to temperatures of 350°C to 500°C at 2 kbar confining pressure, equivalent to a depth of 7.6 km (Spencer, 1975; Kern, 1978; Christensen, 1979). At higher pressures (4 kbar at a depth of 15.3 km), higher temperatures, of ∿600°C, were necessary for a 6 percent velocity reduction (Fielitz, 1971; Kern, 1978). In light of these experimental results and the heat flow interpretation of Morgan et al. (1977), high temperatures within the 5.7 km/s low velocity body relative to adjacent areas may be responsible for much of 6 percent P-wave velocity reduction.

Major changes in temperature and composition across the caldera boundary are more than enough to independently or jointly account for the 6 percent velocity decrease. However, other factors such as a decrease in effective pressure (Todd and Simmons, 1972), thermoartesian pressure caused by thermal expansion of water (White et al., 1975), and opening of cracks due to dilatancy all may cause reductions in P-wave velocities (Nur, 1972). These latter effects are considered small, but we can not discount their effect.

4.0 km/s Low Velocity Zone

Two zones of pronounced low-velocity, V_p = 4.0 km/s, have been modeled within the P_g-layer. We will first consider the northeastern low velocity zone where the velocity decrease of 30 percent is interpreted to be associated with a concomittant density decrease of 9 percent as discussed in the previous section.

Data on the effect of high temperatures on seismic velocities for crystalline rocks thought to make up the upper crust is sparse. However, experiments show that for temperatures up to 750°C, velocity decreases of not more than 10 percent can be expected for rocks at a confining pressure of 4 kbar, equivalent to a depth of 15.3 km (Fielitz, 1971; Kern, 1978). Larger velocity reductions are observed at lower confining pressures with a maximum decrease of 25 percent for a granite at 650°C and a confining pressure of 1 kbar (Kern, 1978). In fact, velocities in granites have been shown to increase as a function of temperature once the α/β quartz transition is passed at 650-700°C (depending on the confining pressure) and, in one case, the velocity surpassed the original value within 50°C of the transition (Fielitz, 1971). Even with increased pore pressures of up to 1 kbar, exptrapolation of velocity versus temperature data indicate that melting would begin before a velocity decrease of 30 percent is reached (Spencer, 1975).

Velocity variations due to major compositional changes are not considered a likely source for the observed velocity anomaly. Rocks that exhibit P-wave velocities as low as 4.0 km/s are generally felsic extrusive rocks or unconsolidated sediments. While these materials may be found at depths of 2 to 4 km, neither would be expected at a depth of 13 km, the bottom of the P_g-layer. According to Birch's law, that generally holds for

solid materials in the range of crustal velocities and pressure (Chung, 1972), the 4.0 km/s low velocity body should exhibit a velocity decrease of 0.75 g/cm^3 that would correspond to a density of 1.90 g/cm^3; well below the modeled density of 2.40 g/cm^3.

Therefore, while the effects summarized above may contribute to the observed velocity reduction, it does not appear that they can alone produce the observed 30 percent velocity decrease. A more plausible explanation for such a decrease in velocity is partial melting.

Experimental measurements of P-wave velocity for rocks heated through their melting temperatures have largely been confined to volcanic rocks. P-wave velocities of 2 to 3 km/s have been measured for molten lavas and glasses ranging in composition from basaltic to rhyolitic (Murase and Suzuki, 1966). Below the temperatures associated with complete melting, temperature-versus-velocity results are highly variable as P-wave velocities of 4.0 km/s were observed for several rock types in the temperature range of 700-1200°C (Murase and Suzuki, 1966; Murase and McBirney, 1973). Murase and Suzuki (1966) observed that the temperature at which the velocity began to decrease was a function of silica content, i.e., as rocks increased in silica content, higher temperatures were required to produce a velocity change.

Two-phase aggregates have received attention from a theoretical point of view. Equations for wave velocity and attenuation in a porous medium were initially developed by Biot (1956) and Eshelby (1957), and have been applied in recent years by several investigators. The results of theoretical calculations indicate that, in general, the wave velocity in the aggregate varies directly with wave velocity in the solid, inversely with fluid

compressibility, inversely with fluid concentration, and inversely with the flatness of the fluid inclusions (Iyer et al., 1980). Since these generalizations indicate that several factors affect the seismic velocity in a two-phase media, a single P-wave velocity cannot by itself, uniquely define the properties of a partial melt system. However, if some of these properties are known or assumed, a P-wave velocity measurement can yield some useful information.

The interpretation of a partial melt model for the northeastern low velocity zone in Yellowstone requires some theoretical considerations since experimental results are limited. O'Connell and Budiansky (1977) have calculated P- and S-wave velocities for fluid-saturated cracked solids and have shown specific applications to partial melts. The flow of fluids between randomly-oriented interconnected cracks is presented as the principle mechanism for seismic loss. In their riscoelastic model the most important parameter is crack density, $\varepsilon = (2N/\pi)(A^2/P)$ where N is the number of cracks per unit volume and A and P are the area and perimeter of the cracks, respectively. Extrapolation of the results of O'Connell and Budiansky (1977) to the observed velocity decrease of 30 percent for the northeastern low velocity zone implies a melt fraction of 5 percent to 30 percent by volume depending on the viscosity of the melt fluid and the frequency of the seismic signal. Figure 13 shows the melt percent as a function of the melt-fluid viscosity and wave frequency for a velocity decrease of 30 percent extrapolated from O'Connell and Budiansky (1977).

It should be noted that the aspect ratios of randomly oriented elliptical cracks have an important effect on the theoretical velocity decrease. For the data in Figure 13, aspect ratios of 10^{-1} - 10^{-4} were assumed with values near 10^{-1} dominating. Van der Molen and Paterson (1979)

have shown experimentally that, under hydrostatic conditions, melt is formed in granite along 90 percent of the grain boundaries. The melt films have random orientation and constant thickness throughout the speciman with a dominant aspect ratio of 10^{-1} (van der Molen and Paterson, 1979). Thus, it appears that the assumptions of O'Connell and Budiansky (1977) concerning random orientation and aspect ratios are geologically realistic.

Viscosity coefficients for molten rocks are highly variable, usually ranging from 10^1 to 10^8 P (Sakuma, 1953; Murase and Suzuki, 1966; Shaw, 1972; Murase and McBirney, 1973; O'Connell and Budiansky, 1977). For a rhyolitic magma with viscosity η equal to 10^6 P and a seismic frequency of 10 Hz typical of our P_g-recording, a velocity reduction of 30 percent implies a melt fraction of 9 percent. Based on laboratory meausurements melt concentrations of this magnitude are generally associated with granites at temperatures of 800-920°C (Arzi, 1978; van der Molen and Paterson, 1979).

Mavko (1980) has shown that if melt exists in a tubular geometry rather than as penny-shaped films assumed for O'Connell and Budiansky (1977) models, a larger melt fraction is required to effect a similar velocity decrease. In particular, a melt fraction of 25-30 percent would be necessary for the tubular geometry to produce the same 30 percent velocity decrease attributed to the 9 percent melt fraction in the film model (Mavko, 1980). The density of 2.40 g/cm^3 interpreted for the northeastern low velocity body from gravity modeling suggests a melt fraction of 50 percent based on the densities of rhyolitic magma and solid granite. Therefore, the theoretical results of O'Connell and Budiansky (1977) may represent a lower bound on the melt percent which, in the case of the northeastern 4.0 km/s low velocity body, may range from 10 to 50 percent.

The implication that high temperatures are associated with the northeastern low velocity zone is supported by other geological and geophysical

observations. The Hot Spring Basin Group, the largest hydrothermal system in the park, is located above the postulated low velocity zone (Figure 9). Because of the inaccessability of the area, few workers have visted the basin, however, the large amount of present-day fumerole activity and extensive native sulphur deposits suggests the presence of high temperatures (R. O. Fournier, personal communication, 1980) consistent with a shallow source of heat. Based on: (1) the areal distribution and magnitude of the velocity anomaly, (2) the evidence for unusually high temperatures, and (3) the Quaternary volcanic history of the caldera, the northeastern low-velocity zone may be interpreted as a zone of partial melt, felsic in composition with a melt fraction of 10 to 50 percent.

It should be emphasized that the theoretical derivation of seismic velocities by O'Connell and Budiansky (1977) assumes a random orientation of the fluid inclusions. While this assumption is supported by experimental observations under hydrostatic conditions, van der Molen and Paterson (1979) have shown that for conditions of differential stress, deformed specimens exhibit a thinning or complete absence of melt film along grain boundaries and cracks at a high angle to the maximum compressive principal stress while grain boundaries and cracks in nearly axial orientations show an increase in melt film thickness. Van der Molen and Paterson (1979) suggest that the preferred orientations, showing an increase in melt films normal to the least principal compressive stress, may contribute to anistropy in wave velocities through zones of partial melt. This suggestion when applied to Yellowstone, leads to some interesting observations.

No fault plane solutions have been determined for the immediate area around the northeastern low-velocity zone and it appears to be relatively aseismic compared to other areas of Yellowstone (Smith et al., 1977). However,

a series of northwest-trending normal faults display postglacial movement (Love, 1961) suggesting that the area has experienced northeast-southwest extension. Based on the results of van der Molen and Paterson (1979), this stress field could be responsible for anisotropy in the zone of partial melt resulting in a lower velocity for waves propogating in a southwestward direction relative to waves crossing in a southeastward direction. This is consistent with the seismic data as the several rays crossing the low velocity body from the northeast (shotpoint 1) arrive approximately 0.5 to 1 second later relative to the few rays which cross from the northwest (shopoint 6).

An interpretation of the NE-caldera 4.0 km/s low velocity body as a partial magma melt is attractive because of the presence of the Quaternary volcanism and the high heat flow that infer a close magmatic association. However interpretation attributes at least part of the low velocity body to the presence of a large volume of steam and water associated with the hydrothermal activity that is evident from the presence of the Hot Springs Basin. This model, a gas phase (steam), can occur from the surface to the critical temperature $\sim$370°C corresponding to the critical 1-2 km (Morgan et al., 1977), i.e. the corresponding depth at which steam is indistinguishable from water. A large volume of steam in a highly porous media can produce the same 30% velocity reduction. In this model the 4.0 km/s low velocity zone may be a composite; the upper-portion above the critical depth composed of steam filled fractured and altered rhyolites and the lower portion, a hot water filled porous body located above a partial melt. The detailes of the body configuration are not resolvable with our data, i.e. only the average velocity and density can be resolved.

We have shown in the previous section that the low-velocity body appears to extend to midcrustal depths of at least 13 km, far below a critical depth of 1-2 km and would argue for a partial melt at depth.

Interpretation of the southwest caldera, 4.0 km/s low-velocity zone, near Old Faithful, is not conclusive but interpretation of profile 2A2BENE indicates that a velocity decrease of 30 percent occurs between shotpoint 2A2B and West Thumb. There is a possibility that this postulated low velocity zone may represent a zone of high attenuation with no significant velocity constrast with respect to the surrounding crust. Figure 14 shows two seismograms from shotpoint 2B recorded at about 6 km west of West Thumb. The pick shown for station 2755 was identified as a first arrival associated with the P_g-branch, thought to have been delayed by the low velocity body. While a sharp increase in amplitude occurs at the same time at station 410, there is also an emergent phase about 1 second earlier best seen at station 410. If this earlier pick is indeed the P_g-arrival, then an interpretation would not require the presence of a 4.0 km/s low velocity body. Therefore, it is possible that the delayed arrivals used to define the southwestern low velocity body were actually later arrivals that passed below the zone of high attenuation, while the first arrivals passing through the body have been attenuated so much that the seismic signals cannot be seen above the noise level.

If however, the interpreted velocity decrease of 30 percent estimated for the southwestern low velocity body is correct, the partial melt interpretation is consistent with the observation of extensive hydrothermal features in the area. The postulated low velocity body is located beneath the Lower, Midway, and Upper Geyser Basins where the convective heat flow ranges from 41,000 to 58,000 mW/m^2 (Fournier et al., 1976). To the south, the low velocity

body underlies the Shoshone Geyser Basin, several hot springs, and volcanic vents associated with some of the youngest (70,000-105,000 yrs) rhyolite flows in the park.

The southwestern low velocity zone is elongated in the north-south direction (Figure 6) consistent with trends of Cenozoic structures to the south of the Yellowstone caldera. Smith and Christiansen (1980) suggest that a fault zone associated with the uplift of the Teton range may extend northward beneath the rhyolitic flows of the caldera. Thus a northward extension of the Teton fault zone beneath the Quaternary volcanic flows would coincide with this postulated low-velocity zone and could provide a conduit for the flow of magma or hot waters into the upper-crust. Also, if the extensional stress regime associated with the Teton fault persists within the caldera, a greater decrease in velocity would be expected in the east-west direction relative to the north-south (van der Molen and Paterson, 1979). Though only four raypaths cross the low velocity body in a northerly direction, these few arrivals show no large delays such as observed on profile 2A2BENE.

The presence of a partial melt responsible for the southwestern low velocity zone is not, however, indicated by the gravity data (Figure 9). One possible explanation for the lack of a significant density contrast is that the melt zone is more mafic in composition than the "granitic" layer within which it lies. Basalt melts commonly have densities similar to crystalline granite (Murase and McBirney, 1973), and therefore, no significant density contrast would be expected.

Interpretations other than the partial melt model can also be applied to the southwestern low velocity body with less drastic assumptions than a change in state as suggested above. The flow of water in a fractured zone could also cause a velocity decrease similar to that described for a partial

melt (O'Connell and Budiansky, 1977). If the flow was distributed along north-trending fractures, a small amount of water could give rise to the variable delay pattern observed in the seismic data (van der Molen and Paterson, 1979). This interpretation also correlates with the surface hydrothermal phenomena whose location may be controlled by northward extension of the Teton fault zone.

CONCLUSIONS

A geologic model for the upper-20 km crust beneath Yellowstone National Park has been interpreted from seismic refraction and gravity data. This three-dimensional model includes lateral variations in velocity and density that are thought to reflect a heterogeneous composition and effects of high temperature. Figure 15 summarizes a geologic interpretation of the seismic and gravity data and demonstrates four anomalous crustal layers relative to the "normal" crustal section outside the Yellowstone volcanic area of Tertiary basic breccias and Paleozoic sediments overlying Precambrian granitic gneisses. These anomalous features include: (1) a 2.8 km/s surface layer of rhyolite flows, and lake sediments that form the surface deposits of caldera and ranges in thickness from 1.5 to 2.0 km; (2) a 13 to 16 km thick 5.7 ±0.05 km/s layer of inferred granitic composition whose horizontal extent includes the Yellowstone caldera and a portion of the northeast section of the park. This layer appears to be hot; (3) a 4.0 ±0.5 km/s body northeast of the caldera rim, that can be modeled as a partial-melt or a highly porous steam or mixed steam/hot water body with an areal extent of 200 km^2 that extends from near-surface to 2 km below sea level to a depth of 11 to 15 km; and (4) a fluid-filled fracture zone in the Upper Geyser Basin area that exhibits low velocity or possibly high attenuation.

In this framework, the Yellowstone "Hot Spot", with regard to its expression in the crust, is largely associated with a cooling granitic batholith that extends to mid-crustal depth of ~15 km as suggested by Daly (1911) and more recently by R. L. Christiansen (written communication, 1978). However contemporary uplift of up to 15 mm/yr measured across the

Yellowstone caldera (Pelton and Smith, 1979) indicates that magmatic resurgence may be taking place within a region that may be coincident within the 5.7 km/s body. The low velocity 4.0 km/s body appears to represent zones of high temperatures associated with zones of partial melt or large steam volumes near the Hot Springs Basin group or simply fluid saturated fracture zones.

In conclusion, the seismic refraction data and crustal model presented here were best interpreted with restraints from gravity and heat flow data combined with geologic models. Geologic models such as those in Figure 15 can provide useful constraints and initial models for other interpretations such as the inversion of local earthquake data and teleseismic P-wave delays, crustal uplift models, magma volume generation, etc.

REFERENCES

Arzi, A. A., Critical phenomena in the rheology of partially melted rocks, Tectonophysics, 44, 173-184, 1978.

Biot, M. A., Theory of propagation of elastic waves in a fluid-saturated porous solid. I. Low-frequency range, J. Acoust. Soc. Am., 28, 162-178, 1956

Birch, F., The velocity of compressional waves in rocks to 10 kilobars, Part 2, J. Geophys. Res., 66, 2199-2224, 1961.

Black, P. R., Seismic and thermal constraints on the physical properties of the continental crust, Ph.D. thesis, Purdue University, Indiana, 1978.

Blank, H. R., Jr., and Gettings, M. E., Complete Bouguer Gravity Map: Yellowstone-Island Park Region, U.S. Geological Survey Open-file Map 74-22, 1974.

Brown, C. W., Cenozoic stratigraphy and structural geology, northeast Yellowstone Park, Wyoming and Montana, Geol. Soc. Am. Bull., 72, 1173-1193, 1961

Christensen, N. I., Compressional wave velocities in rocks at high temperatures and pressures, critical thermal gradients, and crustal low-velocity zones, J. Geophys. Res., 84, 6849-6857, 1979.

Christiansen, R. L., and H. R. Blank, Jr., Volcanic stratigraphy of the Quaternary rhyolite plateau in Yellowstone National Park, U.S. Geological Survey Professional Paper 729-B, 18 pp, 1972.

Chung, D. H., Birch's law: why is it so good? Science, 177, 261-263, 1972.

Daly, R. A., The nature of volcanic action, Proc. Am. Acad. Arts. Sci. 47, 45-122, 1911.

Eaton, G. P., R. L. Christiansen, H. M. Iyer, A. M. Pitt, D. R. Mabey, H. R. Blank, Jr., I. Zietz, and M. E. Gettings, Magma beneath Yellowstone National Park, Science, 188, 787-796, 1975.

Eshelby, J. D., The determination of the elastic field of an ellipsoidal inclusion, and related problems, Proc. Roy. Soc. London, Ser. A, 241, 376-396, 1957.

Evoy, J. A., Precision gravity reobservations and simultaneous inversion of gravity and seismic data for subsurface structure of Yellowstone, M.S. thesis, University of Utah, Salt Lake City, Utah, 1978.

Fielitz, K., Elastic wave velocities in different rocks at high pressure and temperature up to 750°C, Z. Geophys., 37, 943-946, 1971.

Fournier, R. O., D. E. White, and A. H. Truesdell, Convective heat flow in Yellowstone National Park, in Proceedings of the Second U.N. Symposium on Development and Use of Geothermal Resources, 1, 731-739, U.S. Government Printing Office, Washington D. C., 1976.

Iyer, H. M., J. R. Evans, G. Zandt, R. M. Stewart, J. Coakley, and J. Ruloff, A deep magma body under the Yellowstone caldera: Delineation using teleseismic P-wave residuals and tectonic interpretation, Geol. Soc. Am. Bull., in press, 1981.

Kern, H., The effect of high temperature and high confining pressure on compressional wave velocities in quartz-bearing and quartz-free igneous and metamorphic rocks, Tectonophysics, 44, 185-203, 1978.

Love, J. D., Reconnaissance study of Quaternary faults in and south of Yellowstone National Park, Wyoming, Geol. Soc. Am. Bull., 72, 1749-1764, 1961.

Mavko, G. M., Velocity and attenuation in partially molten rocks, J. Geophys. Res., 85, 5173-5189, 1980.

Morgan, P., D. D. Blackwell, R. E. Spafford, and R. B. Smith, Heat flow measurements in Yellowstone Lake and the thermal structure of the Yellowstone caldera, J. Geophys. Res., 82, 3710-3732, 1977.

Murase, T., and A. R. McBirney, Properties of some common igneous rocks and their melts at high temperatures, Geol. Soc. Am. Bull., 84, 3563-3592, 1973.

Murase, T., and T. Suzuki, Ultrasonic velocities of longitudinal waves in molten rocks, J. Fac. Sci. Hokkaido Univ., Ser. VII, 2, 272-285, 1966.

Nur, A., Dilatancy, pore fluids, and premonitory variations of t_s/t_p travel times, Bull. Seismol. Soc. Am., 62, 1217-1222, 1972.

O'Connell, R. J., and B. Budiansky, Viscoelastic properties of fluid-saturated cracked solids, J. Geophys. Res., 82, 5719-5735, 1977.

Otis, R. M., R. B. Smith, and R. J. Wold, Geophysical surveys of Yellowstone Lake, Wyoming, J. Geophys. Res., 82, 2705-2717, 1977.

Plouff, D., Derivation of formulas and FORTRAN programs to compute gravity anomalies of prisms, U.S. Geological Survey Open-file Report USGS-GD-75-015, 90 pp., 1975.

Sakuma, S., Elastic and viscous properties of volcanic rocks at high temperatures. Part 3. Oosima lava, Bull. Earthq. Res. Inst., 31, 291-303, 1953.

Schilly, M. M., Interpretation of crustal seismic refraction and reflection profiles from Yellowstone and the eastern Snake River Plain, M.S. thesis, Univ. of Utah, Salt Lake City, Utah, 1979.

Schilly, M. M., R. B. Smith, J. Ansorge, J. H. Lehman, and L. W. Braile, Detailed crustal structure of the Yellowstone region, Jour. Geophy Res. (this volume), 1981.

Shaw, H. R., Viscosities of magmatic silicate liquids: an empirical method of prediction, Am. J. Sci., 272 870-893, 1972.

Smith, R. B. and R. L. Christiansen, Yellowstone Park as a window on the earth's interior, Sci. Am., 242, 104-117, 1980.

Smith, R. B., L. W. Braile, M. M. Schilly, J. Ansorge, C. Prodehl, M. Baker, J. H. Healey, St. Mueller, and R. Greensfelder, The Yellowstone-Snake River Plain seismic profiling experiment: General crustal structure of Yellowstone, Jour. Geophys. Res., (this volume), 1981.

Smith, R. B., R. T. Shuey, J. R. Pelton, and J. P. Bailey, Yellowstone hot spot: Contemporary tectonics and crustal properties from earthquake and aeromagnetic data, J. Geophys. Res., 82, 3665-3676, 1977.

Smith, R. L., and H. R. Shaw, Igneous-related geothermal systems, Assessment of Geothermal Resources of the United States-1975, U.S. Geological Survey Circ. 726, 58-83, 1975.

Smithson, S. B., Densities of metamorphic rocks, Geophysics, 36, 690-694, 1971.

Smithson, S. B., and E. R. Decker, A. Continental crustal model and its geothermal implications, Earth and Planetary Science Letters, 22, 215-225, 1974.

Smithson, S. B., and R. J. Ebens, Interpretation of data from a 3.05 km borehole in Precambrian crystalline rocks, Wind River Mountains, Wyoming, J. Geophys. Res., 76, 7079-7087, 1971.

Spencer, J. W., Ultrasonic velocities in rocks under crustal conditions, Ph.D. thesis, Stanford University, California, 1975.

Talwani, M., and M. Ewing, Rapid computation of gravitational attraction of three-dimensional bodies of arbitrary shape, Geophysics, 25, 203-225, 1960.

Todd, T., and G. Simmons, Effect of pore pressure on the velocity of compressional waves in low-porosity rocks, J. Geophys. Res., 77, 3731-3743, 1972.

U.S. Geological Survey, Geologic Map of Yellowstone National Park, U.S. Geological Survey Miscellaneous Geologic Investigations Map I-711, 1972.

van der Molen, I. and M. S. Paterson, Experimental deformation of partially-melted granite, Contrib. Mineral. Petrol., 70, 299-318, 1979.

White, D. E., R. O. Fournier, L. J. P. Muffler, and A. H. Truesdell, Physical results of research drilling in thermal areas of Yellowstone National Park, Wyoming, U.S. Geological Survey Professional Paper 892, 70 pp., 1975.

Zandt, G., Study of three-dimensional heterogeneity beneath seismic arrays in central California and Yellowstone, Wyoming, Ph.D. thesis, Massachusetts Institute of Technology, Massachusetts, 1978.

Table 1. P_g-velocities in the Yellowstone area

Profile	Geographic Area	P_g-Velocity (km/s)	Number of Observations
Outer Caldera			
6S	Mammoth-Norris	6.05	5
G9S	Jackson Lake-Jackson	6.06	11
1SW	Tower Jct.-Madison Jct.	6.06	17
1W	Shotpoint 1-Mammoth	5.95	11
GE	Mammoth-Shotpoint 1	6.13	9
Inner Caldera			
6SE	Norris-Fishing Bridge	5.75	4
6S	Madison Jct.-Pitchstone Plateau	5.65	11
G9N	West Thumb-Madison Jct.	5.72	10
G9NNE	Pitchstone Plateau-Fishing Bridge	5.70	12

Table 2. Shotpoint Delay Times, a_s; P-wave Velocities; and Layer Thickness For Near-Surface Layering At Yellowstone

Shotpoint	Azimuth Range (degrees)	Layer Velocity (km/s)	Layer Thickness (km)	a_s (sec)
1	180-360	4.8	0.8	.10
6	0-110	3.6 4.8	0.5 2.5	.43
6	111-360	3.6	1.4	.31
G9	35-210	3.6 4.8	1.1 2.0	.50
2A2B	0-180	3.0 4.9	1.0 4.4	.82
9	90-160	3.6	2.7	.60
9	170-89	3.6	1.8	.40

ILLUSTRATION CAPTIONS

Figure 1. Map of Yellowstone region showing seismic stations, shotpoint locations and profiles.

Figure 2. Seismic profile 6S, western Yellowstone National Park.

Figure 3. Profile 1W, northern Yellowstone National Park.

Figure 4a. Delay-time model: layer over a half-space with an irregular interface.

Figure 4b. Delay-time model: layer over a half-space with an irregular interface and horizontally inhomogeneous velocity distribution.

Figure 5. Station delay times for P_g-branch in Yellowstone. All values are positive.

Figure 6. Map showing distribution of surface-layer velocities used in delay-time analysis. Where two layers were present above the P_g-layer, both velocities (km/s) and the thickness (km) of the top layer (in parentheses) are given.

Figure 7. Map of raypath coverage for Yellowstone used in delay-time analysis.

Figure 8. Map of upper-crustal P_g-velocity distribution in Yellowstone.

Figure 9. Map of P_g-velocity distribution, complete Bouguer gravity field, and hydrothermal areas of Yellowstone.

Figure 10. Map of depths to the top of the P_g-layer in Yellowstone.

Figure 11. Complete Bouguer gravity map of Yellowstone (modified from Blank and Gettings, 1974). Gravity stations shown by triangles. Profile A-A' is line of density-velocity cross-section.

Figure 12. Northeast-southwest cross-sections through three-dimensional seismic P-wave velocity model (a) and corresponding density model (b).

Figure 13. Crack density and corresponding melt percent (by volume) necessary for a 30% velocity decrease as a function of melt fluid viscosity and wave frequency (modified from O'Connell and Budiansky, 1977).

ILLUSTRATION CAPTIONS (continued)

Figure 14. Portion of seismic profile 2A2BENE recorded near West Thumb that displays possible ambiguity in phase identification.

Figure 15. Geologic cross-section through the upper-crust of Yellowstone based on interpretation of seismic refraction and gravity data. See Figure 11 for cross-section location.

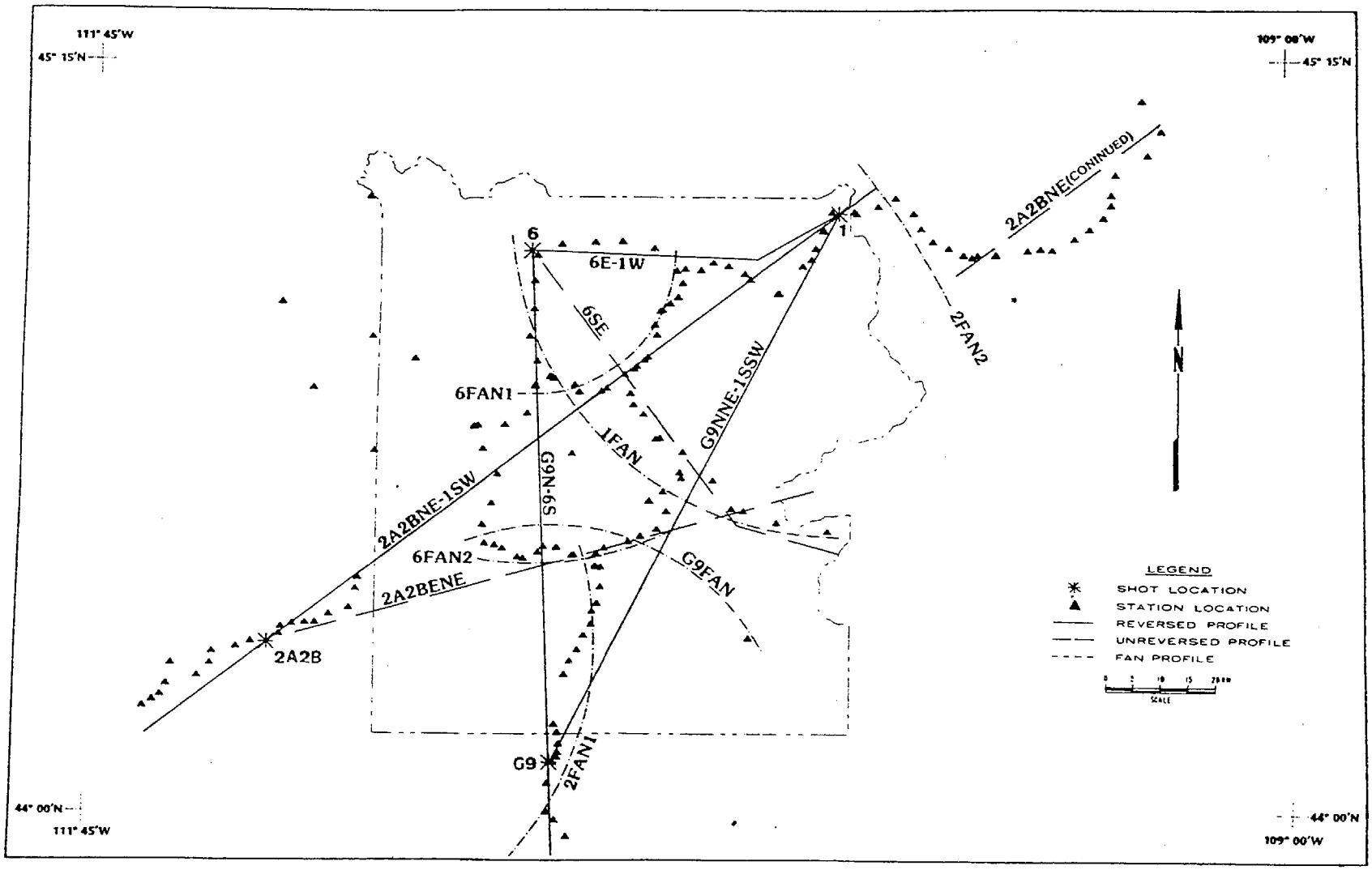
111° 45'W
45° 15'N
109° 00'W
45° 15'N
6
6E-1W
1
2A2BNE(CONTINUED)
6SE
2FAN2
6FAN1
1FAN
G9NNE-1SSW
2A2BNE-1SW
G9N-6S
6FAN2
G9FAN
2A2BENE
2A2B
G9
2FAN1
N
LEGEND
SHOT LOCATION
STATION LOCATION
REVERSED PROFILE
UNREVERSED PROFILE
FAN PROFILE
SCALE
44° 00'N
111° 45'W
44° 00'N
109° 00'W

Figure 1

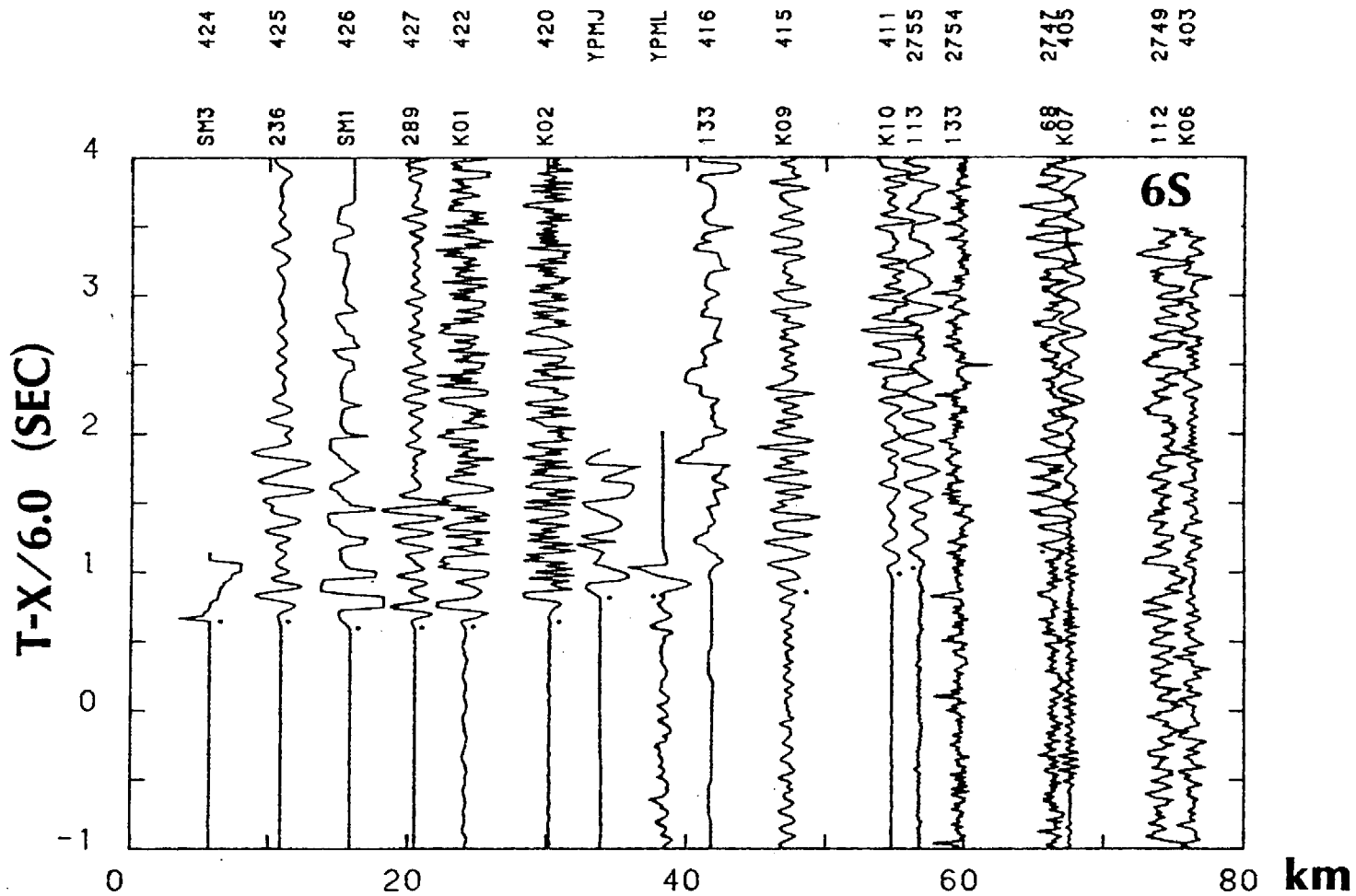
T-X/6.0 (SEC)
4
3
2
1
0
-1
0
20
40
60
80
km
6S
SM3 424
236 425
SM1 426
289 427
K01 422
K02 420
YPMJ
YPML
133 416
K09 415
K10 411
113 2755
133 2754
K08 2747
K07 405
112 2749
K06 403

Figure 2

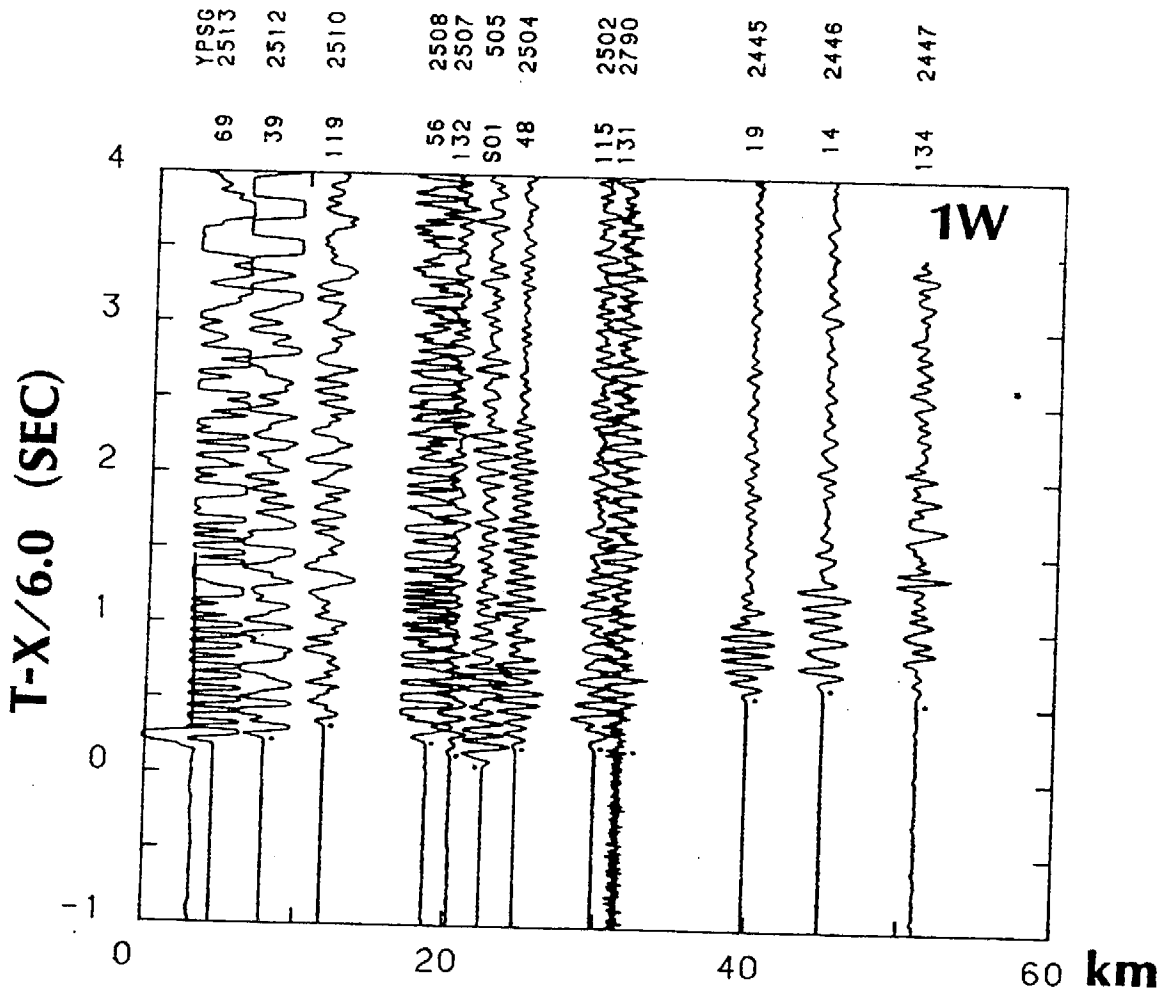
YPSG
2513
2512
2510
2508
2507
505
2504
2502
2790
2445
2446
2447
69
39
119
56
132
501
48
115
131
19
14
134
1W
T-X/6.0 (SEC)
4
3
2
1
0
-1
0
20
40
60
km

Figure 3

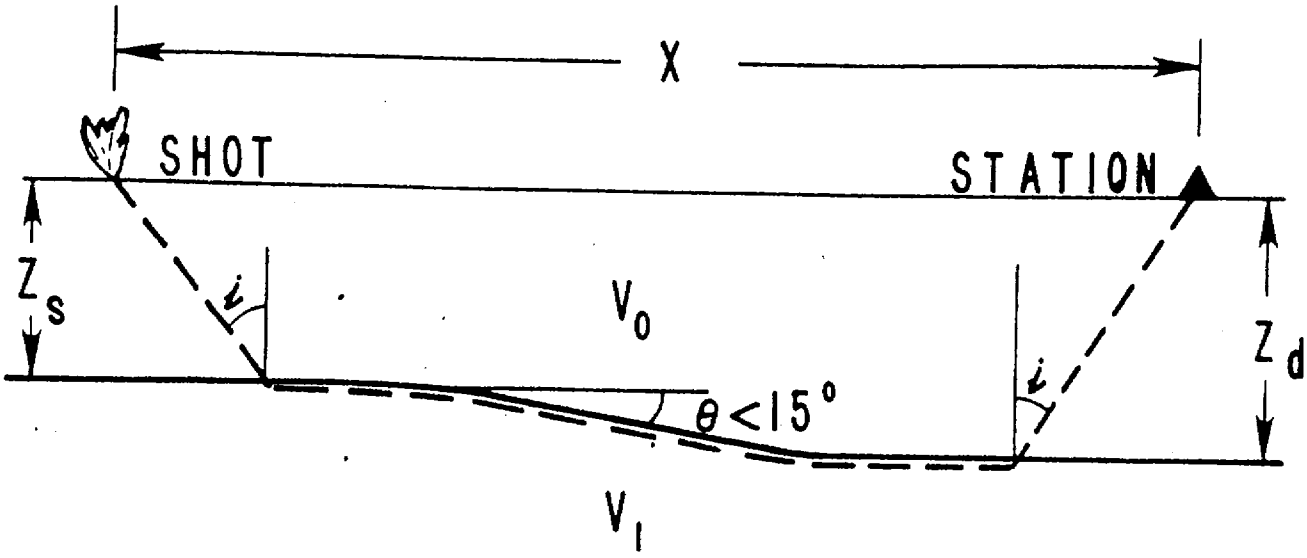
X
SHOT
STATION
Z_s
i
V_0
Z_d
$\theta < 15°$
V_1

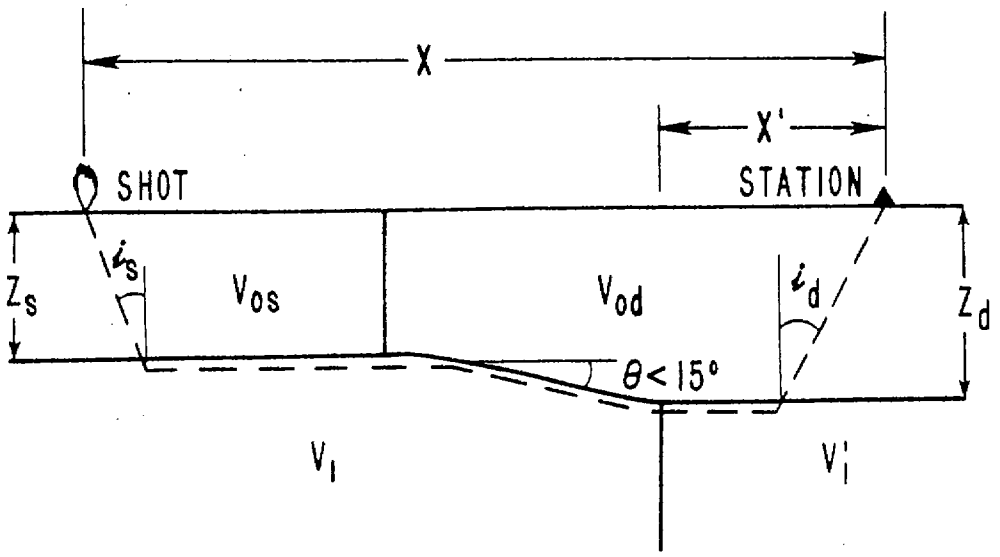
X
X'
SHOT
STATION
Z_s
i_s
V_{os}
V_{od}
i_d
Z_d
$\theta < 15°$
V_1
V_1'

Figure 4

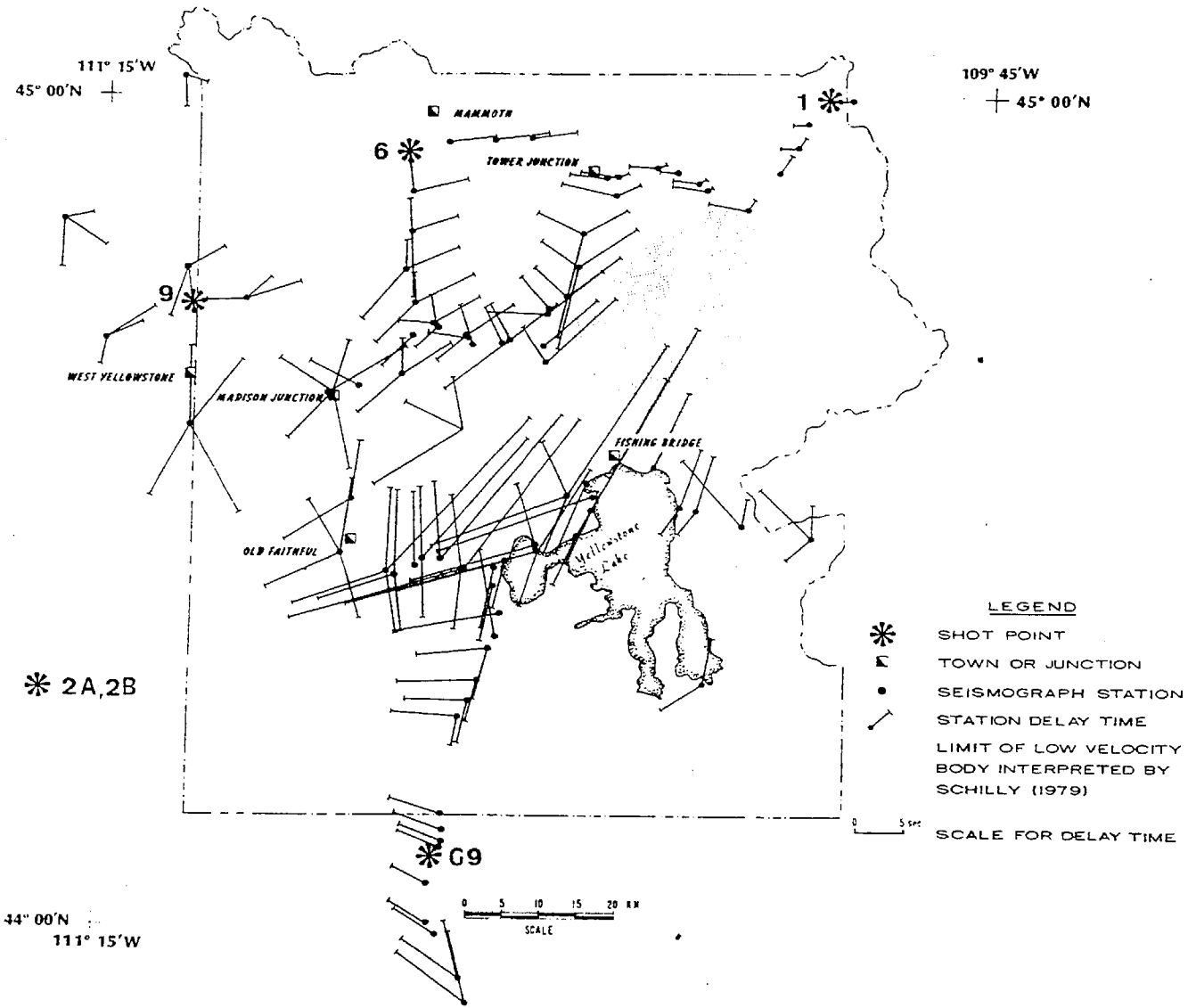
111° 15'W
45° 00'N
109° 45'W
45° 00'N
MAMMOTH
TOWER JUNCTION
WEST YELLOWSTONE
MADISON JUNCTION
FISHING BRIDGE
OLD FAITHFUL
Yellowstone Lake
1
6
9
2A,2B
G9
0 5 10 15 20 KM
SCALE
44° 00'N
111° 15'W
LEGEND
SHOT POINT
TOWN OR JUNCTION
SEISMOGRAPH STATION
STATION DELAY TIME
LIMIT OF LOW VELOCITY BODY INTERPRETED BY SCHILLY (1979)
0 5 sec
SCALE FOR DELAY TIME

Figure 5

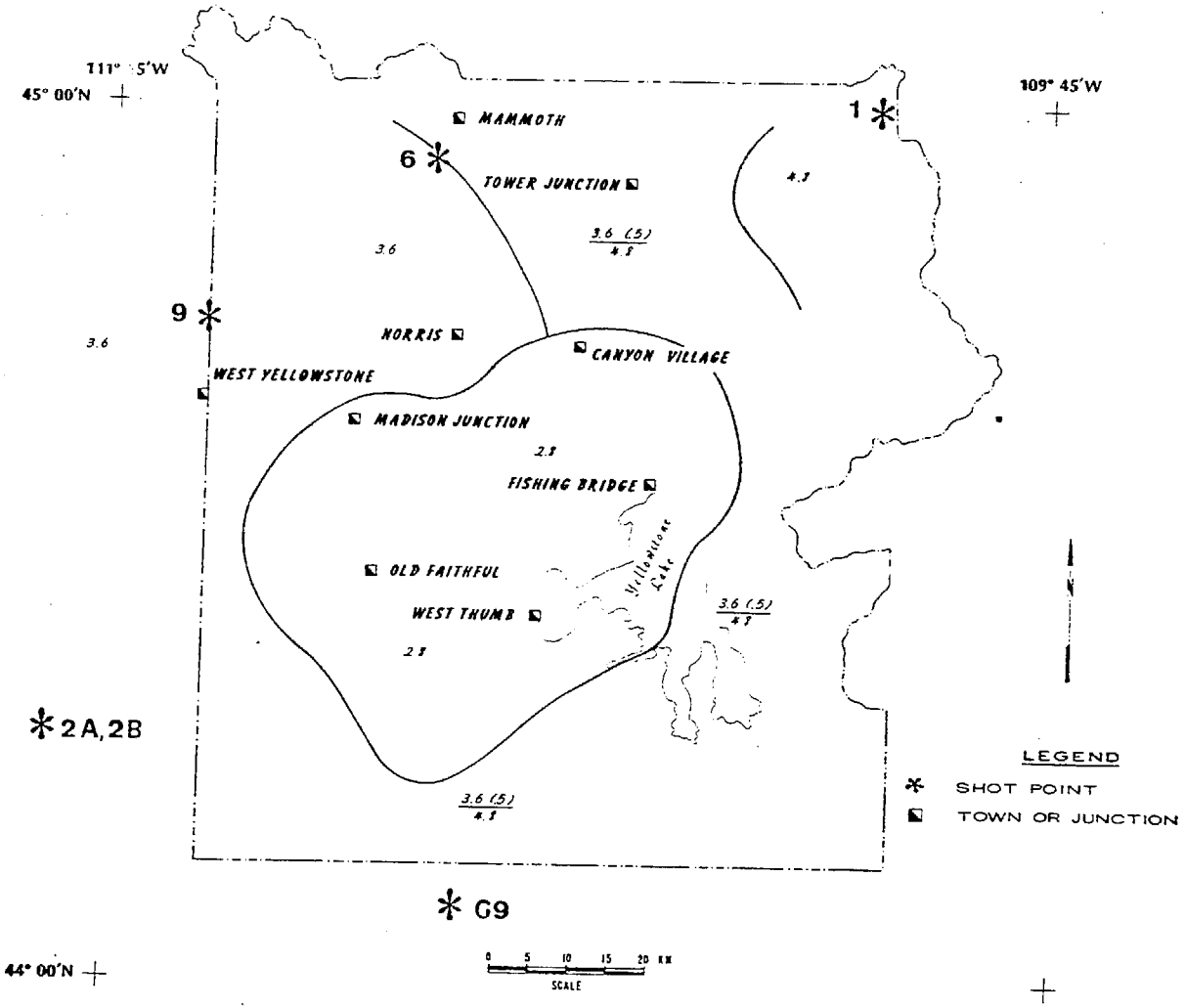
111° 15'W
45° 00'N
109° 45'W
MAMMOTH
TOWER JUNCTION
NORRIS
CANYON VILLAGE
WEST YELLOWSTONE
MADISON JUNCTION
FISHING BRIDGE
OLD FAITHFUL
WEST THUMB
Yellowstone Lake
1
6
9
2A,2B
G9
3.6
4.3
2.3
3.6 (5)
4.3
LEGEND
SHOT POINT
TOWN OR JUNCTION
44° 00'N
0 5 10 15 20 KM
SCALE

Figure 6

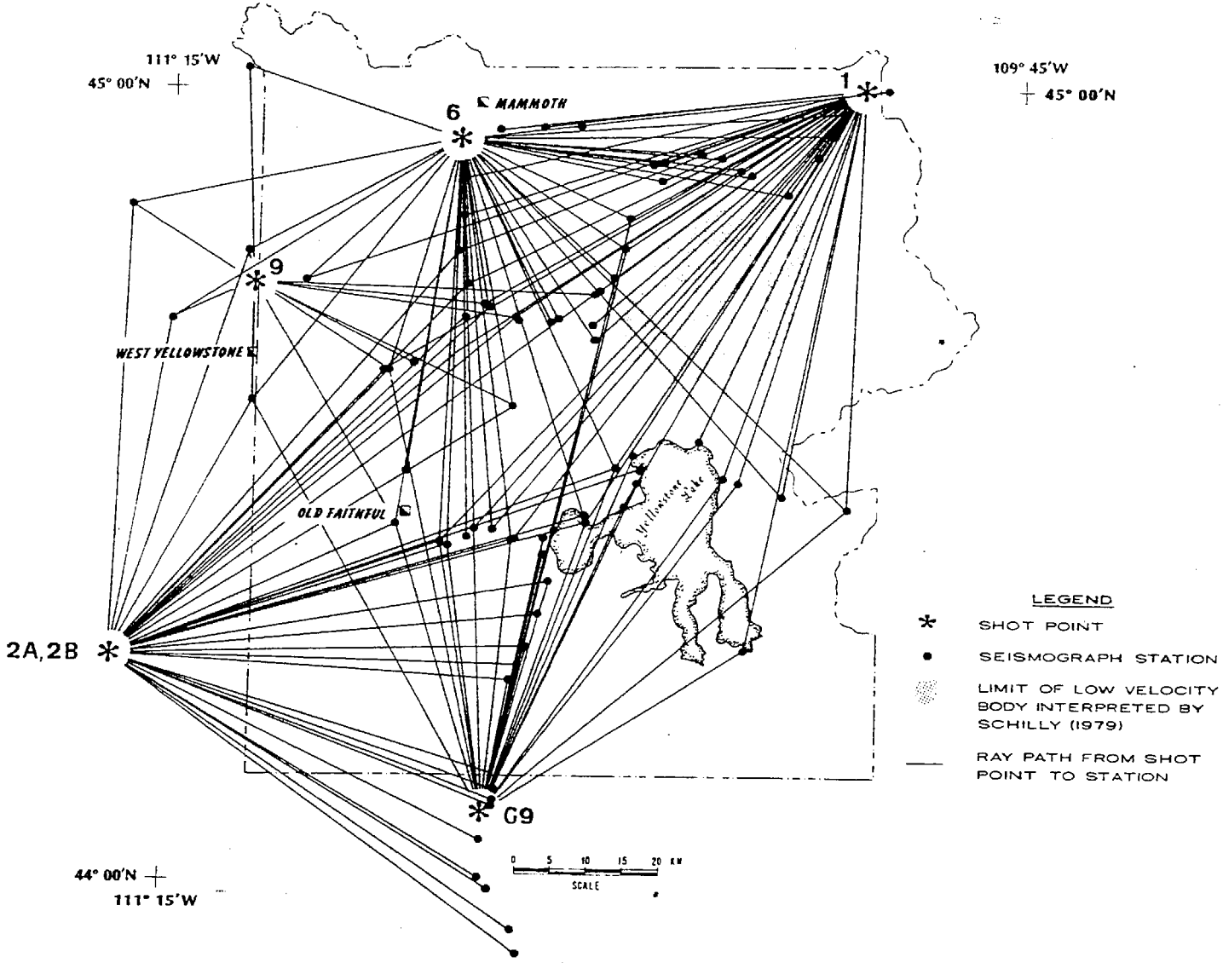
111° 15'W
45° 00'N
109° 45'W
45° 00'N
1
6
MAMMOTH
9
WEST YELLOWSTONE
OLD FAITHFUL
Yellowstone Lake
2A,2B
G9
44° 00'N
111° 15'W
0 5 10 15 20 KM
SCALE
LEGEND
SHOT POINT
SEISMOGRAPH STATION
LIMIT OF LOW VELOCITY BODY INTERPRETED BY SCHILLY (1979)
RAY PATH FROM SHOT POINT TO STATION

Figure 7

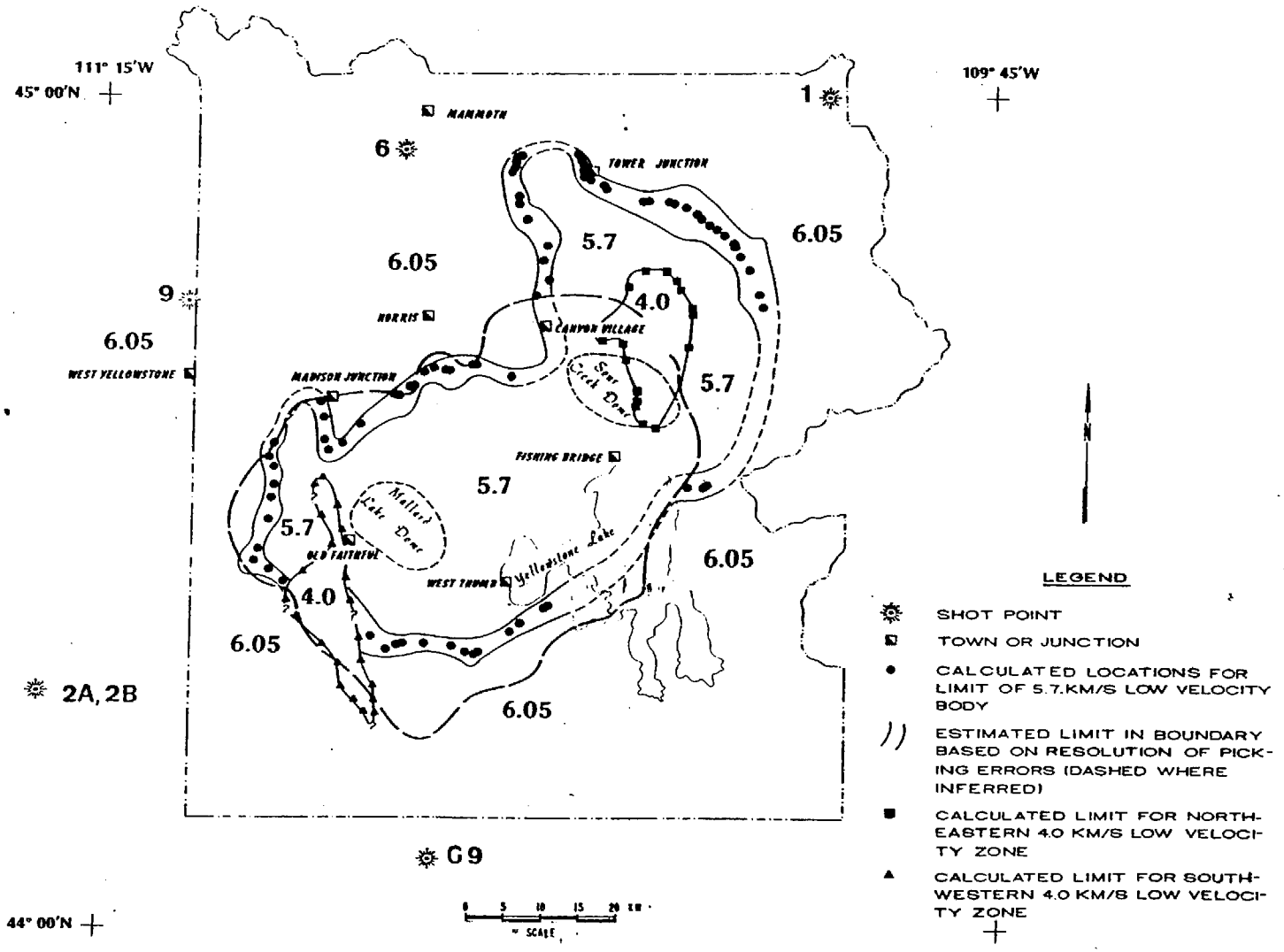
111° 15'W
45° 00'N
109° 45'W
MAMMOTH
TOWER JUNCTION
NORRIS
CANYON VILLAGE
WEST YELLOWSTONE
MADISON JUNCTION
FISHING BRIDGE
OLD FAITHFUL
WEST THUMB
Yellowstone Lake
6.05
5.7
4.0
1
2A, 2B
G9
44° 00'N
LEGEND
SHOT POINT
TOWN OR JUNCTION
CALCULATED LOCATIONS FOR LIMIT OF 5.7 KM/S LOW VELOCITY BODY
ESTIMATED LIMIT IN BOUNDARY BASED ON RESOLUTION OF PICKING ERRORS (DASHED WHERE INFERRED)
CALCULATED LIMIT FOR NORTHEASTERN 4.0 KM/S LOW VELOCITY ZONE
CALCULATED LIMIT FOR SOUTHWESTERN 4.0 KM/S LOW VELOCITY ZONE

Figure 8

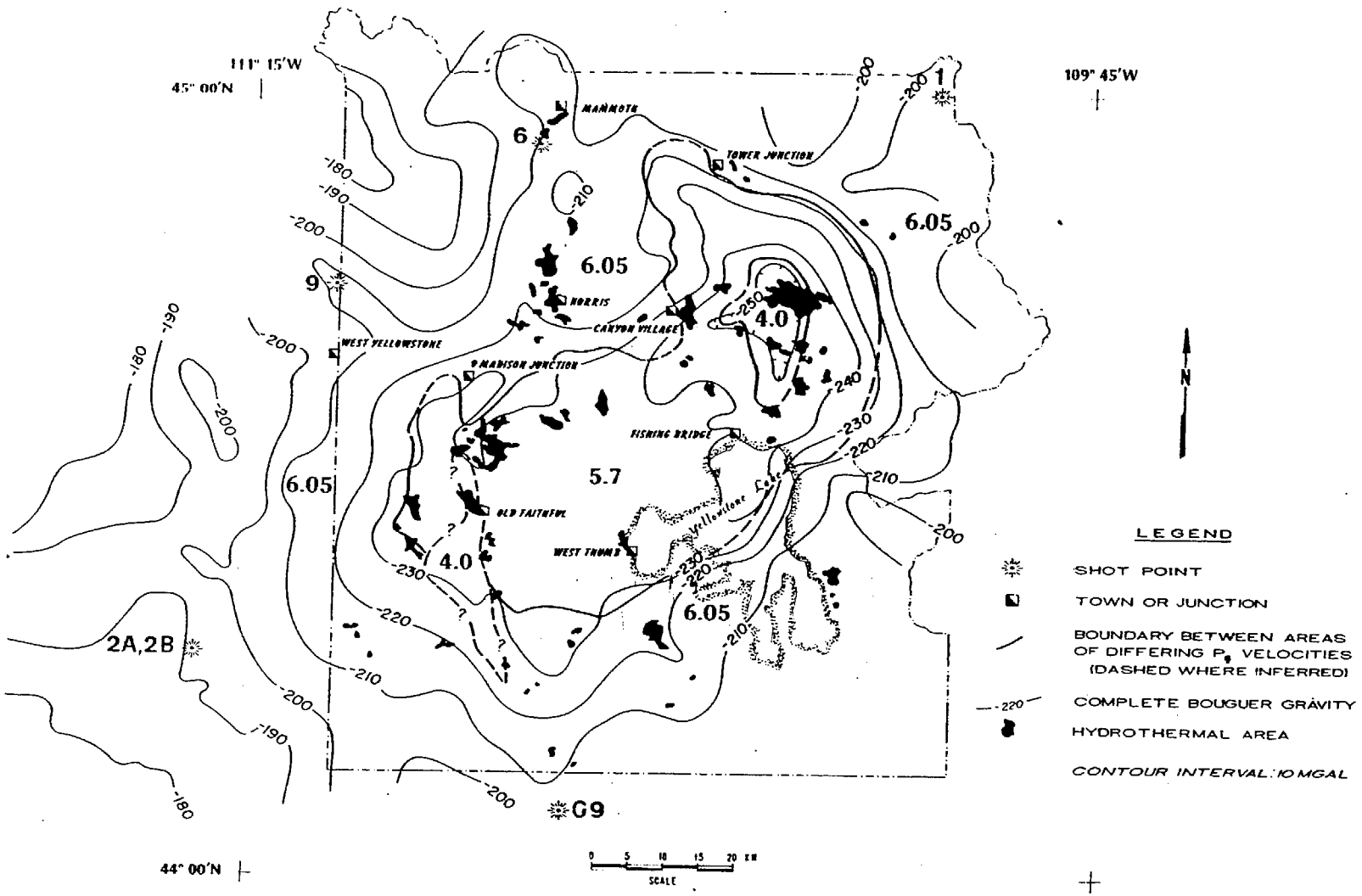
111° 15'W
45° 00'N
109° 45'W
44° 00'N
MAMMOTH
TOWER JUNCTION
NORRIS
CANYON VILLAGE
WEST YELLOWSTONE
MADISON JUNCTION
FISHING BRIDGE
OLD FAITHFUL
WEST THUMB
Yellowstone Lake
6
1
9
2A,2B
G9
6.05
5.7
4.0
LEGEND
SHOT POINT
TOWN OR JUNCTION
BOUNDARY BETWEEN AREAS OF DIFFERING P_g VELOCITIES (DASHED WHERE INFERRED)
COMPLETE BOUGUER GRAVITY
HYDROTHERMAL AREA
CONTOUR INTERVAL 10 MGAL
N
0 5 10 15 20 KM
SCALE

Figure 9

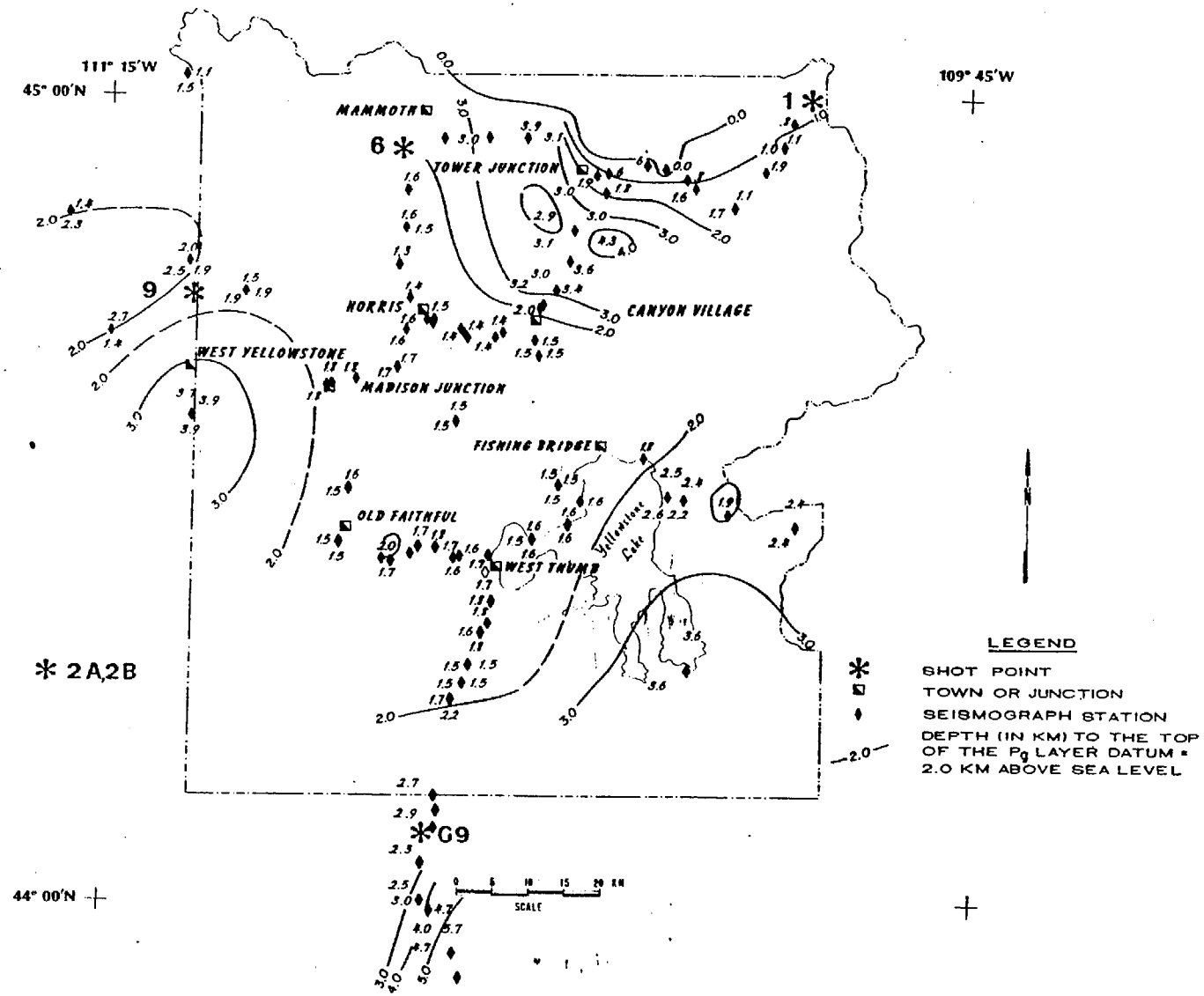
111° 15'W
45° 00'N
109° 45'W
44° 00'N
MAMMOTH
TOWER JUNCTION
NORRIS
CANYON VILLAGE
WEST YELLOWSTONE
MADISON JUNCTION
FISHING BRIDGE
OLD FAITHFUL
WEST THUMB
Yellowstone Lake
1
6
9
2A,2B
G9
SCALE
0 5 10 15 20 KM
LEGEND
SHOT POINT
TOWN OR JUNCTION
SEISMOGRAPH STATION
DEPTH (IN KM) TO THE TOP OF THE Pg LAYER DATUM = 2.0 KM ABOVE SEA LEVEL

Figure 10

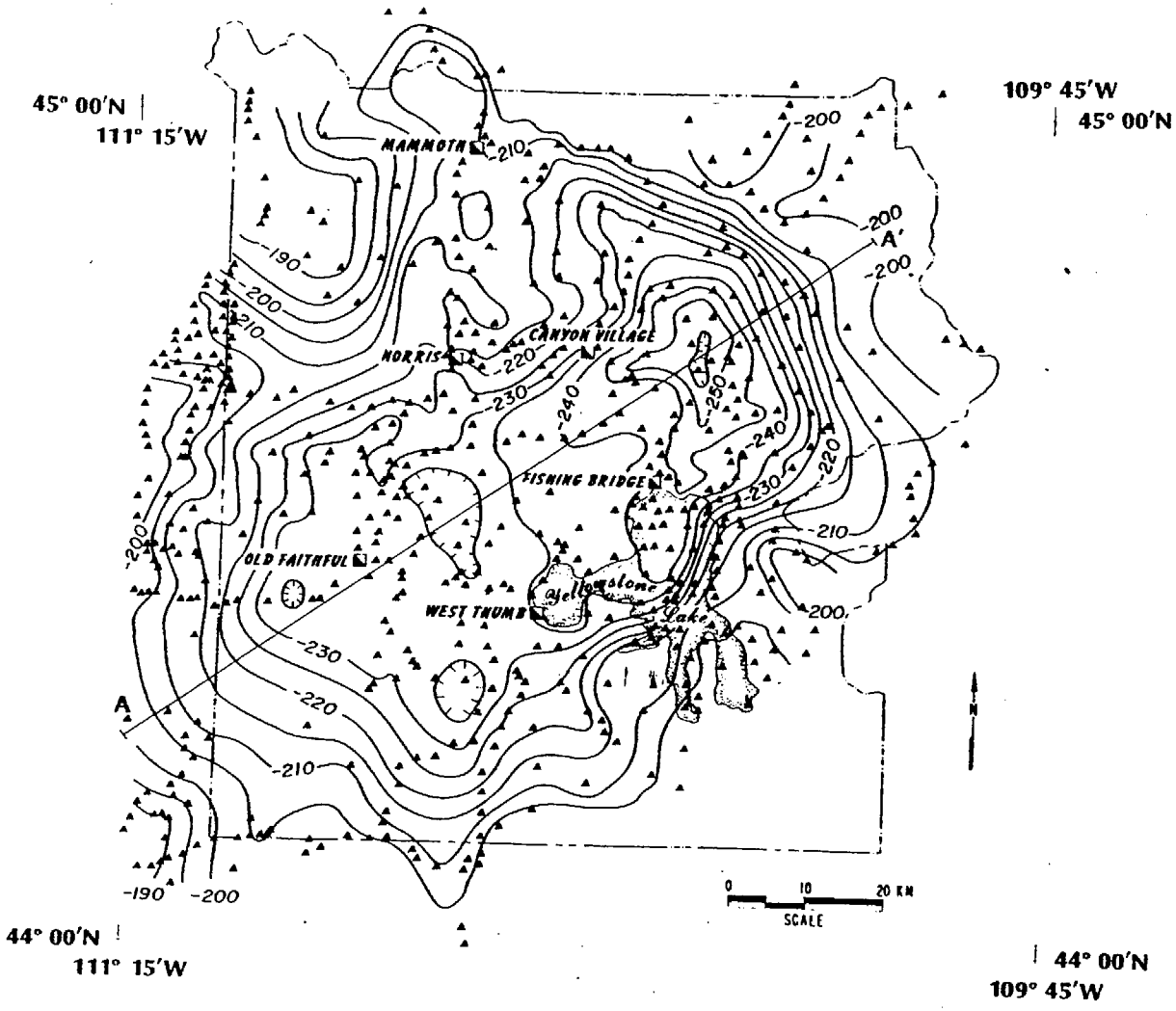
45° 00'N
111° 15'W
109° 45'W
45° 00'N
MAMMOTH
NORRIS
CANYON VILLAGE
FISHING BRIDGE
OLD FAITHFUL
WEST THUMB
Yellowstone Lake
A
A'
-190
-200
-210
-220
-230
-240
-250
N
0 10 20 KM
SCALE
44° 00'N
111° 15'W
44° 00'N
109° 45'W

Figure 11

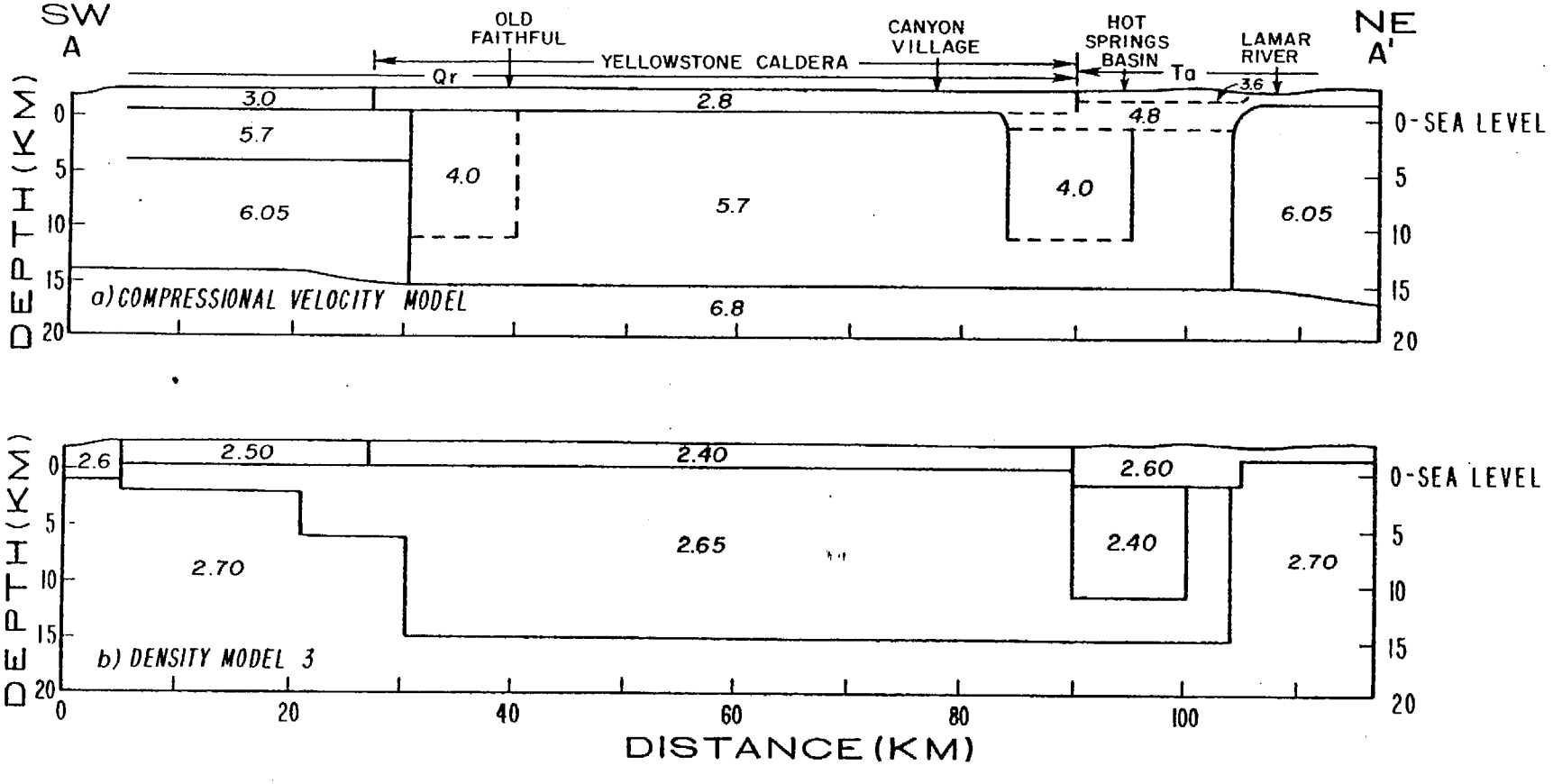
SW
A
NE
A'
OLD FAITHFUL
YELLOWSTONE CALDERA
CANYON VILLAGE
HOT SPRINGS BASIN
LAMAR RIVER
Qr
Ta
3.6
3.0
2.8
4.8
5.7
4.0
6.05
5.7
4.0
6.05
6.8
a) COMPRESSIONAL VELOCITY MODEL
DEPTH (KM)
0-SEA LEVEL
2.6
2.50
2.40
2.60
2.70
2.65
2.40
2.70
b) DENSITY MODEL 3
0
20
40
60
80
100
DISTANCE (KM)

Figure 12

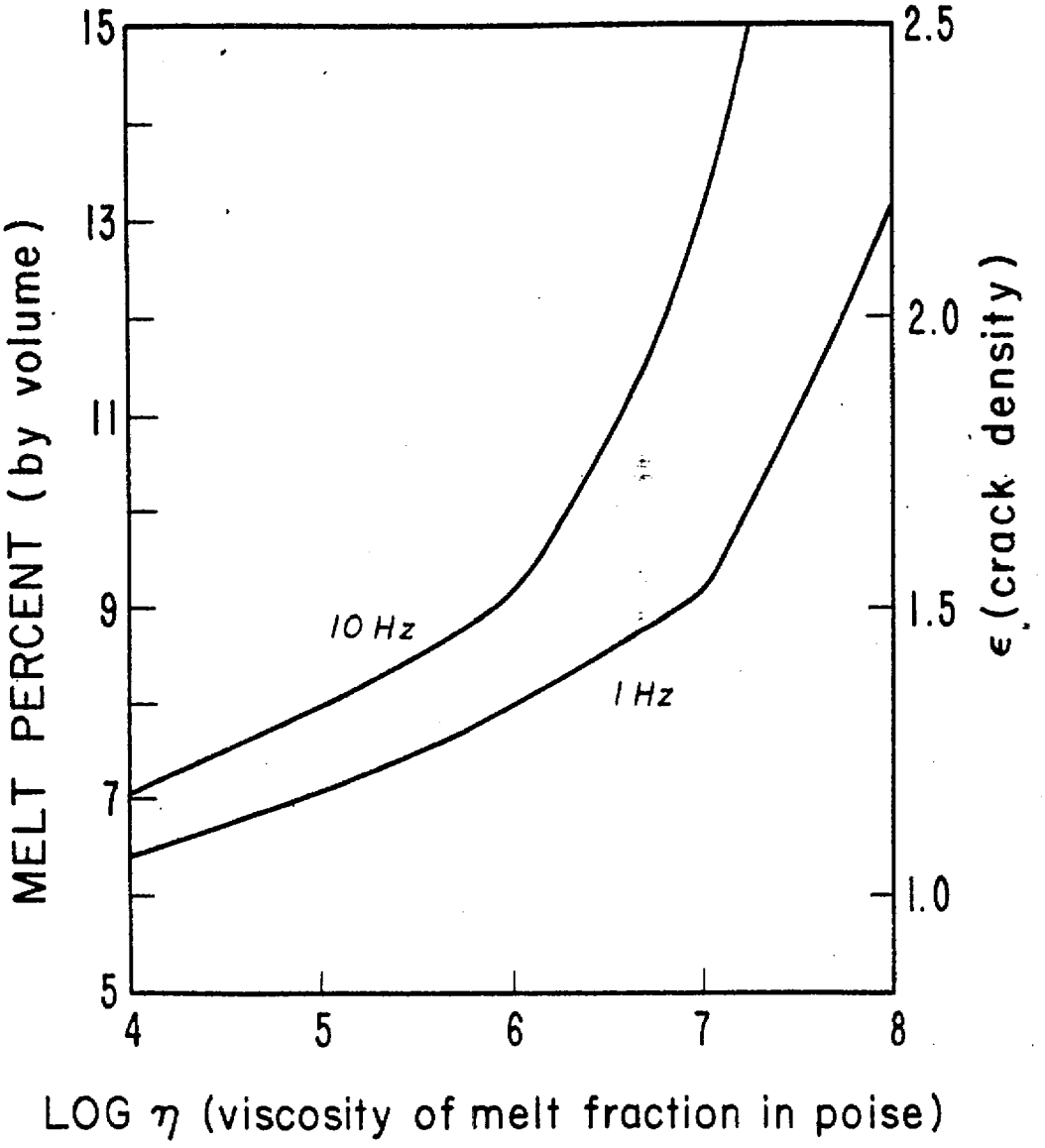
15
13
11
9
7
5
MELT PERCENT (by volume)
2.5
2.0
1.5
1.0
ε (crack density)
10 Hz
1 Hz
4
5
6
7
8
LOG η (viscosity of melt fraction in poise)

Figure 13

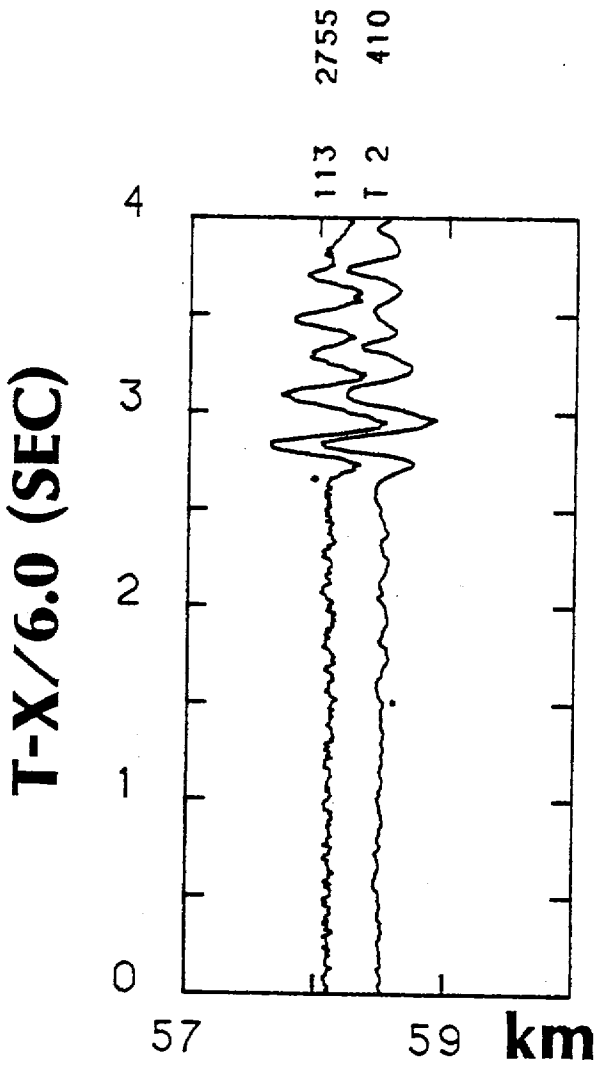

Figure 14

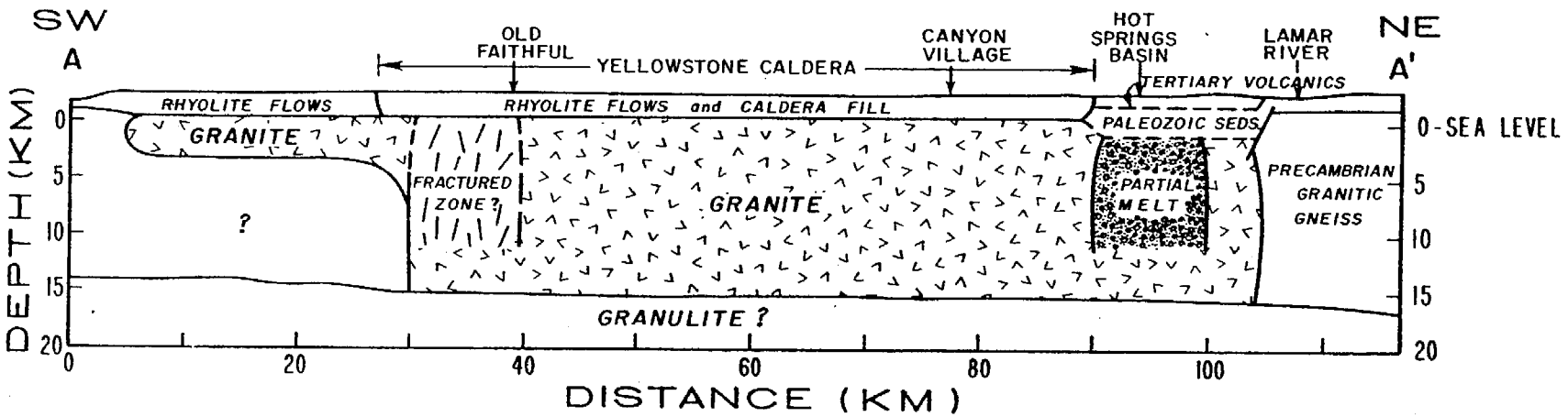
SW
A
OLD FAITHFUL
YELLOWSTONE CALDERA
CANYON VILLAGE
HOT SPRINGS BASIN
LAMAR RIVER
NE
A'
TERTIARY VOLCANICS
RHYOLITE FLOWS
RHYOLITE FLOWS and CALDERA FILL
PALEOZOIC SEDS.
GRANITE
FRACTURED ZONE?
GRANITE
PARTIAL MELT
PRECAMBRIAN GRANITIC GNEISS
?
GRANULITE ?
DEPTH (KM)
0
5
10
15
20
0-SEA LEVEL
0
20
40
60
80
100
DISTANCE (KM)

Figure 15

GEOPHYSICAL RESEARCH LETTERS, VOL. 7, NO. 12, PAGES 1029-1032, DECEMBER 1980

SEISMIC VELOCITY AND Q-STRUCTURE OF THE UPPER MANTLE LID AND LOW VELOCITY ZONE FOR THE EASTERN GREAT BASIN

K. H. Olsen,[1] L. W. Braile,[2] and P. A. Johnson[1]

[1]Geosciences Division, Los Alamos Scientific Laboratory, Los Alamos, New Mexico 87545
[2]Department of Geosciences, Purdue University, West Lafayette, Indiana 47907

Abstract. A 100-km-long record section of NTS explosions recorded in the eastern Snake River Plains ($7^{o}<\Delta<8^{o}$) shows the cusp of critical refractions from the steepened P velocity gradient at the bottom of the upper mantle LVZ. Synthetic seismograms calculated with a modified reflectivity program have been used to derive a regional velocity model of the upper mantle beneath the eastern Great Basin. The model suggests that observed very weak P_n arrivals are due to a slight negative velocity gradient below the Moho and that no high velocity mantle lid exists in this region.

Introduction

The seismic velocity versus depth structure of the upper mantle and lower crust beneath tectonically active areas of the western United States has been studied extensively for nearly 20 years. This has been possible because Nevada Test Site (NTS) underground explosions and western U.S. and Mexican earthquakes provide frequent seismic sources in an area well covered by seismograph stations. Compressional velocity distributions have mainly been determined by integrating the slope of the travel time curve, $dT/d\Delta$, using the Herglotz-Wiechert method. The required travel time (T) versus distance (Δ) data have been analysed from short-period recordings obtained along long-range profiles (Archambeau et al., 1969; Masse et al., 1972) and/or from apparent velocities measured directly across large seismic arrays (Johnson, 1967). Recently, availablility of high speed computers and development of sophisticated synthetic seismogram modeling techniques make it practical to fit the travel time and amplitude data by a trial and error procedure (Burdick and Helmberger, 1978; Wiggins and Helmberger, 1973). The important advantage of the synthetic seismogram method is that it makes optimum use of amplitude data and detailed waveform fitting to derive P velocity structure.

Many compressional and shear wave studies show that a major feature of the mantle structure beneath the western U.S. is a low velocity zone (LVZ) in the depth range between 60 and 300 km. It is well known that significant lateral variations in LVZ properties (thickness, depth, values of minimum S and P velocities, presence or absence of a lithospheric "lid," etc.) occur over distances of several hundred kilometers and perhaps to even finer scales (Burdick and Helmberger, 1978; York and Helmberger, 1973; Romanowicz and Cara, 1980). On the other hand, Burdick and Helmberger (1978) suggest mantle structure deeper than about 300 km is more uniform over a global scale and therefore amenable to modeling using widely spaced sources and seismograph stations if emphasis is placed on long period body wave arrivals at distances beyond 10°. Here we report on a record section of NTS explosions taken with matched short-period instruments having a sufficiently small station spacing (8 km) and yet long enough (∿100 km) to identify at least three distinct (T, Δ) branches for P waves whose raypaths bottom in the uppermost mantle beneath a small area in east-central Nevada. Modeling of the arrival times, amplitudes, and waveforms using a reflectivity method synthetic seismogram program (Kind, 1978; Fuchs and Müller, 1971) enables us to perturb the generic western U.S. models into a crust-upper mantle model which gives fine details of the LVZ transition in this region.

Observations

Our observations are recordings of two NTS nuclear explosions obtained while our equipment was deployed in eastern Idaho during the Yellowstone-Snake River Plains (Y-SRP) cooperative seismic profiling experiment (Braile et al., 1979). Twelve special high-explosive shots plus blasts at two quarries were used as sources for crustal profiles in eastern Idaho and Yellowstone Park. Figure 1a shows the area of the Y-SRP experiment; Figure 1b indicates those stations that were recorded on an approximate radial line to two NTS explosions on September 27, 1978 (Table 1). Because RUMMY and DRAUGHTS explosion sites were within 3 km of each other, our observed record sections are nearly identical except DRAUGHTS amplitudes are about 1/4 RUMMY amplitudes. We discuss only the better signal-to-noise RUMMY seismograms.

Instrumentation consisted of 13 vertical component short-period (1 Hz natural frequency) seismometers. Ten of these were telemetered to a centrally located site and recorded on analog magnetic tape; the three southernmost instruments were recorded on portable smoked paper units and FM tape recorders. All records were digitized at 100 samples per second and filtered (0-3 Hz) for this analysis.

The reduced-time, true relative amplitude record section for the RUMMY explosion is displayed in Figure 2. Three separate compressional phases within the first four seconds are marked on Figure 2a; our reasoning in so identifying these arrivals is as follows:

(1) The very first arrivals with an apparent velocity of 7.8-7.9 km/s are so weak that they could easily be missed on initial inspection. From the Y-SRP refraction data, we determined that the M-discontinuity is 40 km below these stations and the mantle P_n velocity is close to 7.9 km/s. An enlarged view of the first 12 seconds is shown in Figure 2b where the consistency of the P_n arrivals across the spread is more apparent. These Snake River Plains seismic stations had quite low background noise so the implication is that a true headwave P_n arrival will rarely be seen at distances beyond 600 km in the western U.S., except from events of $m_b \gtrsim 6$. In these SRP seismograms the ratio of the amplitudes of the P_n arrivals to those of the $\overline{P}$ phase is smaller than 0.005. (The $\overline{P}$ energy arrives at reduced times greater than 32 seconds so is not shown in Figure 2a). Other investigators (e.g., Hill, 1972, 1973) have commented that P_n energy at these distances is probably very

Paper number 80L1475.

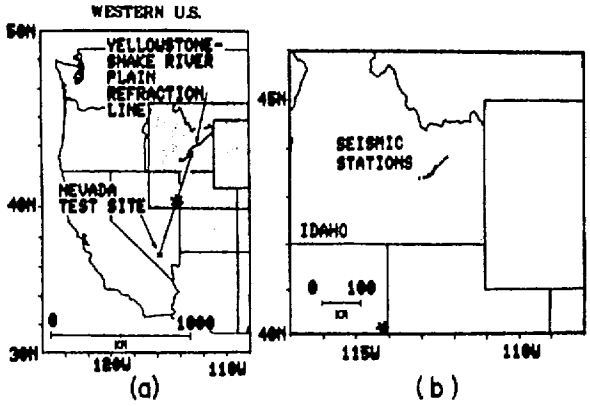

Figure 1. (a) Location map of the western U.S. with relative positions of the Nevada Test Site and the Y-SRP refraction line. (b) Enlargement showing seismic stations in Idaho used for the September 27 observations. Asterisk denotes the approximate area in the Great Basin for mantle ray turning points from NTS explosions.

weak and that care must be taken when attempting to extend the P_n branch during long range refraction profiling.

(2) Following P_n by about three seconds are stronger arrivals also having apparent velocities close to 8 km/s. A striking feature of Figure 2a is that beyond 780 km the amplitude of the second arriving phase increases rapidly with distance and the dominant frequency is noticably lower ($\sim$0.6 Hz) than the frequencies for Δ<780 km and for the P_n phase (both $\sim$1.6 Hz). This qualitative observation strongly suggests that the rapid increase of the low frequency phase for Δ< 780 km is a manifestation of a critical distance effect and that the high frequency energy has been attenuated along the travel path. The obvious place for this to occur is during the two-way transit of energy through the mantle LVZ (which also has a high anelasticity, i.e., low Q). These critical refractions are shown schematically in the ray diagram of Figure 3; we follow the convention of Archambeau et al. (1969) in labeling this cusp phase P_1.

(3) The higher frequency second arrivals for Δ< 780 km we attribute to large angle reflections from an interface lying mainly above the LVZ. These reflections are overtaken and overwhelmed by P_1 for Δ<780. Because of the apparent velocity near 8 km/s, the high frequency content, and travel time just longer than P_n, the synthetic seismogram modeling discussed below suggests this reflection occurs at the base of the mantle lid and hence our notation of P_{lid}.

Modeling

Our technique in modeling the record section was to first use a fast asymptotic ray theory computer program (Červený, 1979) to fit travel times and approximate amplitudes. For more exact modeling we then used a reflectivity method program developed by Kind (1978), which properly accounts for the effects of a buried source and thus allows computation of complete seismograms. One advantage of the reflectivity method over Cagniard-de Hoop techniques (Helmberger, 1973; Helmberger and Burdick, 1979) is that Q values can be individually assigned to each model layer rather than distributed over the entire path as part of a linear operator.

Burdick and Helmberger's (1978) T-7 model was adopted as the starting model for compressional wave velocities in the crust and mantle. The generic T-7 model was constructed mainly from long period data to the NW and SE of NTS—with emphasis on velocity structure below 200 km (arrivals for $\Delta \gtrsim 10^o$). Since our observations are in the range $7^o < \Delta < 8^o$, we perturbed the initial model only at depths above 250 km. The T-7 model has a P_n velocity of 7.95 km/s with a positive gradient below the M-discontinuity to 8.05 km/sec at the bottom of the lid at 65 km. A substantial LVZ for P-velocities is included below 65 km (Figure 5).

We did not calculate synthetics for shear wave phases but were required to include a realistic S-velocity structure because shear wave velocity contrasts can have a major influence on P-wave reflection coefficients—especially for large angles of incidence. Priestly and Brune (1978) used dispersion of fundamental mode Rayleigh and Love waves to derive a shear velocity model in the eastern Great Basin very close to the area of the mantle turning points of this study. The combined P- and S-velocity model, T-7/PB, is shown in Figure 5 along with Poisson's ratio (σ) calculated from the tabulated velocities.

The modified reflectivity synthetics for the T-7/PB velocity model are shown in Figure 4a for an extended range from 600 km to 960 km. The P_1 phase can be seen only for distances beyond 840 km and reduced times greater than 13 seconds. In order to bring the synthetic P_1 phase into agreement with the observed arrival times and to shift the cusp from $\sim$820 km back to $\sim$780 km it was necessary to bring the gradient at the

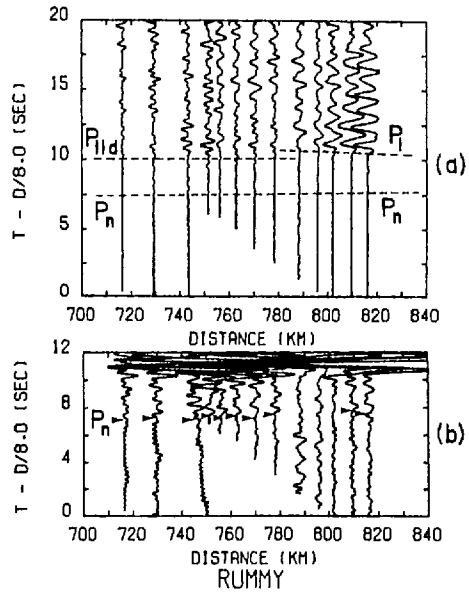

Figure 2. (a) True relative amplitude record section of P-wave arrivals from RUMMY. (b) Same as (a) with increased amplitudes to show weak P_n phase.

TABLE 1. NTS Explosions of September 27, 1978

Name	Origin Time (GMT)	Coordinates Lat.	Long.	Depth (m)	Surf.Elev. (m)	Magnitude (m_b)
DRAUGHTS	1700:00.071	37.074°N	116.020°W	442	1262	5.0
RUMMY	1720:00.076	37.080°N	116.051°W	640	1253	5.7

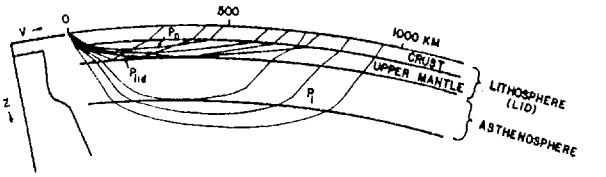

Figure 3. Schematic ray diagram showing the head wave phase P_n, the P_1 phase critically refracted from the gradient near the bottom of the LVZ, and the P_{lid} phase reflected from the base of the mantle lid.

bottom of the LVZ to shallower depths and to make slight adjustments to its curvature. Also note from Figure 4a that the T-7/PB model gives too large amplitudes for P_n arrivals, and the P_{lid} phase from the discontinuity at 65 km depth arrives about 2.5 seconds too early so is superimposed on the P_n phase throughout much of the 600-960 km range. The result of perturbing the T-7/PB velocity model to better match the observations of Figure 2 is model A-10 shown in Figure 5. The A-10 synthetics are compared with the original T-7/PB model in Figure 4b and with the more limited distance range observations in Figure 6.

Discussion

We can summarize the nature and reasons for the various model perturbations as follows:

(1) The steepened positive P-velocity gradient in the lower part of the LVZ has been raised in order to fit the arrival times and cusp distance of the P_1 phase.

(2) In order to match the observed weak P_n, a slight negative gradient just below the M-discontinuity is required instead of the positive gradient of the generic T-7 model. In fact, our A-10 P-velocity model suggests that, beneath this part of the Great Basin, the LVZ may be in contact with the crust at the M-discontinuity. Similar indications of the absence of a high velocity lid in parts of the western U.S. have been cited by Archambeau et al. (1969) (especially for their SHOAL-FALLON SE profile).

(3) The large negative discontinuity at a depth of 65 km present in both the T-7 P-velocities and the Priestly-Brune model appears to be too shallow to properly match the observed P_{lid}-P_n travel time delay. The observed delay is better reproduced if the discontinuity is at about 100 km depth.

(4) The calculated amplitudes of the P_{lid} reflection are much too large if the T-7/PB velocity

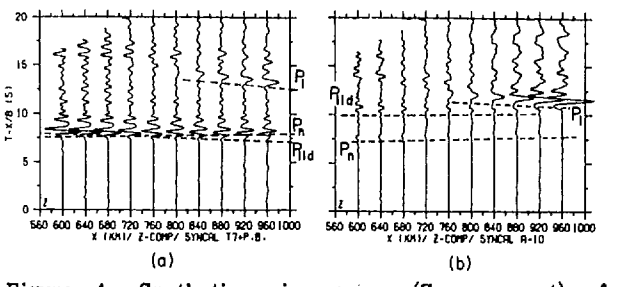

Figure 4. Synthetic seismograms (Z-component) of early compressional phase arrivals from (a) the generic T-7/PB model and (b) the A-10 mantle model (Figure 5) which match the observations in the 720 to 820-km range. Travel time curves calculated from the Cerveny program. Amplitude multiplied by distance for convenient plotting.

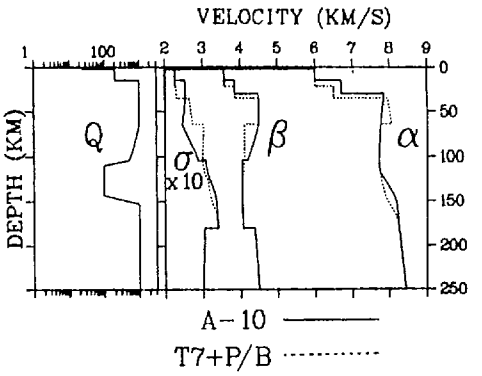

Figure 5. P-velocity (α) and S-velocity (β) versus depth plots for the T-7/PB and A-10 models. Assumed Q-structure for both models shown at left. σ is Poisson's ratio.

contrasts (-0.3 km/s for P, -0.39 km/s for S) are used at a depth of ∿100 km. In fact, by including the effect of S-velocity contrasts on the P-wave reflection coefficients, we can match observed P_{lid} amplitudes by keeping the P-velocity contrast at zero and relying entirely on an S contrast of -0.15 km/s to produce the effect on these wide angle reflections. In moving the bottom of the S-velocity lid from a depth of 65 km proposed by Priestly and Brune to the ∿100 km required in our A-10 model, we introduced a negative gradient in the S-velocities between these two depths; a similar negative gradient can be seen in the higher mode inversions by Cara (1979), but these are not plotted in Figure 5. Hill (1972) and Hales (1969) previously reported arrivals following P_n by two to three seconds at distances of ∿600 km in sections from long range refraction experiments in the Columbia Plateau (EDZOE experiment) and the central U.S. (EARLY RISE), respectively. Their interpretations—using travel time information only—suggest a thin (∿10 km), sharp, but high velocity (8.0 to 8.4 km/s) lid at depths of 90-100 km is present in those regions. Our Great Basin data agrees in placing a discontinuity (which is perhaps the "boundary" between the lithosphere and the athenosphere) at ∿100 km but our P-velocity contrast cannot be as pronounced as those implied by Hill and Hales and still give rise to the comparitively weak amplitudes that we observe in the 750 km range.

(5) the Q-structure (for P-waves) used for the A-10 model was a generalization of proposed values that have appeared in recent literature. The most important segment is the low value centered in the LVZ. A Q_α value in the range between 50 and 100 appears to adequately attenuate the higher frequency components

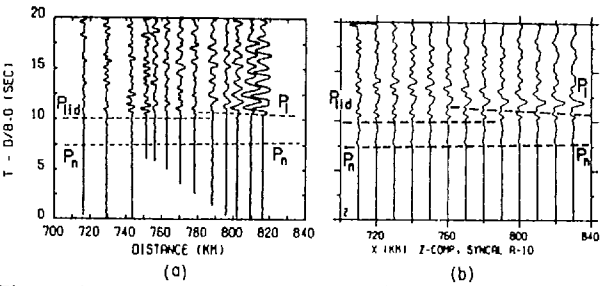

Figure 6. Comparison of observed (a) and synthetic (b) seismogram record sections for the 720 to 820-km distance range.

of the P_1 phase. $Q_\alpha > 100$ in the LVZ does not attenuate P_1 enough, whereas $Q_\alpha \sim 25$ completely obliterates the P_1 phase in the synthetics. Our value of $50 < Q_\alpha < 100$ is of the same order as that deduced by Helmberger (1973) from Cagniard-de Hoop techniques.

(6) One possible shortcoming of the A-10 model is the failure to reproduce details of the oscillations of the observed P_1 phase. We do not believe this to be a result of an inadequately detailed source spectrum, since a comparison of the explosion source spectrum algorithm used in the modified reflectivity code is reasonably represented by the source spectrum plus instrument response function calculated from known physical parameters of these explosions (Mueller and Murphy, 1971). Archambeau et al. (1969) observed compressional wave energy spread out in long, rather complicated oscillatory wave trains near caustics and attributed this to interference between refracted and reflected components near the cusp. Our model layer thicknesses (~5 km) in the region of the lower depths of the LVZ (120-150 km) are of the same order as the wavelengths (~10 km) of the dominant short period energy. Thus, we believe the oscillatory P_1 trains may be due to small details of fine structure in the transition zone which we have not yet attempted to model at the required resolution.

In conclusion, relatively minor adjustments in the T-7/PB model for the western U.S. yield an uppermost mantle structure that reproduces in detail the upper mantle arrivals and very weak P_n observed in the Great Basin.

Acknowledgments. We especially thank Rainer Kind for the modified reflectivity computer program used in our analysis. We appreciate the assistance of our LASL colleagues, E. F. Homuth and T. G. Handel with the observations and J. N. Stewart for computer advice. Cooperation of the Idaho National Engineering Laboratory during the field work is appreciated. K. H. O., P. A. J., and the LASL field team were supported by the U.S. Department of Energy. L. W. B. acknowledges support from NSF grants EAR-77-23351 and EAR-77-23707 and ONR grant N00014--75-C-0972. Field data were collected during research partially sponsored by the NSF grants and by USGS Geothermal Exploration Program grant 14-08-0001-G-532.

References

Archambeau, C. B., Flinn, E. A., and Lambert, D. G., Fine structure of the upper mantle, J. Geophys. Res., 74, 5825-5865, 1969.

Braile, L. W., Smith, R. B., Ansorge, J., Baker, M. R., Prodehl, C., Healy, J. H., Mueller, S., Olsen, K. H., Priestly, K., and Brune, J., The Yellowstone-Snake River Plain seismic profiling experiment: eastern Snake River Plain (abs.), EOS Trans. AGU, 60, 941, 1979.

Burdick, L. J. and Helmberger, D. V., The upper mantle P velocity structure of the western United States, J. Geophys. Res., 83, 1699-1712, 1978.

Cara, M., Lateral variations of S velocity in the upper mantle, Geophys. J. Roy. Astron. Soc., 57, 649-670, 1979.

Červený, V., Accuracy of ray theoretical seismograms, J. Geophys., 46, 135-149, 1979.

Fuchs, K. and Müller, G., Computation of synthetic seismograms with the reflectivity method and comparison with observations, Geophys. J. Roy. Astron. Soc., 23, 417-433, 1971.

Hales, A. L., A seismic discontinuity in the lithosphere, Earth and Planet. Science Letters, 7, 44-46, 1969.

Helmberger, D. V., On the structure of the low velocity zone, Geophys. J. Roy. Astron. Soc., 34, 251-263, 1973.

Helmberger, D. V. and Burdick, L. J., Synthetic seismograms, Ann. Rev. of Earth and Planetary Sciences, 7, 417-442, 1979.

Hill, D. P., Critically refracted waves in a spherically symmetric radially heterogeneous earth model, Geophys. J. Roy. Astron. Soc., 34, 251-263, 1973.

Hill, D. P., Crustal and upper mantle structure of the Columbia Plateau from long range seismic-refraction measurements, Geol. Soc. America Bulletin, 83, 1639-1648, 1972.

Johnson, L. R., Array measurements of P velocities in the upper mantle, J. Geophys. Res., 72, 6309-6323, 1967.

Kind, R., The reflectivity method for a buried source, J. Geophys. Res., 44, 603-612, 1978.

Masse, R. P., Landisman, M., and Jenkins, J. B., An investigation of the upper mantle compressional velocity distribution beneath the Basin and Range province, Geophys. J. Roy. Astron. Soc., 30, 19-36, 1972.

Mueller, R. A. and Murphy, J. R., Seismic characteristics of underground nuclear detonations: Part 1, seismic spectrum scaling, Bull. Seismol. Soc. Am., 61, 1675-1692, 1971.

Priestly, K. and Brune, J., Surface waves and the structure of the Great Basin of Nevada and Western Utah, J. Geophys. Res., 83, 2265-2272, 1978.

Romanowicz, B. A. and Cara, M., Reconsideration of the relations between S and P station anomalies in North America, Geophys. Research Letters, 7, 417-420, 1980.

Wiggins, R. A. and Helmberger, D. V., Upper mantle structure of the western United States, J. Geophys. Res., 78, 1870-1880, 1973.

York, J. E. and Helmberger, D. V., Low-velocity zone variations in the southwestern United States, J. Geophys. Res., 78, 1883-1886, 1973.

(Received September 7, 1980;
accepted October 7, 1980.)

SEISMOGRAMS OF EXPLOSIONS AT REGIONAL DISTANCES IN THE WESTERN U.S.: OBSERVATIONS AND REFLECTIVITY METHOD MODELING

K.H. Olsen
L.W. Braile

To be published in Proceedings of the NATO Advanced Study Institute:
"Identification of Seismic Sources - Earthquakes or Underground Explosion",
(Held 8-18 September 1980, Oslo, Norway)

SEISMOGRAMS OF EXPLOSIONS AT REGIONAL DISTANCES IN THE WESTERN UNITED STATES: OBSERVATIONS AND REFLECTIVITY METHOD MODELING

K. H. Olsen[1] and L. W. Braile[2]

[1] Geosciences Division, Los Alamos National Laboratory, Los Alamos, New Mexico 87545, U.S.A.
[2] Geoscience Department, Purdue University, West Lafayette, Indiana 47907, U.S.A.

ABSTRACT. Seismic energy propagating through vertically and laterally varying structures of the earth's crust and lower lithosphere-uppermost mantle is responsible for the numerous and complex seismic phases observed on short-period seismograms at regional distance ranges (100 to 2000 km). Recent advances in techniques for computing synthetic seismograms make it practical to calculate complete seismograms that realistically model many features of regional phases. A modified reflectivity method program is used to interpret some details of record sections of Nevada Test Site (NTS) underground explosions that were observed 700 to 800 km from the sources.

I. INTRODUCTION

Regional seismic phases recorded by high-gain, short-period or broadband instruments are likely to play an increasingly important role in seismic source location and identification as acceptable magnitude thresholds are pushed to lower levels. From the standpoint of complexity of seismograms, the epicentral distance range between ~200 km and the transition to simpler teleseismic waveforms around 2000 km presents many challenges to the seismic analyst. In this range, propagation paths can traverse the crust, the lower lithosphere, and the uppermost mantle where both vertical and lateral heterogeneities strongly influence waveform characteristics. Good observational data are rare for testing analysis techniques developed for regional problems. In contrast to the numerous detailed crustal refraction/reflection profiles that have been obtained from many parts of the world out to distances ~200 km, relatively few long-range

profiles exist where station spacing is sufficiently tight to facilitate a clear interpretation of the onset, development, and amplitude vs. distance behavior of the many observable phases. Thus, although signals from sources of interest may be easily observable at regional distances, derivation of source parameters from observations at sparsely located observatories or arrays will require careful analysis and modeling of the intricacies of wave propagation at these scales.

Phases of interest in regional identification studies fall into two main categories: large amplitude, long duration, but somewhat indistinct wave groups such as Lg and $\bar{P}$; and body waves (mainly compressional) that appear either as first arrivals or closely following as possible wide angle reflections/near-critical refractions from interfaces and/or steep velocity gradients in the deep crust, lower lithosphere, and uppermost mantle. The Lg and $\bar{P}$ phases are often the largest amplitude features on regional short-period seismograms, but a clear explanation of how Lg and $\bar{P}$ propagate is still lacking [1]; this lack perhaps is reflected in the fact that seismologists frequently use the notations $\bar{P}$ or P_g interchangeably in reference to a broad, large amplitude phase following P_n. We adopt the $\bar{P}$ notation here. The phase in question propagates very well in the western United States, but attenuates rapidly in the eastern U.S. A group velocity around 6 km/s implies $\bar{P}$ propagates as compressional waves multiply reflected within the crust--which may thus act as a waveguide. Similarly, the ~3.5 km/s group velocity for Lg suggests shear waves multiply reflecting within the crustal layers. Some authors [2] prefer to treat Lg as a superposition of higher mode Love and Rayleigh waves propagating in a nearly laterally homogeneous, vertically layered crust. In any case, the propagation physics is complicated and will require quite sophisticated synthetic seismogram codes to properly model and interpret observed waveforms.

Record sections of long-range seismic refraction profiles often show one or more nearly parallel travel time (T) vs. distance (Δ) branches following within several seconds of first arrivals [3, 4, 5]. Each secondary branch may be traceable only over a distance interval of 50 to 200 km before being replaced in a "shingle-like" fashion with another branch or set of arrivals [5, 6, 19]. These are usually interpreted as parts of cusp phases arising from critical refractions and/or wide-angle reflections from first order discontinuities or steep velocity gradients in the upper mantle. Archambeau et al. [7] and Burdick and Helmberger [8], for example, have derived velocity vs. depth models for the major features of the upper mantle beneath the U.S. by a joint analysis of travel times, amplitude vs. distance variations, and waveform fitting of the first few compressional arrivals observed at widely separated seismograph

stations throughout the U.S. These and similar models by others are most valid for depths greater than about 250 km. Although these analyses suggest that the main features of mantle structure at depths below about 300 km (corresponding to compressional first arrivals at epicentral ranges beyond ~1500 km) may be more uniform over a global scale [8], it is known that significant lateral variations in lower lithosphere and uppermost mantle properties occur beneath the continents on regional and perhaps even finer scales [8, 9, 10, 11]. In the depth range between the Moho and ~300 km, several types of structural variations have been suggested in the literature that would give rise to wide angle reflections, converted phases, and similar closely spaced arrivals on seismograms at regional ranges. These include the presence or absence of the S-wave and/or the P-wave low velocity zone (LVZ) in the asthenosphere, high velocity mantle lids [12, 13], alternating lamellae of positive and negative velocity gradients [6, 19], etc. These early arriving phases often have better defined onsets than the $\bar{P}$ and Lg phases and, since they are observed at distances beyond that where a true head wave Pn arrival can be expected, they may be useful in regional source location and identification. In order to make use of the information contained in these arrivals (especially the amplitude vs. distance behavior for particular paths of interest), it will be necessary to use modern sophisticated synthetic seismogram techniques to derive localized fine scale details from generalized crust-mantle models.

The purpose of this paper is to explore a few of the problems in modeling regional short-period seismograms by means of a modified reflectivity method [14] computer program developed by R. Kind [15]. This numerical program accounts for the effects of a buried source and is thus capable of computing 'complete' seismograms--including refracted waves, surface reflected body waves such as the pP phase, and surface waves. The effects of anelastic attenuation (Q) for each layer are included as an integral part of the method [15]. The most severe limitation of the technique for studies of regional seismograms is the assumption of lateral homogeneity (this is also a limitation for normal modes summation techniques). An item of interest will be the extent synthetics can be made to match observed waveforms under this restriction.

Two problems are considered. The first, labeled the B-3 model for brevity, employs a simple model consisting of three layers in the crust without velocity gradients and an almost uniform velocity mantle. A large range of apparent surface phase velocities is used in order to display S phases and surface waves. The second calculation, the A-10 model, treats the mantle structure in detail, but confines attention to compressional phases near ther start of the seismogram. The more

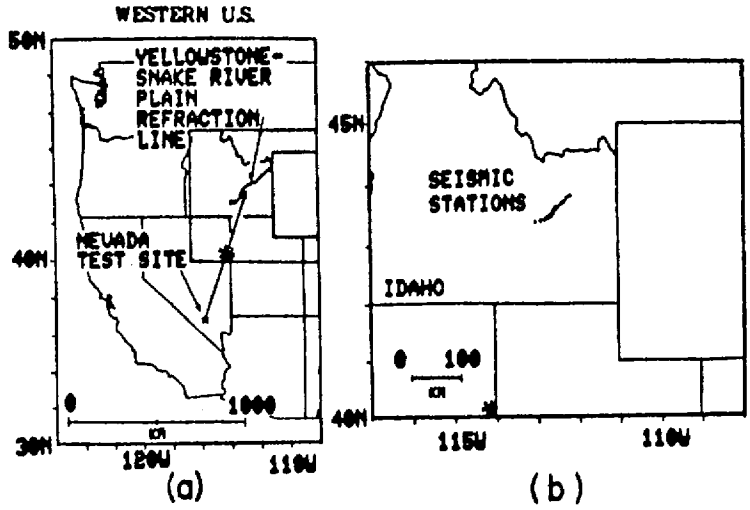

Fig. 1. (a) Location map of the western United States with relative positions of the Nevada Test Site and the Y-ESRP recording line. (b) Enlargement showing positions of stations that recorded the 27 September 1978 RUMMY explosion. Asterisk denotes approximate area for mantle ray turning points from NTS explosions.

important conclusions of the A-10 model are summarized here--a fuller discussion of this calculation and the implications for uppermost mantle structure beneath the western U.S. can be found in a previous publication [16].

A comparison of the synthetic seismogram calculations has been made with a 100-km-long record section of short-period vertical component seismograms obtained in eastern Idaho during the 1978 Yellowstone-Eastern Snake River Plains (Y-ESRP) seismic profiling experiment. For these observations, the sources were underground nuclear explosions at the Nevada Test Site (NTS) at distances between 720 and 820 km from the nearly radially oriented linear station array (Fig. 1). Only the records from the largest NTS explosion, the m_b = 5.7 RUMMY event at 1720:00.076 GMT, 27 September 1978, are reproduced here since they have the best signal-to-noise ratio of the three NTS explosions observed during the experiment. Additional details of the Y-ESRP instrumentation, experiment, and data can be found elsewhere [16].

2. COMPUTATIONAL TECHNIQUE

As discussed by Kind [15] and by Fuchs and Müller [14], the reflection coefficient and time shift calculations in the reflectivity method are carried out in the frequency domain and then Fourier transformed to plot seismograms. We included Müller's [17] earth flattening approximation in both of our problems to account for earth curvature effects. Both P and S velocities are independently specified in all calculations, since the reflection coefficients are functions of both P and S velocity contrasts at non-normal incidence angles and are required even when only computing P phases over a narrow time window. In the A-10 calculation, for example, the departure of the P/S velocity ratio in a layer from that given by Poisson's ratio = 1/4 is an important factor in our interpretation [16]. Densities are given by a Birch's Law relation (density = 0.252 + 0.3788*P velocity). The attenuation factor Q_α for P waves was chosen as 25 in the source layers, 200 in the upper crust, and 1000 in the lower crust and the uppermost mantle layers; for the LVZ modeling of the A-10 model, Q_α in the asthenospheric layers was adjusted as part of the fitting procedure (see Fig. 5). The attenuation factor for S waves was always assumed to be $4Q_\alpha/9$ [20]. The explosive source algorithm [16] was used with the source buried at a depth of 0.640 km in a layer of P velocity = 3.55 km/s. These were close to actual field values for the NTS RUMMY explosion. Time intervals, number of samples, and computed lengths of seismograms were chosen so that the dominant frequency of the source spectrum was 1.6 Hz for the A-10 calculation--again close to the observed value. In order to save computer time for the extended duration B-3 seismogram sections, the parameters were chosen so that the dominant frequency of the source was shifted to 0.25 Hz; although this was low compared to observed frequencies, we felt it was adequate for the puposes of this initial study. To avoid long computer runs, the wave field was only computed within a limited phase velocity window: 1 km/s to 20 km/s for B-3, and 6.5 km/s to 1000 km/s for A-10. These integration limits sometimes introduced spurious single cycle "phases" at these apparent velocities in the computed record sections. The limit velocities were chosen so as to not overlap or interfere with arrivals of interest in the observations. In the record section plots, the amplitudes of each trace have been multiplied by station distance to maintain a convenient scaling of the amplitudes of the phases which are subject to geometrical spreading and attenuation due to anelasticity.

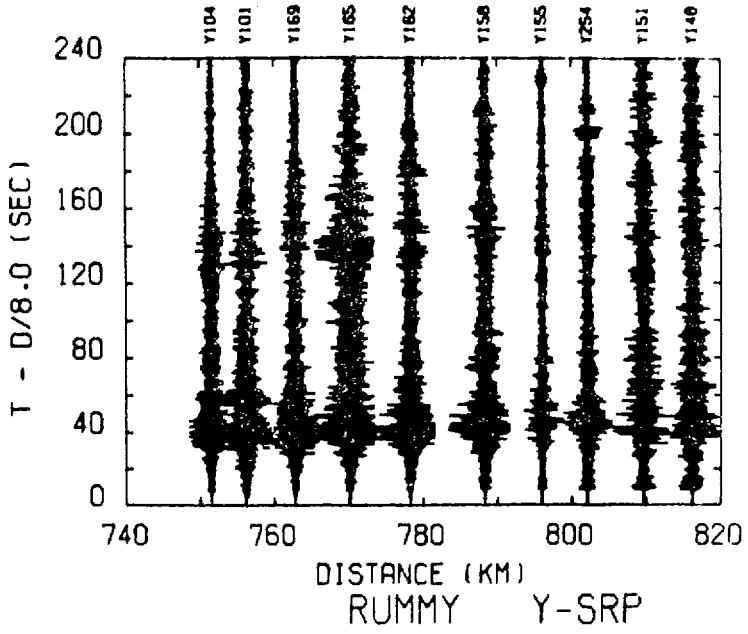

Fig. 2. Vertical component low time resolution seismic record section of the RUMMY explosion as recorded at Snake River Plains stations. The time scale is compressed to show envelope behavior; individual waveforms not readily seen. The $\bar{P}$ phase is the broad feature at reduced times between 30 and 60 s. Upward ground motion to the left.

3. DISCUSSION

3.1 The Extended Time Seismograms: B-3 Model

Figure 2 is a true relative amplitude vertical component record section of the RUMMY explosion recorded on ten matched short-period (1 Hz natural frequency) instruments deployed in the eastern Snake River Plains (Fig. 1). Although the time scale is too compressed to reveal many details of the waveforms, several important overall features can be noted. The broad (~40-second-long) envelope of the $\bar{P}$ phase appears at reduced times between approximately 30 to 60+ seconds, and is the largest amplitude feature on the record. In contrast, the Lg phase expected at reduced times of ~130+ seconds (an average velocity of about 3.5 km/s) is poorly developed on these unfiltered records; it is only obvious at the 770-km station. A few impulsive arrivals can be seen (such as the first arrivals at reduced time ~10 seconds, which will be discussed in Sec. 3.2, and perhaps an Sn [?] phase at t_{red}~80 seconds and ~780 km), but the

impression one gets by viewing this observed section is that the correlations seem to be better described as broad energy correlations rather than phase correlations. A similar conclusion is suggested by seismograms from central Asia shown in the paper of Ruzaikin et al. [1]. A coherent structure in the $\bar{P}$ and Lg phases is difficult to trace from station to station even though the stations are only separated by 8 km on the average.

The results of an attempt to model late time arrivals over a regional distance range is shown in Fig. 3. A rudimentary, almost trivial, crust/mantle velocity structure was assumed that consisted of three constant velocity layers in the crust overlaying a nearly constant velocity halfspace. (A slight negative gradient in P velocity was introduced just below the Moho in order to suppress the Pn amplitudes as required by the observations; see Sec. 3.2.) We note several points.

(a) The seismogram section from 100 to 900 km and the enlarged individual record for 800 km shows a surprising amount of complexity at times beyond the first arrivals even though an extremely simple earth model and source function is used. Groups corresponding to the $\bar{P}$ and Lg phases can be identified.

(b) There appears to be a considerable amount of S-wave energy although none is present in the explosion source algorithm. This is probably due to P-to-S and S-to-P, etc., conversions at interfaces and to multiples which the program adequately includes.

(c) The calculated dispersed fundamental mode Rayleigh wave is very large. There are at least two reasons this Rayleigh wave is not representative of the observations. First, no corrections for the short-period bandpass response of the seismometers were included in the synthetics. Second, the assumed source spectrum has too much energy at the longer periods as compared with a near point-source representative of a NTS explosion, thus over enhancing the Rayleigh waves. Long-period Rayleigh waves from actual underground explosions are probably generated or modified and enhanced by mechanisms such as spall closure and/or tectonic strain release; these mechanisms are not adequately treated by the explosion algorithm used for the present calculation.

(d) Because the calculated seismogram sections are quite complicated even for this simple earth model, they give the impression that broad "packets of energy" can be more readily correlated than any well defined phases--for at least the $\bar{P}$ and Lg phases. This was the case with the observations in Fig. 2. In order to better understand the gross behavior of these phases with distance and to identify the origin of obscure features, it will be necessary to include calculations of the horizontal

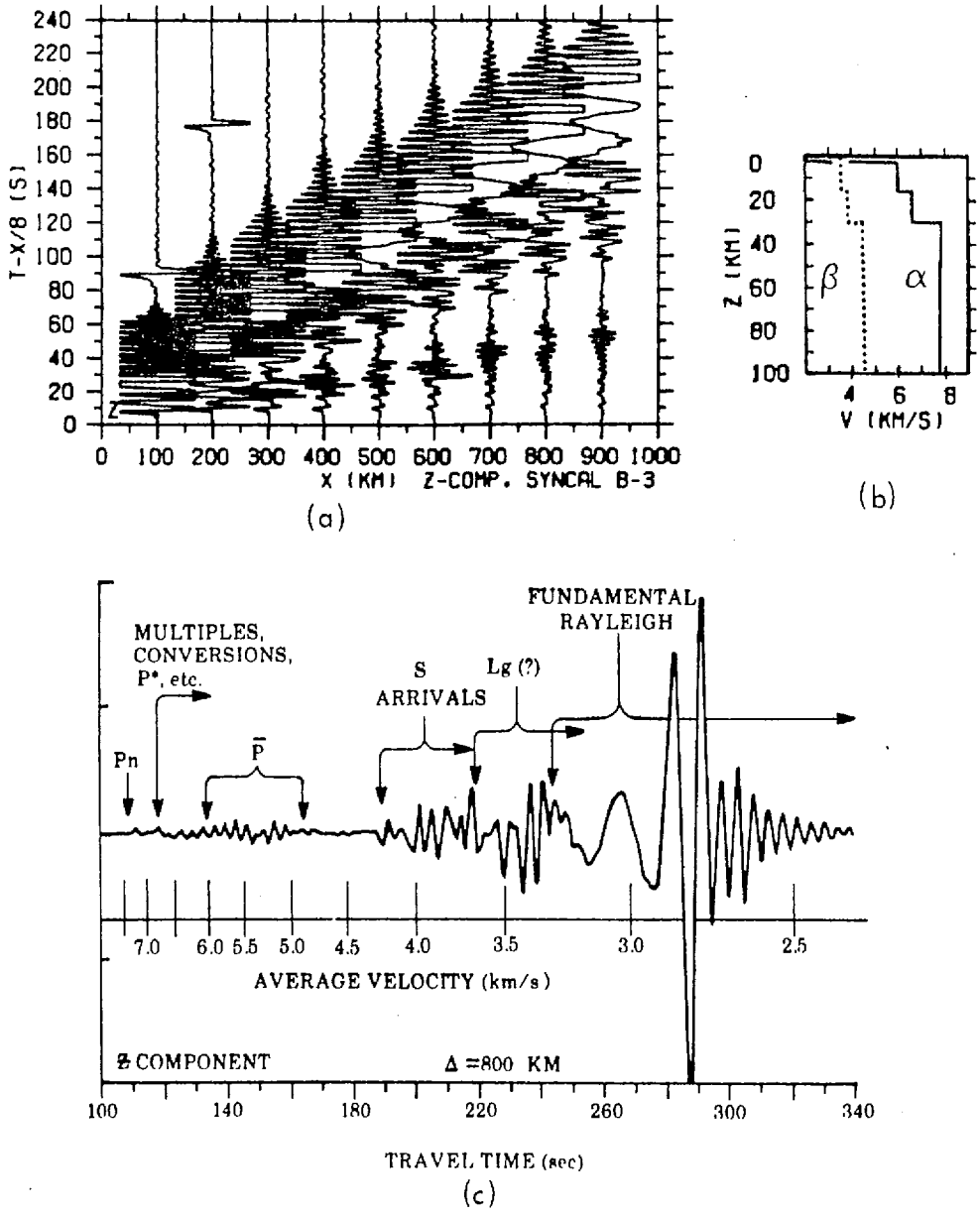

Fig. 3. (a) Synthetic seismogram vertical component record section calculated from the P and S velocity vs. depth structure (Model B-3) shown in (b). (c) Expanded plot of the synthetic seismogram at the 800-km distance. Approximate arrival time and average velocity windows for different phases or groups are indicated; the phase velocities of the different wave types are equal to or slightly greater than the average velocities. The Rayleigh waves on plot (a) are arbitrarily clipped in plotting to avoid large overlays in the seismograms.

(radial) component and to perform calculations at small station separation to increase recognizability of phase correlations.

These results suggest that the modified reflectivity method, even with the restrictive assumption of lateral homogeneity, can be a useful technique in understanding the intricacies of Lg and P phases and the types of earth structures that most affect them. In addition, these studies suggest that observations of complex and apparently-incoherent seismic phase arrivals--even over short distances--do not necessarily imply strong lateral heterogeneity in crustal structure. Parameter studies would help identify those aspects where refinements due to lateral heterogeneity and/or scattering need to be considered in order to better match observations.

3.2 Early Time Arrivals: A-10 Model

Figures 4a and 4b are enlarged portions of the first few seconds of the digitized RUMMY vertical component seismograms (see also Fig. 2) that show details of the earliest arrivals. We have interpreted [16] this record section in terms of three different compressional phases, all having apparent velocities close to 8 km/s: (a) an extremely weak leading arrival labeled Pn, which was lost in the background noise for the two other, lower yield, NTS shots that were also recorded during the Y-ESRP experiments; (b) a stronger phase labeled P_{lid} follows Pn by about two or three seconds for epicentral distances between 700 and 780 km; (c) beyond 780 km, the P_{lid} phase appears to be overtaken and overwhelmed by a low-frequency phase, P_l, whose amplitude increases rapidly with distance out to at least the farthest station of the linear array. The detailed reasons for these labels and identifications are discussed in [16]; they can be summarized as follows.

The phase labeled Pn could be a wide angle reflection from a weak P-velocity contrast in the lower lithosphere below the Moho rather than a true headwave (in the strict sense of the mathematical definition) that travels along the M-discontinuity interface over the entire 800-km path. However, the sub-Moho P velocity (7.7 to 7.9 km/s) in this region of the Great Basin is known to be close to both the average and the apparent velocity observed in Figs. 2 and 4. This, plus the fact that other travel time arguments [16] suggest there is no evidence for mantle lids or other thin but fairly high gradient zones down to a depth of about 100 km, argues that the most straightforward explanation for this arrival is that it is a P_n-type phase. We calculate that the energy at 800 km is greatly reduced because the wave travels in a region beneath the Moho that has a slight negative velocity gradient.

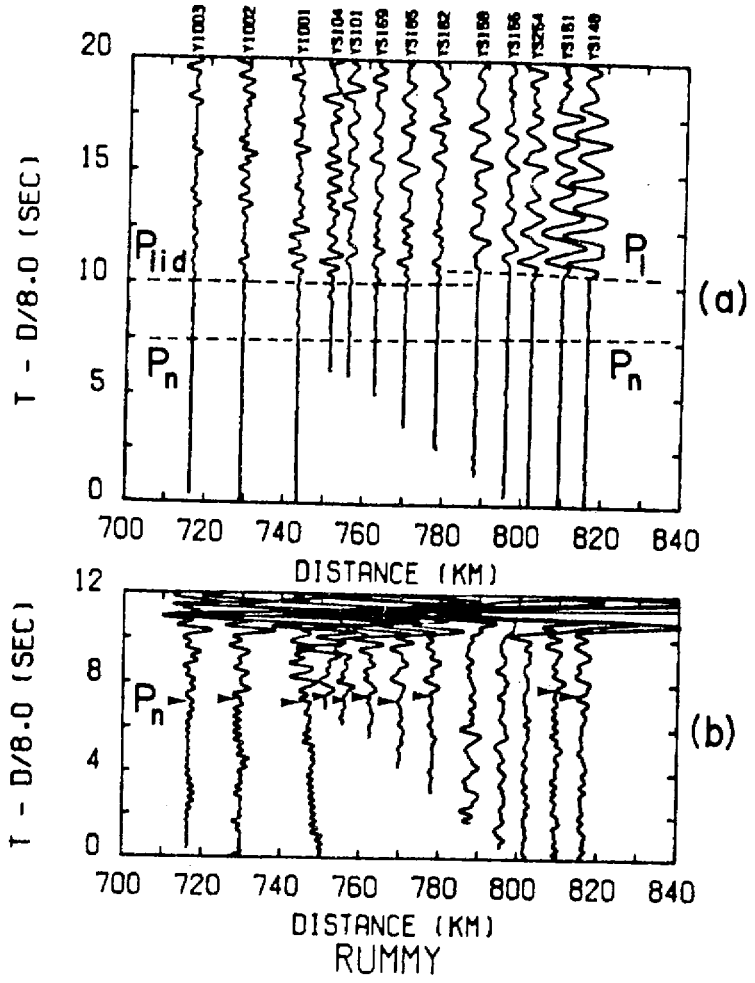

Fig. 4. (a) True relative amplitude record section of early compressional arrivals from the RUMMY explosion. (b) Same as (a) with increased amplitudes to show weak P_n phase. Upward motion to the left. All traces low pass filtered at 3 Hz.

The sudden onset at about 780 km and subsequent rapid amplitude growth of the P_l phase indicates it is the cusp of the critically refracted P-waves from the steep velocity gradient at the base of the asthenospheric low velocity zone. The observed dominant low frequency content is then explained by the attenuation of the high frequency components as the energy travels first downward and then back up through the very low-Q region of the LVZ. The notation of P_l for this phase follows the convention established by Archambeau et al. [7].

The travel times, moderate amplitudes, and relatively high frequency content imply the phase identified as P_{lid} is a wide angle reflection from a discontinuity near the base of the mantle lid (= top of LVZ) in this area.

The conclusions concerning these three early arriving compressional phases summarized above were confirmed by using the modified reflectivity program to quantitatively model the arrival times, amplitudes, and waveforms in the first 15 seconds of the record sections. The procedure was to begin with a generic P-velocity vs. depth model for the western U.S. (the T-7 model) derived from a wider data set by Burdick and Helmberger [8] and then to perturb the model to achieve a better fit [16]. Because of the influence of S-velocity contrasts on the P-wave reflectivity calculations, an S-velocity vs. depth model derived by Priestly and Brune [18] from an analysis of Rayleigh and Love wave dispersion on paths crossing the area of interest in the Great Basin of Eastern Nevada was incorporated into the synthetic seismogram modeling. The starting T-7 and Priestly-Brune (P/B) velocity models are shown by dotted lines in Fig. 5. The generic T-7 P-wave model has a pronounced mantle lid with a strong positive P-velocity gradient beneath the Moho for depths from 33 to 65 km. Calculation of synthetics for this lid structure gave very large amplitudes for the "P_n" arrival, which was superimposed on a strong reflection from the base of the lid at 65 km [16]. Thus, the T-7 + P/B starting model gave results very different from observations. However, as seen in Fig. 5, only small changes to the initial model were necessary to match the observations. To bring the calculated synthetic seismograms into agreement with observations, the gradient at the base of the LVZ had to be raised to shallower depths and the positive gradient lid replaced with a smooth but gradual negative gradient starting at the M-discontinuity. The final model, A-10, that matches observations is shown by the solid lines in Fig. 5. Figure 6 is the comparison between the observed and synthetic record sections. Interestingly, no discontinuity in P-velocity is necessary to explain the P_{lid} reflections; the reflections can be adequately modeled by a small negative step in S velocities at a depth of about 100 km. The synthetics, however, do not seem to adequately model the long oscillatory trains following the P_1 phase onset. This is probably due to interference effects caused by fine structure in the lower LVZ velocity gradient that we have not yet modeled by thin enough layers in the calculation [16].

These calculations illustrate that synthetic modeling techniques can be helpful in phase identification and in quantitative calculations of amplitude vs. distance behavior and waveform characteristics. With a sophisticated reflectivity method calculation we were able to model several important features of

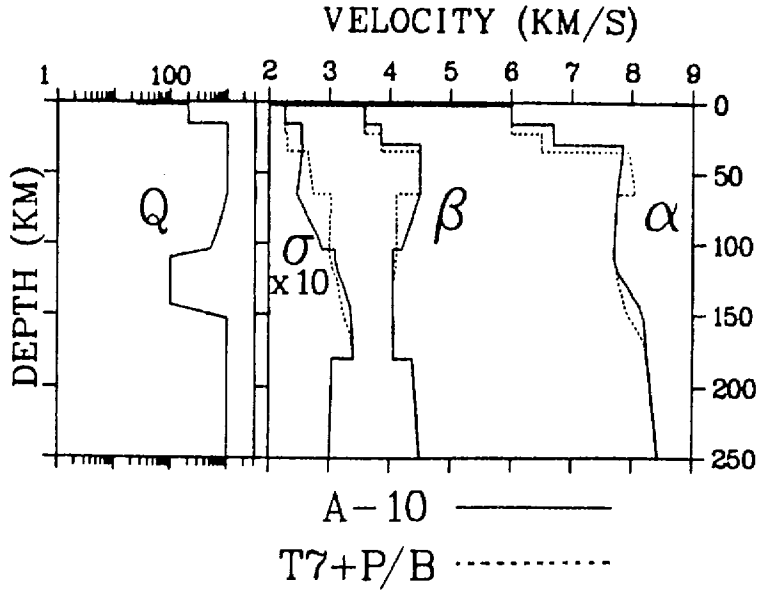

Fig. 5. P-velocity (α) and S-velocity (ß) vs. depth plots for the T-7/Priestly-Brune and A-10 models. Assumed Q structure at left: σ (dimensionless) is Poisson's ratio.

regional short-period seismograms. The technique appears promising in advancing knowledge of wave propagation and source identification at regional distance ranges.

ACKNOWLEDGMENTS

We especially thank Rainer Kind for making available to us the modified reflectivity method computer program that we have adapted for our analyses. Paul A. Johnson was responsible for the computer runs. We thank Terry C. Wallace and Mike Shore for discussions and for reviewing the manuscript. The calculational and data reduction efforts for this research were supported by the U.S. Department of Energy and partially by ONR Earth Physics Program grant N00014-75-C-0972 to L.W.B. The Snake River Plains data were collected during research partially funded by the U.S. National Science Foundation (grant EAR-77-23707 to the University of Utah and EAR-77-23357 to Purdue University) and by the U.S.G.S. Geothermal Research Program grant 14-08-0001-G-532 to Purdue.

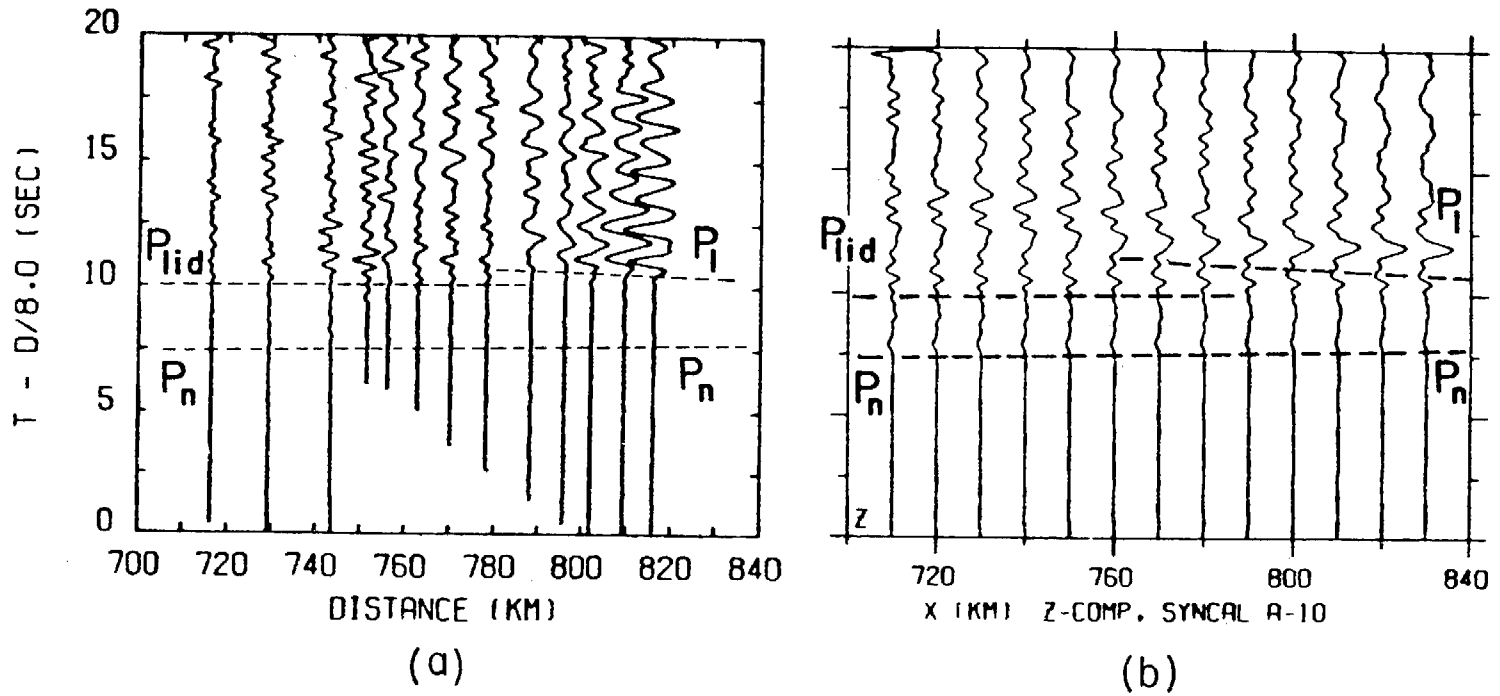

Fig. 6. Comparison of the observed (a) record section with the synthetic section calculated from the A-10 model (b).

REFERENCES

1. A. I. Ruzaikin, I. L. Nersesov, V. I. Khalturin, and P. Molnar, J. Geophys. Res. 82, pp. 307-316, 1977.
2 L. Knopoff, F. Schwab, K. Nakanishi, and F. Chang, Geophys. J. R. Astr. Soc. 39, pp. 41-70, 1974.
3. V. Z. Ryaboi, Izv. (Bull.) Acad. Sci. USSR, Geophys. Ser., AGU Trans. 3, pp. 177-184, 1966.
4. R. P. Masse, Bull. Seism. Soc. Am. 63, pp. 911-935, 1973.
5. A. Hirn, L. Steinmetz, R. Kind, and K. Fuchs, Z. Geophys. 39, pp. 363-384, 1973.
6. R. Kind, J. Geophys. 40, pp. 189-202, 1974.
7. C. B. Archambeau, E. A. Flinn, and D. G. Lambert, J. Geophys. Res. 74, pp. 5825-5865, 1969.
8. L. J. Burdick and D. V. Helmberger, J. Geophys. Res. 83, pp. 1699-1712, 1978.
9. J. E. York and D. V. Helmberger, J. Geophys. Res. 78, pp. 1883-1886, 1973.
10. M. Cara, Geophys J. R. Astr. Soc. 57, pp. 649-670, 1979.
11. B. A. Romanowicz and M. Cara, Geophys. Res. Lett. 7, pp. 417-420, 1980.
12. A. L. Hales, Earth and Planet. Sci. Lett. 7, pp. 44-46, 1969.
13. D. P. Hill, Geol. Soc. Am. Bull. 83, pp. 1639-1648, 1972.
14. K. Fuchs and G. Müller, Geophys. J. R. Astr. Soc. 23, pp. 417-433, 1971.
15. R. Kind, J. Geophys. 44, pp. 603-612, 1978.
16. K. H. Olsen, L. W. Braile, and P. A. Johnson, Geophys. Res. Lett. 7, pp. 1029-1032, 1980.
17. G. Müller, J. Geophys. 42, pp. 429-436, 1977.
18. K. Priestly and J. Brune, J. Geophys. Res. 83, pp. 2265-2272.
19. K. Fuchs, Tectonophysics 56, pp. 1-15, 1979.
20. L. Knopoff, Rev. Geophys. 2, pp. 625-660, 1964.